The Dissertation Committee for Rik Dey

certifies that this is the approved version of the following dissertation:

Theoretical and Experimental Studies on Topological Insulators and Topological Insulator Based Spintronic Devices

Committee:

Sanjay K. Banerjee, Supervisor

Leonard F. Register, Co-Supervisor

Maxim Tsoi

Jean Incorvia

Edward T. Yu

Theoretical and Experimental Studies on Topological Insulators and Topological Insulator Based Spintronic Devices

by

Rik Dey

Dissertation

Presented to the Faculty of the Graduate School

of the University of Texas at Austin

in Partial Fulfillment

of the Requirements

for the Degree of

Doctor of Philosophy

The University of Texas at Austin

August 2019

Acknowledgments

I would like to thank my supervisor Dr. Sanjay Banerjee, for giving me the great opportunity to work in his group, and for his invaluable advice and guidance throughout my research. This work would not have been possible without the continuous help and support from him. I also thank him for giving me the freedom to work in my own way, which has helped me to develop my knowledge, skills and experience.

I would like to thank my co-supervisor Dr. Leonard Register for his continuous guidance and help throughout my PhD study. I have learned a lot from his many invaluable suggestions and insights. I sincerely thank him for his endless effort to make this work publishable.

I would also like to thank Dr. Maxim Tsoi, Dr. Jean Incorvia, and Dr. Edward Yu, for being in my dissertation committee, and for their suggestions and advice to my research.

I am grateful to many teachers in my life throughout, and I would like to thank all of them for their beautiful teachings that have helped me in many ways towards my PhD.

I would like to thank all my group members, past and present, for helping me on numerous occasions, on an everyday basis. I specially thank Anupam Roy, Sarmita Majumder, Bahniman Ghosh, Sushant Shonde and Samaresh Guchhait. I also thank my colleagues Tanmoy Pramanik, Nitin Prasad, Aquian Bhatti, Xian Wu, Sai Subrahmanya Teja, Hema C P Movva, Stefano Larentis, Kyounghwan Kim, Omar Mohammed, Atresh Sanne, Maruthi Yogesh, Hasibul Alam Dalim, Sayema Chowdhury, Amithraj Valsraj, Dax Crum, Urmimala Roy, and others for many useful discussions and conversations.

My sincere thanks goes to the staffs of Microelectronics Research Center, especially Ricardo Garcia, William James and Johnny Johnson for training me on the tools and helping me whenever I needed it. I would also like to thank Jean Toll, Melanie Gulick and Christine Wood for their help in all the administrative matter.

Finally, I would like to thank my parents, *Ma* and *Baba*, for their unconditional love and support, and for motivating me throughout my graduate research.

Theoretical and Experimental Studies on Topological Insulators and Topological Insulator Based Spintronic Devices

Rik Dey, Ph.D.

The University of Texas at Austin, 2019

Supervisor: Sanjay K. Banerjee

Co-Supervisor: Leonard F. Register

Three dimensional (3D) topological insulators (TIs) are unique materials with insulating bulk and two dimensional (2D) metallic surface states having spin-momentum locked Dirac-band dispersion. The remarkable property of spin-momentum locking of the 2D surface states provides an opportunity for manipulating the coupled spin and charge degrees of freedom of electrons on the surface of a 3D TI by controlling one or the other. The charge current-induced spin polarization of the 2D surface states of a 3D TI and subsequent diffusion or tunneling of spin current in an adjacent material, or conversion of spin current to charge current on the surface of a 3D TI, are a few among many effects of this spin-momentum locking, which renders TIs as promising candidates for spintronic applications.

In this dissertation, we provide a theoretical description of the electronic transport of the TI surface states in proximity to a non-magnetic (NM) or a ferromagnetic (FM) material, and derive the transport equations based on quantum kinetic equation of non-equilibrium Greens function. The transport equations are solved for appropriate boundary conditions to obtain the efficiency of the spin current-to-charge current conversion in TI/NM/FM or TI/FM heterostructure, or to calculate the efficiency of the detection of charge current induced spin polarization on the surface of a TI with FM tunnel contacts. We find that these efficiencies strongly depend on the tunnel conductance of the interface and decreases with increasing tunnel conductance, implying the necessity of design optimization of the tunnel interface in actual devices.

Here, we also describe low-temperature magnetotransport measurements on an epitaxial Bi_2Se_3 thin film, and identify the contribution of the surface states and the quasi-2D bulk states to the transport from localization and interaction effects. We present two-terminal resistance measurement with FM and NM contacts on the surface of epitaxial and exfoliated Bi_2Te_3 films, and find change of resistance with reversal of the FM magnetization direction. We also measure magnetic hysteresis properties of sputtered Bi_2Te_3-Fe heterostructure and obtain enhancement of coercive field of Fe in the heterostructure, which could be due to strong spin-orbit coupling proximity effect arising from the Bi_2Te_3 film.

Table of Contents

List of Figures

Chapter 1

Introduction

The three-dimensional (3D) topological insulators (TIs) are novel materials with bulk states having a non-zero band gap and gapless metallic two-dimensional (2D) surface states having a Dirac-cone band dispersion with spin-momentum helical locking protected by the time-reversal symmetry[1, 2, 3, 4, 5, 6]. Because of the spin-momentum helical locking of these time-reversal symmetry protected 2D surface states of a 3D TI, the surface states possess unique quantum-mechanical property called the π- Berry phase that get revealed in various electrical transport of these surface states as weak antilocalization (WAL) effect, Shubnikov-de Haas (SdH) oscillations, quantum Hall effect (QHE), Aharonov-Bohm (AB) effect, to name a few[1, 2, 3]. Also, the spin-momentum locking of the surface states gives rise to a way of manipulating the spin via charge and vice versa[7, 8], such as charge current-induced spin-polarization of the surface states, conversion of charge current to spin current known as the Edelstein effect (EE)[9], and conversion of spin current to charge current known as the inverse Edelstein effect (IEE)[10]. The charge current-induced spin polarization of the TI surface states and generation of a spin current in an adjacent ferromagnet (FM) from the charge current on the TI surface can be used to torque the FM efficiently[7, 8, 11, 12, 13]. Also, for low-energy switching of nanomagnets on the TI surface, novel mechanism has been proposed based on Ruderman-Kittel-Kasuya-Yosida (RKKY) interactions mediated by the surface states of a TI and controlled by an external gate[14]. Various exciting properties of the TI surface states, which are consequences of the spin-momentum locked Dirac-cone band structure, provide TIs a suitable platform for potential spintronic applications[7, 8, 15, 16].

The existence of gapless surface states with insulating bulk is a consequence of strong spin-orbit coupling (SOC) that leads to the band inversion[1, 2, 3]. The heavy metals, such as Bi and Sb, have strong SOC, and compounds with these elements are predicted to be possible candidates for 3D TIs[1, 2, 3, 4, 5, 6]. By calculating the band structure from first principles and verifying it experimentally, it was shown in the literature that binary compounds Bi_2Se_3, Bi_2Te_3, Sb_2Te_3, and ternary as well as quaternary compounds with various combinations of Bi, Sb, Te and Se, are 3D TI materials[1, 2, 3].

In this work, we grow and use the binary TIs Bi_2Se_3 and Bi_2Te_3 for various experiments, and in next section we will describe only the crystal structure of these binary TIs. However, the band structure and various properties of the TI surface states that we will discuss in upcoming sections are true for other TIs as well. We only discuss those properties of the TI surface states that are relevant to this work, the discussion of other exciting and exotic properties of the TIs can be found in many excellent reviews on this subject in the literature.

1.1 Crystal structure of binary TIs: Bi_2Se_3 and Bi_2Te_3

Figure 1.1 shows the crystal structure of the binary TIs Bi_2Se_3 which has rhombohedral crystal structure with five-atom unit cell[5]. The three primitive lattice vectors t_1, t_2, t_3 and one quintuple layer (QL) consisting of five atomic layers are shown in Figs. 1.1(a) and 1.1(c). The five atomic layers in a QL are stacked in A-B-C manner as shown in Figs. 1.1(b) and 1.1(c). As shown in Fig. 1.1(c), both Bi1 and Bi1' atoms are equivalent and both Se1 and Se1' atoms are equivalent from symmetry point of view. The third Se2 atom is different from Se1 or Se1' and is the inversion center for the inversion in which Bi1 goes to Bi1' and Se1 goes to Se1'. The crystal structure of Bi_2Te_3 is same as that of Bi_2Se_3 with the Se atom replaced by the Te atom[5]. The interactions between two QLs are van-der

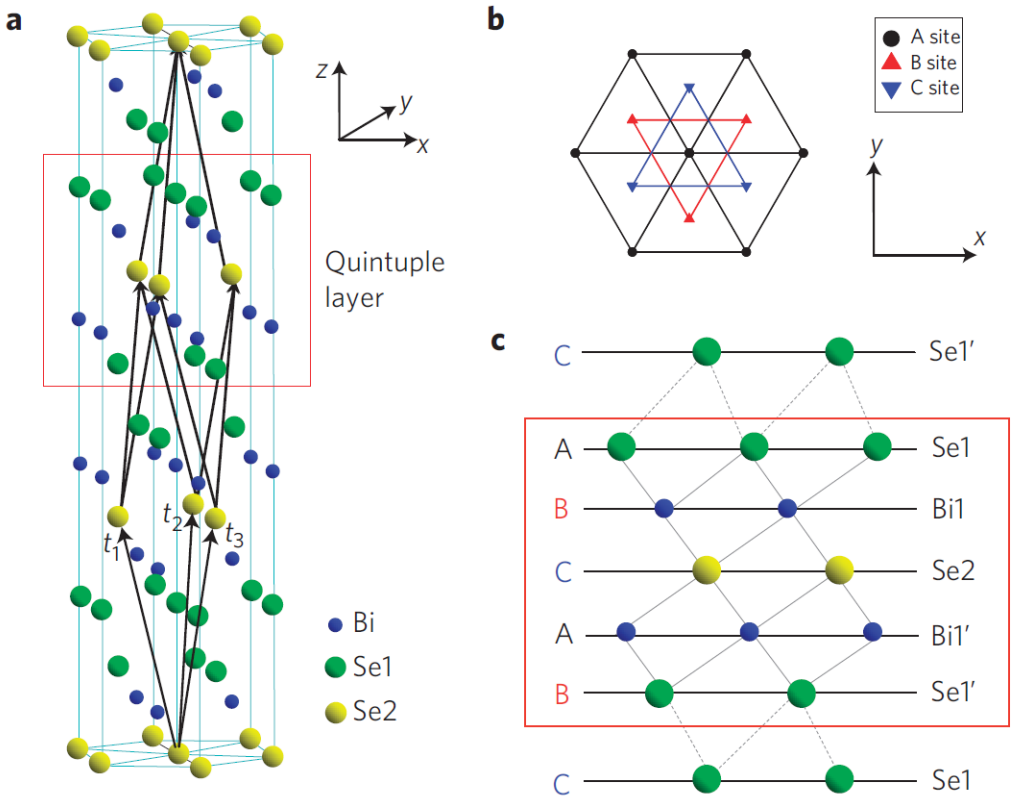

Figure 1.1: Crystal structure of Bi_2Se_3 showing arrangement of the constituent atoms: (a) The crustal structure of Bi_2Se_3 showing three primitive lattice vectors $t_{1,2,3}$ and a quintuple layer (QL) indicated by red box, (b) Top view of the crystal structure, (c) Side view of the quintuple layer. Reprinted by permission from Macmillan Publishers Limited: Nature, *Nature Physics* **5**, 438-442, "Topological insulators in Bi_2Se_3, Bi_2Te_3 and Sb_2Te_3 with a single Dirac cone on the surface", H. Zhang, C.-X. Liu, X.-L. Qi, X. Dai, Z. Fang, and S.-C. Zhang, Copyright 2009. Available: https://doi.org/10.1038/nphys1270. (Ref. [5] in this dissertation)

Waals interactions, whereas within a QL the interactions between the atoms are covalent and stronger, which makes the material a layered material.

1.2 Different growth methods for Bi_2Se_3 and Bi_2Te_3

Bi_2Se_3 and Bi_2Te_3 are layered material and can be easily exfoliated from bulk single crystal which can be grown by Bridgman method. The direct growth of thin films of Bi_2Se_3

and Bi_2Te_3 can be achieved by van-der Waals epitaxy on different substrates, such as Si(100), Si(111), GaAs, InAs, mica, sapphire, SiO_2 on Si, with various different growth techniques such as molecular beam epitaxy (MBE), chemical vapor deposition (CVD), pulsed laser deposition (PLD) and sputtering[17]. In this work we have grown thin films of Bi_2Se_3 and Bi_2Te_3 on smooth reconstructed Si(111)-(7×7) surfaces in an MBE chamber, and also sputtered Bi_2Te_3 thin films on Si(100), SiO_2 on Si and sapphire substrates.

1.3 Band structure of the TI surface states

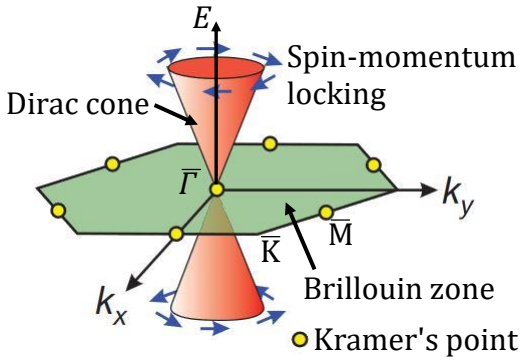

Figure 1.2: Band structure of the TI surface states showing Dirac cone dispersion: Dirac cone is centered at the $\bar{\Gamma}$ point in the Brillouin zone and the spin-momentum helical locking of the surface states are shown. Adapted by permission from Macmillan Publishers Limited: Nature, *Nature* **460**, 1101-1105, "A tunable topological insulator in the spin helical Dirac transport regime", D. Hsieh, Y. Xia, D. Qian, L. Wray, J. H. Dil, F. Meier, J. Osterwalder, L. Patthey, J. Checkelsky, N. P. Ong, A. V. Fedorov, H. Lin, A. Bansil, D. Grauer, Y. S. Hor, R. J. Cava, and M. Z. Hasan, Copyright 2009. Available: https://doi.org/10.1038/nature08234. (Ref. [6] in this dissertation)

The 2D surface states of 3D TI materials can be described by a low energy effective Hamiltonian around the Dirac point, which is the Γ point in the reciprocal space as shown in Fig. 1.2. The low energy effective Hamiltonian of the gapless TI surface states is[1, 2, 3]

$$H = \hbar v_F (k_y \sigma_x - k_x \sigma_y), \tag{1.1}$$

where $\hbar$ is the reduced Planck constant, v_F is the Fermi velocity of the TI surface states, k_x, k_y are the x and y components of the in-plane momentum, and σ_x, σ_y are the Pauli spin matrices. The spin-momentum helical locking of the surface states given by the Hamiltonian in Eq. 1.1 are sown in Fig. 1.2. The dispersion relation of the surface state Hamiltonian is linear and is given by $E(k) = \hbar v_F k$, where $k = \sqrt{k_x^2 + k_y^2}$.

The actual Hamiltonian of the surface states describing the band-structure away from the Dirac point can deviate from that given in Eq. 1.1, and become non-linear with a slight curvature. For Bi_2Se_3, such non-idealities are much less than in Bi_2Te_3, and constant energy Fermi surface remains spherical away from the Dirac point[1, 2, 3]. However, in Bi_2Te_3, because of hexagonal warping, there will be additional cubic term in the Hamiltonian in Eq. 1.1 and the constant energy Fermi surface for Bi_2Te_3 deviates significantly from being spherical[1, 2, 3].

1.4 Surface states and bulk states in TI thin films

In thin films of TIs, the two opposite surfaces of the thin films get coupled below a certain thickness limit (typically 4 nm or less), and there will be a gap opening in the band structure of the surface states around what would otherwise be the Dirac point[19, 20, 21]. Also, in the thin film, the bulk states of the TI will be divided into separate quasi-2D sub-bands because of the confinement of the wave-functions in the surface normal direction due to finite thickness[18]. Figure 1.3 shows the evolution of the band structure of the surface states and the bulk states of a TI as the thickness of the TI decreases.

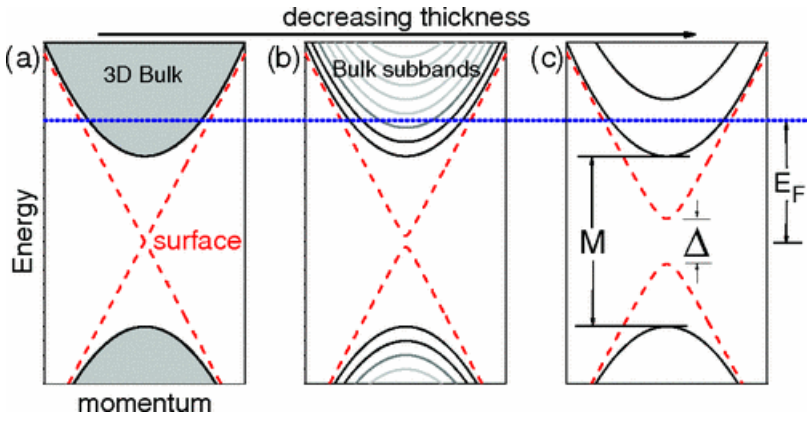

Figure 1.3: Evolution of TI band structure in thin films with decreasing thickness: (a) TI band structure for a thick film showing linear dispersion of the surface states, (b) as thickness increases, the bulk-states divides into sub-bands and there is a gap opening near the Dirac point for the surface states, (c) band structure of the surface states and the bulk states in an ultra-thin film showing the Fermi level E_F, the gap Δ of the surface states and the gap M of the bulk states around the Dirac point. Reprinted figure with permission from: Hai-Zhou Lu and Shun-Qing Shen, *Physical Review B* **84**, 125138 (2011), Copyright 2011 by the American Physical Society. Available: https://doi.org/10.1103/PhysRevB.84.125138. (Ref. [18] in this dissertation)

1.5 Weak localization effect from the bulk states and weak antilocalization effect from the surface states in TI thin films

Weak localization (WL) and weak antilocalization (WAL) effects are pure quantum mechanical phenomenons due to wave nature of electrons and the properties of the spin nature of the bulk states and the surface states of a TI[22]. Without any coupling of the spin degree of freedom with the motion of the electrons, the electronic wave functions of two time reversed path interfere constructively which enhances the probability of finding an electron in a certain position making electron localized in space. The effect of localization of electrons reduces the transmission probability of the electrons, thus increases the resistance from that predicted by the Drude model. The quantum mechanical correction to the Drude conductivity due to localization of the electrons is known as the WL effect[22].

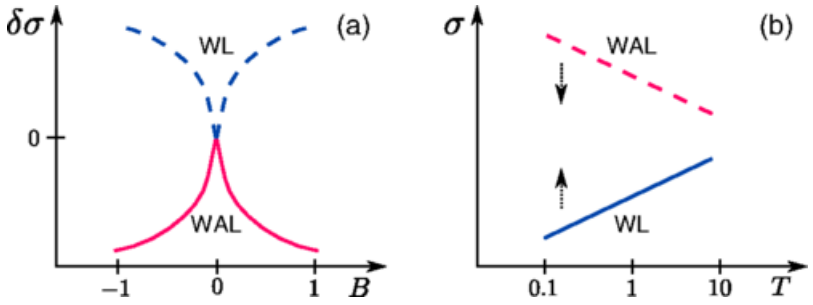

Figure 1.4: Change of conductance with applied magnetic field and with temperature due to destruction of WL and WAL: (a) Change of conductance ($\delta\sigma$) is positive with an applied magnetic field B for WL and negative with the applied field B for WAL, (b) Conductance (σ) increases with increasing temperature T for WL and decreases with the increasing T for WAL. Reprinted figure with permission from: Hai-Zhou Lu and Shun-Qing Shen, *Physical Review Letters* **112**, 146601 (2014), Copyright 2014 by the American Physical Society. Available: https://doi.org/10.1103/PhysRevLett.112.146601. (Ref. [23] in this dissertation)

In case of TI surface states, because of spin-momentum locking there is an additional π Berry phase associated with the electronic wave-function that causes destructive interference of electronic wave-functions in two time-reversed path instead of the constructive interference[23, 24, 25, 26]. The destructive interference of electronic wave-functions thus de-localizes the electrons and increases the transmission probability of the electrons, thus reduces the resistance from that predicted by the Drude model. The quantum mechanical correction to the Drude conductivity due to the de-localization of the electrons is known as the WAL effect.

In an applied magnetic field, the constructive or the destructive interference of the electronic wave-function is lost because of acquiring random phases for different paths. In case of TI surface states, the loss of destructive interference leads to a loss of de-localization of the electrons and the conductance decreases (resistance increases) with the magnetic field B which is a signature of WAL as shown in Fig. 1.4(a). However, the opposite happens in case of WL, and with the applied magnetic field, the constructive interference of electronic wave-function and the localization of the electrons are lost, hence the conductance increases

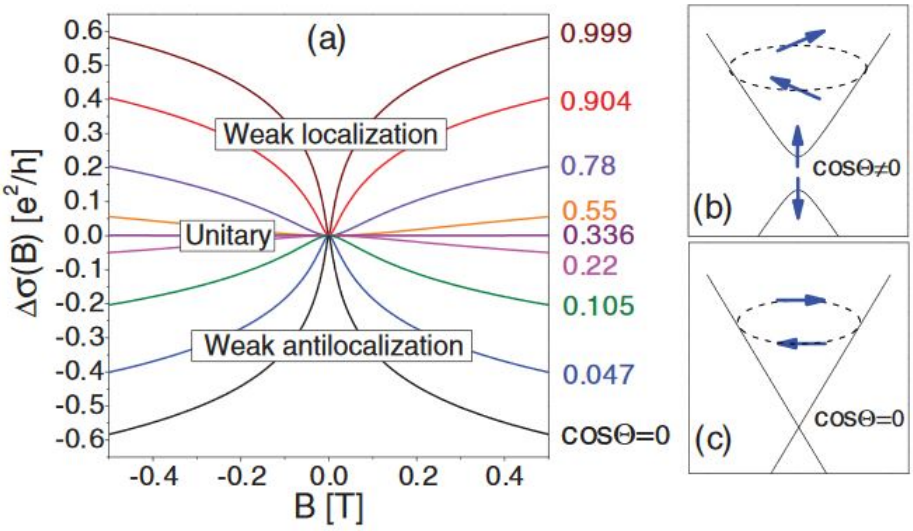

Figure 1.5: Change of conductance with applied magnetic field due to destruction of WL and WAL in TI thin films: (a) Change of conductance ($\Delta\sigma$) with an applied magnetic field B for WL to unitary to WAL behavior, (b) Schematics of the spin-momentum locking of the electrons near the gap and deep into the bulk, (c) Schematics of the spin-momentum locking of the electrons in a Dirac cone without any gap opening. Reprinted figure with permission from: Hai-Zhou Lu and Shun-Qing Shen, *Physical Review B* **84**, 125138 (2011), Copyright 2011 by the American Physical Society. Available: https://doi.org/10.1103/PhysRevB.84.125138. (Ref. [18] in this dissertation)

(resistance decreases) with the magnetic field B as shown in Fig. 1.4(a). Similarly, with increasing temperature, the interference of the electronic wave-functions is destroyed, and the conductance decreases (resistance increases) with the temperature T for WAL and the conductance increases (resistance decreases) with the temperature T for WL, as shown in Fig. 1.4(b). For both the cases of WAL and WL, the change of the conductivity is logarithmic with temperature as shown in Fig. 1.4(b). The electron-electron interaction effect (EEI) also gives rise to logarithmic temperature dependent conductivity, however the slope of the logarithmic temperature dependent conductivity curve is different from what is obtained in case of WAL or WL effect.

It was shown theoretically that the electrons in the surface states and the quasi-2D bulk states of a thin TI film could give rise to behavior ranging from WL to WAL depending on

the position of the Fermi level in the surface states and the bulk state[18, 23, 26], as shown in Fig. 1.5(a)-(b). If the Fermi level lies deep into the band, then the spin-momentum helical locking is almost intact which corresponds to $\cos\Theta \approx 0$ and WAL effect will be observed. If the Fermi level lies near the gap, the spin-momentum locking is completely lost which corresponds to $\cos\Theta \approx 1$ and WL effect will be observed. In case of a thick TI film, the Dirac cone dispersion of the surface states remains intact which corresponds to $\cos\Theta = 1$ irrespective of the position of the Fermi level, as shown in Fig. 1.5(c).

1.6 Charge current-induced spin polarization of the TI surface states

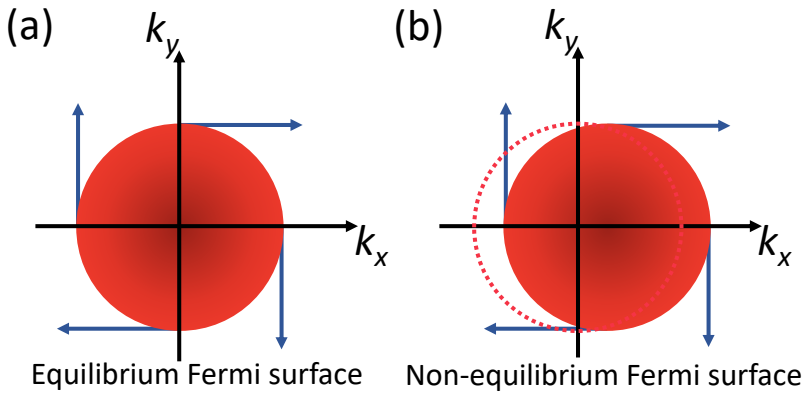

Figure 1.6: Charge current-induced spin polarization of the TI surface states: (a) Equilibrium Fermi surface with no net charge current and no net spin polarization, (b) Non-equilibrium Fermi surface shifted in k-space resulting in a net charge current and associated net spin polarization.

Due to the spin momentum locking of the surface states of a TI, a charge current flowing on the TI surface will produce a non-zero spin polarization of the surface states as shown in Fig. 1.6. In equilibrium, the Fermi surface is centered around zero in the k-space, and there will be no net charge current or spin polarization on the TI surface, as shown in Fig. 1.6(a). In non-equilibrium condition, due to an applied electric field, the Fermi surface will

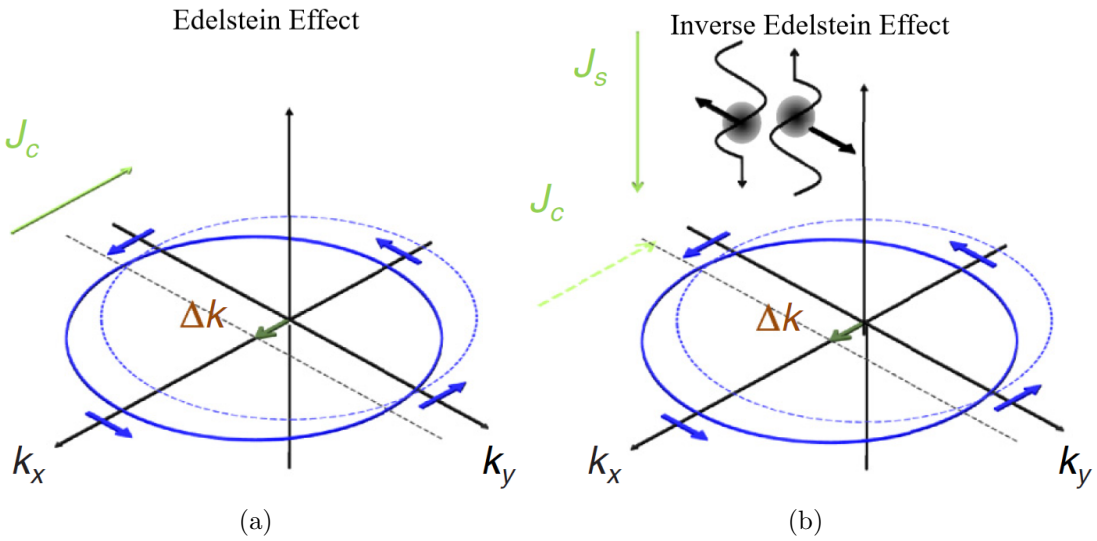

Figure 1.7: Edelstein effect and inverse Edelstein effect from the TI surface states: (a) Edelstein effect (EE), (b) Inverse Edelstein effect (IEE). Reprinted figure with permission from: S. Zhang and A. Fert, *Physical Review B* **94**, 184423 (2016), Copyright 2016 by the American Physical Society. Available: https://doi.org/10.1103/PhysRevB.94.184423. (Ref. [27] in this dissertation)

be shifted in the k-space and a net charge current will flow on the TI surface. Due to the shift of the Fermi surface in the k-space, there will be a net non-zero spin polarization on the TI surface associated with the charge current flow, as shown in Fig. 1.6(b).

1.7 Edelstein effect and inverse Edelstein effect from TI surface states

The charge current induced spin polarization of the TI surface states could create a diffusive or tunnel spin current in an adjacent material, and this charge current-to-spin current conversion is known as the Edelstein effect (EE)[9, 27]. Alternately, a spin current injected onto the surface of a TI will create an imbalance of the spin-polarized electrons on the TI surface, and because of the spin-momentum locking of the surface states, the

injected spin-polarized electrons will preferentially move in one direction giving rise to a charge current flowing on the TI surface. This spin current-to-charge current conversion is known as the inverse Edelstein effect (IEE)[10, 27].

Figure 1.7(a) and 1.7(b) show schematically the phenomenon of the EE and the IEE arising from the spin-momentum locking of the TI surface states[27]. The charge current-induced spin polarization of the TI surface states can be detected experimentally using FM voltage probes on the TI surface[28, 29, 30, 31, 32, 33, 34, 35, 36, 37, 38, 39, 40]. The charge current-induced spin polarization and the EE can be used to switch a FM on the surface of a TI using field-like torques from the charge current-induced spin-polarization and spin-transfer torque from the spin current produced by the EE effect[7, 8, 11, 12, 13]. The IEE can be detected experimentally either by injecting pure spin current from spin-pumping in a FM[41, 42, 43, 44, 45, 46, 47, 48, 49] or by injecting spin-polarized charge current from a FM to the surface of a TI through a tunnel barrier[31], and measuring the induced open circuit voltage at the two ends of the TI surface.

1.8 Detection of IEE from spin-pumping experiment

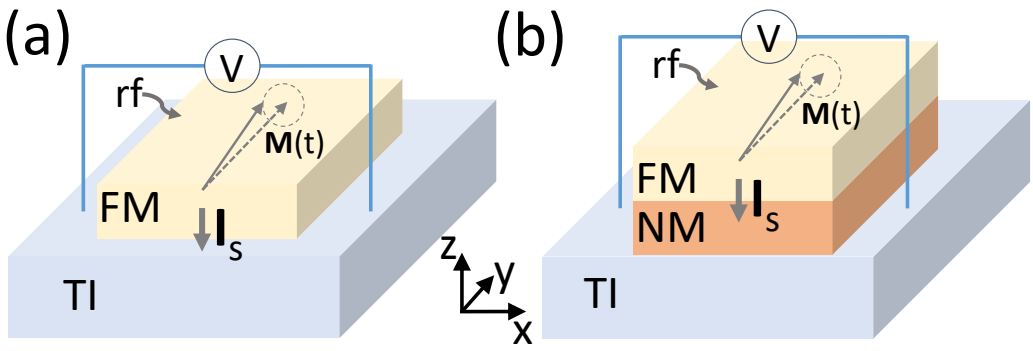

Figure 1.8: Detection of the inverse Edelstein effect from the TI surface states in spin-pumping experiments: (a) TI/FM heterostructure, (b) TI/NM/FM heterostructure.

In the spin-pumping experiment, a pure spin current is generated by spin precession in the FM and flows to the TI surface either directly in a TI/FM heterostructure, as shown in Fig. 1.8(a)[43, 44, 45, 46, 47], or through a nonmagnetic metal (NM) layer in a TI/NM/FM heterostructure, as shown in Fig. 1.8(b)[42, 48, 49]. The injected spin current on the TI surface produces a charge current on the surface of the TI because of spin-momentum helical locking of the TI surface states. If the two ends of the TI surface are shorted, then a charge current will flow on the surface and can be measured by an external circuit. However, in the experiment as shown in Figs. 1.8(a) and 1.8(b), an open circuit voltage was measured by an external electrical circuit. The open circuit voltage is developed to oppose the flow of the induced charge current on the TI surface due to the injected spin current and is a measure of the spin current-to-charge current conversion efficiency.

1.9 Detection of IEE from spin-polarized tunneling experiment

In the spin polarized tunneling experiment in a TI/tunnel barrier(TB)/FM heterostructure as shown in Fig. 1.9, a charge current is injected from the FM onto the surface of the TI[31]. Because of the density of state polarization of majority and minority spins in the FM, the injected charge current is spin-polarized and will produce a transverse charge current on the TI surface due to the spin momentum helical locking of the surface states. An open circuit voltage is developed to oppose the flow of the transverse charge current on the TI surface and is measured by an external electrical circuit.

As shown in Fig. 1.9, a charge current is passed from the FM to the TI surface and extracted at one ends of the TI surface such that the current path on the TI surface is aligned with magnetization direction of the FM, in the y-direction as shown in Fig. 1.9. In the experiment, it was shown that the open-circuit voltage, which was measured transverse

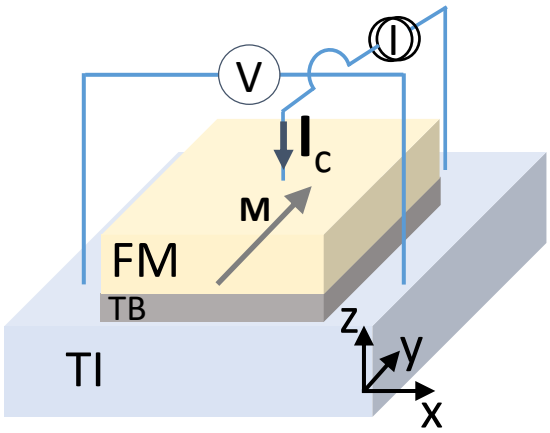

Figure 1.9: Detection of the inverse Edelstein effect from the TI surface states in a spin-polarized tunneling experiment.

to the direction of the current path, along the x-direction as shown in Fig. 1.9, changes sign as the magnetization of the FM is reversed. The change of sign of the measured voltage upon reversing the magnetization of the FM happens because the induced charge current produced by the spin-polarized electrons flows in the opposite direction of that before, hence the sign of the transverse voltage, which opposes the flow of the electrons, also gets reversed.

1.10 Detection of charge current-induced spin polarization of TI surface states

The spin momentum helical locking of the band structure of the 2D surface states of a 3D TI ensures that the orientations of the spins of the surface states will lie on the surface plane of the TI at right angle relative to the charge flow. Such spin polarization of the surface states due to the charge transport on the surface of a TI was detected experimentally in four-terminal and three-terminal measurement geometry with FM tunnel contacts, as shown in Figs. 1.10(a) and 1.10(b), respectively.

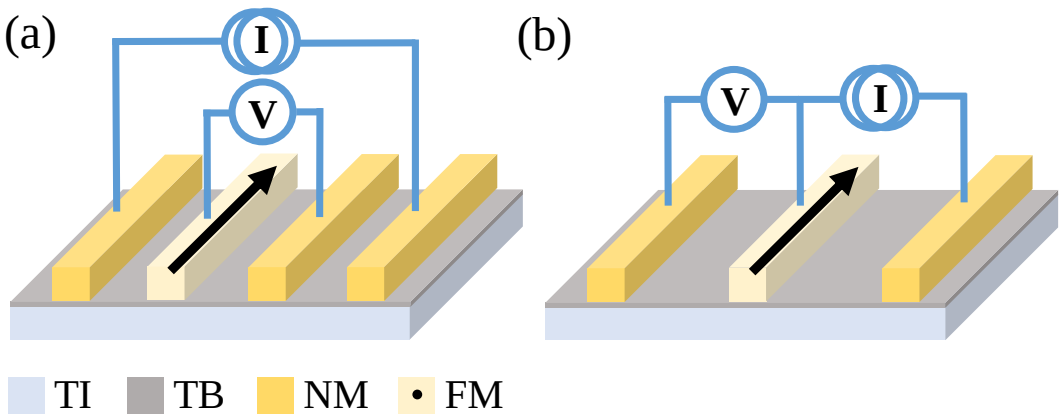

Figure 1.10: Detection of the charge current-induced spin polarization of the TI surface states: (a) Four-terminal measurement geometry, (b) Three-terminal measurement geometry.

The magnitude of the charge current-induced spin polarization of the TI surface states is proportional the charge current density on the TI surface, and the spin-polarization direction is perpendicular to the direction of the current on the surface of the TI[33, 50, 51, 52, 53, 54]. It was shown that the measured voltages on the FM contacts in the experiments shown in Fig. 1.10 depend on the magnitude of the charge current on the TI surface and the projection of the FM magnetization direction to the current-induced spin polarization direction of the TI surface states[33, 50, 51, 52, 53, 54]. The necessity of the tunnel contact to measure such spin-voltage was demonstrated clearly with controlled experiments without a tunnel barrier[28, 29, 30, 31, 32, 33, 34, 35, 36, 37, 38, 39, 40].

In a multi-terminal spin-detection measurement, the resistance always obeys Onsager reciprocity, i.e., $R_{ab,cd}(+\vec{M}) = R_{cd,ab}(-\vec{M})$, where $R_{ab,cd}$ is the resistance measured with current injected between contacts a and b, voltage measured between contacts c and d, and the FM having magnetization $\vec{M}$[50, 54, 55]. It was shown experimentally that the Onsager reciprocity relation is satisfied in three-terminal and four-terminal measurement geometries[28, 29, 30, 31, 32, 33, 34, 35, 36, 37, 38, 39, 40]. However, in a two-terminal measurement in which the current and the voltage contacts are the same, Onsager reciprocity

dictates that the resistance remains the same even after the magnetization of the FM is reversed, i.e., $R_{ab,ab}(+\vec{M}) = R_{ab,ab}(-\vec{M})$. In the literature, two-terminal measurement with two FM contacts on the surface of TIs showed different resistance when the magnetization of both the FMs are reversed, which violates the Onsager reciprocity[56, 57]. In this work, we report two-terminal measurement with a FM and a NM contact on the surface of Bi_2Te_3.

1.11 Outline of the dissertation

This dissertation presents theoretical and experimental studies on TIs and TI based devices for spintronic applications. In the following, we briefly outline the main focus of each of the upcoming chapters:

In chapter 2, we develop the theory of IEE on the surface of a TI in a spin-pumping experiment as illustrated in section 1.8. The transport equations for the TI surface states coupled to the adjacent NM are derived both from semi-classical Boltzmann transport equation and quantum kinetic theory based on non-equilibrium Green's function. Then we solve the transport equations on the TI surface for a given a spin current injected onto the TI surface through the NM to find the spin current-induced charge-current on the TI surface for the short circuit case, or to find the induced open-circuit voltage which is measured in an experiment as described in section 1.8.

In chapter 3, we develop the theory of IEE on the surface of a TI in a spin-polarized tunneling experiment as discussed in section 1.9. The transport equations for the TI surface states coupled to the adjacent FM are derived from quantum kinetic theory based on non-equilibrium Green's function, and then we solve the transport equations on the TI surface given a charge current injected from the FM to the TI surface for a rectangular geometry of

the TI/FM heterostructure. We calculate the open-circuit voltage in the transverse direction that is measured in the experiment as mentioned in section 1.9. We find that the magnitude of the open-circuit voltage decreases with increasing tunnel conductance of the interface supporting the importance of the tunnel barrier used in the experiment.

In chapter 4, we extend the work of the previous chapter, i.e., chapter 3, and provide a different way of deriving the transport equations on the TI surface coupled to the FM starting from quantum kinetic theory based on non-equilibrium Green's function. We solve transport equations to calculate the voltage measured in three- and four-terminal measurement geometries consisting of FM and NM contacts in a spin detection experiment as discussed in section 1.10. The efficiency of the spin-detection is calculated and it is found that the efficiency decreases with increasing tunnel conductance of the TI/FM contact indicating the necessity of tunnel contact in such experiments. We also show that the Onsager reciprocity relation remains valid in multi-terminal and two-terminal measurements on the surface of a diffusive TI.

In chapter 5, low temperature magnetotransport properties of an epitaxially grown Bi_2Se_3 thin film are studied extensively. We identify both the surface state and bulk state contributions to the transport in the thin film from logarithmic temperature dependent conductivity correction due to WAL from the surface states and WL from the bulk states along with EEI effects from both the surface states and the bulk states, as discussed in section 1.5. Considering WAL effect from the surface states and WL localization effects from the bulk states, the magnetoresistance of the thin film are analyzed for magnetic field applied perpendicular, parallel or tilted to the plane of the sample surface.

In chapter 6, we discuss the experimental result obtained in a two terminal resistance measurement in an applied magnetic field with one FM and other NM contact deposited on

the surface of epitaxially grown and exfoliated Bi_2Te_3 films. It is found that the two-terminal resistance changes when the FM magnetization direction changes with the applied magnetic field that lies in the plane of the surface and is perpendicular to the current flow on the TI surface. As discussed in section 1.10, the change of two-terminal resistance with reversal of FM magnetization direction violates Onsager reciprocity. We propose alternate explanation of the experimental results indicating role of long-lived nuclear spins of Bi in Bi_2Te_3.

In chapter 7, the sputter deposition of Bi_2Te_3 thin films and Bi_2Te_3-Fe heterostructure is described, which could be useful for various spintronics application. We discuss the condition for obtaining good quality crystalline sputtered Bi_2Te_3 thin films and also measure basic magnetic properties on Bi_2Te_3-Fe heterostructure grown by sputtering. We present results indicating the influence of the underlying Bi_2Te_3 layer on the magnetic properties of Fe.

Finally, chapter 8 summarizes the work done in this dissertation and proposes possible directions for future research.

Chapter 2

Theory of inverse Edelstein effect on the surface of topological insulator due to spin-pumping

Three dimensional (3D) spin current density injected onto the surface of a topological insulator (TI) produces a two dimensional (2D) charge current density on the surface of the TI because of spin-momentum locking of the 2D surface states of the TI, which is known as the inverse Edelstein effect (IEE)[10, 27]. In the literature, the IEE on the surface of a material with high spin-orbit coupling (SOC) or on the surface of a TI was measured by flowing spin current onto the surface generated by spin pumping in a ferromagnetic metal (FM) and measuring the induced open circuit voltage between the two ends of the surface[41, 42, 43, 44, 45, 46, 47, 48, 49]. However, a non-magnetic metal (NM) spacer layer also was introduced in such experiments[41, 42, 48, 49] so that the spin current density produced by spin pumping in the FM flows through the NM to the surface of the high SOC material or the TI surface, as shown in Fig. 2.1. The ratio of the 2D surface charge current density on the TI surface to the 3D spin current density injected across the TI/NM interface, which is defined as the IEE length, is a measure of the spin-to-charge current conversion efficiency. In the literature, a theory of IEE on the surface of a TI for a given spin current by spin-pumping from a FM was considered[59, 60], although, the effect of the coupling of material proximity to the TI surface states was not taken into account. Here,

Parts of this chapter have been published as Ref. [58]: R. Dey, N. Prasad, L. F. Register, and S. K. Banerjee, "Conversion of spin current into charge current in a topological insulator: Role of the interface", *Physical Review B*, **97**, 174406 (2018), Copyright 2018 by the American Physical Society. Available: https://doi.org/10.1103/PhysRevB.97.174406. Contribution of the dissertator: The dissertator, Rik Dey, performed the theoretical calculations, wrote the manuscript, and is the corresponding author of this publication.

we consider IEE in a TI/NM/FM heterostructure[48, 49], and model the transport of the TI surface states considering coupling of the NM to these surface states.

In this chapter, we derive the transport equation in a TI/NM heterostructure and solve for the electrochemical potential and charge current density on the TI surface given a spin current density from the FM flowing through the NM to the TI surface. We show that both the IEE relaxation time and the transport relaxation time on the TI surface are modified by the interface transmission time of the electrons that tunnel between the NM and the TI surface. The correction becomes significant when the transmission time across the interface becomes comparable to or less than the original momentum scattering time on the TI surface. We also found that the size of the device affects the open-circuit voltage that is measured at the two ends of the TI surface. Our results indicate the continued importance of the interface to obtain a better spin-to-charge current conversion and a limitation to the conversion efficiency due to the quality of the interface as well as the size of the device.

2.1 Background and Motivation

In a theoretical paper by Zhang and Fert[27], it was shown that the IEE length is exactly equal to the mean free path on the TI surface independent of the electron transmission rate across the interface. However, we find that the IEE length will be modified due to the interface transmission rate, and the IEE relaxation rate will be determined by the momentum scattering rate and the interface transmission rate. We show that the transmission rate across the interface gives a non-zero contribution to the transport relaxation rate on the TI surface as well as to the IEE relaxation rate over and above any surface hybridization effects, and the IEE length is always less than the original mean free path on the TI surface without the interface.

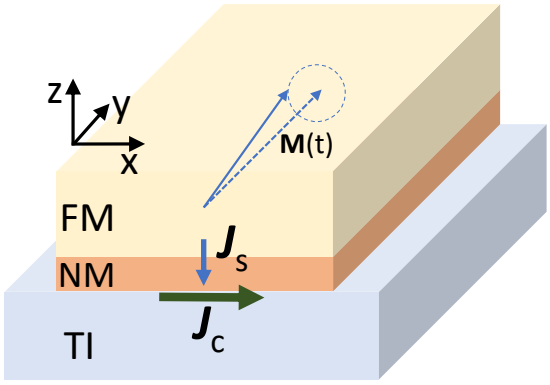

Figure 2.1: Schematics of spin current-to-charge current conversion on the surface of the TI in TI-NM-FM heterostructure with spin current generated by spin-pumping: A rotating magnetization $\mathbf{M}(t)$ around the y-direction in the FM produces y-component of the spin current density $\mathbf{J}_s$ flowing in the z-direction to the NM. The spin current density $\mathbf{J}_s$ flows from the NM to the TI surface through the interface and produces a charge current density $\mathbf{J}_c$ in the x-direction on the TI surface.

In the following sections, we first derive the transport equations on the TI surface in a TI/ NM heterostructure using the spinor Boltzmann equation following Zhang and Fert[27]. However, we consider the general Boltzmann equation incorporating an inhomogeneous diffusion term to show a modification of the transport relaxation time due to the finite interface transmission time. Also, we provide an alternate approach based on quantum kinetic equation using Keldysh Green's function that reproduces the results of the semi-classical Boltzmann equation. Then, we obtain the solution of the transport equations on the TI surface in the steady-state homogeneous case showing a modification of the IEE relaxation time because of the finite interface transmission time. Furthermore, we consider the case in which an open circuit voltage is measured on the two ends of the TI, and solve the coupled transport equations on the TI surface and in the NM as well. We find that the device dimension plays an important role to the IEE efficiency in such experiments along with the crucial importance of the interface in obtaining a better spin-to-charge current conversion.

2.2 Derivation of transport equations on the TI surface coupled to the NM from semi-classical Boltzmann transport equation

We start with the spinor Boltzmann equation for the surface states of the TI in a TI/NM bilayer, given by

$$\partial_{\mathrm{T}}\hat{g}_{\mathbf{p}} + \mathbf{v}\cdot\nabla_{\mathbf{R}}\hat{g}_{\mathbf{p}} = \sum_{\mathbf{k}}\Gamma_{\mathbf{kp}}(\hat{f}_{\mathbf{k}} - \hat{g}_{\mathbf{p}}) + \sum_{\mathbf{p}'}\Delta_{\mathbf{pp}'}(\hat{g}_{\mathbf{p}'} - \hat{g}_{\mathbf{p}}), \tag{2.1}$$

where $\hat{f}_{\mathbf{k}}$ and $\hat{g}_{\mathbf{p}}$ are the non-equilibrium spinor distribution functions in the NM and the TI surface states, respectively. Here, $\mathbf{k}$ is the 3D momentum of the states in the NM and $\mathbf{p}$ is the 2D momentum of the TI surface states. The velocity operator for the surface states is $\mathbf{v} = (1/\hbar)\partial H/\partial\mathbf{p} = v_{\mathrm{F}}(\hat{\mathbf{z}}\times\boldsymbol{\sigma})$, where $H = \hbar v_{\mathrm{F}}\,\boldsymbol{\sigma}\cdot(\mathbf{p}\times\hat{\mathbf{z}})$ is the Hamiltonian of the surface states, v_{F} is the Fermi velocity, $\hat{\mathbf{z}}$ is the unit vector along the surface normal direction, $\boldsymbol{\sigma}$ is the vector consisting of three Pauli spin matrices, $\hat{\mathbf{p}} = \mathbf{p}/p$ is the unit vector along the momentum direction, and p is the magnitude of $\mathbf{p}$. The first term in the left hand side of Eq. (2.1) represents the time derivative and the second term represents diffusion in the 2D surface of the TI, where T is the time and $\mathbf{R}$ is the 2D position vector on the TI surface.

Because we find the interface tunneling rate is crucial in the transport, we will elaborate on the derivation of the interface tunneling rate and the assumptions made therein. The first term on the right hand side of Eq. (2.1) represents tunneling across the interface with the tunneling probability $\Gamma_{\mathbf{kp}}$ given from the Fermi's Golden Rule as $\Gamma_{\mathbf{kp}} = (2\pi/\hbar)|T_{\mathbf{kp}}|^2\delta(\epsilon_{\mathbf{k}} - \epsilon_{\mathbf{p}})$, where $T_{\mathbf{kp}}$ is the tunneling matrix element between the NM and the TI surface states given by $|T_{\mathbf{kp}}|^2 = |\langle\psi_{\mathbf{k}}(\mathbf{r})\chi_{\mathbf{k}}|V_{\mathrm{tun}}(\mathbf{r})|\psi_{\mathbf{p}}(\mathbf{r})\chi_{\mathbf{p}}\rangle|^2$, where $V_{\mathrm{tun}}(\mathbf{r})$ is the tunneling potential, and $\mathbf{r}$ is the 3D position vector. The orbital part of the wave functions are $\psi_{\mathbf{k,p}}(\mathbf{r})$, and the spin part of the wave functions are $\chi_{\mathbf{k,p}}$. If the interface is considered to be rough enough

to randomize momentum and the tunneling potential is assumed to be spin-independent and rectangular barrier-like in the surface normal direction, the interface potential can be modeled by $V_{\rm tun}(\mathbf{r}) = v_0 \Sigma_{i=1}^{N_{\rm S}} \delta(\mathbf{r}_\parallel - \mathbf{R}_i^{\rm S}) V_{\rm t}(z)$, where the roughness of the interface is modeled by $N_{\rm S}$ randomly distributed short-range delta potentials at positions $\mathbf{R}_i^{\rm S}$ at the interface, $\mathbf{r}_\parallel$ is the component of $\mathbf{r}$ parallel to the interface, and $V_{\rm t}(z)$ is a rectangular barrier function along the z-direction. The orbital part of the wave functions are assumed to be of the form $\psi_{\mathbf{k},\mathbf{p}}(\mathbf{r}) = \phi_{\mathbf{k},\mathbf{p}}(\mathbf{r}_\parallel)\xi_{\mathbf{k},\mathbf{p}}(z)$, where the $\phi_{\mathbf{k},\mathbf{p}}(\mathbf{r}_\parallel)$'s are considered to be plane waves. After an averaging over the random distribution of the tunneling centers $\mathbf{R}_i^{\rm S}$, we obtain

$$\Gamma_{\mathbf{kp}} = \frac{\pi v_0^2 n_{\rm s} C_{\rm t}}{\hbar A} \left[\sigma_0 + \boldsymbol{\sigma} \cdot (\hat{\mathbf{p}} \times \hat{\mathbf{z}})\right] \delta(\epsilon_{\mathbf{k}} - \epsilon_{\mathbf{p}}), \tag{2.2}$$

where $n_{\rm s} = N_{\rm S}/A$ is the roughness defect density of the interface, A is the surface area, and the overlap of the wave functions of the TI surface states and of the NM in the tunneling region is $C_{\rm t} = |\langle \xi_{\mathbf{k}}(z)|V_{\rm t}(z)|\xi_{\mathbf{p}}(z)\rangle|^2$, which is presumed to be independent of the momentum of the electrons tunneling across the interface[61]. The tunneling potential is considered to be spin independent, so the spinor dependent part in Eq. (2.2) arises from the projection operator $\frac{1}{2}[\sigma_0 + \boldsymbol{\sigma}\cdot(\hat{\mathbf{p}}\times\hat{\mathbf{z}})]$ which projects states to the upper band of the TI Hamiltonian[27]. The interface tunneling probability given by Eq. (2.2) is completely momentum randomizing, as considered by Zhang and Fert[27]. Here, we further consider the case of a smooth interface, in which the tunneling potential can be modeled by $V_{\rm tun}(\mathbf{r}) = v_{\rm c} V_{\rm t}(z)$ to be constant everywhere on the interface, and the tunneling probability becomes

$$\Gamma_{\mathbf{kp}} = \frac{\pi v_{\rm c}^2 C_{\rm t}}{\hbar A} \left[\sigma_0 + \boldsymbol{\sigma} \cdot (\hat{\mathbf{p}} \times \hat{\mathbf{z}})\right] (2\pi)^2 \delta(\mathbf{k}_\parallel - \mathbf{p}) \, \delta(\epsilon_{\mathbf{k}} - \epsilon_{\mathbf{p}}), \tag{2.3}$$

implying that the in-plane momentum $\mathbf{k}_\parallel$ is conserved in the tunneling process. The rough and the smooth interface assumed are the extreme limits of the interface roughness model with a Gaussian distributed surface roughness potential, and the interface transmission time

depends on the nature of the interface.

The second term on the right hand side of Eq. (2.1) denotes scattering between the state $\mathbf{p}$ and $\mathbf{p}'$ of the TI surface states due to defects or impurities close to the interface, with the scattering probability $\Delta_{\mathbf{p}\mathbf{p}'}$ given by the Fermi's Golden Rule as $\Delta_{\mathbf{p}\mathbf{p}'} = (2\pi/\hbar)|U_{\mathbf{p}\mathbf{p}'}|^2\delta(\epsilon_{\mathbf{p}} - \epsilon_{\mathbf{p}'})$, where $U_{\mathbf{p}\mathbf{p}'}$ is the scattering matrix element between the state $\mathbf{p}$ and $\mathbf{p}'$ given by $|U_{\mathbf{p}\mathbf{p}'}|^2 = \langle|\langle\psi_{\mathbf{p}}(\mathbf{r})|V_{\rm dis}(\mathbf{r})|\psi_{\mathbf{p}'}(\mathbf{r})\rangle|^2\rangle|\langle\chi_{\mathbf{p}}|\chi_{\mathbf{p}'}\rangle|^2$. Here we model a short range, spin-independent disorder potential by $V_{\rm dis}(\mathbf{r}) = u_0\Sigma_{j=1}^{N_{\rm I}}\delta(\mathbf{r}_{\parallel} - \mathbf{R}_j^{\rm I})V_{\rm d}(z)$, where $\mathbf{R}_j^{\rm I}$'s are the position of the $N_{\rm I}$ impurities in the direction parallel to the surface, and $V_{\rm d}(z)$ represents an average value of the impurity potential due to the impurities near the interface. After averaging over the random impurity positions parallel to the surface, the scattering matrix element is evaluated to be $|U_{\mathbf{p}\mathbf{p}'}|^2 = (u_0^2 n_{\rm i} C_{\rm d}/A)\frac{1}{2}(1+\hat{\mathbf{p}}\cdot\hat{\mathbf{p}}')$, where $n_{\rm i} = N_{\rm I}/A$ is the impurity concentration, $C_{\rm d} = |\langle\xi_{\mathbf{p}}(z)|V_{\rm d}(z)|\xi_{\mathbf{p}'}(z)\rangle|^2$, and $|\langle\chi_{\mathbf{p}}|\chi_{\mathbf{p}'}\rangle|^2 = \frac{1}{2}(1+\hat{\mathbf{p}}\cdot\hat{\mathbf{p}}')$ where $\chi_{\mathbf{p}}$ satisfies $\boldsymbol{\sigma}\cdot(\hat{\mathbf{p}}\times\hat{\mathbf{z}})\chi_{\mathbf{p}} = \chi_{\mathbf{p}}$. So, we have

$$\Delta_{\mathbf{p}\mathbf{p}'} = \frac{\pi u_0^2 n_{\rm i} C_{\rm d}}{\hbar A}(1+\hat{\mathbf{p}}\cdot\hat{\mathbf{p}}')\delta(\epsilon_{\mathbf{p}} - \epsilon_{\mathbf{p}'}). \tag{2.4}$$

Because the band-structure of the surface states is isotropic in the $\mathbf{p}$-space within the considered energy range, the conservation of energy also implies conservation of the magnitude of momentum in the scattering process.

The solution to Eq. (2.1) can be obtained by considering $\hat{f}_{\mathbf{k}} = \hat{f}^0_{\mathbf{k}} + \delta\hat{f}_{\mathbf{k}}$ and $\hat{g}_{\mathbf{p}} = \hat{g}^0_{\mathbf{p}} + \delta\hat{g}_{\mathbf{p}}$, where $\hat{f}^0_{\mathbf{k}} = f_{\rm FD}(\epsilon_{\mathbf{k}})\sigma_0$ and $\hat{g}^0_{\mathbf{p}} = \frac{1}{2}[\sigma_0 + \boldsymbol{\sigma}\cdot(\hat{\mathbf{p}}\times\hat{\mathbf{z}})]f_{\rm FD}(\epsilon_{\mathbf{p}})$ are the equilibrium distribution functions for the NM and the TI surface states, respectively, where $f_{\rm FD}$ is the Fermi-Dirac distribution. We can write $\delta\hat{f}_{\mathbf{k}} = (\mathrm{f}_0\sigma_0 + \mathbf{f}\cdot\boldsymbol{\sigma})\delta(\epsilon_{\mathbf{k}} - \epsilon_{\rm F})$ and $\delta\hat{g}_{\mathbf{p}} = \hat{h}(\theta)\delta(\epsilon_{\mathbf{p}} - \epsilon_{\rm F})$, which amounts to considering quasi-particle excitations at the Fermi energy $\epsilon_{\rm F}$. We consider f_0 and $\mathbf{f}$ are independent of the solid angle Ω in the Fermi surface of the NM, and $\hat{h}(\theta)$ is a function

of the angle $\theta = \tan^{-1}(p_y/p_x)$ in the Fermi surface of the TI surface state, reflecting the dispersion relations of the NM and the TI, respectively. Performing the summations over momentum by the following integrations: $\Sigma_{\mathbf{k}} \to V \int N_k(\epsilon_{\mathbf{k}}) d\epsilon_{\mathbf{k}} \int d\Omega/(4\pi)$ (where $V = Ad$ is the volume of the NM, A is the surface area of the bilayer, and d is the thickness of the NM) and $\Sigma_{\mathbf{p}} \to A \int N_p(\epsilon_{\mathbf{p}}) d\epsilon_{\mathbf{p}} \int d\theta/(2\pi)$ (where $N_k(\epsilon_{\mathbf{k}})$ and $N_p(\epsilon_{\mathbf{p}})$ are the per spin density of states (DOS) in the NM and of the TI surface states, respectively), and the integration over $\epsilon_{\mathbf{p}}$ of Eq. (2.1) gives

$$\begin{aligned}\partial_T \hat{h}(\theta) + v_F\ (\hat{\mathbf{z}} \times \boldsymbol{\sigma}) \cdot \nabla_{\mathbf{R}} \hat{h}(\theta) =& \frac{1}{\tau_t}[\sigma_0 + \boldsymbol{\sigma} \cdot (\hat{\mathbf{p}} \times \hat{\mathbf{z}})](f_0 \sigma_0 + \mathbf{f} \cdot \boldsymbol{\sigma} - \hat{h}(\theta)) \\ &+ \frac{1}{\tau_p}\Big\langle (1 + \hat{\mathbf{p}} \cdot \hat{\mathbf{p}}')(\hat{h}(\theta') - \hat{h}(\theta)) \Big\rangle.\end{aligned} \tag{2.5}$$

Here $\langle ... \rangle$ denotes the average over the angle θ', τ_t is the interface transmission time, and τ_p is the momentum scattering time. In case of a rough interface with momentum randomizing tunneling, the interface transmission time is defined from Eq. (2.2) as

$$\frac{1}{\tau_t} = \sum_{\mathbf{k}} \frac{\pi v_0^2 n_s C_t}{\hbar A} \delta(\epsilon_{\mathbf{k}} - \epsilon_F) = \pi v_0^2 n_s C_t N_m d/\hbar, \tag{2.6}$$

with N_m being the 3D DOS in the NM at the Fermi energy. In case of a smooth interface, the interface transmission time is redefined from Eq. (2.3) as

$$\frac{1}{\tau_t} = \sum_{\mathbf{k}} \frac{\pi v_c^2 C_t}{\hbar A} (2\pi)^2 \delta(\mathbf{k}_\parallel - \mathbf{p}_F) \delta(\epsilon_{\mathbf{k}} - \epsilon_F) = \pi v_c^2 C_t N_{m,1} d/\hbar, \tag{2.7}$$

where $\mathbf{p}_F$ is the Fermi momentum in the TI, and $N_{m,1}$ is the one-dimensional (1D) DOS in the NM at the Fermi energy with the condition that the in-plane momentum is conserved, i.e., $\mathbf{p}_F^2 + k_z^2 = \mathbf{k}_F^2$, with $\mathbf{k}_F$ being the Fermi momentum in the NM. So, for a smooth interface, tunneling is possible if the cross section of the 3D Fermi surface is larger than the 2D Fermi surface, i.e., $\mathbf{k}_F > \mathbf{p}_F$. For large 2D Fermi surface, i.e., $\mathbf{p}_F > \mathbf{k}_F$, there will be no tunneling

$(1/\tau_{\rm t}=0)$ if the interface is smooth. From Eq. (2.4), we define the momentum scattering time (between the Bloch states) on the TI surface as

$$\frac{1}{\tau_{\rm p}}=\sum_{\mathbf{p}}\frac{\pi u_0^2 n_{\rm i} C_{\rm d}}{\hbar A}\delta(\epsilon_{\mathbf{p}}-\epsilon_{\rm F})=\pi u_0^2 n_{\rm i} C_{\rm d} N/\hbar, \tag{2.8}$$

where N is the 2D DOS of the TI surface states at the Fermi energy.

The solution for $\hat{h}(\theta)$ is obtained by considering that the non-equilibrium distribution function for the surface states has a spinor form that is proportional to the upper band projection operator of the TI surface state Hamiltonian, i.e., $\hat{h}(\theta)=\mathrm{h}_0(\theta)[\sigma_0+\boldsymbol{\sigma}\cdot(\hat{\mathbf{p}}\times\hat{\mathbf{z}})]$, where $\mathrm{h}_0(\theta)$ is a scalar function times identity in spin space and can be written in terms of s- and p-wave components, i.e., $\mathrm{h}_0(\theta)=\mathrm{h_s}+\hat{\mathbf{p}}\cdot\mathbf{h}_{\rm a}$, with $\mathrm{h_s}$ and $\mathbf{h}_{\rm a}$ being independent of θ. Taking trace of Eq. (2.5) in the spin space and integrating out the s- and p-wave components, we obtain

$$\partial_{\rm T}\mathrm{h_s}+\frac{v_{\rm F}}{2}\nabla_{\mathbf{R}}\cdot\mathbf{h}_{\rm a}=\frac{2}{\tau_{\rm t}}\left(\frac{\mathrm{f}_0}{2}-\mathrm{h_s}\right), \tag{2.9a}$$

$$\partial_{\rm T}\mathbf{h}_{\rm a}+v_{\rm F}\nabla_{\mathbf{R}}\mathrm{h_s}=\frac{2}{\tau_{\rm t}}\left(\hat{\mathbf{z}}\times\frac{\mathbf{f}}{2}\right)-\left(\frac{2}{\tau_{\rm t}}+\frac{1}{2\tau_{\rm p}}\right)\mathbf{h}_{\rm a}. \tag{2.9b}$$

The charge density n and the current density $\mathbf{J}$ on the TI surface are given by

$$n=\frac{(-e)}{A}\sum_{\mathbf{p}}\mathrm{Tr}(\delta\hat{g}_{\mathbf{p}})=-2eN\mathrm{h_s}, \tag{2.10a}$$

$$\mathbf{J}=\frac{(-e)}{A}\sum_{\mathbf{p}}\mathrm{Tr}(\mathbf{v}\delta\hat{g}_{\mathbf{p}})=-eNv_{\rm F}\mathbf{h}_{\rm a}. \tag{2.10b}$$

The charge density $n_{\rm m}$ and the spin density $\boldsymbol{s}_{\rm m}$ (in the unit of electron charge density) in

the NM are given by

$$n_{\rm m} = \frac{(-e)}{V}\sum_{\mathbf{k}} {\rm Tr}(\delta\hat{f}_{\mathbf{k}}) = -2eN_{\rm m}{\rm f}_0, \tag{2.11a}$$

$$\boldsymbol{s}_{\rm m} = \frac{(-e)}{V}\sum_{\mathbf{k}} {\rm Tr}(\boldsymbol{\sigma}\delta\hat{f}_{\mathbf{k}}) = -2eN_{\rm m}\mathbf{f}. \tag{2.11b}$$

We define the charge electrochemical potential $\mu_{\rm m}$ in the NM by the relation $n_{\rm m} = 2e^2N_{\rm m}\mu_{\rm m}$, where the factor of 2 is for spin degeneracy (as $N_{\rm m}$ is the per spin DOS), and define the spin electrochemical potential $\boldsymbol{\mu}_{\rm s}$ by the relation $\boldsymbol{s}_{\rm m} = e^2N_{\rm m}\boldsymbol{\mu}_{\rm s}$. From Eq. (2.11) we obtain ${\rm f}_0 = -e\mu_{\rm m}$ and $\mathbf{f} = -e\boldsymbol{\mu}_{\rm s}/2$. Using Eq. (2.10), the following modified continuity equation on the TI surface is obtained from Eq. (2.9a),

$$\partial_{\rm T} n + \nabla_{\mathbf{R}}\cdot\mathbf{J} = \frac{2}{\tau_{\rm t}}(e^2N\mu_{\rm m} - n). \tag{2.12}$$

Fourier transforming Eq. (2.9b) to the frequency domain ($\partial_{\rm T} \to -i\omega$) gives the charge current density on the TI surface,

$$\mathbf{J} = \frac{1}{(1-i\omega\tau_{\rm tr})}\left[-\frac{v_{\rm F}^2\tau_{\rm tr}}{2}\nabla_{\mathbf{R}}n + e^2Nv_{\rm F}\frac{\tau_{\rm tr}}{\tau_{\rm t}}\left(\hat{\mathbf{z}}\times\frac{\boldsymbol{\mu}_{\rm s}}{2}\right)\right], \tag{2.13}$$

where $\tau_{\rm tr}$ is the modified transport relaxation time (momentum relaxation time) defined as

$$\frac{1}{\tau_{\rm tr}} = \frac{1}{2\tau_{\rm p}} + \frac{2}{\tau_{\rm t}}. \tag{2.14}$$

(The factor of 2 in $2/\tau_{\rm t}$ could be absorbed in the definition of $\tau_{\rm t}$ in Eqs. (2.6) and (2.7) by redefining the DOS in the NM considering both the spins.) In absence of tunneling from the NM, the transport relaxation time (momentum relaxation time) on the TI surface is $\tau_{\rm tr}^0 = 2\tau_{\rm p}$, where the factor of 2 is due to the increasing attenuation of scattering with increasing scattering angle because of the helical spin-momentum locking in the TI, including

elimination of direct backscattering where the spin components of the initial and final electronic states are orthogonal. The first term in the right hand side of Eq. (2.13) represents diffusion, where $D' = v_{\rm F}^2 \tau_{\rm tr}/2$ is the modified diffusion constant because the transmission rate across the interface modifies transport relaxation time by the relation given in Eq. (2.14), while the diffusion constant on the pristine TI surface (without any tunneling) is given by $D = v_{\rm F}^2 \tau_{\rm tr}^0/2$. The spin current density $\mathbf{J}_{\rm s,1}$ through the TI/NM interface (in the unit of charge current density) is given by

$$\mathbf{J}_{\rm s,1} = \frac{(-e)}{A} \sum_{\mathbf{p},\mathbf{k}} {\rm Tr}\Big[\boldsymbol{\sigma}\Gamma_{\mathbf{kp}}(\hat{f}_{\mathbf{k}} - \hat{g}_{\mathbf{p}})\Big] = \frac{2}{v_{\rm F}\tau_{\rm t}}\left(e^2 N v_{\rm F}\frac{\boldsymbol{\mu}_{\rm s}}{2} - \mathbf{J}\times\hat{\mathbf{z}}\right). \tag{2.15}$$

2.3 Derivation of the transport equations on the TI surface coupled to the NM from quantum kinetic equation

The spin-charge dynamics of the TI surface states coupled to the NM through a tunnel barrier can be obtained from the quantum kinetic equation written in terms of the Keldysh Green's function. We follow the approach given by Kopnin *et. al.*[62] and Kopnin *et. al.*[63]. To start with, we consider the full system Hamiltonian

$$H_{\rm tot} = H_{\rm S} + H_{\rm D} + H_{\rm T} + H_{\rm M}. \tag{2.16}$$

Here, the TI surface state Hamiltonian $H_{\rm S}$ is given by

$$H_{\rm S} = \lambda \int {\rm d}^2{\rm R}\; a_\alpha^\dagger(\mathbf{R})\big[\epsilon_{\rm S}(\mathbf{R}) - \epsilon_{\rm F}\sigma_0 - e\phi\sigma_0\big]_{\alpha\beta} a_\beta(\mathbf{R}), \tag{2.17}$$

where $\epsilon_{\rm S}(\mathbf{R}) = -i\hbar v_{\rm F}\;(\hat{\mathbf{z}}\times\boldsymbol{\sigma})\cdot\nabla_{\mathbf{R}}$, $\mathbf{R}$ is the 2D position vector on the TI surface, $\epsilon_{\rm F}$ is the Fermi energy and ϕ is the electrostatic potential of any electric field on the TI surface.

$a^\dagger_\alpha(\mathbf{R})$, $a_\beta(\mathbf{R})$ are the creation and annihilation operators on the TI surface with the spin index (α, β), and these operators are normalized to the thickness λ of the TI surface states such that the equal-time anti-commutator satisfies $\{a_\alpha(\mathbf{R}), a^\dagger_\beta(\mathbf{R}')\} = \lambda^{-1}\delta(\mathbf{R}-\mathbf{R}')\delta_{\alpha\beta}$, and repeated spin indices will imply summation over them. The impurities on the TI surface are modeled by the disorder Hamiltonian H_{D} which is

$$H_{\mathrm{D}} = \lambda \int \mathrm{d}^2\mathrm{R}\ a^\dagger_\alpha(\mathbf{R}) V_{\mathrm{D}}(\mathbf{R}) a_\alpha(\mathbf{R}), \tag{2.18}$$

where $V_{\mathrm{D}}(\mathbf{R}) = V_0 \Sigma_{j=1}^{N_{\mathrm{I}}} \delta(\mathbf{R}-\mathbf{R}^{\mathrm{I}}_j)$ represents short ranged spin-independent disorder potential and the integration of the envelope function of the surface state of the TI over the surface normal direction is already included in the average value V_0. The coupling of the TI surface states to the NM through the tunnel barrier is described by a tunneling Hamiltonian H_{T}, which captures the transmission of the electron in and out of the TI surface states as

$$H_{\mathrm{T}} = \lambda \int \mathrm{d}^2\mathrm{R} \int \mathrm{d}^3\mathrm{r}\ \left[b^\dagger_\alpha(\mathbf{r}) T_{\alpha\beta}(\mathbf{r}, \mathbf{R}) a_\beta(\mathbf{R}) + a^\dagger_\alpha(\mathbf{R}) T^\dagger_{\alpha\beta}(\mathbf{R}, \mathbf{r}) b_\beta(\mathbf{r}) \right], \tag{2.19}$$

where $b^\dagger_\alpha(\mathbf{r})$, $b_\beta(\mathbf{r})$ are the creation and annihilation operators in the NM satisfying the equal-time anti-commutator $\{b_\alpha(\mathbf{r}), b^\dagger_\beta(\mathbf{r}')\} = \delta(\mathbf{r}-\mathbf{r}')\delta_{\alpha\beta}$, $\mathbf{r}$ is the 3D position vector in the NM, and the tunneling matrix obeys $T^\dagger_{\alpha\beta}(\mathbf{R}, \mathbf{r}) = T^*_{\beta\alpha}(\mathbf{r}, \mathbf{R})$. The creation and the annihilation operators in the NM and on the TI surface anti-commutes with each other, i.e. $\{a_\alpha(\mathbf{R}), b^\dagger_\beta(\mathbf{r}')\} = 0$. We consider the tunneling to be instantaneous, and also we will assume a spin conserving and site-to-site (local) tunneling at the interface, in which case the tunneling matrix can be written as $T_{\alpha\beta}(\mathbf{r}, \mathbf{R}) = t(\mathbf{R})\delta(\mathbf{r}_\parallel - \mathbf{R})\delta(z)\delta_{\alpha\beta}$, where $t(\mathbf{R})$ already includes the overlap of the envelope functions in the NM and the surface state of the TI. We

consider that the Hamiltonian in the NM is given by

$$H_{\mathrm{M}} = \int \mathrm{d}^3\mathrm{r}\ b^\dagger_\alpha(\mathbf{r})\big[\epsilon_{\mathrm{m}}(\mathbf{r}) - \epsilon_{\mathrm{F}}\sigma_0 - e\phi_{\mathrm{m}}\sigma_0\big]_{\alpha\beta} b_\beta(\mathbf{r}), \tag{2.20}$$

where $\epsilon_{\mathrm{m}}(\mathbf{r}) = [\frac{1}{2m_{\mathrm{c}}}(-i\hbar\nabla_{\mathbf{r}})^2 + \epsilon_{\mathrm{b}}]\sigma_0$ with m_{c} being the effective mass of the conduction band in the NM and ϵ_{b} being the band offset of the bottom of the conduction band in the NM with respect to the Dirac point of the TI surface state, and ϕ_{m} is the electrostatic potential of any electric field in the NM.

We consider the following non-equilibrium Green's function defined in the Schwinger-Keldysh time contour

$$\begin{aligned}
i(G_{\mathrm{S}})_{\alpha\beta}(\mathbf{R}_1,\tau_1;\mathbf{R}_2,\tau_2) &= \langle T_\tau a_\alpha(\mathbf{R}_1,\tau_1)a^\dagger_\beta(\mathbf{R}_2,\tau_2)\rangle,\\
i(G_{\mathrm{T}})_{\alpha\beta}(\mathbf{r}_1,\tau_1;\mathbf{R}_2,\tau_2) &= \langle T_\tau b_\alpha(\mathbf{r}_1,\tau_1)a^\dagger_\beta(\mathbf{R}_2,\tau_2)\rangle,\\
i(G_{\mathrm{M}})_{\alpha\beta}(\mathbf{r}_1,\tau_1;\mathbf{r}_2,\tau_2) &= \langle T_\tau b_\alpha(\mathbf{r}_1,\tau_1)b^\dagger_\beta(\mathbf{r}_2,\tau_2)\rangle.
\end{aligned} \tag{2.21}$$

Here G_{S} is the Green's function for the TI surface states, G_{T} is the mixed Green's function for tunneling, and G_{M} is the Green's function in the NM neglecting the back reaction of the TI surface states, i.e. G_{M} satisfies

$$(G_{\mathrm{M}})^{-1}_{\alpha\gamma}(\mathbf{r}_1,\tau_1)(G_{\mathrm{M}})_{\gamma\beta}(\mathbf{r}_1,\tau_1;\mathbf{r}_2,\tau_2) = \hbar\delta(\mathbf{r}_1-\mathbf{r}_2)\delta(\tau_1-\tau_2)\delta_{\alpha\beta}, \tag{2.22}$$

where $(G_{\mathrm{M}})^{-1}(\mathbf{r},\tau) = i\hbar\partial_\tau - \epsilon_{\mathrm{m}}(\mathbf{r}) + U_{\mathrm{M}}$. From the Heisenberg equation of motion for the creation and annihilation operators, the equation of motion for the mixed Green's functions can be derived as

$$(G_{\mathrm{M}})^{-1}_{\alpha\gamma}(\mathbf{r}_1,\tau_1)(G_{\mathrm{T}})_{\gamma\beta}(\mathbf{r}_1,\tau_1;\mathbf{R}_2,\tau_2) = \lambda\int \mathrm{d}^2\mathrm{R}'\ T_{\alpha\gamma}(\mathbf{r}_1,\mathbf{R}')(G_{\mathrm{S}})_{\gamma\beta}(\mathbf{R}',\tau_1;\mathbf{R}_2,\tau_2). \tag{2.23}$$

Equation (2.22) and (2.23) gives

$$
\begin{aligned}
&(G_{\mathrm{T}})_{\alpha\beta}(\mathbf{r}_1,\tau_1;\mathbf{R}_2,\tau_2) \\
&= \frac{\lambda}{\hbar}\int \mathrm{d}\tau'\mathrm{d}^2\mathrm{R}'\mathrm{d}^3\mathrm{r}'(G_{\mathrm{M}})_{\alpha\mu}(\mathbf{r}_1,\tau_1;\mathbf{r}',\tau')T_{\mu\nu}(\mathbf{r}',\mathbf{R}')(G_{\mathrm{S}})_{\nu\beta}(\mathbf{R}',\tau';\mathbf{R}_2,\tau_2).
\end{aligned}
\tag{2.24}
$$

The Dyson equation for the Green's function of the TI surface states becomes

$$
\begin{aligned}
&(G_{\mathrm{S}})^{-1}_{\alpha\gamma}(\mathbf{R}_1,\tau_1)(G_{\mathrm{S}})_{\gamma\beta}(\mathbf{R}_1,\tau_1;\mathbf{R}_2,\tau_2) \\
&-\int \mathrm{d}^2\mathrm{R}'\mathrm{d}\tau'(\Sigma_{\mathrm{S}})_{\alpha\gamma}(\mathbf{R}_1,\tau_1;\mathbf{R}',\tau')(G_{\mathrm{S}})_{\gamma\beta}(\mathbf{R}',\tau';\mathbf{R}_2,\tau_2) = \frac{\hbar}{\lambda}\delta(\mathbf{R}_1-\mathbf{R}_2)\delta(\tau_1-\tau_2)\delta_{\alpha\beta},
\end{aligned}
\tag{2.25}
$$

where $(G_{\mathrm{S}})^{-1}(\mathbf{R},\tau) = i\hbar\partial_\tau - \epsilon_{\mathrm{S}}(\mathbf{R}) + \epsilon_{\mathrm{F}}\sigma_0$, and Σ_{S} is the self energy due to tunneling and disorder, i.e. $\Sigma_{\mathrm{S}} = \Sigma_{\mathrm{T}} + \Sigma_{\mathrm{D}}$. The self-energy for tunneling will be given by

$$
(\Sigma_{\mathrm{T}})_{\alpha\beta}(\mathbf{R}_1,\tau_1;\mathbf{R}_2,\tau_2) = \frac{\lambda}{\hbar}\int \mathrm{d}^3\mathrm{r}'\mathrm{d}^3\mathrm{r}''T^{\dagger}_{\alpha\mu}(\mathbf{R}_1,\mathbf{r}')(G_{\mathrm{M}})_{\mu\nu}(\mathbf{r}',\tau_1;\mathbf{r}'',\tau_2)T_{\nu\beta}(\mathbf{r}'',\mathbf{R}_2). \tag{2.26}
$$

For $T_{\alpha\beta}(\mathbf{r},\mathbf{R}) = t(\mathbf{R})\delta(\mathbf{r}_{\parallel}-\mathbf{R})\delta(z)\delta_{\alpha\beta}$, we obtain

$$
(\Sigma_{\mathrm{T}})_{\alpha\beta}(\mathbf{R}_1,\tau_1;\mathbf{R}_2,\tau_2) = \frac{\lambda}{\hbar}t(\mathbf{R}_1)(G_{\mathrm{M}})_{\alpha\beta}(\mathbf{R}_1,z_1=0,\tau_1;\mathbf{R}_2,z_2=0,\tau_2)t(\mathbf{R}_2). \tag{2.27}
$$

The self energy for disorder is given by

$$
(\Sigma_{\mathrm{D}})_{\alpha\beta}(\mathbf{R}_1,\tau_1;\mathbf{R}_2,\tau_2) = \frac{\lambda}{\hbar}V_{\mathrm{D}}(\mathbf{R}_1)(G_{\mathrm{S}})_{\alpha\beta}(\mathbf{R}_1,\tau_1;\mathbf{R}_2,\tau_2)V_{\mathrm{D}}(\mathbf{R}_2). \tag{2.28}
$$

By analytical continuation from the Schwinger-Keldysh time contour to the real time axis, Eqs. (2.22)-(2.28) can be written in terms of Keldysh space Green's functions $\check{G}_{\mathrm{i}}$ (i = S,T,M)

and self energies $\check{\Sigma}_{\rm j}$ (j = S,T,D)

$$\check{G}_{\rm i} = \begin{pmatrix} G_{\rm i}^{\rm R} & G_{\rm i}^{\rm K} \\ 0 & G_{\rm i}^{\rm A} \end{pmatrix}, \ \check{\Sigma}_{\rm j} = \begin{pmatrix} \Sigma_{\rm j}^{\rm R} & \Sigma_{\rm j}^{\rm K} \\ 0 & \Sigma_{\rm j}^{\rm A} \end{pmatrix}, \tag{2.29}$$

where $G_{\rm i}^{\rm R,A,K}$ ($\Sigma_{\rm j}^{\rm R,A,K}$) are the retarded, advanced and Keldysh Green's functions (self energies), all of which are 2×2 matrices in spin space with variables $(\mathbf{R}_1, t_1; \mathbf{R}_2, t_2)$ with t_1, t_2 being real time variables. A function $A(\mathbf{R}_1, t_1; \mathbf{R}_2, t_2)$ can be Wigner transformed to $\tilde{A}(\mathbf{R}, \mathrm{T}; \mathbf{p}, \omega)$ by doing a coordinate transformation to the center-of-mass coordinates $(\mathbf{R}, \mathrm{T})$ and relative coordinates $(\delta\mathbf{R}, \delta\mathrm{t})$, and performing Fourier transforms of these relative coordinates to momentum and frequency variable $(\mathbf{p}, \omega)$. We define the modified Wigner transformed function $A(\mathbf{R}, \mathrm{T}; \mathbf{p}, \epsilon)$ in terms of momentum and energy $(\mathbf{p}, \epsilon = \hbar\omega)$ by $\tilde{A}(\mathbf{R}, \mathrm{T}; \mathbf{p}, \omega) = \hbar A(\mathbf{R}, \mathrm{T}; \mathbf{p}, \epsilon)$, which is related to $A(\mathbf{R}_1, t_1; \mathbf{R}_2, t_2)$ by

$$A(\mathbf{R}_1, t_1; \mathbf{R}_2, t_2) = \int \frac{\mathrm{d}\epsilon}{2\pi} \frac{\mathrm{d}^2\mathrm{p}}{(2\pi)^2} A(\mathbf{R}, \mathrm{T}; \mathbf{p}, \epsilon) e^{i(\mathbf{p}\cdot\delta\mathbf{R} - \frac{\epsilon}{\hbar}\delta\mathrm{t})}. \tag{2.30}$$

We use the lowest order gradient expansion to express the Wigner transform of a product function to the product of Wigner transformed function, which gives the following relation for the modified Wigner transformed functions

$$(AB)(\mathbf{R}, \mathrm{T}; \mathbf{p}, \epsilon) = \hbar A(\mathbf{R}, \mathrm{T}; \mathbf{p}, \epsilon) B(\mathbf{R}, \mathrm{T}; \mathbf{p}, \epsilon). \tag{2.31}$$

The Keldysh component of the Wigner transformed left-right subtracted Dyson equation, written in terms of the modified Wigner transformed Green's function and self energy, gives

the quantum kinetic equation

$$\begin{aligned}&\partial_{\mathrm{T}} G_{\mathrm{S}}^{\mathrm{K}} - e\ \partial_{\mathrm{T}}\phi\ \partial_{\epsilon} G_{\mathrm{S}}^{\mathrm{K}} + \frac{1}{2}\big\{\mathbf{v}\cdot\nabla_{\mathbf{R}}, G_{\mathrm{S}}^{\mathrm{K}}\big\} + \frac{i}{\hbar}\left[\epsilon_{\mathrm{S}}(\mathbf{p}), G_{\mathrm{S}}^{\mathrm{K}}\right] + e\ \nabla_{\mathbf{R}}\phi\cdot\nabla_{\mathbf{p}} G_{\mathrm{S}}^{\mathrm{K}} \\ &= -i\big[\ \big(\Sigma_{\mathrm{S}}^{\mathrm{R}} G_{\mathrm{S}}^{\mathrm{K}} - G_{\mathrm{S}}^{\mathrm{K}}\Sigma_{\mathrm{S}}^{\mathrm{A}}\big) - \big(G_{\mathrm{S}}^{\mathrm{R}}\Sigma_{\mathrm{S}}^{\mathrm{K}} - \Sigma_{\mathrm{S}}^{\mathrm{K}} G_{\mathrm{S}}^{\mathrm{A}}\big)\ \big],\end{aligned} \tag{2.32}$$

where $\epsilon_{\mathrm{S}}(\mathbf{p}) = \hbar v_{\mathrm{F}}\boldsymbol{\sigma}\cdot(\mathbf{p}\times\hat{\mathbf{z}})$ and $\mathbf{v} = v_F(\hat{\mathbf{z}}\times\boldsymbol{\sigma})$. We consider time-independent electric field, so $\partial_{\mathrm{T}}\phi = 0$ in Eq. (2.32).

The self energy is due to disorder on the TI surface and tunneling from the NM. For the disorder potential $V_{\mathrm{D}}(\mathbf{R}) = V_0\Sigma_{j=1}^{N_{\mathrm{I}}}\delta(\mathbf{R}-\mathbf{R}_j^{\mathrm{I}})$, from Eq. (2.28) the disorder self energy becomes, after impurity averaging,

$$\check{\Sigma}_{\mathrm{D}}(\mathbf{R}_1, t_1; \mathbf{R}_2, t_2) = \frac{\lambda V_0^2 n_{\mathrm{i}}}{\hbar}\delta(\mathbf{R}_1 - \mathbf{R}_2)\check{G}_{\mathrm{S}}(\mathbf{R}_1, t_1; \mathbf{R}_2, t_2), \tag{2.33}$$

and the Wigner transformed disorder self energy reads

$$\check{\Sigma}_{\mathrm{D}}(\mathbf{R}, \mathrm{T}; \mathbf{p}, \epsilon) = \frac{\lambda V_0^2 n_{\mathrm{i}}}{\hbar}\int\frac{\mathrm{d}^2\mathrm{p}'}{(2\pi)^2}\check{G}_{\mathrm{S}}(\mathbf{R}, \mathrm{T}; \mathbf{p}', \epsilon). \tag{2.34}$$

We introduce the 2D quasi-classical Green's functions for the TI surface states as

$$\check{g}_{\mathrm{S}}(\mathbf{R}, \mathrm{T}; \mathrm{p}_{\mathrm{F}}\hat{\mathbf{p}}, \epsilon) = \frac{i\lambda}{\pi}\int \mathrm{d}\xi_{\mathrm{S}}\ \check{G}_{\mathrm{S}}(\mathbf{R}, \mathrm{T}; \mathbf{p}, \epsilon), \tag{2.35}$$

where $\xi_{\mathrm{S}} = \hbar v_{\mathrm{F}} p - \epsilon_{\mathrm{F}}$, and the ξ_{S} integration is performed near the Fermi surface. As the quasi-classical Green's function is peaked at the Fermi energy, the following *ansatz* holds

$$\check{G}_{\mathrm{S}}(\mathbf{R}, \mathrm{T}; \mathbf{p}, \epsilon) = -\frac{i\pi}{\lambda}\check{g}_{\mathrm{S}}(\mathbf{R}, \mathrm{T}; \mathrm{p}_{\mathrm{F}}\hat{\mathbf{p}}, \epsilon)\delta(\xi_{\mathrm{S}}). \tag{2.36}$$

The disorder self-energy now can be written as

$$\check{\Sigma}_{\rm D}(\mathbf{R},{\rm T};\mathbf{p},\epsilon)=-\frac{i}{\tau_{\rm p}}\langle\check{g}_{\rm S}(\mathbf{R},{\rm T};{\rm p_F}\hat{\mathbf{p}},\epsilon)\rangle, \tag{2.37}$$

where $\langle ...\rangle$ denotes angular averaging in the $\mathbf{p}$ space and we define $1/\tau_{\rm p}=\pi V_0^2 n_{\rm i} N/\hbar$.

To calculate the tunneling self energy, we first consider the interface being rough which can be modeled by a random distribution of tunneling centers $\mathbf{R}_i^{\rm S}$ with $t(\mathbf{R})=t_0\Sigma_{i=1}^{N_{\rm S}}\delta(\mathbf{R}-\mathbf{R}_i^{\rm S})$. Then, averaging over the tunneling centers, the tunneling self energy is given by

$$\check{\Sigma}_{\rm T}(\mathbf{R}_1,t_1;\mathbf{R}_2,t_2)=\frac{\lambda t_0^2 n_{\rm s}}{\hbar}\delta(\mathbf{R}_1-\mathbf{R}_2)\check{G}_{\rm M}(\mathbf{R}_1,z_1=0,t_1;\mathbf{R}_2,z_2=0,t_2), \tag{2.38}$$

and after the Wigner transform it becomes

$$\check{\Sigma}_{\rm T}(\mathbf{R},{\rm T};\mathbf{p},\epsilon)=\frac{\lambda t_0^2 n_{\rm s}}{\hbar}\int\frac{{\rm d}^3{\rm k}'}{(2\pi)^3}\check{G}_{\rm M}(\mathbf{R},z=0,{\rm T};\mathbf{k}',\epsilon), \tag{2.39}$$

where $\check{G}_{\rm M}(\mathbf{r}_\parallel,z,{\rm T};\mathbf{k},\epsilon)$ is the Wigner transform with respect to the 3D position and time coordinates. Now, we consider the 3D quasi-classical Green's function in the NM defined as

$$\check{g}_{\rm M}(\mathbf{r},{\rm T};{\rm k_F}\hat{\mathbf{k}},\epsilon)=\frac{i}{\pi}\int{\rm d}\xi_{\rm M}\ \check{G}_{\rm M}(\mathbf{r},{\rm T};\mathbf{k},\epsilon), \tag{2.40}$$

where $\xi_{\rm M}=\hbar^2k^2/(2m)+\epsilon_{\rm b}-\epsilon_{\rm F}$, $k_{\rm F}$ is the Fermi momentum in the NM and the $\xi_{\rm M}$ integration is performed near the Fermi surface. Since the quasi-classical Green's function is peaked at the Fermi energy, the Green's function satisfies following *ansatz*

$$\check{G}_{\rm M}(\mathbf{r},{\rm T};\mathbf{k},\epsilon)=-i\pi\check{g}_{\rm M}(\mathbf{r},{\rm T};{\rm k_F}\hat{\mathbf{k}},\epsilon)\delta(\xi_{\rm M}). \tag{2.41}$$

So the tunneling self-energy can be written as

$$\check{\Sigma}_{\mathrm{T}}(\mathbf{R},\mathrm{T};\mathbf{p},\epsilon)=-\frac{i}{\tau_{\mathrm{t}}}\langle\check{g}_{\mathrm{M}}(\mathbf{R},z=0,\mathrm{T};\mathrm{k_F}\hat{\mathbf{k}},\epsilon)\rangle, \tag{2.42}$$

where $\langle ...\rangle$ denotes angular averaging in the $\mathbf{k}$ space and we define $1/\tau_{\mathrm{t}}=\pi t_0^2 n_{\mathrm{s}} N_{\mathrm{m}}\lambda/\hbar$.

In case of a smooth interface, the tunneling can be modeled by $t(\mathbf{R})=t_{\mathrm{c}}$ being constant, and the Wigner transform tunneling self energy will be

$$\begin{aligned}\check{\Sigma}_{\mathrm{T}}(\mathbf{R},\mathrm{T};\mathbf{p},\epsilon)&=\frac{\lambda t_{\mathrm{c}}^2}{\hbar}\int\frac{\mathrm{d}k_z'}{2\pi}\check{G}_{\mathrm{M}}(\mathbf{R},z=0,\mathrm{T};\mathbf{p},k_z',\epsilon)\\&=\frac{\lambda t_{\mathrm{c}}^2}{\hbar}\int\frac{\mathrm{d}^3\mathrm{k}'}{(2\pi)^3}\check{G}_{\mathrm{M}}(\mathbf{R},z=0,\mathrm{T};\mathbf{k}_{\parallel}',k_z',\epsilon)(2\pi)^2\delta(\mathbf{k}_{\parallel}'-\mathbf{p}),\end{aligned} \tag{2.43}$$

where the in-plane momentum conservation holds. Using the *ansatz* Eq. (2.41) for the Green's function, and in case of the 3D quasi-classical Green's function being isotropic in the $\mathbf{k}$ space, i.e., being independent of the solid angle in the $\mathbf{k}$ space, we obtain same relation for the tunneling self energy as Eq. (2.42) with a redefined tunneling time given by $1/\tau_{\mathrm{t}}=\pi t_c^2 N_{\mathrm{m},1}\lambda/\hbar$.

In the quasi-classical limit, the Fermi energy is the largest energy scale, so the lowest order solution to the Green's function $G_{\mathrm{S}}^{\mathrm{K}}$ is given by the one that commutes with the term $\epsilon_{\mathrm{S}}(\mathbf{R})$ in the commutator in Eq. (2.32). Also, the normalization condition satisfied by the Keldysh Green's function $\check{G}_{\mathrm{S}}$ allows that the retarded and advanced Green's functions of the TI surface states can be obtained from the upper band projector of the TI surface state Hamiltonian[64, 65, 66, 67], i.e.,

$$G_{\mathrm{S}}^{\mathrm{R,A}}(\mathbf{p},\epsilon)=\frac{1}{2\lambda}\frac{\sigma_0+\boldsymbol{\sigma}\cdot(\hat{\mathbf{p}}\times\hat{\mathbf{z}})}{\epsilon-\xi_{\mathrm{S}}\pm i0^+}. \tag{2.44}$$

The retarded and advanced quasi-classical Green's functions and the disorder self energies

are then given by,

$$g_{\rm S}^{\rm R,A} = \pm\frac{1}{2}[\sigma_0 + \boldsymbol{\sigma}\cdot(\hat{\mathbf{p}}\times\hat{\mathbf{z}})],\ \Sigma_{\rm D}^{\rm R,A} = \mp\frac{i}{2\tau_{\rm p}}\sigma_0. \tag{2.45}$$

We consider the following *ansatz* for the Keldysh component $g_{\rm S}^{\rm K}(\hat{\mathbf{p}},\epsilon) = g_{\rm S}^{0}(\hat{\mathbf{p}},\epsilon)[\sigma_0 + \boldsymbol{\sigma}\cdot(\hat{\mathbf{p}}\times\hat{\mathbf{z}})]$, which means that the spin and momentum is locked for the TI surface states even in the non-equilibrium situation. In the diffusive limit, we can expand $g_{\rm S}^{0}(\hat{\mathbf{p}},\epsilon)$ in spherical harmonics[64, 65, 66, 68], i.e., $g_{\rm S}^{0}(\hat{\mathbf{p}},\epsilon) = {\rm g_s}(\epsilon) + \hat{\mathbf{p}}\cdot\mathbf{g}_{\rm a}(\epsilon)$, and solve the kinetic equation, i.e., Eq. (2.32). The actual non-equilibrium charge density $n_{\rm neq}$ on the surface of the TI will be obtained from $g_{\rm S}^{\rm K}(\hat{\mathbf{p}},\epsilon)$ by[67, 69]

$$n_{\rm neq} = \frac{eN}{2}\int {\rm d}\epsilon \frac{\rm Tr}{2}[\langle g_{\rm S}^{\rm K}(\hat{\mathbf{p}},\epsilon)\rangle] - e^2N\phi = \frac{eN}{2}\int {\rm d}\epsilon\ {\rm g_s}(\epsilon) - e^2N\phi. \tag{2.46}$$

We define the effective non-equilibrium charge density n by subsuming the contribution of the electrostatic potential ϕ, by the relation $n = n_{\rm neq} + e^2N\phi$. Hence, we have

$$n = \frac{eN}{2}\int {\rm d}\epsilon \frac{\rm Tr}{2}[\langle g_{\rm S}^{\rm K}(\hat{\mathbf{p}},\epsilon)\rangle] = \frac{eN}{2}\int {\rm d}\epsilon\ {\rm g_s}(\epsilon). \tag{2.47}$$

The current density $\mathbf{J}$ on the TI surface is given by

$$\mathbf{J} = \frac{eN}{2}\int {\rm d}\epsilon \frac{\rm Tr}{2}[\langle \mathbf{v} g_{\rm S}^{\rm K}(\hat{\mathbf{p}},\epsilon)\rangle] = \frac{eN}{2}\int {\rm d}\epsilon\ \frac{v_{\rm F}}{2}\mathbf{g}_{\rm a}(\epsilon). \tag{2.48}$$

The retarded and advanced Green's functions in the NM are given by

$$G_{\rm M}^{\rm R,A}(\mathbf{k},\epsilon) = \frac{1}{\epsilon - \xi_{\rm M} \pm i0^+}\sigma_0, \tag{2.49}$$

so the retarded and advanced quasi-classical Green's functions and the tunneling self energies

are obtained to be

$$g_{\rm M}^{\rm R,A} = \pm\sigma_0,\ \Sigma_{\rm D}^{\rm R,A} = \mp\frac{i}{\tau_{\rm t}}\sigma_0. \tag{2.50}$$

We consider the effect of the applied charge and the spin potential in the NM through the Keldysh component of the Green's function in the NM $g_{\rm M}^{\rm K}(\hat{\mathbf{k}},\epsilon)$. From Eq. (2.42), the tunneling self energy only depends on $g_{\rm M}^{\rm K}(z=0,\hat{\mathbf{k}},\epsilon)$, so we only consider $g_{\rm M}^{\rm K}(\hat{\mathbf{k}},\epsilon)$ at the interface $z=0$, but will write $g_{\rm M}^{\rm K}(\hat{\mathbf{k}},\epsilon)$ instead for brevity. The Keldysh component of the Green's function in the NM can be written as $g_{\rm M}^{\rm K}(\hat{\mathbf{k}},\epsilon) = [{\rm g}_{\rm M}^0(\hat{\mathbf{k}},\epsilon)\sigma_0 + \boldsymbol{\sigma}\cdot\mathbf{g}_{\rm M}(\hat{\mathbf{k}},\epsilon)]$. Further, the charge and spin densities in the NM, and the corresponding charge and spin electrochemical potentials in the NM will refer to the values at the interface and not be explicitly written afterwards. The actual non-equilibrium charge density $n_{\rm neq,m}$ in the NM is given by[67, 69]

$$n_{\rm neq,m} = \frac{eN_{\rm m}}{2}\int {\rm d}\epsilon \frac{\rm Tr}{2}[\langle g_{\rm M}^{\rm K}(\hat{\mathbf{k}},\epsilon)\rangle] - e^2N_{\rm m}\phi_{\rm m} = \frac{eN_{\rm m}}{2}\int {\rm d}\epsilon\ \langle {\rm g}_{\rm M}^0(\hat{\mathbf{k}},\epsilon)\rangle - e^2N_{\rm m}\phi_{\rm m}. \tag{2.51}$$

We define the effective non-equilibrium charge density $n_{\rm m}$ in the NM by subsuming the contribution from the electrostatic potential $\phi_{\rm m}$ by the relation $n_{\rm m} = n_{\rm neq,m} + e^2N_{\rm m}\phi_{\rm m}$. Hence, we have

$$n_{\rm m} = \frac{eN_{\rm m}}{2}\int {\rm d}\epsilon \frac{\rm Tr}{2}[\langle g_{\rm M}^{\rm K}(\hat{\mathbf{k}},\epsilon)\rangle] = \frac{eN_{\rm m}}{2}\int {\rm d}\epsilon\ \langle {\rm g}_{\rm M}^0(\hat{\mathbf{k}},\epsilon)\rangle. \tag{2.52}$$

The spin density $\boldsymbol{s}_{\rm m}$ (in the unit of electron charge density) in the NM is obtained from

$$\boldsymbol{s}_{\rm m} = \frac{eN_{\rm m}}{2}\int {\rm d}\epsilon \frac{\rm Tr}{2}[\langle \boldsymbol{\sigma} g_{\rm M}^{\rm K}(\hat{\mathbf{k}},\epsilon)\rangle] = \frac{eN_{\rm m}}{2}\int {\rm d}\epsilon\ \mathbf{g}_{\rm M}(\epsilon). \tag{2.53}$$

We define the full charge electrochemical potential $\mu_{\rm m}$ and the spin electrochemical potential $\boldsymbol{\mu}_{\rm s}$ in the NM given by $n_{\rm m} = 2e^2N_{\rm m}\mu_{\rm m}$ and $\boldsymbol{s}_{\rm m} = e^2N_{\rm m}\boldsymbol{\mu}_{\rm s}$. So, we obtain $\mu_{\rm m}$ and $\boldsymbol{\mu}_{\rm s}$ in terms

of the quasi-classical Green's functions as

$$\mu_{\rm m} = \frac{1}{4e}\int {\rm d}\epsilon\ {\rm g}^0_{\rm M}(\epsilon),\ \boldsymbol{\mu}_{\rm s} = \frac{1}{2e}\int {\rm d}\epsilon\ \mathbf{g}_{\rm M}(\epsilon). \tag{2.54}$$

After doing $\xi_{\rm S}$ integration of the Eq. (2.32), and using Eqs. (2.42) and (2.45), we obtain

$$\begin{aligned}\partial_{\rm T} g^{\rm K}_{\rm S} + \frac{1}{2}v_{\rm F}\big\{\hat{\mathbf{z}}\times\boldsymbol{\sigma}\cdot\nabla_{\mathbf{R}}, g^{\rm K}_{\rm S}\big\} + iv_{\rm F}p_{\rm F}[\boldsymbol{\sigma}\cdot(\hat{\mathbf{p}}\times\hat{\mathbf{z}}), g^{\rm K}_{\rm S}] = -\frac{g^{\rm K}_{\rm S} - \langle g^{\rm K}_{\rm S}\rangle}{\tau_{\rm p}} \\ + \frac{1}{2\tau_{\rm p}}\big\{\boldsymbol{\sigma}\cdot(\hat{\mathbf{p}}\times\hat{\mathbf{z}}), \langle g^{\rm K}_{\rm S}\rangle\big\} - \frac{2g^{\rm K}_{\rm S}}{\tau_{\rm t}} + \frac{1}{2\tau_{\rm t}}\big\{\sigma_0 + \boldsymbol{\sigma}\cdot(\hat{\mathbf{p}}\times\hat{\mathbf{z}}), \langle g^{\rm K}_{\rm M}\rangle\big\}.\end{aligned} \tag{2.55}$$

Now using the *ansatz* for $g^{\rm K}_{\rm S}$, after taking trace of Eq. (2.55) and integrating out the s- and p-wave components, we obtain

$$\partial_{\rm T}{\rm g}_{\rm s} + \frac{1}{2}v_{\rm F}\nabla_{\mathbf{R}}\cdot\mathbf{g}_{\rm a} = \frac{2}{\tau_{\rm t}}\left(\frac{{\rm g}^0_{\rm M}}{2} - {\rm g}_{\rm s}\right), \tag{2.56a}$$

$$\partial_{\rm T}\mathbf{g}_{\rm a} + v_{\rm F}\nabla_{\mathbf{R}}{\rm g}_{\rm s} = \frac{2}{\tau_{\rm t}}\left(\hat{\mathbf{z}}\times\frac{\mathbf{g}_{\rm M}}{2}\right) - \left(\frac{2}{\tau_{\rm t}} + \frac{1}{2\tau_{\rm p}}\right)\mathbf{g}_{\rm a}, \tag{2.56b}$$

which is equivalent to Eq. (2.9). After ϵ integration of Eq. (2.56a) and using the Eqs. (2.47), (2.48) and (2.54), we obtain the modified continuity equation on the TI surface i.e., Eq. (2.12). Similarly, after ϵ integration of Eq. (2.56b), the current density $\mathbf{J}$ is obtained to be the same as Eq. (2.13).

The spin current density across the TI/NM interface (in the unit of charge current density) will be given by $\mathbf{J}_{\rm s,1} = -e\lambda{\rm d}\mathbf{s}/{\rm d}t = -e\lambda(i/\hbar)[H_{\rm T}, \mathbf{s}]$ by the Heisenberg's equation of motion, where $\mathbf{s} = \langle a^\dagger_\alpha(\mathbf{R}, t)\boldsymbol{\sigma}_{\alpha\beta}a_\beta(\mathbf{R}, t)\rangle$. Applying the equation of motion to the operators, we obtain

$$\mathbf{J}_{\rm s,1} = \frac{-e\lambda}{\hbar}\int {\rm d}^3{\rm r}\ {\rm Tr}\Big[\boldsymbol{\sigma}\Big(G^<_{\rm Tc}(\mathbf{R}, t; \mathbf{r}, t)T(\mathbf{r}, \mathbf{R}) - T^\dagger(\mathbf{R}, \mathbf{r})G^<_{\rm T}(\mathbf{r}, t; \mathbf{R}, t)\Big)\Big]. \tag{2.57}$$

Here, the complex conjugate tunneling Green's function $(G_{\mathrm{Tc}})_{\alpha\beta}(\mathbf{R}, t_1; \mathbf{r}, t_2)$ is equal to $(G_{\mathrm{T}})^*_{\beta\alpha}(\mathbf{r}, t_2; \mathbf{R}, t_1)$, and $G^<_{\mathrm{Tc}}, G^<_{\mathrm{T}}$ are the corresponding lesser Green's function. From Eq. (2.24), we obtain for the complex conjugate tunneling Green's function

$$\begin{aligned}&(G_{\mathrm{Tc}})_{\alpha\beta}(\mathbf{R}_1, \tau_1; \mathbf{r}_2, \tau_2)\\&= \frac{\lambda}{\hbar}\int \mathrm{d}\tau' \mathrm{d}^2\mathrm{R}' \mathrm{d}^3\mathrm{r}' (G_{\mathrm{S}})_{\alpha\mu}(\mathbf{R}_1, \tau_1; \mathbf{R}', \tau') T^\dagger_{\mu\nu}(\mathbf{R}', \mathbf{r}') (G_{\mathrm{M}})_{\nu\beta}(\mathbf{r}', \tau'; \mathbf{r}_2, \tau_2).\end{aligned} \tag{2.58}$$

We write Eqs. (2.24), (2.58) and (2.26) in a simpler form as $G_{\mathrm{T}} = \frac{\lambda}{\hbar} G_{\mathrm{M}} T G_{\mathrm{S}}$, $G_{\mathrm{Tc}} = \frac{\lambda}{\hbar} G_{\mathrm{S}} T^\dagger G_{\mathrm{M}}$ and $\Sigma_{\mathrm{T}} = \frac{\lambda}{\hbar} T^\dagger G_{\mathrm{M}} T$, where the integrations over the internal variables are implicit. Then, from Eq. (2.57), $\mathbf{J}_{\mathrm{s}}$ can be written as

$$\mathbf{J}_{\mathrm{s},1} = \frac{-e\lambda}{\hbar}\ \mathrm{Tr}\left[\boldsymbol{\sigma}\Big(G^<_{\mathrm{Tc}} T - T^\dagger G^<_{\mathrm{T}}\Big)\right]. \tag{2.59}$$

By using Langreth rule[70] for the lesser function of product of three functions, which is given by

$$(ABC)^< = A^R B^R C^< + A^R B^< C^A + A^< B^A C^A, \tag{2.60}$$

$G^<_{\mathrm{Tc}}, G^<_{\mathrm{T}}$ can be written as

$$G^<_{\mathrm{T}} = \frac{\lambda}{\hbar}\left[G^R_{\mathrm{M}} T G^<_{\mathrm{S}} + G^<_{\mathrm{M}} T G^A_{\mathrm{S}}\right],\ G^<_{\mathrm{Tc}} = \frac{\lambda}{\hbar}\left[G^R_{\mathrm{S}} T^\dagger G^<_{\mathrm{M}} + G^<_{\mathrm{S}} T^\dagger G^A_{\mathrm{M}}\right]. \tag{2.61}$$

Here we have used the fact that the instantaneous tunneling T is neither retarded nor advanced and diagonal in Keldysh space, i.e. $T^R = T^A = T$ and $T^< = T^> = 0$, and similarly for $T^\dagger$. Inserting Eq. (2.61), and using the relation for Σ_{T}, Eq. (2.59) is written as

$$\mathbf{J}_{\mathrm{s},1} = \frac{-e\lambda}{\hbar}\ \mathrm{Tr}\left[\boldsymbol{\sigma}\Big(G^R_{\mathrm{S}}\Sigma^<_{\mathrm{T}} + G^<_{\mathrm{S}}\Sigma^A_{\mathrm{T}} - \Sigma^R_{\mathrm{T}} G^<_{\mathrm{S}} - \Sigma^<_{\mathrm{T}} G^A_{\mathrm{S}}\Big)\right]. \tag{2.62}$$

Now the lesser functions in Eq. (2.62) can be written in terms of retarded, advanced and

Keldysh component as $G_{\rm S}^{<} = \frac{1}{2}[G_{\rm S}^{K} - G_{\rm S}^{R} + G_{\rm S}^{A}]$ and $\Sigma_{\rm T}^{<} = \frac{1}{2}[\Sigma_{\rm T}^{K} - \Sigma_{\rm T}^{R} + \Sigma_{\rm T}^{A}]$. In the calculation of non-equilibrium quantities, only the Keldysh component is important[69], so $\mathbf{J}_{\rm s}$ is given by

$$\mathbf{J}_{\rm s,1} = \frac{-e\lambda}{\hbar}\,\frac{\rm Tr}{2}\Big[\boldsymbol{\sigma}\Big(G_{\rm S}^{R}\Sigma_{\rm T}^{K} + G_{\rm S}^{K}\Sigma_{\rm T}^{A} - \Sigma_{\rm T}^{R}G_{\rm S}^{K} - \Sigma_{\rm T}^{K}G_{\rm S}^{A}\Big)\Big]. \tag{2.63}$$

The above equation, i.e., Eq. (2.63), is written in coordinate representation and the product of two functions implies integration over the internal coordinates. The Eq. (2.63) can be written in terms of the modified Wigner transformed function in which the transformation of the product of two functions will be given by Eq. (2.31). So, in terms of the modified Wigner transformed functions, $\mathbf{J}_{\rm s}$ can be written as

$$\mathbf{J}_{\rm s,1} = -e\lambda\int\frac{{\rm d}\epsilon}{2\pi}\frac{{\rm d}^2{\rm p}}{(2\pi)^2}\,\frac{\rm Tr}{2}\Big[\boldsymbol{\sigma}\Big(G_{\rm S}^{R}\Sigma_{\rm T}^{K} + G_{\rm S}^{K}\Sigma_{\rm T}^{A} - \Sigma_{\rm T}^{R}G_{\rm S}^{K} - \Sigma_{\rm T}^{K}G_{\rm S}^{A}\Big)\Big]. \tag{2.64}$$

Using Eqs. (2.36), (2.42), (2.45) and (2.50), the above equation, i.e., Eq. (2.65), can be written in terms of the quasi-classical Green's functions as

$$\mathbf{J}_{\rm s,1} = \frac{eN}{2}\int{\rm d}\epsilon\int\frac{{\rm d}\theta}{2\pi}\frac{\rm Tr}{2}\Big[\boldsymbol{\sigma}\Big(-\frac{2g_{\rm S}^{\rm K}}{\tau_{\rm t}} + \frac{1}{2\tau_{\rm t}}\big\{\sigma_0 + \boldsymbol{\sigma}\cdot(\hat{\mathbf{p}}\times\hat{\mathbf{z}}), \langle g_{\rm M}^{\rm K}\rangle\big\}\Big)\Big] \tag{2.65}$$

It is clear from Eq. (2.65) that the spin current density across the interface will be obtained from taking trace over the spin Pauli matrices of the tunneling term, i.e. the last two terms in Eq. (2.55). Now, using the *ansatz* for $g_{\rm S}^{\rm K}$ and $g_{\rm M}^{\rm K}$, and using the definitions for $\mathbf{J}$ and $\boldsymbol{\mu}_{\rm s}$ from Eqs. (2.48) and (2.54), we get the equation for $\mathbf{J}_{\rm s,1}$, i.e. Eq. (2.15).

2.4 Solution of the transport equations under steady state spatially homogeneous conditions

Now we solve the non-equilibrium distribution function for the TI surface states under steady state spatially homogeneous conditions as per Zhang and Fert[27]. The assumption of a slowly varying in position charge electrochemical potential in the NM with respect to the electrochemical potential (or equivalently the effective non-equilibrium charge density n) on the TI surface is valid since the NM has much higher conductivity than the TI surface. In the next section, we show that under the assumption of a homogeneous charge electrochemical potential μ_{m} in the NM, the effective charge density n and the charge current density $\mathbf{J}$ on the TI surface surface become homogeneous in case of a short circuit between the two ends of the surface of the TI if either the applied spin electrochemical potential $\boldsymbol{\mu}_{\mathrm{s}}$ in the NM or the applied spin current density $\mathbf{J}_{\mathrm{s},1}$ from the NM to the TI surface through the TI/NM interface is assumed to be homogeneous. Under this homogeneous condition, we also show that the applied position-independent charge electrochemical potential μ_{m} in the NM will be balanced by a position-independent effective non-equilibrium charge density given by $n = e^2 N \mu_{\mathrm{m}}$. After defining the full electrochemical potential μ on the TI surface by $n = e^2 N \mu$, we obtain $\mu = \mu_{\mathrm{m}}$, i.e., a position-independent electrochemical potential on the TI surface which is perfectly balanced by a position-independent electrochemical potential in the NM. Then, the charge current density $\mathbf{J}$ on the TI surface becomes

$$\mathbf{J} = \frac{e^2 N v_{\mathrm{F}} \tau_{\mathrm{p}}}{4\tau_{\mathrm{p}} + \tau_{\mathrm{t}}} (\hat{\mathbf{z}} \times \boldsymbol{\mu}_{\parallel}), \tag{2.66}$$

where $\boldsymbol{\mu}_s = \boldsymbol{\mu}_\parallel + \mu_\perp \hat{\mathbf{z}}$, where $\mu_\perp = \boldsymbol{\mu}_s \cdot \hat{\mathbf{z}}$. Substituting Eq. (2.66) into Eq. (2.15), we find the spin current density $\mathbf{J}_s$ through the interface to be

$$\mathbf{J}_{s,1} = \frac{e^2 N}{4\tau_p + \tau_t}\left(1 + \frac{2\tau_p}{\tau_t}\right)\boldsymbol{\mu}_\parallel + \frac{e^2 N}{\tau_t}\mu_\perp \hat{\mathbf{z}}. \tag{2.67}$$

We note that the expression for the spin current density in Eq. (2.67) derived here differs from the one in the previous work of Zhang and Fert[27], despite the fact that we started with the same physical assumptions as theirs. Equation (2.67) indicates that the spin current density is induced by both the in-plane ($\boldsymbol{\mu}_\parallel$) and out-of-plane ($\mu_\perp$) components of the spin electrochemical potential. The coefficients for both terms are different from each other. Furthermore, the coefficient for the in-plane component in Eq. (2.67) differs from that provided by Zhang and Fert[27]. This difference becomes significant when the interface transmission time is comparable to or smaller than the momentum scattering time. The physical and practical significance of the difference will be addressed below.

Now we consider the physical meaning of the coefficients in the expression of $\mathbf{J}_{s,1}$ given in Eq. (2.67). It can be seen from Eq. (2.67) that the spin current density across the interface is directly proportional to the interface tunneling rate, $1/\tau_t$, if we consider pure out-of-plane component of the spin electrochemical potential (i.e., $\boldsymbol{\mu}_\parallel = 0$). In addition, in case of a pure in-plane component of the spin electrochemical potential (i.e., $\mu_\perp = 0$) in both limits of τ_p, $\tau_p \gg \tau_t$ and $\tau_p \ll \tau_t$, the spin current density across the interface also is proportional to the interface tunneling rate and, thus, depends on the barrier thickness, although the proportionality constant varies by a factor of 2 between these two limits. The spin current-to-charge current conversion efficiency is measured by the IEE length defined as $\lambda_{IEE} \equiv |\mathbf{J}|/|\mathbf{J}_{s,1}|$, which is found to be, in case of a pure in-plane spin-electrochemical

potential,

$$\lambda_{\mathrm{IEE}} = l_{\mathrm{p}} \Big/ \Big(1 + \frac{2\tau_{\mathrm{p}}}{\tau_{\mathrm{t}}}\Big), \tag{2.68}$$

where $l_{\mathrm{p}} \equiv v_{\mathrm{F}}\tau_{\mathrm{p}}$ is the mean free path on the TI surface. If the orientation of the spins in the spin current injected from the NM to the TI surface is purely out-of-plane, i.e., $\boldsymbol{\mu}_{\parallel} = 0$, from Eq. (2.66), there will be no charge current on the TI surface, because the spins of the carriers on the TI surface can only be oriented in-plane, since we have assumed an ideal helical Dirac Hamiltonian for the TI surface states with spins locked to the momentum on the 2D surface. In a real TI system, there will be hexagonal warping present, and in the thin film of TI there can be an additional gap opening around the Dirac point, which will provide a non-vanishing out-of-plane component to the spins of the TI surface states. In these cases, the charge current on the TI surface will be non-zero and will depend on the degree of the non-idealities of the Hamiltonian if the injected spins are out-of-plane. However, the ideal model of linear Dirac cone dispersion for the TI surface states remains valid if the Fermi energy lies away from the bulk bands, and away from the Dirac point in the thin TI films. In the experiment, the orientation of the spins in injected spin current through the interface is in-plane, so the IEE length is always less than the mean free path, i.e., $\lambda_{\mathrm{IEE}} < l_{\mathrm{p}}$, because of the correction factor $(1 + 2\tau_{\mathrm{p}}/\tau_{\mathrm{t}})$ in Eq. (2.68) with non-zero and finite τ_{p} and τ_{t}. This correction factor can be viewed as a modification of the IEE relaxation time τ_{IEE}, which is defined by $\lambda_{\mathrm{IEE}} \equiv v_{\mathrm{F}}\tau_{\mathrm{IEE}}$. So, the IEE relaxation time can be written as

$$\frac{1}{\tau_{\mathrm{IEE}}} = \frac{1}{\tau_{\mathrm{p}}} + \frac{2}{\tau_{\mathrm{t}}}. \tag{2.69}$$

Physically, both Eq. (2.14) and Eq. (2.69) exhibit an additional relaxation term in the helically locked TI surface states due to exchange of electrons across the interface, apart from scattering within the TI, that modifies the transport relaxation time and the IEE relaxation

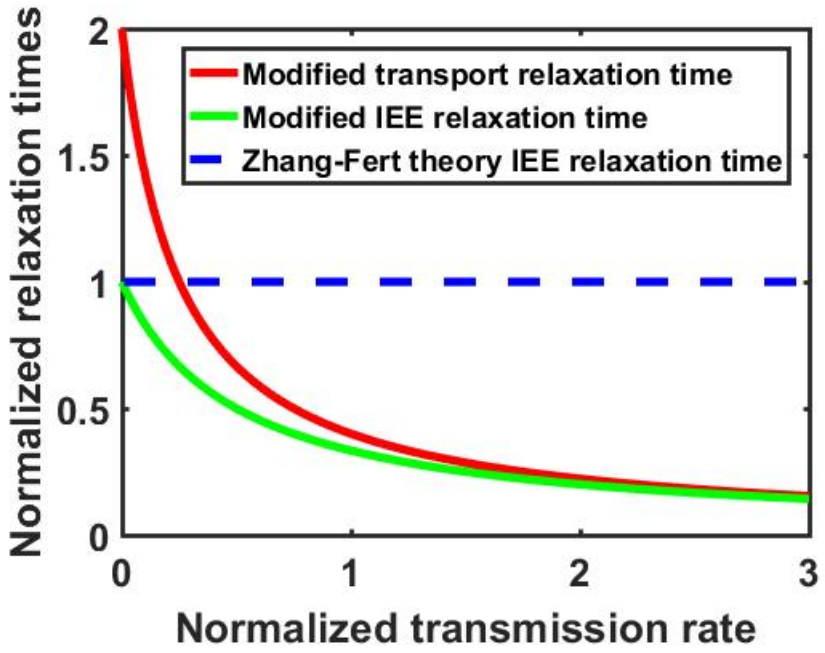

Figure 2.2: Variation of the normalized transport relaxation time and the normalized IEE relaxation time with the normalized transmission rate: The results shown by solid lines are obtained here, and the result shown by dotted line was obtained by Zhang and Fert[27].

time on the TI surface, respectively. The relaxation is a result of injection (extraction) of electrons from (to) the TI with a tilted-in-**p**-space quasi-Fermi level to (from) the flat-in-**k**-space spin electrochemical potential $\boldsymbol{\mu}_{\rm s}$ in the NM, which promotes injection and extraction of electrons. We find that the effects of the interface on the relaxation times are directly related through the interface transmission rate as shown in Fig. 2.2. In Fig. 2.2, we have plotted the variation of relaxation times normalized with respect to the momentum scattering time (i.e., the normalized transport relaxation time $\tau_{\rm tr}/\tau_{\rm p}$ and the normalized IEE relaxation time $\tau_{\rm IEE}/\tau_{\rm p}$) with the normalized transmission rate $\tau_{\rm p}/\tau_{\rm t}$. It is clear from Eq. (2.12) that the interface conductance is proportional to $2e^2N/\tau_{\rm t}$, and, so the variation of the relaxation times with the transmission rate in Fig. 2.2 also shows the variation with the interface conductance. Zhang and Fert[27] only pointed to a modification of the IEE relaxation rate due to the hybridization of the states of the TI and the NM (as well as

the bulk of the TI) through modification of the momentum relaxation rate $1/\tau_{\rm p}$ (through the overlap integral $C_{\rm d}$ in Eq. (2.8)), which, of course, remains relevant to this work as well. We find that such hybridization also modifies the IEE relaxation rate through interface transmission characterized by the rate $1/\tau_{\rm t}$ (through the overlap integral $C_{\rm t}$ in Eqs. (2.6) and (2.7)), with the resulting correction given by Eq. (2.68) becoming significant when the interface transmission rate $1/\tau_{\rm t}$ between the NM and the TI is comparable to or greater than the momentum relaxation rate $1/\tau_{\rm p}$. The hybridization of the states depend on the thickness and quality of the tunnel barrier. This finding is important because an absence of a tunnel barrier between the TI and the NM will lead to a higher interface transmission rate (limited only by the Landauer-Buttiker formula in the case of an ideal interface[71]) and, thus, a lower IEE relaxation time $\tau_{\rm IEE}$ than when a tunnel barrier is present at the interface.

Because of spin-pumping from the FM to the NM, there will be a spin current density $\mathbf{J}_{\rm s,2}$ flowing from the FM to the NM though the NM/FM interface given by

$$\mathbf{J}_{\rm s,2} = \frac{eG_{\rm mix}}{\pi\hbar}\left(\frac{\hbar}{2}\hat{\mathbf{m}}\times\frac{d\hat{\mathbf{m}}}{dt} - e\boldsymbol{\mu}_{\rm s}\right), \tag{2.70}$$

where $G_{\rm mix}$ is the mixing conductance of the NM/FM interface, $\hat{\mathbf{m}}$ is the magnetization direction of the FM. In case of the thickness d of the NM being much smaller that the spin diffusion length $\lambda_{\rm s}$ in the NM, we can assume that the spin electrochemical potential $\boldsymbol{\mu}_{\rm s}$ in the NM remains the same independent of the position inside the NM. Then, the spin current density $\mathbf{J}_{\rm s,2}$ through the NM/FM interface will be the same as the spin current density $\mathbf{J}_{\rm s,2}$ through the TI/NM interface. If the value of $\hat{\mathbf{m}}\times\frac{d\hat{\mathbf{m}}}{dt}$ lies in the plane of the devices as shown in Fig. 2.1, then we would have $\boldsymbol{\mu}_{\rm s} = \boldsymbol{\mu}_{\parallel}$ (i.e., $\mu_{\perp}\hat{\mathbf{z}} = 0$), and, from Eq. (2.67), we would obtain the spin current density $\mathbf{J}_{\rm s,2}$ through the TI/NM interface given by

$$\mathbf{J}_{\rm s,1} = \frac{e^2N}{4\tau_{\rm p}+\tau_{\rm t}}\left(1+\frac{2\tau_{\rm p}}{\tau_{\rm t}}\right)\boldsymbol{\mu}_{\rm s}. \tag{2.71}$$

2.5 Validity of steady state spatially homogeneous conditions

In the spin-pumping experiments as shown Fig. 2.1, the time average value of the term $\hat{\mathbf{m}} \times \frac{d\hat{\mathbf{m}}}{dt}$ remains the same and can be made oriented along the y-direction as shown in Fig 2.1, i.e., $\langle \hat{\mathbf{m}} \times \frac{d\hat{\mathbf{m}}}{dt} \rangle = I_{\rm s}^0 \, \hat{\mathbf{y}}$. Hence, we can consider steady state for the electrical transport on the TI surface and in the NM, and only the y-component of the spin electrochemical potential in the NM will be non-zero, i.e., $\boldsymbol{\mu}_{\rm s} = \mu_{\rm s,y} \, \hat{\mathbf{y}}$. Then, the problem can be considered as 1D problem with the transport direction taken to be in the x direction, and the charge current density on the TI surface can be written as $\mathbf{J} = j_x \hat{x}$. Since, the spin current density across the interface will have only y component, we can write $\mathbf{J}_{\rm s,1} = {\rm J}_{\rm s,1} \hat{y}$ and $\mathbf{J}_{\rm s,2} = {\rm J}_{\rm s,2} \hat{y}$. Then, from Eq. (2.70), the spin current density ${\rm J}_{\rm s,2}$ through the TI/NM interface is

$$ {\rm J}_{\rm s,2} = \frac{e G_{\rm mix}}{\pi \hbar} \left(\frac{\hbar}{2} I_{\rm s}^0 - e \mu_{\rm s,y} \right). \tag{2.72} $$

The continuity equation for the TI surface states, i.e. Eq. (2.12) becomes

$$ {\rm d}_x j_x = \frac{2}{\tau_{\rm t}} (e^2 N \mu_{\rm m} - n), \tag{2.73} $$

and from Eq. (2.13) the charge current density j_x on the TI surface becomes

$$ j_x = -\frac{v_{\rm F}^2 \tau_{\rm tr}}{2} {\rm d}_x n - e^2 N v_{\rm F} \frac{\tau_{\rm tr}}{\tau_{\rm t}} \frac{\mu_{\rm s,y}}{2}. \tag{2.74} $$

Then, from Eq. (2.15), the spin current density ${\rm J}_{\rm s,1}$ can be written as

$$ {\rm J}_{\rm s,1} = \frac{2}{v_{\rm F} \tau_{\rm t}} \left(e^2 N v_{\rm F} \frac{\mu_{\rm s,y}}{2} + j_x \right). \tag{2.75} $$

In the following, we solve the transport equations, Eqs. (2.73) and (2.74), on the TI surface analytically considering charge electrochemical potential $\mu_{\rm m}$ in the NM being spatially homogeneous and the two ends of the TI surface being shorted, with either the spin electrochemical potential $\mu_{\rm s,y}$ in the NM being homogeneous or the spin current density $\rm J_{s,1}$ across the interface being homogeneous.

First, we assume that $\mu_{\rm m}$ and $\mu_{\rm s,y}$ in the NM to be homogeneous. In steady state, Eqs. (2.73) and (2.74) give the differential equation $\partial_x^2 n' = n'/l'^2$ for the new variable $n' = (n - e^2 N \mu_{\rm m})$, where the characteristic length l is given by $l' = v_{\rm F}\sqrt{\tau_{\rm tr}\tau_{\rm t}}/2$. The solution to n' is given by $n'(x) = A_+ e^{x/l'} + A_- e^{-x/l'}$. In case of a short circuit between the two ends of the surface of the TI, we apply the boundary condition that the electrochemical potential on the TI surface at the two ends to be same, i.e., $n'(+L/2) = n'(-L/2)$, and the current going into the TI surface to be same as the current coming out of the TI surface (as there is no current leaking out through the NM or the FM), i.e., $j_x(+L/2) = j_x(-L/2)$. The condition $n'(+L/2) = n'(-L/2)$ gives $A_+ = A_- = A$ and the current density $j_x = -(v_{\rm F}^2\tau_{\rm tr}/2l)A(e^{x/l'} - e^{-x/l'}) - \rm J_0$, where $\rm J_0 = e^2 N v_F \tau_{tr} \mu_{s,y}/2\tau_t$. Now the condition $j_x(+L/2) = j_x(-L/2)$ is true only if $A = 0$, i.e., $n' = 0$, which implies $n = e^2 N \mu_{\rm m}$, and since $n = e^2 N \mu$, we obtain $\mu = \mu_{\rm m}$. So the electrochemical potential μ on the TI surface becomes homogeneous and balances any charge electrochemical potential $\mu_{\rm m}$ in the NM. Also, the charge current density j_x on the TI surface becomes homogeneous and is given by $j_x = -\rm J_0$. As both $\mu_{\rm s,y}$ and j_x are homogeneous, so the current density $\rm J_{s,1}$ through the interface also becomes homogeneous and is given by $\rm J_{s,1} = J_0/v_F \tau_{IEE}$.

Next we assume $\mu_{\rm m}$ in the NM and $\rm J_{s,1}$ across the interface to be homogeneous. From Eqs. (2.73), (2.74) and (2.75), we obtain a new differential equation $\partial_x^2 n' = n'/l'^2$, where the length l' is given by $l'^2 = v_{\rm F}\sqrt{\tau_{\rm IEE}\tau_{\rm t}/2}$. The solution to n' will be given by $n'(x) = A_+ e^{x/l'} + A_- e^{-x/l'}$. As discussed in the previous paragraph, for short circuit case the

boundary condition $n'(+L/2) = n'(-L/2)$ gives $A_+ = A_- = A$ and the current density $j_x = -(v_F^2 \tau_{IEE}/l')A(e^{x/l'} - e^{-x/l'}) - v_F \tau_{IEE} J_{s,1}$. As the spin current density across the interface is assumed to be homogeneous, the condition $j_x(+L/2) = j_x(-L/2)$ is true only if $A = 0$, which implies $n = e^2 N \mu_m$, and since $n = e^2 N \mu$, we obtain $\mu = \mu_m$. So the effective charge density n is homogeneous, and also the charge current density j_x on the TI surface becomes homogeneous and is given by $j_x = -v_F \tau_{IEE} J_{s,1}$. As both j_x and $J_{s,1}$ are homogeneous, the spin electrochemical potential $\mu_{s,y}$ in the NM turns out to be spatially homogeneous as well. Hence, a homogeneous condition for either $\mu_{s,y}$ or $J_{s,1}$, in case of short-circuit we have a homogeneous solution for n and j_x on the TI surface.

2.6 Consideration of the transport in the NM

To model the transport in the NM, we consider all the charge current densities and the spin current densities that flow to the NM from the TI through the TI/NM interface as well as from the FM through the NM/FM interface because of spin-pumping. The right side of the current continuity equation on the TI surface, i.e., Eq. (2.12), is the tunneling charge current density flowing from the NM to the TI surface through the TI/NM interface. So, an equal and opposite tunneling charge current density flows from the TI to the NM through the interface, which is given by (from Eq. (2.12))

$$J_{c,1} = \frac{2}{\tau_t}\big(n - e^2 N \mu_m\big), \tag{2.76}$$

where we denote $J_{c,1}$ as the 2D charge current density flowing to the NM through the TI/NM interface (1^{st} interface). In spin pumping from the FM to the NM, the charge current pumped to the NM will be zero, and to a good approximation, the electrochemical potentials in the FM will become equal to the electrochemical potentials in the NM. So, the charge current

density $J_{c,2}$ through the NM/FM interface (2^{nd} interface) will be zero, i.e., $J_{c,2} = 0$. Then, the charge transport equation in the NM is given by

$$\partial_t n_m + \nabla_{\mathbf{r}} \cdot \mathbf{J}_c = \frac{J_{c,1}}{d}, \tag{2.77}$$

where $\mathbf{r}$ is the 3D position vector in the NM and $\mathbf{J}_c = -D_m \nabla_{\mathbf{r}} n_m = -\sigma_m \nabla_{\mathbf{r}} \mu_m$ is the charge current density in the NM with D_m being the diffusion constant in the NM and $\sigma_m = 2e^2 N_m D_m$ being the conductivity of the NM, and d is the thickness of the NM. In Eq. (2.77), we assume that the thickness of the NM is small so that injected 2D charge current density $J_{c,1}$ is distributed uniformly over the thickness of the NM. Similarly, the spin transport equation in the NM is given by

$$\partial_t \boldsymbol{s}_m + \vec{\nabla}_{\mathbf{r}} \cdot \vec{\mathbf{J}}_s = \frac{1}{d}\left(\mathbf{J}_{s,1} + \mathbf{J}_{s,2}\right) - \frac{\boldsymbol{s}_m}{\tau_s}, \tag{2.78}$$

where $\vec{\mathbf{J}}_s = -D_m \vec{\nabla}_{\mathbf{r}} \boldsymbol{s}_m = -(\sigma_m/2)\vec{\nabla}_{\mathbf{r}} \boldsymbol{\mu}_s$ is the spin current in the NM, and τ_s is the spin diffusion time in the NM, and we have used arrow to denote the components of the spin current density in real-space whereas boldface is used to denotes the components in spin space. In Eq. (2.78), we also assume that the total injected 2D spin current density ($\mathbf{J}_{s,1} + \mathbf{J}_{s,2}$) are distributed uniformly over the thickness of the NM. In the following, we also assume that thickness d of the NM is much smaller that the spin diffusion length λ_s in the NM, where $\lambda_s = D_m \tau_s$, so that the charge and the spin electrochemical potentials of the NM, μ_m and $\boldsymbol{\mu}_s$, respectively, do not change along the z-direction.

As discussed in the previous section, we can consider steady state for the transport on the TI surface and in the NM, and the time average value of the term $\hat{\mathbf{m}} \times \frac{d\hat{\mathbf{m}}}{dt}$ can be taken to be along the y-direction as shown in Fig 2.1, i.e., $\langle \hat{\mathbf{m}} \times \frac{d\hat{\mathbf{m}}}{dt} \rangle = I_s^0 \, \hat{\mathbf{y}}$. Then, only the y-component of the spin electrochemical potential in the NM will be non-zero, i.e., $\boldsymbol{\mu}_s = \mu_{s,y} \, \hat{\mathbf{y}}$

and $\boldsymbol{s}_{\rm m} = s_y\ \hat{\mathbf{y}}$, where $s_y = e^2 N_{\rm m}\mu_{\rm s,y}$. We also consider that the transport in the y-direction is uniform, and the charge current density on the TI surface and both the charge and spin current densities in the NM will be in the x-direction only, i.e., $\mathbf{J} = j_x\hat{\mathbf{x}}$, $\mathbf{J}_{\rm c} = j_{c,x}\hat{\mathbf{x}}$ and $\vec{\mathbf{J}}_{\rm s} = j^x_{s,y}\hat{\mathbf{x}}$, where $j_{c,x} = -\sigma_{\rm m}{\rm d}_x\mu_{\rm m}$ and $j^x_{s,y} = -(\sigma_{\rm m}/2){\rm d}_x\mu_{\rm s,y}$. Then, the coupled transport equations on the TI surface and in the NM become 1D. The 1D transport equations on the TI surface are given by Eqs. (2.73) and (2.74). The 1D charge transport equations in the NM is given by

$$ {\rm d}_x j_{c,x} = \frac{{\rm J}_{\rm c,1}}{d}, \tag{2.79} $$

and, the 1D spin transport equation in the NM is given by

$$ {\rm d}_x j^x_{s,y} = \frac{1}{d}\Big({\rm J}_{\rm s,1} + {\rm J}_{\rm s,2}\Big) - \frac{s_y}{\tau_{\rm s}}. \tag{2.80} $$

From Eq. (2.74) we obtain

$$ j_x = -\frac{\sigma}{(1+\xi)}\left[{\rm d}_x\mu + \frac{\xi}{2l}\mu_{\rm s,y}\right], \tag{2.81} $$

where $l = v_{\rm F}\tau^0_{\rm tr} = 2v_{\rm F}\tau_{\rm p} = 2l_{\rm p}$ is the transport relaxation length (momentum relaxation length) on the pristine TI surface, $\sigma = e^2 ND$ is the conductivity of the pristine TI surface, $D = v^2_{\rm F}\tau^0_{\rm tr}/2$ is the diffusion constant on the pristine TI surface (without tunneling from the NM), and $\xi = 2\tau^0_{\rm tr}/\tau_{\rm t} = 4\tau_{\rm p}/\tau_{\rm t}$ is four times the normalized transmission rate $\tau_{\rm p}/\tau_{\rm t}$. Using Eq. (2.74) into Eq. (2.73), we obtain the following 1D differential equation for the electrochemical potential μ on the TI surface,

$$ {\rm d}^2_x\mu - \frac{2\xi(1+\xi)}{l^2}\Big(\mu - \mu_{\rm m}\Big) + \frac{\xi}{2l}{\rm d}_x\mu_{\rm s,y} = 0. \tag{2.82} $$

From Eq. (2.79) we obtain that the electrochemical potential $\mu_{\rm m}$ in the NM satisfies the

following 1D differential equation

$$\mathrm{d}_x^2\mu_\mathrm{m} - \frac{2\xi r}{l^2}\Big(\mu_\mathrm{m} - \mu\Big) = 0, \tag{2.83}$$

where $r = \sigma/(\sigma_\mathrm{m} d)$ is the dimensionless ratio of the conductivity of the TI surface and the normalized (with respect of the thickness d of the NM) conductivity of the NM (since the 2D conductivity of the TI surface and the 3D conductivity of the NM have different dimensions, r is a dimensionless quantity). From Eqs. (2.72), (2.75), and (2.80), we obtain the following 1D differential equation for the spin-electrochemical potential $\mu_{\mathrm{s,y}}$ of the NM,

$$\mathrm{d}_x^2\mu_{\mathrm{s,y}} - \left[\frac{1}{\lambda_\mathrm{s}^2} + \frac{1}{\lambda_\mathrm{m}^2} + \frac{\xi(2+\xi)r}{(1+\xi)l^2}\right]\mu_{\mathrm{s,y}} + \frac{2\xi r}{(1+\xi)l}\mathrm{d}_x\mu + i_\mathrm{s}^0 = 0, \tag{2.84}$$

where, $\lambda_\mathrm{s}^2 = D_\mathrm{m}\tau_\mathrm{s}$, $\lambda_\mathrm{m}^2 = \pi\hbar\sigma_\mathrm{m} d/2e^2 G_\mathrm{mix}$, and $i_\mathrm{s}^0 = (eG_\mathrm{mix}/\pi\sigma_\mathrm{m} d)I_\mathrm{s}^0$. Since, both $\lambda_\mathrm{s}, \lambda_\mathrm{m}$ are intrinsic property of the NM and the NM/FM interface, respectively, we define λ_i by $\frac{1}{\lambda_\mathrm{i}^2} = \frac{1}{\lambda_\mathrm{s}^2} + \frac{1}{\lambda_\mathrm{m}^2}$, and λ_i does not depend on the TI/NM interface. Equations (2.82)-(2.84) are the coupled transport equations in the heterostructure, and we next solve the transport equations with proper boundary conditions on the two ends of the TI surface and the NM. Here, we do not model the transport in the FM, which will be the case if the FM is an insulator.

2.7 Solution method for the coupled transport equations on the TI surface and in the NM

We consider that there will be no charge and spin current flowing out of the two ends of the NM, i.e., $\mathrm{d}_x\mu_\mathrm{m} = 0$ and $\mathrm{d}_x\mu_{\mathrm{s,y}} = 0$ at $x = \pm L/2$, where L is the length of the heterostructure in the x-direction. In the case of a short-circuit of the two ends of the TI surface, as shown

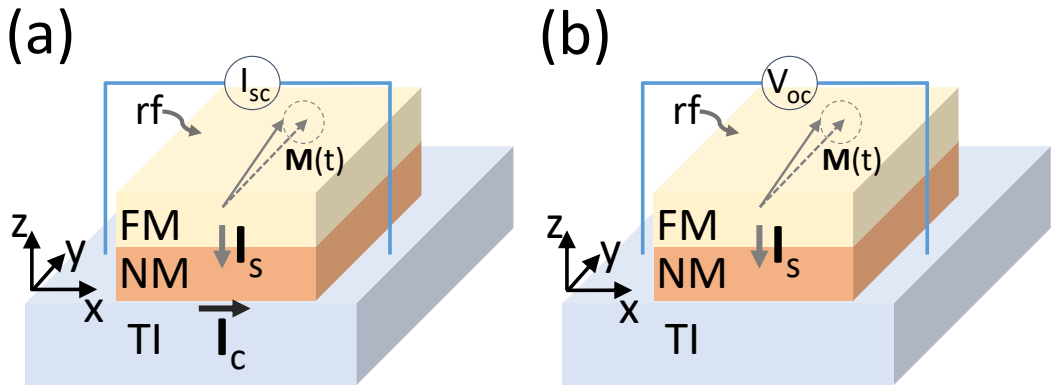

Figure 2.3: Schematics of detection of the IEE from the TI surface states in a spin-pumping experiment in TI/NM/FM heterostructure: (a) In case of short-circuit of the two ends of the TI surface, a short circuit current I_{sc} is detected. (b) In case of open circuit at the two ends of the TI surface, an open circuit voltage V_{oc} is measured.

in Fig. 2.3(a), the boundary condition on the TI surface will be $\mu(+L/2) = \mu(-L/2)$ and $j_x(+L/2) = j_x(-L/2) = I/W$, where W is the width of the heterostructure in the y-direction, and I will be determined from the solution of Eqs. (2.82)-(2.84) for given $i_{\rm s}^0$. In the case of an open-circuit at the two ends of the TI surface, as shown in Fig. 2.3(b), the boundary condition on the TI surface will be $j_x(+L/2) = j_x(-L/2) = 0$ (i.e. $I = 0$), however, the potential difference $\Delta\mu = \mu(+L/2) - \mu(-L/2)$ will be of interest for given $i_{\rm s}^0$.

From Eqs. (2.82) and (2.83), we obtain

$$\begin{aligned} & {\rm d}_x^2\mu + \frac{\xi}{2l}{\rm d}_x\mu_{\rm s,y} + \frac{(1+\xi)}{r}{\rm d}_x^2\mu_{\rm m} = 0 \\ \Longrightarrow\ & {\rm d}_x\mu + \frac{\xi}{2l}\mu_{\rm s,y} + \frac{(1+\xi)}{r}{\rm d}_x\mu_{\rm m} = i_{\rm c}, \end{aligned} \tag{2.85}$$

where $i_{\rm c}$ is some constant. From the boundary conditions ${\rm d}_x\mu_{\rm m} = 0$ at $x = \pm L/2$ and $j_x(\pm L/2) = I/W$ (where $I = 0$ for the open-circuit condition), using Eq. (2.81) we find $i_{\rm c} = -(1+\xi)I/\sigma W$. In the case of short-circuit condition, $i_{\rm c}$ will be determined for given $i_{\rm s}^0$, and in the case of open-circuit condition $i_{\rm c} = 0$. Taking derivative of Eq. (2.83) and

eliminating $\mathrm{d}_x\mu$ using Eq. (2.85), we obtain

$$\mathrm{d}_x^3\mu_\mathrm{m} - \frac{2\xi}{l^2}(1+\xi+r)\mathrm{d}_x\mu_\mathrm{m} + \frac{2\xi r}{l^2}i_\mathrm{c} - \frac{\xi^2 r}{l^3}\mu_\mathrm{s,y} = 0. \tag{2.86}$$

Similarly, after eliminating $\mathrm{d}_x\mu$ from Eq. (2.84) using Eq. (2.85), we obtain

$$\mathrm{d}_x^2\mu_\mathrm{s,y} - \frac{\mu_\mathrm{s,y}}{\lambda_1^2} + \frac{2\xi r}{(1+\xi)l}i_\mathrm{c} - \frac{2\xi}{l}\mathrm{d}_x\mu_\mathrm{m} + i_\mathrm{s}^0 = 0, \tag{2.87}$$

where we define λ_1 by $\frac{1}{\lambda_1^2} = \frac{1}{\lambda_\mathrm{i}^2} + \frac{2\xi r}{l^2}$. From Eqs. (2.86) and (2.87), after eliminating μ_m we obtain the following differential equation only involving $\mu_\mathrm{s,y}$,

$$\mathrm{d}_x^4\mu_\mathrm{s,y} - \left[k^2 + \frac{1}{\lambda_1^2}\right]\mathrm{d}_x^2\mu_\mathrm{s,y} + \frac{k^2}{\lambda_2^2}\mu_\mathrm{s,y} = k^2(i_\mathrm{c}^0 + i_\mathrm{s}^0), \tag{2.88}$$

where, $k^2 = 2\xi(1+\xi+r)/l^2$, $\frac{1}{\lambda_2^2} = \frac{1}{\lambda_\mathrm{i}^2} + \frac{\xi r(2+\xi+2r)}{(1+\xi+r)l^2}$, and $i_\mathrm{c}^0 = \frac{2\xi r^2}{(1+\xi)(1+\xi+r)l}i_\mathrm{c}$. Equation (2.88) is a non-homogeneous differential equation for $\mu_\mathrm{s,y}$, and the solution is given by

$$\mu_\mathrm{s,y} = A_+e^{q_1 x} + A_-e^{-q_1 x} + B_+e^{q_2 x} + B_-e^{-q_2 x} + \lambda_2^2(i_\mathrm{c}^0 + i_\mathrm{s}^0), \tag{2.89}$$

where q_1, q_2 are given by

$$q_{1,2} = \left[\frac{1}{2}\left(k^2 + \frac{1}{\lambda_1^2}\right) \pm \sqrt{\frac{1}{4}\left(k^2 + \frac{1}{\lambda_1^2}\right)^2 - \frac{k^2}{\lambda_2^2}}\right]^{\frac{1}{2}}. \tag{2.90}$$

Similarly, from Eqs. (2.86) and (2.87), after eliminating $\mu_\mathrm{s,y}$ we obtain the following differential equation for μ_m,

$$\mathrm{d}_x^5\mu_\mathrm{m} - \left[k^2 + \frac{1}{\lambda_1^2}\right]\mathrm{d}_x^3\mu_\mathrm{m} + \frac{k^2}{\lambda_2^2}\mathrm{d}_x\mu_\mathrm{m} = \frac{k^2}{\lambda_2^2}E, \tag{2.91}$$

where we define E to be,

$$E = \frac{(1+\xi)l}{2\xi r} i_{\rm c}^0 - \frac{\xi r}{2(1+\xi+r)l} \lambda_2^2 (i_{\rm c}^0 + i_{\rm s}^0). \tag{2.92}$$

Equation (2.91) is a non-homogeneous differential equation for $\mu_{\rm m}$, and the solution is given by

$$\mu_{\rm m} = C_+ e^{q_1 x} + C_- e^{-q_1 x} + D_+ e^{q_2 x} + D_- e^{-q_2 x} + Ex + E_0, \tag{2.93}$$

where, E_0 is the constant of integration. The solution of $\mu_{\rm m}$ in Eq. (2.93) and the solution of $\mu_{\rm s,y}$ in Eq. (2.89) must satisfy Eqs. (2.86) and (2.87). Using Eqs. (2.89) and (2.93) into Eq. (2.86) (or equivalently in Eq. (2.87)), we obtain that the constants $C_\pm, D_\pm$ are related to $A_\pm, B_\pm$, respectively, by

$$C_\pm = \pm \frac{\xi^2 r}{l^3} \frac{A_\pm}{q_1^2(q_1^2 - k^2)}, \; D_\pm = \pm \frac{\xi^2 r}{l^3} \frac{B_\pm}{q_2^2(q_2^2 - k^2)}. \tag{2.94}$$

The four coefficients $A_\pm, B_\pm$ are determined from the four boundary conditions $\mathrm{d}_x \mu_{\rm m} = 0$ and $\mathrm{d}_x \mu_{\rm s,y} = 0$ at $x = \pm L/2$. We obtain $A_+ = A_- = A$, $B_+ = B_- = B$, where A, B are given by

$$\begin{aligned} A &= \frac{\frac{l^3 E}{2\xi^2 r} q_2 (q_1^2 - k^2)(q_2^2 - k^2) \frac{\tanh(q_2 L/2)}{\cosh(q_1 L/2)}}{[q_1(q_1^2 - k^2)\tanh(q_1 L/2) - q_2(q_2^2 - k^2)\tanh(q_2 L/2)]}, \\ B &= \frac{-\frac{l^3 E}{2\xi^2 r} q_1 (q_1^2 - k^2)(q_2^2 - k^2) \frac{\tanh(q_1 L/2)}{\cosh(q_2 L/2)}}{[q_1(q_1^2 - k^2)\tanh(q_1 L/2) - q_2(q_2^2 - k^2)\tanh(q_2 L/2)]}. \end{aligned} \tag{2.95}$$

So, we also obtain $C_+ = -C_- = C$, $D_+ = -D_- = D$, where C, D are given by

$$C = \frac{\xi^2 r}{l^3} \frac{A}{q_1^2(q_1^2 - k^2)}, \; D = \frac{\xi^2 r}{l^3} \frac{B}{q_2^2(q_2^2 - k^2)}. \tag{2.96}$$

Hence, the solution for $\mu_{\rm s,y}$ can be written as

$$\mu_{\rm s,y} = 2A\cosh(q_1 x) + 2B\cosh(q_2 x) + \lambda_2^2(i_{\rm c}^0 + i_{\rm s}^0), \tag{2.97}$$

and, the solution for $\mu_{\rm m}$ can be written as

$$\mu_{\rm m} = 2C\sinh(q_1 x) + 2D\sinh(q_2 x) + Ex + E_0. \tag{2.98}$$

The solution for μ is obtained from Eq. (2.83) to be

$$\mu = 2C\left(1 - \frac{q_1^2 l^2}{2\xi r}\right)\sinh(q_1 x) + 2D\left(1 - \frac{q_2^2 l^2}{2\xi r}\right)\sinh(q_2 x) + Ex + E_0. \tag{2.99}$$

The integration constant E_0 is undetermined and only appears in the charge electrochemical potentials of the TI and the NM. Since, only the potential difference is physical, we can set $E_0 = 0$ without loss of generality (gauge fixing for the charge electrochemical potential). Equations (2.97)-(2.99) will give the solution of the coupled transport equations, i.e., Eqs. (2.82)-(2.84), where the constants A, B are given by Eq. (2.95), the constants C, D are given by Eq. (2.96), and the constant E is given by Eq. (2.92).

2.8 Solutions for short-circuit and open-circuit conditions

In case of a short-circuit of the two ends of the TI surface, as shown in Fig. 2.3(a), the same amount of charge current will be injected in and extracted out of the TI surface, and we have the boundary condition $\mu(+L/2) = \mu(-L/2)$ and $j_x(+L/2) = j_x(-L/2) = I/W$. Using $\mu(+L/2) = \mu(-L/2)$ in Eq. (2.99), we obtain that $A = B = C = D = E = 0$. Hence, from Eq. (2.89) we obtain that $\mu_{\rm s,y}$ is spatially constant, and the solution derived

with the assumption of homogeneous condition remains valid. We define the IEE efficiency by $J/(l_{\rm p}J_{s,2})$, where $J = I/W$ is the 2D charge current density on the TI surface and $J_{s,2}$ is the 3D spin current density through the TI/NM interface given in Eq. (2.72). It should be noted that the IEE efficiency defined by $J/(l_{\rm p}J_{s,2})$ is the normalized IEE relaxation time $\tau_{\rm IEE}/\tau_{\rm p}$ in case of short-circuit condition.

In case of an open-circuit at the two ends on the TI surface, as shown in Fig. 2.3(a), the boundary condition will be $j_x(+L/2) = j_x(-L/2) = 0$ (i.e. $I = 0$ implying $i_c = 0$ and so $i_c^0 = 0$). Substituting $i_c^0 = 0$ in the above solution of E derived in Eq. (2.92) for a given $i_{\rm s}^0 \neq 0$, we calculate μ on the TI surface from Eq. (2.99) and the potential difference $\Delta\mu = \mu(+L/2) - \mu(-L/2)$. We also calculate the spatial average 3D spin current density $J_{s,avg}$ through the TI/NM interface after integrating Eq. (2.72) over the length L, and define the IEE efficiency by $(\Delta\mu/L)/(l_{\rm p}J_{s,avg})$.

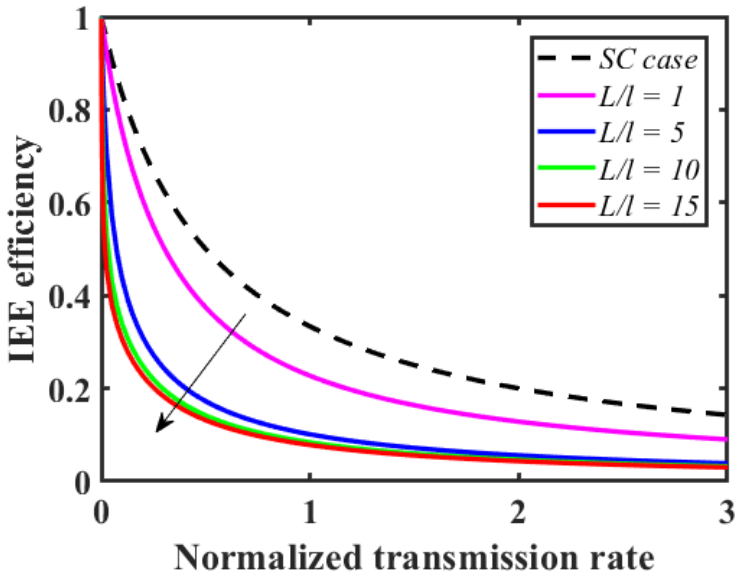

Figure 2.4: Variation of the IEE efficiency with the normalized transmission rate for short-circuit and open-circuit conditions: The dotted line shows the efficiency in case of short-circuit (SC) which is independent of L, the solid lines are the efficiencies in case of open-circuit (OC) with $\lambda_{\rm i}/l = 200$, $r = 0.5$, and different values of $L/l = 1, 5, 10, 15$.

Figure 2.4 shows the IEE efficiency, which is a measure of the spin-to-charge current conversion efficiency of the interface, with the normalized transmission rate $\tau_{\rm p}/\tau_{\rm t}$ across the interface for both the short-circuit (SC) and the open-circuit (OC) case for the device parameter of $\lambda_{\rm i}/l = 200$, $r = 0.5$, and different values of $L/l = 1, 5, 10, 15$. The efficiency measured in the open-circuit condition is significantly lower than that in the short-circuit condition for values of L larger than the transport relaxation length l on the pristine TI surface. This is because the assumption of spatial homogeneity is no longer valid in the open-circuit condition, and the electrochemical potentials on the TI surface as well as in the NM become position dependent and balances themselves to maintain the open boundary condition. The efficiency in the open-circuit condition saturates as the values of L are increased, as shown in Fig. 2.4. In actual experiment, the efficiency that is measured corresponds to that for the open-circuit condition. However, we find that the efficiency decreases with increasing conductance of the TI/NM interface for both the short-circuit and the open-circuit conditions.

2.9 Comparison to experimental results

In a recent experiment on the Edelstein magnetoresistance of the Rashba 2D electron gas (2DEG) at the Bi_2O_3/Cu interface[72], a phenomenological model is used for the total relaxation time of spin states in the Rashba 2DEG/metal interface consisting of spin relaxation time at the interface and spin relaxation time out of the interface into the metal. Our theory gives an explanation of the phenomenological model that has been used to explain the Edelstein magnetoresistance of the Rashba 2DEG, in which the spin relaxation time at the interface is equivalent to the momentum relaxation time (or the transport relaxation time as we call it) on the TI surface in our model. The momentum relaxation time is same as the

spin relaxation time on the TI surface because of the spin-momentum locking on the TI surface states. The spin relaxation time out of the interface into the metal is equivalent to the interface tunneling time across the interface. Our result also could explain the experimental observation of a short τ_{IEE} at an interface with a metal, such as in the interface between the Rashba 2DEG at Bi/Ag interface[41] or the topological insulator α-Sn/Ag interface[42], but a longer τ_{IEE} for Rashba 2DEG at STO/LAO oxide interface[73, 74]. Further experiments on TI/oxide interfaces compared to TI/metal interfaces will be of interest to see the effect of the interface transmission rate in the spin current-to-charge current conversion efficiency.

2.10 Summary

In summary, we have studied the spin-charge transport on a TI surface coupled to a metal through a tunnel barrier and derived various parameters related to the transport, including the transport relaxation time, the IEE relaxation time and the spin-to-charge conversion efficiency of the bilayer when the metal has a pure spin bias. We found that the interface transmission rate plays a crucial role in determining the transport relaxation rate, the IEE relaxation rate, and the spin-to-charge conversion efficiency. In particular, we found that reducing the barrier thickness to the point that the interface transmission and the momentum relaxation rates are comparable reduces the spin-to-charge conversion efficiency. However, increasing the barrier thickness reduces the absolute spin injection. Thus, performance optimization will require careful barrier design.

Chapter 3

Theory of inverse Edelstein effect on the surface of topological insulator due to spin-polarized tunneling

The spin-momentum helical locking of the two-dimensional (2D) surface states in a three dimensional (3D) topological insulator (TI) ensures that a charge current on the surface of the TI will be induced by an applied spin current onto the surface, which is known as the inverse Edelstein effect (IEE)[10, 27]. The IEE can be achieved either by injecting pure spin current by spin-pumping from a ferromagnetic metal (FM) layer[42, 43, 44, 45, 46, 47, 49] that we have discussed in the previous chapter, or by injecting spin-polarized charge current by direct tunneling of electrons from the FM to the TI[31] as shown in Fig. 3.1(a). Here, we present a theory of the observed IEE effect in a TI-FM heterostructure for the spin-polarized tunneling experiment as shown schematically in Fig. 3.1(a). If a charge current I_c flowed from the FM to the surface of the TI, because of the density of state (DOS) polarization of the majority and minority electrons in the FM, a spin-polarized charge current flows from the FM to the TI and an effective imbalance of spin-polarized electrons occurs on the surface of the TI. Due to the spin-momentum helical locking of the surface states in the TI, the spin-polarized electrons coming from the FM flow accordingly on the surface of the TI, and the imbalance of spin-polarized electrons creates a difference of transverse charge accumulation appearing on the boundary of the TI surface along the direction orthogonal to the direction

Parts of this chapter have been published as Ref. [75]: R. Dey, L. F. Register, and S. K. Banerjee, "Modeling all-electrical detection of the inverse Edelstein effect by spin-polarized tunneling in a topological-insulator/ferromagnetic-metal heterostructure", *Physical Review B*, **97**, 144417 (2018), Copyright 2018 by the American Physical Society. Available: https://doi.org/10.1103/PhysRevB.97.144417. Contribution of the dissertator: The dissertator, Rik Dey, performed the theoretical calculations, wrote the manuscript, and is the corresponding author of this publication.

of the magnetization of the FM. The difference of charge accumulation is measured as a voltage difference at the two ends of the TI surface. An order of estimate for the observed voltage drop is provided by Liu *et. al.* with a simplifying assumption of uniform current density on the surface of the TI[31]. However, the current density on the TI surface could be non-uniform, and one needs to solve the transport equations on the TI surface, considering current injection from the FM, with proper boundary condition on the TI surface to obtain the distribution of electrochemical potential on the TI surface.

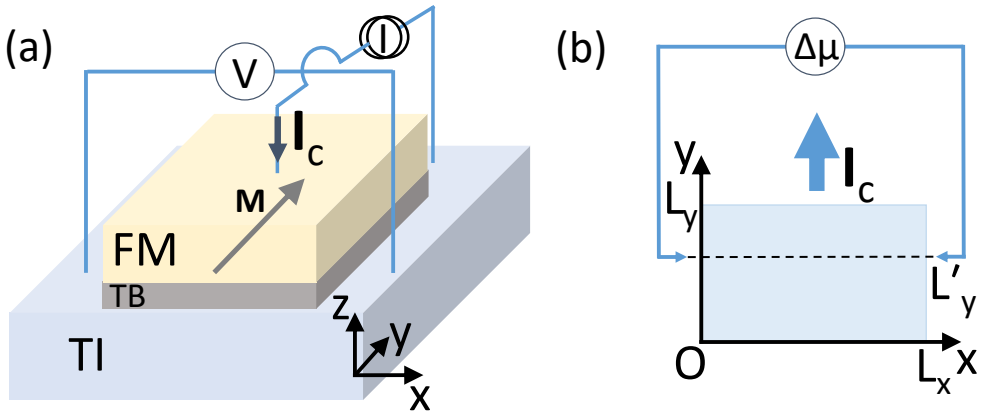

Figure 3.1: Schematics of measuring the IEE on the surface of the TI in a TI-FM heterostructure with spin current generated by spin-polarized tunneling: (a) Device geometry showing the TI-FM vertical stack with the current and voltage probe configurations, (b) Plan view of the rectangular region on the TI surface showing current I_c flowing out of the boundary $y = L_y$ and electrochemical potential drop $\Delta\mu$ measured at $y = L'_y$.

In this chapter, we derive the two-dimensional transport equations on the surface of a diffusive TI, coupled to a FM, starting from quantum kinetic equation. We obtain a second order partial differential equation for the electrochemical potential on the TI surface with a source term due to the tunneling from the FM. We, then, analytically solve the differential equation in a rectangular geometry, with net current flowing along one boundary and no currents at other boundaries as shown in Fig. 3.1(b), to calculate the voltage difference that was measured in the experiment. We show that the voltage difference depends on the magnetization direction and the DOS polarization of the FM, and the voltage difference

changes sign upon reversal of the magnetization direction of the FM which can be used as a detection method for the FM magnetization reversal. We also show that the voltage difference depends on the size of the device and the tunnel conductance of the TI-FM interface and becomes small if the interface conductance is high, which implies the importance of a tunnel barrier in such spin-polarized tunneling experiment.

3.1 Derivation of quantum kinetic equation for the TI surface states coupled to the FM

To derive the quantum kinetic equation describing transport on the TI surface coupled to the FM, we follow the procedure described in chapter 2. We consider the following Hamiltonian for the TI-FM heterostructure shown in Fig. 3.1,

$$H_{\rm tot} = H_{\rm TI} + H_{\rm dis} + H_{\rm FM} + H_{\rm tun}. \tag{3.1}$$

Here, $H_{\rm TI}$ is the low energy effective Hamiltonian for the TI surface states in second-quantized form, which is given by

$$H_{\rm TI} = \lambda \int {\rm d}^2{\rm R} \sum_{\alpha,\beta} c^\dagger_\alpha(\mathbf{R}) \big[\epsilon_{\rm TI}(\mathbf{R}) - \epsilon_{\rm F}\sigma_0 - e\phi\sigma_0\big]_{\alpha\beta} c_\beta(\mathbf{R}), \tag{3.2}$$

where $\epsilon_{\rm TI}(\mathbf{R}) = -i\hbar v_{\rm F}[(\nabla_{\mathbf{R}} \times \hat{\mathbf{z}}) \cdot \boldsymbol{\sigma}]$, $v_{\rm F}$ is the Fermi velocity of the Dirac surface states, $\epsilon_{\rm F}$ is the Fermi energy, $\mathbf{R}$ is the 2D position vector on the TI surface, and ϕ is the electrostatic potential of any electric field on the TI surface. The creation and annihilation operators of the TI surface states are $c^\dagger_\alpha(\mathbf{R})$, $c_\beta(\mathbf{R})$ (where (α, β) are the spin indices) which satisfy the equal-time anti-commutator relation $\{c_\alpha(\mathbf{R}), c^\dagger_\beta(\mathbf{R}')\} = \lambda^{-1}\delta(\mathbf{R} - \mathbf{R}')\delta_{\alpha\beta}$ normalized to the thickness λ of the TI surface states. The disorder Hamiltonian $H_{\rm dis}$ representing the

impurities on the TI surface is given by

$$H_{\rm dis} = \lambda \int {\rm d}^2{\rm R} \sum_{\alpha} c^{\dagger}_{\alpha}(\mathbf{R}) V_{\rm dis}(\mathbf{R}) c_{\alpha}(\mathbf{R}), \tag{3.3}$$

where $V_{\rm dis}(\mathbf{R}) = V_{\rm d} a_{\rm d} \Sigma_{j=1}^{N_{\rm I}} \delta(\mathbf{R} - \mathbf{R}^{\rm I}_j)$ is spin-independent short-ranged impurity potential, $V_{\rm d}$ is the average impurity potential for impurities on and close to the interface, $\mathbf{R}^{\rm I}_j$'s are the locations of the randomly distributed impurities, and and $a_{\rm d}$ is a normalization constant with unit of area for the normalization of the delta function.

We consider the FM Hamiltonian $H_{\rm FM}$, which is given by

$$H_{\rm FM} = \int {\rm d}^3{\rm r} \sum_{\alpha,\beta} d^{\dagger}_{\alpha}(\mathbf{r}) \left[\epsilon_{\rm FM}(\mathbf{r}) - \epsilon_{\rm F}\sigma_0 - e\phi_{\rm c}\sigma_0\right]_{\alpha\beta} d_{\beta}(\mathbf{r}). \tag{3.4}$$

Here, $\epsilon_{\rm FM}(\mathbf{r}) = [-\frac{\hbar^2}{2m_{\rm c}}\nabla^2_{\mathbf{r}} + \epsilon_{\rm b}]\sigma_0 - \Delta_{\rm ex}\mathbf{m}\cdot\boldsymbol{\sigma}$ describes the two spin-splitted bands in the FM, $\mathbf{r}$ is the 3D position vector in the metal, $m_{\rm c}$ is the effective mass for both the conduction bands in the FM, $\epsilon_{\rm b}$ is the band offset relative to the Dirac point of the TI surface states, $\Delta_{\rm ex}$ is the effective strength of exchange interaction between the itinerant s-electrons and the localized d-electrons in the FM, $\hat{\mathbf{m}} = m_x\hat{\mathbf{x}} + m_y\hat{\mathbf{y}} + m_z\hat{\mathbf{z}}$ is the unit vector along the direction of magnetization in the FM, and $\phi_{\rm c}$ is electrostatic potential of any electric field in the FM. The two bands of the FM will be spin splitted with an splitting energy of $2\Delta_{\rm ex}$. The creation and annihilation operators in the metal are $d^{\dagger}_{\alpha}(\mathbf{r})$ and $d_{\beta}(\mathbf{r})$, which satisfy the equal-time anti-commutator $\{d_{\alpha}(\mathbf{r}), d^{\dagger}_{\beta}(\mathbf{r}')\} = \delta(\mathbf{r} - \mathbf{r}')\delta_{\alpha\beta}$. The creation and the annihilation operators in the metal and on the TI surface anti-commutes, i.e., $\{c_{\alpha}(\mathbf{R}), d^{\dagger}_{\beta}(\mathbf{r}')\} = 0$.

The coupling of the TI surface states to the FM is described by a tunneling Hamiltonian $H_{\rm tun}$, which represents the transmission of the electron in and out of the TI surface states

from and to the FM, given by

$$H_{\rm tun} = \lambda \int {\rm d}^2{\rm R} \int {\rm d}^3{\rm r} \sum_{\alpha,\beta} \left[d^\dagger_\alpha(\mathbf{r}) T_{\alpha\beta}(\mathbf{r},\mathbf{R}) c_\beta(\mathbf{R}) + h.c. \right]. \tag{3.5}$$

We consider a site-to-site (local) instantaneous tunneling at the interface, and the tunneling matrix has the form $T_{\alpha\beta}(\mathbf{r},\mathbf{R}) = t_{\alpha\beta} f(\mathbf{R}) \delta(\mathbf{r}_\parallel - \mathbf{R}) \delta(z)$, where $t_{\alpha\beta} f(\mathbf{R})$ describes the nature of the tunneling. The dependence of $t_{\alpha\beta}$ on the spin indices $(\alpha\beta)$ describes whether the tunneling is spin-conserving or spin-selective but spin-non-conserving, and the dependence of $f(\mathbf{R})$ on $\mathbf{R}$ describes whether the tunneling is momentum randomizing or in-plane momentum conserving. In case of a rough interface, the tunneling will be momentum randomizing, and the tunneling is modeled by randomly distributed tunneling centers with $f(\mathbf{R}) = a_{\rm t} \Sigma_{i=1}^{N_{\rm S}} \delta(\mathbf{R} - \mathbf{R}^{\rm S}_i)$, where $\mathbf{R}^{\rm S}_i$'s are the positions of the tunneling centers, and $a_{\rm t}$ is a normalization constant with unit of area for the normalization of the delta function. In case of a smooth interface, the tunneling will be in-plane momentum conserving, and the tunneling is modeled by a position-independent function $f(\mathbf{R})$ (we take $f(\mathbf{R}) = 1$). For spin-conserving tunneling, the tunneling can be modeled by $t_{\alpha\beta} = t_0 \delta_{\alpha\beta}$, where the tunneling from both the bands in the FM to the TI surface states (and vice versa) have the same tunneling strength t_0. For spin-selective but spin-non-conserving tunneling, the tunneling from the two bands in the FM to the TI surface states (and vice versa) will have a different strength, and the tunneling can be modeled by $t_{\alpha\beta} = (t_\uparrow {\rm P}_\uparrow + t_\downarrow {\rm P}_\downarrow)_{\alpha\beta}$. Here, ${\rm P}_{\uparrow,\downarrow} = (\sigma_0 + \mathbf{m}\cdot\boldsymbol{\sigma})/2$ are the projection operators to the two spin splitted bands in the FM, and $t_{\uparrow,\downarrow}$ are the corresponding tunneling strength. If $t_\uparrow \neq t_\downarrow$, the tunneling will be spin-non-conserving, and the spin-conserving tunneling is a special case when $t_\uparrow = t_\downarrow = t_0$.

The quantum kinetic equation, which is obtained from the Keldysh component of the Wigner transformed left-right subtracted Dyson equation after lowest order gradient expan-

sion, is given by

$$\begin{aligned}&\partial_{\rm t}G^{\rm K} - e\ \partial_{\rm t}\phi\ \partial_\epsilon G^{\rm K} + \frac{1}{2}\big\{\mathbf{v}\cdot\nabla_{\mathbf{R}}, G^{\rm K}\big\} + \frac{i}{\hbar}\left[\epsilon_{\rm TI}(\mathbf{p}), G^{\rm K}\right] + e\ \nabla_{\mathbf{R}}\phi\cdot\nabla_{\mathbf{p}}G^{\rm K}\\ &= -i\big[\ \big(\Sigma^{\rm R}G^{\rm K} - G^{\rm K}\Sigma^{\rm A}\big) - \big(G^{\rm R}\Sigma^{\rm K} - \Sigma^{\rm K}G^{\rm A}\big)\ \big],\end{aligned} \tag{3.6}$$

where $\epsilon_{\rm TI}(\mathbf{p}) = \hbar v_{\rm F}(\mathbf{p}\times\hat{\mathbf{z}})\cdot\boldsymbol{\sigma}$ and $\mathbf{v} = v_F(\hat{\mathbf{z}}\times\boldsymbol{\sigma})$. Here, $G^{\rm R,A,K}$ and $\Sigma^{\rm R,A,K}$ are the retarded(R), advanced(A) and Keldysh(K) component of the Wigner transformed Green's functions (G) of the TI surface states and the self energies (Σ) in terms of the variable $(\mathbf{R}, {\rm t}; \mathbf{p}, \epsilon)$, where $(\mathbf{R}, {\rm t})$ are the center-of-mass position and time co-ordinates, and $(\mathbf{p}, \epsilon)$ are the Fourier transformed momentum and energy of the relative position and time co-ordinates. The self energy has contributions from both disorder and tunneling Hamiltonian, i.e. $\Sigma = \Sigma_{\rm dis} + \Sigma_{\rm tun}$, where $\Sigma_{\rm dis}$ is the self-energy due to disorder impurity potential and $\Sigma_{\rm tun}$ is the self-energy due to tunneling from the FM to the TI surface states. We consider time independent electric field, so $\partial_{\rm t}\phi = 0$ in Eq. (3.6).

After impurity averaging, the self energy for disorder is given by

$$\Sigma^{\rm R,A,K}_{\rm dis}(\mathbf{R}, {\rm t}; \mathbf{p}, \epsilon) = \frac{\lambda a_{\rm d}^2 V_{\rm d}^2 n_{\rm i}}{\hbar}\int \frac{{\rm d}^2{\rm p}'}{(2\pi)^2} G^{\rm R,A,K}(\mathbf{R}, {\rm t}; \mathbf{p}', \epsilon), \tag{3.7}$$

where $n_{\rm i}$ is the impurity concentration per unit area on the TI surface. We introduce the quasi-classical Green's function of the TI surface states,

$$g^{\rm R,A,K}(\mathbf{R}, {\rm t}; {\rm p_F}\hat{\mathbf{p}}, \epsilon) = \frac{i\lambda}{\pi}\int {\rm d}\xi_{\rm p}\ G^{\rm R,A,K}(\mathbf{R}, {\rm t}; \mathbf{p}, \epsilon), \tag{3.8}$$

where ${\rm p_F}$ is the Fermi momentum of the TI surface states, $\hat{\mathbf{p}}$ is the unit vector along $\mathbf{p}$, and $\xi_{\rm p} = \hbar v_{\rm F}|\mathbf{p}| - \epsilon_{\rm F}$. In Eq. (3.7), the integration is performed near the Fermi energy and we assume that the Fermi energy is in the conduction band of the TI. Hence, only the projection of the Green's function of the TI surface states to the conduction band is relevant to the

transport, and we have

$$G^{\mathrm{R,A}}(\mathbf{p},\epsilon)=\frac{1}{2\lambda}\frac{\sigma_0+(\hat{\mathbf{p}}\times\hat{\mathbf{z}})\cdot\boldsymbol{\sigma}}{\epsilon-\xi_{\mathrm{p}}\pm i0^{+}}. \tag{3.9}$$

So, the quasi-classical Green's functions and the disorder self energies are give by

$$g^{\mathrm{R,A}}=\pm\frac{1}{2}[\sigma_0+(\hat{\mathbf{p}}\times\hat{\mathbf{z}})\cdot\boldsymbol{\sigma}],\ \Sigma^{\mathrm{R,A}}_{\mathrm{dis}}=\mp\frac{i}{2\tau_{\mathrm{p}}}\sigma_0, \tag{3.10}$$

where τ_{p} is the scattering time (between the Bloch states) on the TI surface and is defined by $1/\tau_{\mathrm{p}}=\pi a_{\mathrm{d}}^2V_{\mathrm{d}}^2n_{\mathrm{i}}N/\hbar$, and N is the DOS of the TI surface states at the Fermi energy. Since the quasi-classical Green's function of the TI surface states will be peaked at the Fermi energy, we have

$$G^{\mathrm{K}}(\mathbf{R},\mathrm{t};\mathbf{p},\epsilon)=-\frac{i\pi}{\lambda}g^{\mathrm{K}}(\mathbf{R},\mathrm{t};\mathrm{p_F}\hat{\mathbf{p}},\epsilon)\delta(\xi_{\mathrm{p}}), \tag{3.11}$$

and, the Keldysh component of Σ_{dis} is given by

$$\Sigma^{\mathrm{K}}_{\mathrm{dis}}(\mathbf{R},\mathrm{t};\mathbf{p},\epsilon)=-\frac{i}{\tau_{\mathrm{p}}}\langle g^{\mathrm{K}}(\mathbf{R},\mathrm{t};\mathrm{p_F}\hat{\mathbf{p}},\epsilon)\rangle, \tag{3.12}$$

where $\langle ...\rangle$ denotes angular averaging over the Fermi contour of the TI surface states.

In case of a rough interface, the retarded, advanced and Keldysh components of the tunneling self energy $\Sigma^{\mathrm{R,A,K}}_{\mathrm{tun}}=\Sigma^{\mathrm{R,A,K}}_{\mathrm{tun}}(\mathbf{R},\mathrm{t};\mathbf{p},\epsilon)$ are obtained after averaging over the random distribution of the tunneling centers, and momentum randomization happens in the tunneling process. As a result, the tunneling self energy is given by

$$\Sigma^{\mathrm{R,A,K}}_{\mathrm{tun}}=\frac{\lambda a_{\mathrm{t}}^2n_{\mathrm{s}}}{\hbar}\int\frac{\mathrm{d}^3\mathrm{k}'}{(2\pi)^3}t^{\dagger}G^{\mathrm{R,A,K}}_{\mathrm{FM}}t, \tag{3.13}$$

where n_{s} is the density of the tunneling centers per unit area, $G^{\mathrm{R,A,K}}_{\mathrm{FM}}=G^{\mathrm{R,A,K}}_{\mathrm{FM}}(\mathbf{R},z=0,\mathrm{t};\mathbf{k}',\epsilon)$ are the retarded, advanced and Keldysh components of the Green's function of the

FM at the interface $z = 0$ with $\mathbf{k}'$ being the 3D momentum in the FM, and $t = (t_\uparrow \mathrm{P}_\uparrow + t_\downarrow \mathrm{P}_\downarrow)$ is the spin-dependent part of the tunneling (note that t is hermitian, i.e., $t^\dagger = t$).

The retarded and advanced Green's functions of the FM are,

$$G^{\mathrm{R,A}}_{\mathrm{FM}}(\mathbf{k}, \epsilon) = \mathrm{P}_\uparrow \frac{1}{\epsilon - \xi_{\mathrm{k}\uparrow} \pm i0^+} + \mathrm{P}_\downarrow \frac{1}{\epsilon - \xi_{\mathrm{k}\downarrow} \pm i0^+}. \tag{3.14}$$

where $\xi_{\mathrm{k}\uparrow,\downarrow} = \frac{\hbar^2}{2m_c}\mathrm{k}^2_{\uparrow,\downarrow} + \epsilon_{\mathrm{b}} \mp \Delta_{\mathrm{ex}} - \epsilon_{\mathrm{F}}$. We consider incoherent superposition of the majority and minority electrons in the FM are contributing to the transport in the FM. So, the Keldysh component of the Green's function of the FM, which will be peaked at the Fermi energy, can be written as

$$G^{\mathrm{K}}_{\mathrm{FM}} = -i\pi \left[\mathrm{P}_\uparrow \tilde{g}^{\mathrm{K}}_\uparrow(\mathrm{k}_{\mathrm{F}\uparrow}\hat{\mathbf{k}}_\uparrow, \epsilon)\delta(\xi_{\mathrm{k}\uparrow}) + \mathrm{P}_\downarrow \tilde{g}^{\mathrm{K}}_\downarrow(\mathrm{k}_{\mathrm{F}\downarrow}\hat{\mathbf{k}}_\downarrow, \epsilon)\delta(\xi_{\mathrm{k}\downarrow}) \right], \tag{3.15}$$

where $\tilde{g}^{\mathrm{K}}_{\uparrow,\downarrow}$ are the Keldysh components of the quasi-classical Green's functions for the majority and minority electrons in the FM, $\mathrm{k}_{\mathrm{F}\uparrow,\downarrow}$ are the Fermi momentum of the majority and minority electrons in the FM, and in Eq. (3.15) the position and time dependence of the Keldysh components of the Green's functions are implicit. It should also be noted that, the Keldysh component of the tunneling self-energy is given by the Keldysh component of the Green's function of the FM evaluated at the interface. However, the assumption of a constant Keldysh component of the Green's function of the FM with position inside the FM will be self-consistent. It is because the thickness of the FM is considered to be small and the conductivity of the FM is much higher than the conductivity of the TI, and, after considering transport inside the FM it can be shown that the variation of the non-equilibrium up/down electrochemical potential of the FM with position inside the FM will be negligible[51].

The retarded, advanced and Keldysh components of the tunneling self energy become

$$\begin{aligned}\Sigma_{\text{tun}}^{\text{R,A}} &= \mp i\big(\gamma_{\uparrow} N_{\uparrow} \text{P}_{\uparrow} + \gamma_{\downarrow} N_{\downarrow} \text{P}_{\downarrow}\big), \\ \Sigma_{\text{tun}}^{\text{K}} &= -i\big(\gamma_{\uparrow} N_{\uparrow} \text{P}_{\uparrow} g_{\uparrow} + \gamma_{\downarrow} N_{\downarrow} \text{P}_{\downarrow} g_{\downarrow}\big),\end{aligned} \tag{3.16}$$

where $\gamma_{\uparrow,\downarrow} = \pi\lambda a_{\text{t}}^2 t_{\uparrow,\downarrow}^2 n_{\text{s}}/\hbar$ are the strengths of tunneling between the up/down spin electrons in the FM and the TI surface states, $N_{\uparrow,\downarrow}$ are the DOS of the majority and minority electrons in the FM at the Fermi energy, and $g_{\uparrow,\downarrow} = \langle \tilde{g}_{\uparrow,\downarrow}^{\text{K}} \rangle$ denotes the value of the Keldysh component of the quasi-classical Green's function for the up/down electrons in the FM after averaging over the solid angle of the respective Fermi surfaces of each spin bands in the FM.

In case of a smooth interface, in-plane momentum conservation happens in the tunneling process, and the tunneling self energy is given by

$$\begin{aligned}\Sigma_{\text{tun}}^{\text{R,A,K}} &= \frac{\lambda a_{\text{t}}^2 n_{\text{s}}}{\hbar} \int \frac{\text{d}^3\text{k}'}{(2\pi)^3} t^{\dagger} G_{\text{FM}}^{\text{R,A,K}} t \; (2\pi)^2 \delta(\mathbf{k}'_{\parallel} - \mathbf{p}) \\ &= \frac{\lambda a_{\text{t}}^2 n_{\text{s}}}{\hbar} \int \frac{\text{dk}'_{\text{z}}}{2\pi} t^{\dagger} G_{\text{FM}}^{\text{R,A,K}}(\mathbf{k}'_{\parallel} = \mathbf{p}) t.\end{aligned} \tag{3.17}$$

Considering diffusive transport in the FM, the Keldysh components of the quasi-classical Green's functions $\tilde{g}_{\uparrow,\downarrow}^{\text{K}}$ for the majority and minority electrons in the FM can be expanded with an isotropic and an anisotropic component (with respect to the momentum direction $\hat{\mathbf{k}}_{\uparrow,\downarrow}$). In the diffusive limit, the isotropic component will be proportional to the electrochemical potentials of the majority and minority electrons in the FM, while the anisotropic component will be determined by the spatial variation (gradient) of the isotropic component. Since the variation of the electrochemical potentials of the majority and minority electrons in the FM will be negligible, the anisotropic component of the quasi-classical Green's functions $\tilde{g}_{\uparrow,\downarrow}^{\text{K}}$ of the FM can be neglected. So, if the quasi-classical Green's functions $\tilde{g}_{\uparrow,\downarrow}^{\text{K}}$ are isotropic in $\mathbf{k}_{\uparrow,\downarrow}$ space, from Eq. (3.17) we obtain that the retarded, advanced and Keldysh components

of the tunneling self energy are given by the same relation as that of Eq. (3.16) with $\gamma_{\uparrow,\downarrow} = \pi\lambda t^2_{\uparrow,\downarrow}/\hbar$, and $N_{\uparrow,\downarrow}$ replaced by the corresponding one-dimensional (1D) DOSs for majority and minority electrons in the FM calculated at the Fermi energy with the constraint of in-plane momentum conservation.

The quantum kinetic equation in terms of the quasi-classical Green's function $g^{\rm K}$ of the TI surface state is obtained after performing $\xi_{\rm p}$ integration of Eq. (3.6), as

$$\begin{aligned}
&\partial_{\rm t} g^{\rm K} + \frac{v_{\rm F}}{2}\big\{\hat{\mathbf{z}}\times\boldsymbol{\sigma}\cdot\nabla_{\mathbf{R}}, g^{\rm K}\big\} + iv_{\rm F}{\rm p}_{\rm F}[(\hat{\mathbf{p}}\times\hat{\mathbf{z}})\cdot\boldsymbol{\sigma}, g^{\rm K}] = -\frac{g^{\rm K}-\langle g^{\rm K}\rangle}{\tau_{\rm p}} \\
&+\frac{1}{2\tau_{\rm p}}\big\{(\hat{\mathbf{p}}\times\hat{\mathbf{z}})\cdot\boldsymbol{\sigma}, \langle g^{\rm K}\rangle\big\} - \big\{(\gamma_\uparrow N_\uparrow {\rm P}_\uparrow + \gamma_\downarrow N_\downarrow {\rm P}_\downarrow), g^{\rm K}\big\} - \big(\gamma_\uparrow N_\uparrow {\rm P}_\uparrow g_\uparrow + \gamma_\downarrow N_\downarrow {\rm P}_\downarrow g_\downarrow\big) \\
&+\frac{1}{2}\big\{(\hat{\mathbf{p}}\times\hat{\mathbf{z}})\cdot\boldsymbol{\sigma}, (\gamma_\uparrow N_\uparrow {\rm P}_\uparrow g_\uparrow + \gamma_\downarrow N_\downarrow {\rm P}_\downarrow g_\downarrow)\big\}.
\end{aligned} \tag{3.18}$$

3.2 Derivation of transport equations on the TI surface coupled to the FM

In the following, we consider spin conserving tunneling, i.e., $t_\uparrow = t_\downarrow = t_0$ and $\gamma_\uparrow = \gamma_\downarrow = \gamma$, and from Eq. (3.18) we obtain

$$\begin{aligned}
&\partial_{\rm t} g^{\rm K} + \frac{v_{\rm F}}{2}\big\{\hat{\mathbf{z}}\times\boldsymbol{\sigma}\cdot\nabla_{\mathbf{R}}, g^{\rm K}\big\} + iv_{\rm F}{\rm p}_{\rm F}[(\hat{\mathbf{p}}\times\hat{\mathbf{z}})\cdot\boldsymbol{\sigma}, g^{\rm K}] = -\frac{g^{\rm K}-\langle g^{\rm K}\rangle}{\tau_{\rm p}} \\
&+\frac{1}{2\tau_{\rm p}}\big\{(\hat{\mathbf{p}}\times\hat{\mathbf{z}})\cdot\boldsymbol{\sigma}, g^{\rm K}\big\} - \gamma\big(\big\{(N_\uparrow {\rm P}_\uparrow + N_\downarrow {\rm P}_\downarrow), g^{\rm K}\big\} + N_\uparrow {\rm P}_\uparrow g_\uparrow + N_\downarrow {\rm P}_\downarrow g_\downarrow\big) \\
&+\frac{\gamma}{2}\big\{(\hat{\mathbf{p}}\times\hat{\mathbf{z}})\cdot\boldsymbol{\sigma}, (N_\uparrow {\rm P}_\uparrow g_\uparrow + N_\downarrow {\rm P}_\downarrow g_\downarrow)\big\}.
\end{aligned} \tag{3.19}$$

The Fermi energy $\epsilon_{\rm F}$ is the largest energy scale compared to all other relevant energy scales available in the system ($\epsilon_{\rm M}$ being the maximum of them), so the lowest order solution (with respect to the perturbation parameter $\epsilon_{\rm M}/\epsilon_{\rm F}$) of $g^{\rm K}$ will commute with $[(\hat{\mathbf{p}}\times\hat{\mathbf{z}})\cdot\boldsymbol{\sigma}]$ and we

can write the following *ansatz*: $g^{\rm K} = g_0(\hat{\mathbf{p}}, \epsilon)[\sigma_0 + (\hat{\mathbf{p}} \times \hat{\mathbf{z}}) \cdot \boldsymbol{\sigma}]$[64, 65, 66]. As we will consider the FM to be magnetized in-plane (i,.e. $m_z = 0$), there will be no gap opening of the TI surface state as well as the coefficient of σ_z in $G^{\rm K}_{\rm FM}$ will be zero, so the perturbation expansion and the *ansatz* for $g^{\rm K}$ will be valid. In general, $g^{\rm K} = {\rm g}'\sigma_0 + {\rm g}''(\hat{\mathbf{p}} \times \hat{\mathbf{z}}) \cdot \boldsymbol{\sigma} + {\rm g}_{\parallel}\hat{\mathbf{p}} \cdot \boldsymbol{\sigma} + {\rm g}_z\sigma_z$. Following the literature[64, 65, 66], it can be shown that $({\rm g}_{\parallel}, {\rm g}_z) \sim \mathcal{O}(\frac{\epsilon_{\rm M}}{\epsilon_{\rm F}})F({\rm g}', {\rm g}'', {\rm g}_{\uparrow}, {\rm g}_{\downarrow})$ for some linear function F, and $\epsilon_{\rm M} = \max(\hbar/\tau_{\rm p}, \hbar\,|\mathbf{q}|\,l/\tau_{\rm p}, \hbar\omega, \hbar\gamma N_{\pm})$, where $(\mathbf{q}, l)$ is the Fourier transform variable of $(\mathbf{R}, T)$. So, ${\rm g}_{\parallel}, {\rm g}_z$ are less than ${\rm g}', {\rm g}''$ by a factor $(\epsilon_{\rm M}/\epsilon_{\rm F}) \ll 1$. After neglecting ${\rm g}_{\parallel}, {\rm g}_z$ in $g^{\rm K}$, it can be shown further that ${\rm g}' = {\rm g}'' = g_0$ will be a solution, hence, the *ansatz* $g^{\rm K} = g_0(\hat{\mathbf{p}}, \epsilon)[\sigma_0 + (\hat{\mathbf{p}} \times \hat{\mathbf{z}}) \cdot \boldsymbol{\sigma}]$ is valid. Inserting the *ansatz* in Eq. (3.19) and taking trace over the spin space, we obtain

$$\begin{aligned}\partial_t g_0 + v_{\rm F}\hat{\mathbf{p}} \cdot \nabla_{\mathbf{R}} g_0 = &-\frac{g_0}{\tau_{\rm p}} + \frac{\langle g_0 \rangle}{\tau_{\rm p}} + \frac{1}{\tau_{\rm p}}\hat{\mathbf{p}} \cdot \langle \hat{\mathbf{p}}' g_0 \rangle - \gamma N_+ g_0 - \gamma N_- g_0\ (\hat{\mathbf{p}} \times \hat{z}) \cdot \mathbf{m} \\ &+ \frac{\gamma}{2}\big(N_{\uparrow} g_{\uparrow} + N_{\downarrow} g_{\downarrow}\big) + \frac{\gamma}{2}\big(N_{\uparrow} g_{\uparrow} - N_{\downarrow} g_{\downarrow}\big)(\hat{\mathbf{p}} \times \hat{z}) \cdot \mathbf{m}.\end{aligned} \tag{3.20}$$

In the literature, Schwab *et al.*[67] derived the charge continuity equation on the TI surface after doing integration over the angle in $\mathbf{p}$ space and energy ϵ of the above equation, i.e. Eq. (3.20). However, the associated modified equation for the charge current density on the TI surface was not derived by Schwab *et al.*[67]. On the other hand, using semi-classical drift-diffusion model with tunneling calculated from the Fermi's Golden Rule, Yokoyama *et al.*[51] showed that both the continuity and the equation for the current density in the TI are modified due to the tunneling from the FM. In the following, we complete the derivation of the modified continuity equation as well as the modified equation for the current density on the TI surface. Our derivation is based on the quantum kinetic equation which differs from the semi-classical formalism used by Yokoyama *et al.*[51] but results in the same equations as derived by them.

In the case of diffusive transport, $g_0(\hat{\mathbf{p}}, \epsilon)$ can be expanded through the zeroth and the first harmonics in 2D[64, 65, 66, 68], i.e. $g_0(\hat{\mathbf{p}}, \epsilon) = \mathrm{g_s}(\epsilon) + \hat{\mathbf{p}} \cdot \mathbf{g_a}(\epsilon)$. The continuity equation and the equation for the current density in the TI will be obtained from Eq. (3.20) by separating the zeroth and the first harmonic components, respectively. Substituting the *ansatz* $\mathrm{g}_0(\hat{\mathbf{p}}, \epsilon)$ in Eq. (3.20), and then performing the integration over the angle in the $\mathbf{p}$ space, we obtain

$$\partial_{\mathrm{T}} \mathrm{g_s} + \frac{v_{\mathrm{F}}}{2} \nabla_{\mathbf{R}} \cdot \mathbf{g_a} = \frac{1}{2}\gamma(N_\uparrow \mathrm{g}_\uparrow + N_\downarrow \mathrm{g}_\downarrow) - \gamma N_+ \mathrm{g_s} + \frac{1}{2}\gamma N_- \mathbf{g_a} \cdot (\hat{\mathbf{m}} \times \hat{\mathbf{z}}), \tag{3.21}$$

where we define $N_\pm = N_\uparrow \pm N_\downarrow$. To separate out the anisotropic part, we multiply Eq. (3.20) by $\hat{\mathbf{p}}$ and do the integration over the angle in the $\mathbf{p}$ space to get

$$\partial_{\mathrm{T}} \mathbf{g_a} + v_{\mathrm{F}} \nabla_{\mathbf{R}} \mathrm{g_s} = -\left(\frac{1}{2\tau_{\mathrm{p}}} + \gamma N_+\right)\mathbf{g_a} + \gamma N_- \mathrm{g_s}\ (\hat{\mathbf{m}} \times \hat{\mathbf{z}}) - \frac{\gamma}{2}(N_\uparrow \mathrm{g}_\uparrow - N_\downarrow \mathrm{g}_\downarrow)(\hat{\mathbf{m}} \times \hat{\mathbf{z}}). \tag{3.22}$$

The effective charge density n and the charge current density $\mathbf{J}$ on the surface of the TI are given by $n = (eN/2)\int \mathrm{d}\epsilon\ \mathrm{g_s}(\epsilon)$ and $\mathbf{J} = (eN/2)\int \mathrm{d}\epsilon\ (v_{\mathrm{F}}/2)\mathbf{g_a}(\epsilon)$[67, 69], as given in Eqs. (2.47) and (2.48) in chapter 2. In the FM contact, the actual non-equilibrium charge densities of the majority and minority spin electrons $n_{\mathrm{neq};\uparrow,\downarrow}$ are given by

$$n_{\mathrm{neq};\uparrow,\downarrow} = \frac{eN_{\uparrow,\downarrow}}{2}\int \mathrm{d}\epsilon \frac{1}{2}\mathrm{Tr}[\mathrm{P}_{\uparrow,\downarrow} g_{\uparrow,\downarrow}(\epsilon)] - e^2 N_{\uparrow,\downarrow}\phi_{\mathrm{c}} = \frac{eN_{\uparrow,\downarrow}}{4}\int \mathrm{d}\epsilon\ g_{\uparrow,\downarrow}(\epsilon) - e^2 N_{\uparrow,\downarrow}\phi_{\mathrm{c}}. \tag{3.23}$$

We define the effective non-equilibrium electron charge densities of the majority and minority spins $n_{\uparrow,\downarrow}$ by $n_{\uparrow,\downarrow} = n_{\mathrm{neq};\uparrow,\downarrow} + e^2 N_{\uparrow,\downarrow}\phi_{\mathrm{c}}$. Hence, by these definitions, we obtain

$$n_{\uparrow,\downarrow} = \frac{eN_{\uparrow,\downarrow}}{4}\int \mathrm{d}\epsilon\ g_{\uparrow,\downarrow}(\epsilon). \tag{3.24}$$

As we have defined the full electrochemical potential μ on the TI surface by $n = e^2 N\mu$, we

also define the full electrochemical potentials $\mu_{\uparrow,\downarrow}$ of the majority and minority spin electrons in the FM by $n_{\uparrow,\downarrow} = e^2 N_{\uparrow,\downarrow}\mu_{\uparrow,\downarrow}$. So, we have

$$\mu_{\uparrow,\downarrow} = \frac{1}{4e}\int \mathrm{d}\epsilon\; g_{\uparrow,\downarrow}(\epsilon). \tag{3.25}$$

The definitions of μ and $\mu_{\uparrow,\downarrow}$ match with those by Schwab *et al*[67]. The effective charge density n_+ and the spin density n_- in the FM can be written as $n_\pm = n_\uparrow \pm n_\downarrow$.

After integrating Eq. (3.21) over the energy ϵ, in steady state the modified continuity equation on the TI surface is obtained,

$$\nabla_{\mathbf{R}} \cdot \mathbf{J} = -\gamma N_+ n + \gamma N n_+ + \frac{\gamma N_-}{v_{\mathrm{F}}}\mathbf{J}\cdot(\hat{\mathbf{m}}\times\hat{\mathbf{z}}). \tag{3.26}$$

Similarly, after integrating Eq. (3.22) over the energy ϵ, in steady state, we obtain the modified equation for the charge current density on the TI surface

$$\mathbf{J} = \frac{1}{(1+\xi)}\left[-D\nabla_{\mathbf{R}} n + \frac{\gamma v_{\mathrm{F}}\tau_{\mathrm{tr}}^0}{2}\big(N_- n - N n_-\big)(\hat{\mathbf{m}}\times\hat{\mathbf{z}})\right], \tag{3.27}$$

where τ_{tr}^0 is the transport relaxation time on the pristine TI surface without any tunneling from the FM, $D = v_{\mathrm{F}}^2\tau_{\mathrm{tr}}^0/2$ is the diffusion constant on the pristine TI surface without any tunneling, and the term $(1+\xi)^{-1}$ is the modification of the diffusion constant due to tunneling, where $\xi = \gamma N_+ \tau_{\mathrm{tr}}^0$ is a dimensionless parameter which is proportional to the interface conductance and denotes the strength of the tunneling. The continuity equation, Eq. (3.27), and the equation for the current density, Eq. (3.26), constitute the transport equations on the TI surface coupled to a FM, which agrees with those by Yokoyama *et al*[51].

In the spin tunneling experiment with the TI-FM heterostructure as shown in Fig 3.1(a), a charge current is applied through the FM and extracted at one end of the TI, and a

transverse voltage drop is measured on the surface of the TI. To do that, we can consider a spatially uniform charge electrochemical potential μ_c being applied in the FM, and the potential in the FM will be constant with position in the FM since the FM conductivity is much higher than the TI conductivity. So there will be no spin electrochemical potential $\mu_s = \mu_\uparrow - \mu_\downarrow$ in the FM, i.e. $\mu_s = 0$, and the electrochemical potential for both the majority and minority electrons in the FM will be $\mu_\uparrow = \mu_\downarrow = \mu_c$ along with $\partial_x \mu_{\uparrow,\downarrow} = \partial_y \mu_{\uparrow,\downarrow} = 0$. Then, from Eqs. (3.26)-(3.27) we obtain the following equation for the electrochemical potential μ on the TI surface,

$$\partial_x^2 \mu + \partial_y^2 \mu - 2b_0 m_y \partial_x \mu + 2b_0 m_x \partial_y \mu + [b_0^2(m_x^2 + m_y^2) - c_0^2](\mu - \mu_c) = 0, \tag{3.28}$$

where $b_0 = \xi\eta/l$ with $\eta = \frac{N_-}{N_+}$ being the DOS polarization of the FM and $l = v_F \tau_{tr}^0$ being the transport relaxation length on the pristine TI surface, and $c_0 = \sqrt{2\xi(1+\xi)}/l$. The current density $\mathbf{J}$ on the TI surface can be written as $\mathbf{J} = j_x \hat{\mathbf{x}} + j_y \hat{\mathbf{y}}$, where the x- and y- components of the current density are given by

$$j_x = -\sigma'[\partial_x \mu - b_0 m_y(\mu - \mu_c)], \tag{3.29a}$$

$$j_y = -\sigma'[\partial_y \mu + b_0 m_x(\mu - \mu_c)]. \tag{3.29b}$$

Here $\sigma' = \sigma/(1+\xi)$ is the modified conductivity of the TI surface due to tunneling from the FM, and $\sigma = e^2 N D$ is the conductivity of the pristine TI surface without tunneling. We define the modified transport relaxation time τ_{tr} given by $\tau_{tr} = \tau_{tr}^0/(1+\xi)$, and the transport relaxation time on the TI surface is modified due to tunneling because tunneling (back and forth) acts as an additional momentum randomizing scattering along with the scattering from impurities on the TI surface.

3.3 An approximate solution of the transport equations

To get an approximate solution of the electrochemical potential μ on the TI surface, we make the assumption that $j_x = 0$ on the TI surface under the FM region[76] in the device geometry shown in Fig. 3.1(b). In the next section, we will solve Eq. (3.28) exactly for different boundary conditions. We will show that the assumption $j_x \approx 0$ is valid if the device dimension along the x-direction is smaller or comparable to the transport relaxation length on the TI surface. To solve equation Eq. (3.28), we make the substitution $(\mu - \mu_c) \to \mu$, which amounts to calculating the electrochemical potential in the TI with respect to that of the FM. The resulting differential equation is a second order homogeneous partial differential equation in μ with no cross derivative $\partial_x \partial_y \mu$, so it can be separated into two second order ordinary differential equations by the separation of variables, i.e., setting $\mu(x, y) = \mu_X(x)\mu_Y(y)$. The domain of the solution is a rectangular region $[0, L_x] \times [0, L_y]$, as shown in Fig. 3.1(b), which is a product of intervals of the two independent variables x and y. After finding solutions for each second order ordinary differential equations with unknown coefficients, the boundary conditions on the rectangular domain are used to find the values of the unknown coefficients. After separating out the functions of the variables x and y, we obtain

$$0 = \mathrm{d}_x^2 \mu_X - 2b_0 m_y \mathrm{d}_x \mu_X + \left(b_0^2 m_y^2 - c_X^2\right)\mu_X, \tag{3.30a}$$

$$0 = \mathrm{d}_y^2 \mu_Y + 2b_0 m_x \mathrm{d}_y \mu_Y + \left(b_0^2 m_x^2 - c_Y^2\right)\mu_Y, \tag{3.30b}$$

where the constants c_X, c_Y satisfy the constraint $c_X^2 + c_Y^2 = c_0^2$. The x- and y- components of the current density becomes

$$j_x = -\sigma'[\mathrm{d}_x\mu_X - b_0 m_y \mu_X]\mu_Y, \tag{3.31a}$$

$$j_y = -\sigma'[\mathrm{d}_y\mu_Y + b_0 m_x \mu_Y]\mu_X. \tag{3.31b}$$

The solutions of $\mu_{X,Y}$ are given by $\mu_X = A_1 e^{r_1 x} + A_2 e^{r_2 x}$ and $\mu_Y = B_1 e^{s_1 y} + B_2 e^{s_2 y}$, if $r_1 \neq r_2$ and $s_1 \neq s_2$, where $r_{1,2} = b_0 m_y \pm c_X$ and $s_{1,2} = -b_0 m_x \pm c_Y$. Then we obtain $j_x = -\sigma' c_X (A_1 e^{r_1 x} - A_2 e^{r_2 x})\mu_Y(y)$ and $j_y = -\sigma' c_Y (B_1 e^{s_1 y} - B_2 e^{s_2 y})\mu_X(x)$. As shown in Fig. 3.1(b), the boundary conditions on the TI surface in the rectangular region $[0, L_x] \times [0, L_y]$ of the TI-FM heterostructure are $j_x(x = 0) = j_x(x = L_x) = 0, \forall y$, $j_y(y = 0) = 0, \forall x$ and $\int \mathrm{d}x j_y(x, y = L_y) = I_\mathrm{c}$. The solution of the boundary condition $j_x = 0, \forall y$ at $x = 0, L_x$, with the assumption of $j_x = 0$ inside the rectangle $\forall x, y$, implies $r_1 = r_2 = b_0 m_y$, i.e. $c_X = 0, c_Y = c_0$. Hence, the solution of μ_X should be given by $\mu_X(x) = (C + Dx)e^{b_0 m_y x}$, and $j_x = -\sigma' D e^{b_0 m_y x}\mu_Y(y)$. The boundary condition $j_x = 0, \forall y$ at $x = 0, L_x$ gives $D = 0$. The constant C can be absorbed in the constants B_1, B_2 of μ_Y, and we obtain $\mu_X(x) = e^{b_0 m_y x}$. The boundary condition $j_y(y = 0) = 0, \forall x$ gives $B_1 = B_2 = B$, and the only unknown constant B is obtained from the remaining condition that the total charge current out of the boundary $y = L_y$ is I_c, i.e., $\int \mathrm{d}x\ j_y(x, y = L_y) = I_\mathrm{c}$. However, the condition $\int \mathrm{d}x\ j_y(x, y = L_y) = I_\mathrm{c}$ is not a boundary condition of the differential equation given in Eq. (3.28), but this condition is physically relevant to obtain the solution of μ within the approximation $j_x = 0$. So, we find the approximate solution of $\mu(x, y)$ to be

$$\mu(x, y) = -\frac{I_\mathrm{c}}{\sigma'} \frac{b_0 m_y e^{b_0 m_y x}}{e^{b_0 m_y L_x} - 1} \frac{e^{-b_0 m_x y} \cosh(c_0 y)}{e^{-b_0 m_x L_y} c_0 \sinh(c_0 L_y)}. \tag{3.32}$$

Now, we consider two special cases, the magnetization of the FM along the x-direction and along the y-direction. For the FM magnetized in the x-direction, i.e. for $m_x = \pm 1, m_y = 0$, using $\lim_{t\to 0} t/(e^t - 1) \to 1$ in Eq. (3.32), we obtain

$$\mu(x,y) = -\frac{I_c}{\sigma'}\frac{1}{L_x}\frac{e^{-b_0 m_x y}\cosh(c_0 y)}{e^{-b_0 m_x L_y} c_0 \sinh(c_0 L_y)}, \tag{3.33}$$

which is independent of x, and so, no voltage drop will be measured at the two ends $x = 0$ and $x = L_x$ on the TI surface. For the FM magnetized in the y-direction, i.e. for $m_x = 0, m_y = \pm 1$, we obtain from Eq. (3.32),

$$\mu(x,y) = -\frac{I_c}{\sigma}\frac{\eta m_y}{2}\frac{e^{\xi\eta m_y x/l}}{(e^{\xi\eta m_y L_x/l} - 1)}\frac{d_0\cosh(d_0 y/l)}{\sinh(d_0 L_y/l)}, \tag{3.34}$$

where we have inserted the values of b_0, c_0 and defined $d_0 = c_0 l = \sqrt{2\xi(1+\xi)}$. As shown in Fig. 3.1(b), we are interested in the electrochemical potential difference $\Delta\mu(L'_y)$ between the two ends $x = 0$ and $x = L_x$ on the TI surface at some $y = L'_y$ given $m_y = \pm 1$, where $\Delta\mu(L'_y) = \mu(x = 0, y = L'_y) - \mu(x = L_x, y = L'_y)$. From Eq. (3.34), we obtain

$$\Delta\mu(L'_y) = \frac{I_c}{\sigma}\frac{\eta m_y}{2}\frac{l}{L_y}\frac{(d_0 L_y/l)\cosh(d_0 L'_y/l)}{\sinh(d_0 L_y/l)}. \tag{3.35}$$

The potential drop $\Delta\mu$ depends on the orientation of the magnetization in the y-direction and changes sign when the magnetization is reversed.

We introduce the dimensionless parameter χ by the relation $\Delta\mu(L'_y) = \chi\eta\frac{I_c}{\sigma}\frac{l}{L_y}\frac{m_y}{2}$ which is the expression given by Liu *et. al.*[31]. From Eq. (3.35), we obtain χ to be $\chi = (d_0 L_y/l)\cosh(d_0 L'_y/l)/\sinh(d_0 L_y/l)$. In general, the parameter η depends both on the FM and on the quality of the interface. For the rough and the smooth interface, the tunneling is momentum randomizing and in-plane momentum conserving, respectively, and the

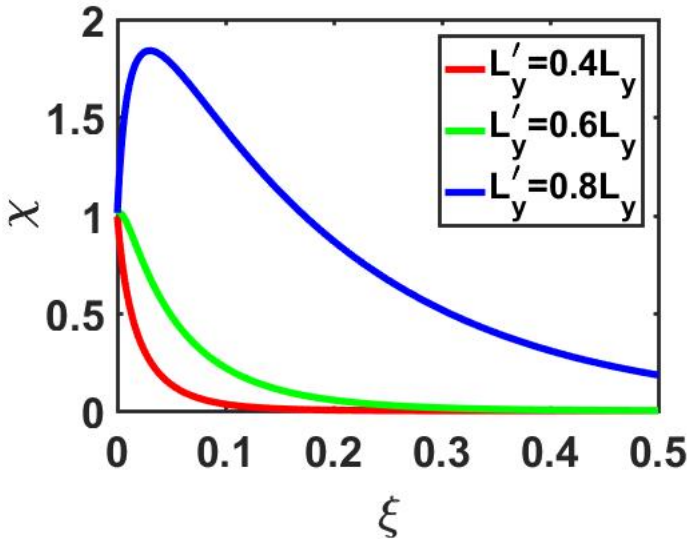

Figure 3.2: Variation of the detection efficiency (χ) with normalized interface tunneling rate (ξ) obtained from approximate solution: Results for different cases with $L'_y = fL_y$ for $f = 0.4, 0.6, 0.8$ and $L_y/l = 20$ are shown.

DOS polarization of the FM η will be given by the 3D and the 1D DOSs for the majority and minority electrons in the FM, respectively. The parameter χ is a function of ξ, where $\xi = \gamma N_+ \tau_{\rm tr}$, γ depends on the nature of the interface, and N_+ will be given by the 3D and the 1D DOSs of the FM for the rough and the smooth interface, respectively. We also show that the parameter χ depends on the geometry of the problem, and in Fig. 3.2 we have plotted the variation of χ with ξ for different values of $L'_y = fL_y$, where $f = 0.4, 0.6, 0.8$ and $L_y/l = 20$. From Fig. 3.2, we observed that the value of χ reduces as ξ increases or the interface conductance increases which indicates the importance of the tunnel barrier in such tunneling experiment[31]. In the limit $\xi \to 0$, we obtain $\chi \to 1$ irrespective of the value of l, L'_y, L_y.

3.4 Exact solution method for the transport equations

To solve Eq. (3.28), we make the following substitution

$$\mu(x,y) = \mu_c + \tilde{\mu}(x,y)e^{b_0(m_y x - m_x y)}. \tag{3.36}$$

Since μ_c is spatially constant, i.e., $\partial_x \mu_c = 0 = \partial_y \mu_c$, using Eq. (3.36) in Eq. (3.28) we obtain

$$\partial_x^2 \tilde{\mu} + \partial_y^2 \tilde{\mu} - c_0^2 \tilde{\mu} = 0. \tag{3.37}$$

After the same substitution, from Eq. (3.29) we obtain

$$j_x = -\sigma' e^{b_0(m_y x - m_x y)} \partial_x \tilde{\mu}, \tag{3.38a}$$

$$j_y = -\sigma' e^{b_0(m_y x - m_x y)} \partial_y \tilde{\mu}. \tag{3.38b}$$

Equation (3.37) is the modified Helmholtz equation which is a second order homogeneous elliptic partial differential equation. We solve Eq. (3.37) by the technique of separation of variables and series solution with appropriate boundary conditions on the boundary of the TI surface of rectangular shape $[0, L_x] \times [0, L_y]$, as shown in Figs. 3.3(a)-(b). For both the device geometries of Figs.3.3(a)-(b), we have open Neumann boundary conditions on three sides of the rectangle given by $j_x(x = 0, y) = 0, \forall y$, $j_x(x = L_x, y) = 0, \forall y$ and $j_y(x, y = 0) = 0, \forall x$. However, for the device geometry of Fig. 3.3(a), we assume Neumann boundary condition of uniform current density injected out of the TI surface, i.e., $j_y(x, y = L_y) = I_c/L_x, \forall x$, where I_c is the total current injected out of the boundary on the TI surface. For the device geometry of Fig. 3.3(b), we assume Dirichlet boundary condition of uniform electrochemical potential $-\mu_0$ applied on the TI surface with respect to the FM, i.e., $\mu(x, y = L_y) = \mu_c - \mu_0, \forall x$.

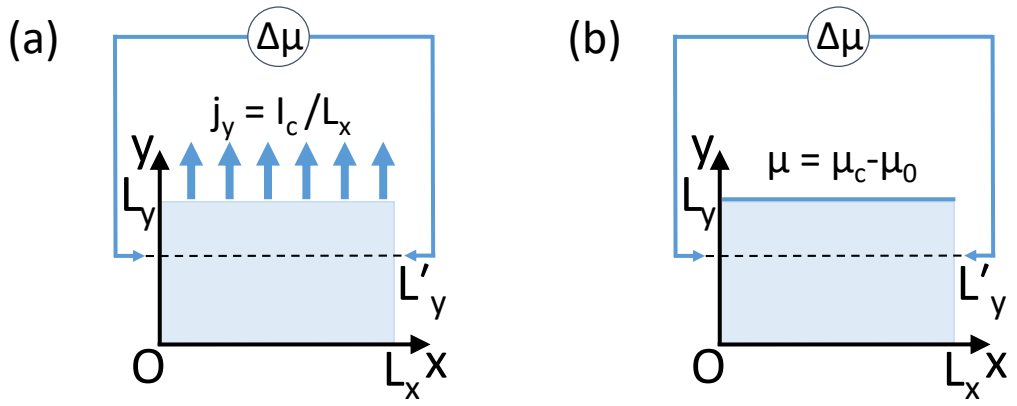

Figure 3.3: Schematics of different boundary conditions on the surface of the TI for measuring IEE by spin-polarized tunneling in a TI-FM heterostructure: (a) Neumann boundary condition $j_y(x, y = L_y) = I_c/L_x, \forall x$, (b) Dirichlet boundary condition $\mu(x, y = L_y) = \mu_c - \mu_0, \forall x$.

After separation of variables, i.e. setting $\tilde{\mu}(x, y) = \tilde{\mu}_X(x)\tilde{\mu}_Y(y)$ in Eq. (3.37), we obtain

$$\frac{\mathrm{d}_x^2\tilde{\mu}_X}{\tilde{\mu}_X} + \frac{\mathrm{d}_y^2\tilde{\mu}_Y}{\tilde{\mu}_Y} = c_0^2. \tag{3.39}$$

From Eq. (3.39), we have $\mathrm{d}_x^2\tilde{\mu}_X = c_X^2\tilde{\mu}_X$ and $\mathrm{d}_y^2\tilde{\mu}_Y = c_Y^2\tilde{\mu}_Y$, where c_X, c_Y can be real or purely imaginary with the constraint $c_X^2 + c_Y^2 = c_0^2$. We obtain the general solutions for $\tilde{\mu}_{X,Y}$ as $\tilde{\mu}_X(x) = A_1 e^{c_X x} + A_2 e^{-c_X x}$ and $\tilde{\mu}_Y(y) = B_1 e^{c_Y y} + B_2 e^{-c_Y y}$. Then, from Eq. (3.38), we have $j_x(x, y) = -\sigma' e(x, y) c_X (A_1 e^{c_X x} - A_2 e^{-c_X x})\tilde{\mu}_Y(y)$ and $j_y(x, y) = -\sigma' e(x, y) c_Y (B_1 e^{c_Y y} - B_2 e^{-c_Y y})\tilde{\mu}_X(x)$, where $e(x, y) = e^{b_0(m_y x - m_x y)}$. The boundary condition $j_x(x = 0, y) = 0, \forall y$ implies $c_X(A_1 - A_2) = 0$ and the boundary conditio $j_x(x = L_x, y) = 0, \forall y$ implies $c_X(A_1 e^{c_X L_x} - A_2 e^{-c_X L_x}) = 0$ (assuming non-trivial solution for $\tilde{\mu}(x, y)$, since if $\tilde{\mu}_Y(y) = 0$, then both the above boundary conditions are satisfied but $\tilde{\mu}(x, y) = 0$). Also, if $c_X = 0$, then we will have $j_x(x, y) = 0, \forall x, y$, which is a strict condition on the current distribution inside the rectangular region on the TI surface, but the current distribution should be determined by other boundary conditions. In the previous section, we assumed that $j_x(x, y) = 0, \forall x, y$ which implied $c_X = 0, c_Y = c_0$. Since $c_X \neq 0$, we get $A_1 = A_2 = \tilde{A}_n$ and

$\tilde{A}_n(e^{c_X L_x} - e^{-c_X L_x}) = 0$. Also, since $\tilde{A}_n \neq 0$ (because $A_1 = A_2 = \tilde{A}_n = 0$ implies $j_x = 0$), c_X cannot be real and must be purely imaginary, i.e, $c_X = \iota c_n$, and we have $\sin(c_n L_x) = 0$, i.e., $c_n = n\pi/L_x, c_Y = c_{Y,n} = \sqrt{c_0^2 + c_n^2}$, where n is an integer. The solution of $\tilde{\mu}_X$ is given by $\tilde{\mu}_X(x) = 2\tilde{A}_n \cos(n\pi/L_x)$. For the boundary condition $j_y(x, y = 0) = 0, \forall x$, we have $B_1 = B_2 = \tilde{B}_n$ (since $\tilde{\mu}_X(x) \neq 0, \forall x$ and $c_Y \neq 0$). So, the solution of $\tilde{\mu}_Y$ is given by $\tilde{\mu}_Y(y) = 2\tilde{B}_n \cosh(\sqrt{c_0^2 + n^2\pi^2/L_x^2}y)$. The general solution for $\tilde{\mu}(x, y)$ is given by the series

$$\tilde{\mu}(x, y) = \sum_{n=0}^{\infty} \tilde{D}_n \cos\left(\frac{n\pi x}{L_x}\right) \cosh\left(\sqrt{c_0^2 + \frac{n^2\pi^2}{L_x^2}}y\right). \tag{3.40}$$

Here, $\tilde{D}_0 = 4\tilde{A}_0\tilde{B}_0$ and $\tilde{D}_n = 8\tilde{A}_n\tilde{B}_n$ for $n \neq 0$ (since the contribution for both positive and negative integer n are the same, and the summation in Eq. (3.40) is only for non-negative integers n). For the device geometry shown in Fig. 3.1(a), the FM magnetization is in the y-direction, so in the rest of the chapter we only consider $m_x = 0, m_y = \pm 1$. Then, the electrochemical potential $\mu(x, y)$ on the TI surface is given by

$$\mu = \mu_c + e^{b_0 m_y x} \sum_{n=0}^{\infty} \tilde{D}_n \cos\left(\frac{n\pi x}{L_x}\right) \cosh\left(\sqrt{c_0^2 + \frac{n^2\pi^2}{L_x^2}}y\right). \tag{3.41}$$

From Eq. (3.38b) and Eq. (3.40), for $m_x = 0$, we have

$$j_y(x, y) = -\sigma' e^{b_0 m_y x} \sum_{n=0}^{\infty} \tilde{D}_n \sqrt{c_0^2 + \frac{n^2\pi^2}{L_x^2}} \cos\left(\frac{n\pi x}{L_x}\right) \sinh\left(\sqrt{c_0^2 + \frac{n^2\pi^2}{L_x^2}}y\right). \tag{3.42}$$

The unknown coefficients $\tilde{D}_n$ will be determined from the boundary condition on either j_y (Neumann condition) or μ (Dirichlet condition) on the boundary $y = L_y$.

3.5 Solution for Neumann boundary condition

For the device shown in Fig. 3.3(a), we have Neumann boundary condition of uniform current density on the boundary $y = L_y$, i.e., $j_y(x, y = L_y) = I_c/L_x, \forall x \in [0, L_x]$. Using Eq. (3.42) in the boundary condition $j_y(x, y = L_y) = I_c/L_x, \forall x \in [0, L_x]$, we get

$$\sum_{n=0}^{\infty} \tilde{E}_n \cos\left(\frac{n\pi x}{L_x}\right) = -\left(\frac{I_c}{\sigma' L_x}\right) e^{-b_0 m_y x}, \tag{3.43}$$

where

$$\tilde{E}_n = \tilde{D}_n \sqrt{c_0^2 + \frac{n^2\pi^2}{L_x^2}} \sinh\left(\sqrt{c_0^2 + \frac{n^2\pi^2}{L_x^2}} L_y\right). \tag{3.44}$$

The left side of Eq. (3.43) is a Fourier series representation of the function on the right side of Eq. (3.43) in the interval $x \in [0, L_x]$. The coefficient $\tilde{E}_0$ is given by

$$\tilde{E}_0 = -\left(\frac{I_c}{\sigma' L_x}\right) \frac{1}{L_x} \int_0^{L_x} \mathrm{d}x \; e^{-b_0 m_y x} = -\left(\frac{I_c}{\sigma' L_x}\right) \frac{(1 - e^{-b_0 m_y L_x})}{b_0 m_y L_x}, \tag{3.45}$$

and, for $n \neq 0$, the coefficients $\tilde{E}_n$'s are obtained as,

$$\begin{aligned} \tilde{E}_n &= -\left(\frac{I_c}{\sigma' L_x}\right) \frac{2}{L_x} \int_0^{L_x} \mathrm{d}x \; e^{-b_0 m_y x} \cos\left(\frac{n\pi x}{L_x}\right) \\ &= -\left(\frac{I_c}{\sigma' L_x}\right) \frac{2 b_0 m_y L_x [1 - (-1)^n e^{-b_0 m_y L_x}]}{(b_0^2 m_y^2 L_x^2 + n^2\pi^2)}. \end{aligned} \tag{3.46}$$

The coefficients $\tilde{D}_n$ are obtained from Eqs. (3.44)-(3.46), and the solution of $\mu(x, y)$ is given by Eq. (3.41) since all the $\tilde{D}_n$'s are known.

For the device geometry shown in Fig. 3.3(a), we obtain

$$\begin{aligned}\Delta\mu(L_y') =& \frac{4m_y I_c}{\sigma'}\Bigg[\frac{\sinh^2(b_0L_x/2)}{b_0^2L_x^2}\frac{b_0L_x}{c_0L_x}\frac{\cosh(c_0L_y')}{\sinh(c_0L_y)} \\ &+ 2\sum_{\substack{n=2k\\k=1}}^{\infty}\frac{\sinh^2(b_0L_x/2)}{(b_0^2L_x^2+n^2\pi^2)}\frac{b_0L_x}{\sqrt{c_0^2L_x^2+n^2\pi^2}}\frac{\cosh\left(\sqrt{c_0^2L_x^2+n^2\pi^2}L_y'/L_x\right)}{\sinh\left(\sqrt{c_0^2L_x^2+n^2\pi^2}L_y/L_x\right)} \\ &- 2\sum_{\substack{n=2k-1\\k=1}}^{\infty}\frac{\cosh^2(b_0L_x/2)}{(b_0^2L_x^2+n^2\pi^2)}\frac{b_0L_x}{\sqrt{c_0^2L_x^2+n^2\pi^2}}\frac{\cosh\left(\sqrt{c_0^2L_x^2+n^2\pi^2}L_y'/L_x\right)}{\sinh\left(\sqrt{c_0^2L_x^2+n^2\pi^2}L_y/L_x\right)}\Bigg].\end{aligned} \tag{3.47}$$

The potential difference $\Delta\mu(L_y')$ depends on the magnetization direction of the FM and changes sign if the magnetization direction of the FM is reversed. In the limit $L_x \to 0$, from Eq. (3.47) we obtain

$$\Delta\mu(L_y') = \frac{I_c}{\sigma}\frac{\eta m_y}{2}\frac{l}{L_y}\frac{(d_0L_y/l)\cosh(d_0L_y'/l)}{\sinh(d_0L_y/l)}, \tag{3.48}$$

where $d_0 = c_0 l = \sqrt{2\xi(1+\xi)}$. Equation (3.48) is what we obtained in with the approximation $j_x = 0$ inside the rectangle, which also makes sense physically since if L_x is small, the variation of j_x will be negligible inside the rectangle, and as $j_x = 0$ on the boundaries $x = 0$ and $x = L_x$, $j_x \approx 0$ will be satisfied inside the rectangle. If $b_0L_x = \xi\eta L_x/l \ll 1$, $c_0L_x = \sqrt{2\xi(1+\xi)}L_x/l \ll 1$, and $L_x \ll L_y' < L_y$, all the terms in Eq. (3.47) for $n \geq 1$ can be neglected with respect to the first term, and $\sinh^2(b_0L_x/2) \approx b_0^2L_x^2/4$ can be used as an approximation in the first term. Then, we obtain Eq. (3.48) as an approximate solution when L_x is less than or comparable to l (since typically ξ and η are smaller than 1, and L_y is larger than l). In the limit $L_x \to 0$, using Eq. (3.48) in the definition of χ, we get $\chi = (d_0L_y/l)\cosh(d_0L_y'/l)/\sinh(d_0L_y/l)$ which is the same as that obtained with the approximation $j_x \approx 0$. In the case of nonzero L_x, we calculate χ from Eq. (3.47).

3.6 Solution for Dirichlet boundary condition

For the device shown in Fig. 3.3(b), on the boundary $y = L_y$ we have Dirichlet boundary condition of uniform electrochemical potential $-\mu_0$ applied to the TI surface with respect to the FM, i.e., $\mu(x, y = L_y) - \mu_c = -\mu_0, \forall x \in [0, L_x]$. Inserting Eq. (3.41) in the boundary condition $\mu(x, y = L_y) - \mu_c = -\mu_0, \forall x \in [0, L_x]$, we get

$$\sum_{n=0}^{\infty} \tilde{F}_n \cos\left(\frac{n\pi x}{L_x}\right) = -\mu_0 e^{-b_0 m_y x}, \tag{3.49}$$

where

$$\tilde{F}_n = \tilde{D}_n \cosh\left(\sqrt{c_0^2 + \frac{n^2\pi^2}{L_x^2}} L_y\right). \tag{3.50}$$

The left side of Eq. (3.49) is a Fourier series representation of the function on the right side of Eq. (3.49) in the interval $x \in [0, L_x]$. The coefficients $\tilde{F}_n$'s are obtained similarly as $\tilde{E}_n$'s in Eqs. (3.45)-(3.46). The coefficient $\tilde{F}_0$ is given by

$$\tilde{F}_0 = -\mu_0 \frac{1}{L_x} \int_0^{L_x} \mathrm{d}x \; e^{-b_0 m_y x} = -\mu_0 \frac{(1 - e^{-b_0 m_y L_x})}{b_0 m_y L_x}, \tag{3.51}$$

and, for $n \neq 0$, the coefficients $\tilde{F}_n$'s are given by

$$\begin{aligned} \tilde{F}_n &= -\mu_0 \frac{2}{L_x} \int_0^{L_x} \mathrm{d}x \; e^{-b_0 m_y x} \cos\left(\frac{n\pi x}{L_x}\right) \\ &= -\mu_0 \frac{2 b_0 m_y L_x [1 - (-1)^n e^{-b_0 m_y L_x}]}{(b_0^2 m_y^2 L_x^2 + n^2\pi^2)}. \end{aligned} \tag{3.52}$$

The coefficients $\tilde{D}_n$ are obtained from Eqs. (3.50)-(3.52), and the solution of $\mu(x, y)$ and $j_x(x, y)$ are given by Eq. (3.41) and (3.42), respectively, since all the $\tilde{D}_n$'s are known.

We calculate the total current I_c on the TI surface on the boundary $y = L_y$ using

$I_{\rm c} = \int {\rm d}x\ j_y(x, y = L_y)$. We obtain

$$
\begin{aligned}
I_{\rm c} = 4\sigma'\mu_0 \Bigg[& \frac{\sinh^2(m_y b_0 L_x/2)}{m_y^2 b_0^2 L_x^2} c_0 L_x \tanh(c_0 L_y) \\
& + 2 \sum_{\substack{n=2k \\ k=1}}^{\infty} \sinh^2(m_y b_0 L_x/2) \left(\frac{m_y b_0 L_x}{m_y^2 b_0^2 L_x^2 + n^2\pi^2} \right)^2 \sqrt{c_0^2 L_x^2 + n^2\pi^2} \tanh\left(\sqrt{c_0^2 L_x^2 + n^2\pi^2} L_y/L_x \right) \\
& - 2 \sum_{\substack{n=2k-1 \\ k=1}}^{\infty} \cosh^2(m_y b_0 L_x/2) \left(\frac{m_y b_0 L_x}{m_y^2 b_0^2 L_x^2 + n^2\pi^2} \right)^2 \sqrt{c_0^2 L_x^2 + n^2\pi^2} \tanh\left(\sqrt{c_0^2 L_x^2 + n^2\pi^2} L_y/L_x \right) \Bigg].
\end{aligned}
\tag{3.53}
$$

From Eqs. (3.53), we observe that the total current $I_{\rm c}$ is the same for both the magnetization directions $m_y = \pm 1$ of the FM. We also calculate the potential difference $\Delta\mu(L_y')$,

$$
\begin{aligned}
\Delta\mu(L_y') = & 4 m_y \mu_0 \Bigg[\sinh^2(b_0 L_x/2) \frac{1}{b_0 L_x} \frac{\cosh(c_0 L_y')}{\cosh(c_0 L_y)} \\
& + 2 \sum_{\substack{n=2k \\ k=1}}^{\infty} \sinh^2(b_0 L_x/2) \frac{b_0 L_x}{(b_0^2 L_x^2 + n^2\pi^2)} \frac{\cosh\left(\sqrt{c_0^2 L_x^2 + n^2\pi^2} L_y'/L_x \right)}{\cosh\left(\sqrt{c_0^2 L_x^2 + n^2\pi^2} L_y/L_x \right)} \\
& - 2 \sum_{\substack{n=2k-1 \\ k=1}}^{\infty} \cosh^2(b_0 L_x/2) \frac{b_0 L_x}{(b_0^2 L_x^2 + n^2\pi^2)} \frac{\cosh\left(\sqrt{c_0^2 L_x^2 + n^2\pi^2} L_y'/L_x \right)}{\cosh\left(\sqrt{c_0^2 L_x^2 + n^2\pi^2} L_y/L_x \right)} \Bigg].
\end{aligned}
\tag{3.54}
$$

From Eqs. (3.54), we observe that the potential difference $\Delta\mu(L_y')$ depends on the magnetization direction of the FM and changes sign upon the reversal of the magnetization direction of the FM. In the limit $L_x \to 0$, the terms in the summation for $n \geq 1$ can be neglected with respect to the first term in both Eqs. (3.53) and (3.54), and we obtain

$$
\begin{aligned}
I_{\rm c} & \approx 4\sigma'\mu_0 \frac{\sinh^2(b_0 L_x/2)}{b_0^2 L_x^2} c_0 L_x \tanh(c_0 L_y), \\
\delta\mu(L_y') & \approx 4 m_y \mu_0 \sinh^2(b_0 L_x/2) \frac{1}{b_0 L_x} \frac{\cosh(c_0 L_y')}{\cosh(c_0 L_y)}.
\end{aligned}
\tag{3.55}
$$

In the limit $L_x \to 0$, using Eq. (3.55) we obtain $\chi = (d_0 L_y/l) \cosh(d_0 L_y'/l)/\sinh(d_0 L_y/l)$ which is the same as that obtained with the approximation $j_x \approx 0$ and also from Eq. (3.48). In the case of nonzero L_x, we calculate χ from Eqs. (3.53)-(3.54).

3.7 Comparison of different solutions

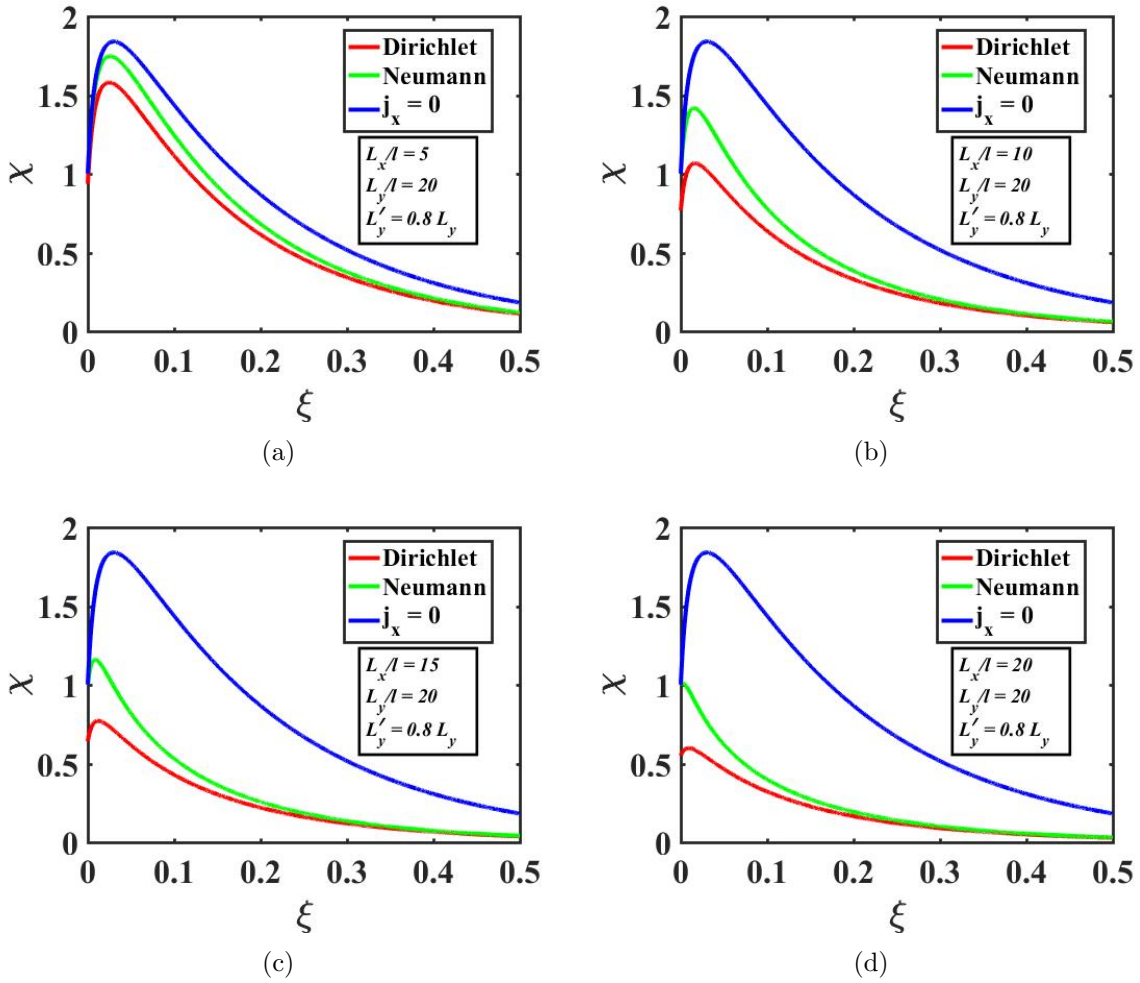

Figure 3.4: Variation of the detection efficiency (χ) with normalized interface tunneling rate (ξ) obtained from exact solutions: The solutions obtained from Neumann boundary condition, Dirichlet boundary condition and $j_y = 0$ approximation are shown for different cases with $L_y/l = 20$, $L'_y = 0.8L_y$ and (a) $L_x/l = 5$, (b) $L_x/l = 10$, (c) $L_x/l = 15$, (d) $L_x/l = 20$.

The dimensionless parameter χ is defined from the relation $\delta\mu(L'_y) = \chi\eta\frac{I_c}{\sigma}\frac{l}{L_y}$, and, χ can be viewed as the efficiency of the device in the detection of the IEE from the TI surface states by spin-polarized tunneling. The dimensionless parameter ξ defined by $\xi = \gamma N_+\tau_{tr}$ is the normalized interface tunneling rate of electrons with respect to the transport relaxation rate

of electrons on the pristine TI surface. In Figs. 3.4(a)-3.4(d), we show how the efficiency χ varies with the normalized tunneling rate ξ for various device geometries and different boundary conditions, for $L_y/l = 20$, $L'_y = 0.8L_y$ and different values of $L_x/l = 5, 10, 15, 20$ shown in figures (a), (b), (c), (d), respectively. We find from Figs. 3.4(a)-3.4(d) that the efficiency decreases as the length of the device in the x direction decreases. In all the cases shown in Figs. 3.4(a)-3.4(d), the efficiency of the tunnel barrier decreases with increasing tunnel conductance of the TI/FM interface indicating the importance of the tunnel contact in the detection of the open circuit voltage measured in the experiment.

3.8 Summary

In summary, starting from quantum kinetic equation we derive the transport equations on the TI surface considering tunneling from the FM in a TI-FM heterostructure. From these transport equations, a second order partial differential equation is obtained for the electrochemical potential in the TI with a source term describing tunneling from the FM. Next, we solve the differential equation analytically in a rectangular geometry, for constant potential applied to the FM and with net current flowing out of one boundary on the TI surface, to get the transverse potential drop at two other boundaries on the TI surface. A non-zero transverse potential difference orthogonal to the direction of the FM magnetization is calculated, which changes sign when the magnetization is reversed and agrees with the experiment used to detect the IEE on the surface of a TI by spin-polarized tunneling. We also show that the potential difference measured in the transverse direction decreases as size of the device in that direction increases. We find that the potential difference depends on the interface tunnel conductance implying the importance of the tunnel barrier in the detection of IEE on the TI surface in such spin-polarized tunneling experiment.

Chapter 4

Theory of spin detection on the surface of topological insulator

The spin-momentum helical locking of the two-dimensional (2D) gapless surface states of a three-dimensional (3D) TI leads to a non-zero spin polarization within the surface states when charge current flows on the surface of the TI[7, 8]. This spin polarization can be detected experimentally using three-terminal or four-terminal measurement set-ups with ferromagnetic metal (FM) tunnel contacts[28, 29, 30, 31, 32, 33, 34, 35, 36, 37, 38, 39, 40]. The voltage detected at the FM contact depends on the direction and the magnitude of the surface charge current as well as the angle between charge current-induced spin polarization direction on the surface of the TI and the magnetization direction of the FM[33, 50, 51, 52, 53, 54]. For the detection of the charge current induced spin polarization on the surface of a TI with a FM in a multi-terminal measurement, the requirement of a tunnel contact was clearly demonstrated in experiments[28, 29, 30, 31, 32, 33, 34, 35, 36, 37, 38, 39, 40].

In a multi-terminal spin-detection experiment, the multi-contact resistance $R_{ab,cd}$ is measured in the experiments, where $R_{ab,cd}(\vec{M}) = V_{cd}/I_{ab}$, V_{cd} is the voltage drop measured from contact c to contact d, and I_{ab} is the current applied from contact a to contact b, and $\vec{M}$ is the magnetization of the FM contact. In such a multi-terminal measurement, the resistance always obeys Onsager reciprocity[55], i.e., $R_{ab,cd}(+\vec{M}) = R_{cd,ab}(-\vec{M})$. The property of the spin-momentum locking of the surface states of a TI results in $R_{ab,cd}(+\vec{M}) \neq R_{ab,cd}(-\vec{M})$ and a variation of the multi-contact resistance with the FM magnetization[28, 29, 30, 31, 32, 33, 34, 35, 36, 37, 38, 39, 40]. However, in a multi-terminal measurement,

$R_{ab,cd}(+\vec{M}) \neq R_{ab,cd}(-\vec{M})$ does not violate the Onsager reciprocity relation which says only that $R_{ab,cd}(+\vec{M}) = R_{cd,ab}(-\vec{M})$, where the voltage and the current contacts are interchanged along with the reversal of the magnetization direction of the FM[50].

In the case of a two-terminal measurement with one FM and one nonmagnetic metal (NM) contact, the Onsager reciprocity relation $R_{ab,ab}(+\vec{M}) = R_{ab,ab}(-\vec{M})$ dictates that the two-terminal resistance will remain unchanged even if the magnetization of the FM is reversed, since the contact pair ab and cd are one and the same. Similarly, in case of a two-terminal measurement with two FM contacts, the Onsager reciprocity relation requires that $R_{ab,ab}(\vec{M}_1, \vec{M}_2) = R_{ab,ab}(-\vec{M}_1, -\vec{M}_2)$, i.e., the resistance will remain the same if the magnetizations of both the FMs, $\vec{M}_1, \vec{M}_2$, are reversed. However, in the literature, it had been posited theoretically that two-terminal resistance between a FM and a NM contact or between two FM contacts on the surface of a TI can change depending on the magnetization of the FM, where the transport on the TI surface was assumed either purely diffusive[67, 77, 78], or purely ballistic[79, 80], or partly diffusive and partly ballistic[81]. Such violations of Onsager reciprocity for two terminal resistance also had been found experimentally on the surface of TIs[56, 57, 82, 83], that we will discuss in chapter 6.

In this chapter, we derive the transport equations on the surface of a diffusive TI coupled to a FM tunnel contact, and then solve the resulting differential equations to obtain the resistances measured in such spin-detection experiments for four-terminal and three-terminal measurement geometries to demonstrate the validity of the Onsager reciprocity relation. Furthermore, we demonstrate the validity of the Onsager reciprocity relation for the two-terminal resistance between a FM and a NM contact or between two FM contacts, showing that the measured resistance is independent of reversal of the magnetization of the FM in the former case, or one or both magnetizations of the two FMs in the latter case consistent with Onsager reciprocity[50, 54, 55]. Here, we also show the importance of the tunnel contact

in such experiments. We find that the spin detection efficiency, or the difference of the measured voltage at the FM contact on reversing the magnetization of the FM, decreases with decreasing resistance of the FM tunnel contact.

4.1 Background and Motivation

In the literature, Schwab *et al.*[67] and Burkov *et al.*[77] found theoretically that the two-terminal resistance measured on the surface ($x-y$ plane) of a diffusive TI between a FM and a NM contact, as shown in Fig. 4.1(a), changes if the magnetization of the FM, which lies in the plane of the surface and normal (y axis) to the direction of transport (x axis), is reversed, which violates the Onsager reciprocity relation. In the theory of Burkov *et al.*[77], the coupled spin and charge diffusion equations on the surface of a TI were derived from density matrix response function formalism in a low-frequency long-wavelength limit, and the spin-charge coupled equations were solved analytically with current injected from a FM contact to the TI surface. However, in their work, the coupling of the FM contact to the TI surface states was not derived inside the theoretical framework, but, rather, was inserted by hand as boundary conditions for the charge current density and the spin current density in the spin-charge coupled diffusion equation of the TI surface states. The resulting two-terminal resistance that was obtained from the solution of the coupled diffusion equations violates the Onsager reciprocity relation. Although, Schwab *et al.*[67] had considered the effect of coupling of the FM contact to the TI surface states through a tunneling self-energy in quantum mechanical Keldysh Green's function approach to derive a modified continuity equation for the charge density on the TI surface, the modification of the charge current density was not considered. Following the approach by Burkov *et al.*[77], i.e., using the same spin-charge coupled diffusion equations on the TI surface and the same boundary conditions

for the charge current density and the spin current density for the FM contact, Taguchi *et al.*[78] calculated the two terminal resistance between two FM contacts on the surface of a diffusive TI, as shown in Fig. 4.1(b), and obtained violation of the Onsager reciprocity relation.

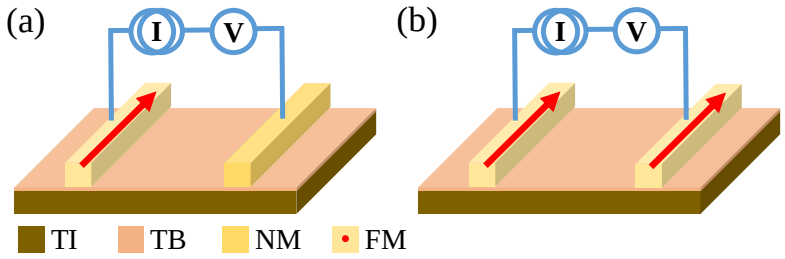

Figure 4.1: Schematics of two-terminal measurements with FM contacts on the TI surface: The measurement set-up consists of (a) one FM and one NM contact, (b) two FM contacts.

In this chapter, we first identify possible reasons behind the theoretical results obtained previously[67, 77, 78] leading to violation of Onsager reciprocity for the two terminal resistance on the surface of a diffusive TI consisting of FM contacts. We show that the coupled spin-charge diffusion equations for the TI surface states obtained by Burkov *et al.*[77] do not satisfy the continuity equation for the charge density, where the charge current density is derived formally from the velocity operator obtained from the Hamiltonian of the TI surface states. However, Burkov *et al.*[77] had defined both the charge current density and the spin current density on the TI surface from the coupled charge and spin transport equations considering continuity of the charge density and the spin density. We show that the definition of the charge current density obtained by them is inconsistent with the formal definition of the charge current density obtained from the Hamiltonian of the TI surface states. Moreover, it was already discussed in the literature[84, 85] that the definition of the spin current density obtained from the continuity equation for the spin density is not applicable for material with spin-momentum locked band structure. The physically measurable spin current density, which was used in the boundary condition for the spin current injection from the FM

to the TI surface in prior works[77, 78], was defined to be the gradient of the spin density on the TI surface. However, the spin current density being proportional to the gradient of the spin density on the TI surface is inconsistent with the formal definition of the spin current density derived from the TI surface state Hamiltonian[84, 85].

We show that the coupled diffusion equations on the surface of a TI are modified due to tunneling of electrons from a FM contact, and the actual effect of the FM contact cannot be taken into account simply by assuming charge current and spin current injection from the FM as boundary conditions. However, Schwab *et al.*[67] had only derived a modification of the continuity equation for the charge density due to tunneling while keeping the equation for charge current density unchanged. That is, the charge current density was given by the gradient of the full non-equilibrium electrochemical potential − re-expressed in their work and this work as the effective non-equilibrium charge density − on the TI surface even after tunneling from the FM. Here, we show that the charge current density on the TI surface also will contain an additional contribution due to tunneling from the FM, along with the gradient of the effective charge density term but with a modified diffusion constant. We demonstrate that if both the modification of the continuity equation for the charge density and the modification of the charge current density due to tunneling from the FM are considered, the two-terminal resistances between a FM and a NM contact or between two FM contacts on the surface of a diffusive TI do, indeed, satisfy the Onsager reciprocity relation. In case of two FM contacts, we also show that the resistance remains the same whether the magnetizations of the two FMs are parallel or anti-parallel, because the initial spin-polarizations of the electrons that undergo tunneling from either of the FMs to the TI surface are lost after momentum scattering on the TI surface due to the spin-momentum locking of the TI surface states.

4.2 Description of the multi-terminal spin-detection measurement set-up

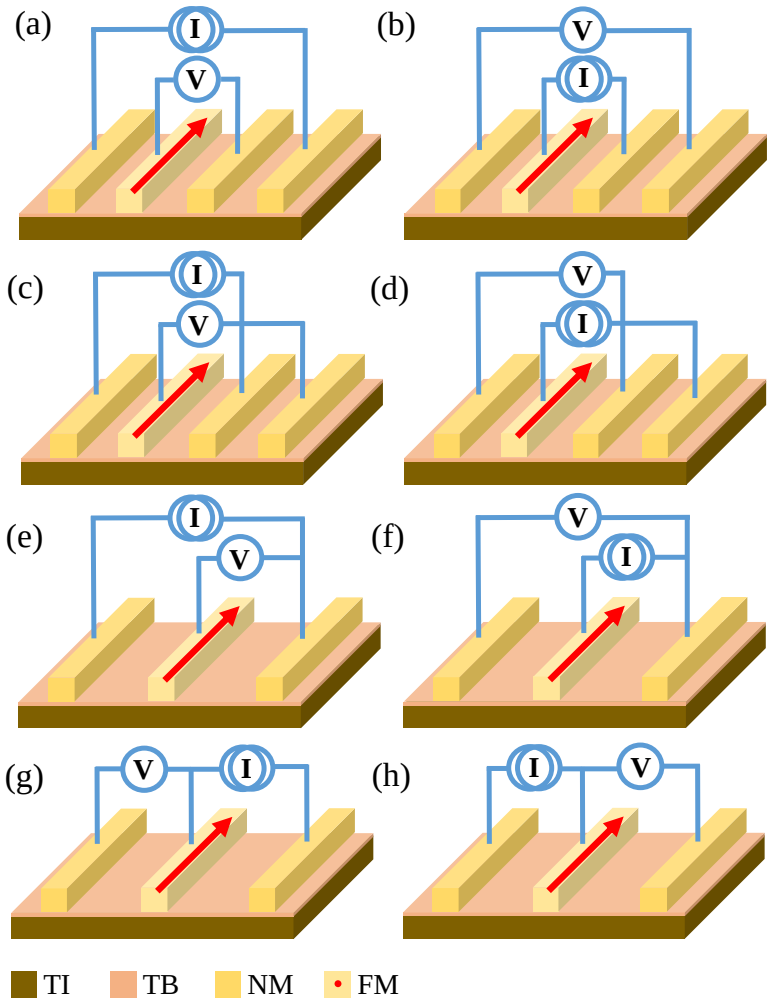

Figure 4.2: Schematics of four-terminal and three-terminal spin-detection experiments on the TI surface: (a)-(d) four-terminal, and (e)-(h) three-terminal measurement set-up.

We address possible one-dimensional (1D) circuit geometries that can be used to detect current-induced spin-polarization on the surface of a TI using four-terminal or three-terminal measurement set-ups. In a four-terminal set-up, the FM contact can be used as a voltage probe to measure the charge current-induced spin polarization on the surface of the TI, as

shown in Figs. 4.2(a) and 4.2(c). In these experiments, the current is passed through two NM contacts and the voltage is measured at the FM contact with respect to another NM contact different from the current injecting contacts. However, the reciprocal circuits, those obtained by flipping the voltage and current contacts of Figs. 4.2(a) and 4.2(c) are shown in Figs. 4.2(b) and 4.2(d), respectively, in which the FM contact will be a current probe, also can be used. In a three-terminal set-up, the FM contact can be used as either a voltage probe with the voltage measured with respect to that on either one of the current injecting NM contacts, as shown in Fig. 4.2(e), or as a current probe, as shown in Fig. 4.2(f), which is the reciprocal circuit of Fig. 4.2(e), or as both voltage and current probes in which the current is passed through a FM and a NM contact and the voltage is measured between the same FM contact and another NM contact placed on other side of the current injecting NM contact, as shown in Figs. 4.2(g) and 4.2(h). The circuits shown in Figs. 4.2(g) and 4.2(h) are reciprocal circuits of each other. We show that the Onsager reciprocity relation is satisfied in each case by analyzing the reciprocal circuit pairs in the mentioned four-terminal and three-terminal measurement set-ups.

4.3 Theory of coupled transport in TI/FM heterostructure

The low-energy effective Hamiltonian of the TI surface states is given by $H(\mathbf{p}) = \hbar v_{\mathrm{F}}(\mathbf{p} \times \hat{\mathbf{z}}) \cdot \boldsymbol{\sigma}$, where $\hbar$ is the reduced Planck constant, v_{F} is the Fermi velocity of the TI surface states, $\mathbf{p}$ is the 2D momentum of the surface states, $\hat{\mathbf{z}}$ is the unit vector along the surface normal direction, and $\boldsymbol{\sigma} = (\sigma_x, \sigma_y, \sigma_z)$ is the vector consisting of the Pauli spin matrices. We consider the transport within the TI surface in the TI/FM contact layer as shown in Fig. 4.4. The momentum scattering among the TI surface states is considered due to random spin-independent short-range impurity potentials on the surface of the TI consistent with both

Schwab *et al.*[67] and Burkov *et al.*[77], neglecting phonon at the considered low temperatures in the experiments. In the work of Schwab *et al.*[67], the coupling of the TI surface states to the FM contacts are modeled by spin-conserving but momentum randomizing tunneling, where the work of Burkov *et al.*[77] did not directly model tunneling. In this work, we mainly focus on the spin-conserving momentum randomizing tunneling between the FM and TI surface states to allow for a direct comparison to the work of Schwab *et al.*[67]. However, we also discuss the effect of spin-non-conserving but spin-selecting, and momentum randomizing or in-plane momentum conserving, tunneling on the spin-detection experiments. Both the effects of tunneling from the FM to the TI surface states and the momentum scattering among the TI surface states are included in the quantum kinetic equation through self energy contributions.

The quantum kinetic equation can be written in terms of the Keldysh component of the quasi-classical Green's function ($\mathrm{g}(\mathbf{R}, \mathrm{t}; \mathrm{p_F}\hat{\mathbf{p}}, \varepsilon)$) of the TI surface states as (Eq. (3.19) in chapter 3),

$$\partial_t \mathrm{g} + \frac{v_\mathrm{F}}{2}\big\{(\hat{\mathbf{z}} \times \boldsymbol{\sigma}) \cdot \nabla_{\mathbf{R}}, \mathrm{g}\big\} + i v_\mathrm{F} \mathrm{p_F}[(\hat{\mathbf{p}} \times \hat{\mathbf{z}}) \cdot \boldsymbol{\sigma}, \mathrm{g}] = -\frac{\mathrm{g} - \langle \mathrm{g} \rangle}{\tau_\mathrm{p}} + \frac{1}{2\tau_\mathrm{p}}\big\{(\hat{\mathbf{p}} \times \hat{\mathbf{z}}) \cdot \boldsymbol{\sigma}, \langle \mathrm{g} \rangle\big\}$$
$$- \gamma\Big(\big\{(N_\uparrow \mathrm{P}_\uparrow + N_\downarrow \mathrm{P}_\downarrow), \mathrm{g}\big\} + N_\uparrow \mathrm{P}_\uparrow \mathrm{g}_\uparrow + N_\downarrow \mathrm{P}_\downarrow \mathrm{g}_\downarrow\Big) + \frac{\gamma}{2}\big\{(\hat{\mathbf{p}} \times \hat{\mathbf{z}}) \cdot \boldsymbol{\sigma}, (N_\uparrow \mathrm{P}_\uparrow \mathrm{g}_\uparrow + N_\downarrow \mathrm{P}_\downarrow \mathrm{g}_\downarrow)\big\}. \tag{4.1}$$

In the above equation, the quasi-classical Green's function $\mathrm{g}(\mathbf{R}, \mathrm{t}; \mathrm{p_F}\hat{\mathbf{p}}, \varepsilon)$ is expressed in terms of the Wigner coordinates $(\mathbf{R}, \mathrm{t}; \mathrm{p_F}\hat{\mathbf{p}}, \varepsilon)$, where $\mathbf{R}$ is the position on the TI surface, t is time, $\mathrm{p_F}$ is the Fermi momentum magnitude of the TI surface states, $\hat{\mathbf{p}} = \mathbf{p}/\mathrm{p_F}$ is the unit vector, and ε is energy. In Eq. (4.1), τ_p is the scattering time between the Bloch states of the TI (τ_p would be the momentum relaxation time on the surface of the TI in the absence of consideration of the overlap of the initial and final states of the TI, where the second term on the second line of Eq. (4.1) then address this spin overlap between initial

and final states of the TI), γ denotes the strength of tunneling between the FM and the TI surface states, $\langle ... \rangle$ denotes angular averaging over the Fermi contour of the TI surface states, $\mathrm{P}_{\uparrow,\downarrow} = (\sigma_0 \pm \hat{\mathbf{m}} \cdot \boldsymbol{\sigma})/2$ are the projection operators to the majority and minority spin bands in the FM, σ_0 is the spin-space identity matrix, $\hat{\mathbf{m}} = (m_x, m_y, m_z)$ is the magnetization direction (a unit vector) of the FM, $N_{\uparrow,\downarrow}$ are the corresponding density of states (DOSs) of the majority and minority spin bands in the FM at the Fermi energy, and $\mathrm{g}_{\uparrow,\downarrow}$ are the non-equilibrium quasi-classical Green's functions of the majority and minority electrons in the FM averaged over the Fermi surface in the FM.

The derivation of Eq. (4.1) is given in detail in chapter 3. However, in chapter 3, to obtain the continuity equation for the charge density and the diffusion equation for the charge current density on the TI surface, we solved the quasi-classical Green's function g of the TI surface states assuming projection of g on the conduction band of the Hamiltonian, i.e., $\mathrm{g} = g_0(\hat{\mathbf{p}}, \varepsilon)[\sigma_0 + (\hat{\mathbf{p}} \times \hat{\mathbf{z}}) \cdot \boldsymbol{\sigma}]$, and expanding the angular dependence of g_0 in the zeroth and the first harmonics, i.e. $g_0(\hat{\mathbf{p}}, \varepsilon) = \mathrm{g_s}(\varepsilon) + \hat{\mathbf{p}} \cdot \mathbf{g}_\mathrm{a}(\varepsilon)$. In this chapter, we proceed differently to derive the transport equations on the TI surface, with one aim of this approach being to connect the work of Burkov *et al.*[77] and that of Schwab *et al.*[67]. In our approach, on one hand, the spin-charge coupled diffusion equations given by Burkov *et al.*[77] can be derived in the absence of tunneling, and it can be shown easily that the spin-charge coupled diffusion equations given by Burkov *et al.*[77] violates the continuity equation for the charge density on the TI surface, where the charge current density on the TI surface is defined using the velocity operator for the surface states $\mathbf{v} = (1/\hbar)\partial H/\partial \mathbf{p} = v_\mathrm{F}(\hat{\mathbf{z}} \times \boldsymbol{\sigma})$. On the other hand, considering the tunneling of carriers between the FM and the TI surface, the modification of the continuity equation for the charge density on the TI surface given by Schwab *et al.*[67] can be obtained, along with a modification of the charge current density that was not considered by Schwab *et al.*[67] but cannot be disregarded.

The quasi-classical Green's function of the TI surface states can be written as $\mathrm{g} = \mathrm{g}_0\sigma_0 + \mathbf{g}\cdot\boldsymbol{\sigma}$, where $\mathbf{g} = (\mathrm{g}_x, \mathrm{g}_y, \mathrm{g}_z)$. By Fourier transforming $\partial_\mathrm{t} \to -i\omega$ and $\nabla_\mathbf{r} \to i\mathbf{q} = (i\mathrm{q}_x, i\mathrm{q}_y)$, and taking trace of Eq. (4.1) after multiplying by identity matrix and each of three Pauli spin matrices, the resulting four equations can be rewritten in a matrix form as

$$\mathbb{K}g = \mathbb{L}(\langle g\rangle + h), \tag{4.2}$$

where $g = (\mathrm{g}_0, \mathrm{g}_x, \mathrm{g}_y, \mathrm{g}_z)^T$ and $h = (\mathrm{h}_0, \mathrm{h}_x, \mathrm{h}_y, \mathrm{h}_z)^T$ are 4×1 column vectors, $\mathbb{K}$ and $\mathbb{L}$ are 4×4 matrices. Here, $\mathrm{h}_0 = \gamma\tau_\mathrm{p}(N_\uparrow \mathrm{g}_\uparrow + N_\downarrow \mathrm{g}_\downarrow)/2$ and $(\mathrm{h}_x, \mathrm{h}_y, \mathrm{h}_z) = \mathbf{h}$ is given by $\mathbf{h} = \gamma\tau_\mathrm{p}(N_\uparrow \mathrm{g}_\uparrow - N_\downarrow \mathrm{g}_\downarrow)\mathbf{m}/2$. The matrix $\mathbb{L}$ is given by

$$\mathbb{L} = \begin{bmatrix} 1 & \sin\theta & -\cos\theta & 0 \\ \sin\theta & 1 & 0 & 0 \\ -\cos\theta & 0 & 1 & 0 \\ 0 & 0 & 0 & 1 \end{bmatrix}, \tag{4.3}$$

where θ is the angle of the $\mathbf{p}$ vector lying on the Fermi contour. The matrix $\mathbb{K}$ is given by

$$\mathbb{K} = \begin{bmatrix} \Omega & i\Delta_y & -i\Delta_x & \Delta_z \\ i\Delta_y & \Omega & 0 & \Omega_{SO}\cos\theta \\ -i\Delta_x & 0 & \Omega & \Omega_{SO}\sin\theta \\ \Delta_z & -\Omega_{SO}\cos\theta & -\Omega_{SO}\sin\theta & \Omega \end{bmatrix}, \tag{4.4}$$

where $\Omega = 1 + \gamma N_+\tau_\mathrm{p} - i\omega\tau_\mathrm{p}$, $\Omega_{SO} = 2\mathrm{p}_\mathrm{F} v_\mathrm{F}\tau_\mathrm{p}$, $\Delta_x = \mathrm{q}_x v_\mathrm{F}\tau_\mathrm{p} + i\gamma N_-\tau_\mathrm{p} m_y$, $\Delta_y = \mathrm{q}_y v_\mathrm{F}\tau_\mathrm{p} - i\gamma N_-\tau_\mathrm{p} m_x$, $\Delta_z = \gamma N_-\tau_\mathrm{p} m_z$, and $N_\pm = N_\uparrow \pm N_\downarrow$. The matrix $\mathbb{K}$ of Eq. (4.4) reduces to the one obtained previously in deriving the diffusion equation on the surface of a TI without a FM[82, 86] after substituting $\gamma = 0$ in the quantities Ω, Δ_x, Δ_y and Δ_z.

To obtain the diffusion equation, one has to solve for $\langle g \rangle$ in Eq. (4.2). Multiplying by $\mathbb{K}^{-1}$ on both sides of Eq. (4.2) and averaging over θ, $\langle g \rangle$ is obtained from the matrix equation

$$\langle g \rangle = \mathbb{D}(\langle g \rangle + h), \tag{4.5}$$

where $\mathbb{D} = \langle \mathbb{K}^{-1}\mathbb{L} \rangle$ is a 4×4 matrix. Equation (4.5) is the most general form of spin-charge coupled transport equation on the surface of a TI coupled to a FM. However, in our case, the calculation of the matrix elements of $\mathbb{D}$ can be further simplified. As shown in Figs. 4.1 and 4.2, we only consider 1D problems with the FM magnetized in the $\pm y$ direction. Therefore, the charge and spin density will be uniform along the y direction on the TI surface. Hence, $\mathrm{q}_y = 0$ and $\mathbf{m} = (0, \pm 1, 0)$, therefore, $\Delta_y = \Delta_z = 0$, and $\mathbb{K}^{-1}$ becomes[82, 86]

$$\frac{\begin{bmatrix} \Omega(\Omega^2 + \Omega_{SO}^2) & -i\sin\theta\cos\theta\Delta_x\Omega_{SO}^2 & i\Delta_x(\Omega^2 + \Omega_{SO}^2\cos^2\theta) & -i\sin\theta\Delta_x\Omega\Omega_{SO} \\ -i\sin\theta\cos\theta\Delta_x\Omega_{SO}^2 & \Omega(\Omega^2 + \Omega_{SO}^2\sin^2\theta + \Delta_x^2) & -\sin\theta\cos\theta\Omega\Omega_{SO}^2 & -\cos\theta(\Omega^2 + \Delta_x^2)\Omega_{SO} \\ i\Delta_x(\Omega^2 + \Omega_{SO}^2\cos^2\theta) & -\sin\theta\cos\theta\Omega\Omega_{SO}^2 & \Omega(\Omega^2 + \Omega_{SO}^2\cos^2\theta) & -\sin\theta\Omega^2\Omega_{SO} \\ i\sin\theta\Delta_x\Omega\Omega_{SO} & \cos\theta(\Omega^2 + \Delta_x^2)\Omega_{SO} & \sin\theta\Omega^2\Omega_{SO} & \Omega(\Omega^2 + \Delta_x^2) \end{bmatrix}}{\Omega^2(\Omega^2 + \Omega_{SO}^2) + \Delta_x^2(\Omega^2 + \Omega_{SO}^2\cos^2\theta)}. \tag{4.6}$$

To obtain $\mathbb{D}$, we need to integrate over angle θ, while the quantities Ω_{SO}, Ω and Δ_x are constants. As the denominator of $\mathbb{K}^{-1}$ is a function of $\cos^2\theta$, by the symmetry of the trigonometric function in the four quadrants $[0, \pi/2)$, $[\pi/2, \pi)$, $[\pi, 3\pi/2)$ and $[3\pi/2, 2\pi)$, after averaging $\mathbb{K}^{-1}\mathbb{L}$ over θ, the non-diagonal terms of the matrix $\mathbb{D}$ relating coupled transport of the $\mathrm{g}_0, \mathrm{g}_y$ components with the $\mathrm{g}_x, \mathrm{g}_z$ components vanish. So, $\mathbb{D}_{0x}, \mathbb{D}_{x0}, \mathbb{D}_{0z}, \mathbb{D}_{z0}, \mathbb{D}_{xy}, \mathbb{D}_{yx}, \mathbb{D}_{yz}, \mathbb{D}_{zy}$ are zero, since $\int_0^{2\pi} \mathrm{d}\theta \sin\theta F(\cos\theta) = 0$ and $\int_0^{2\pi} \mathrm{d}\theta \cos\theta F(\sin\theta) = 0$ for any smooth function F. Therefore, the spin in the x and z directions of the electrons are decoupled from the

charge flow and y-component of spin. However, the charge flow and the y-component of spin of the electrons on the TI surface remain coupled. So we only work with the 2×2 matrix $\mathbb{D}_2$ consisting of $\mathbb{D}_{00}, \mathbb{D}_{0y}, \mathbb{D}_{y0}, \mathbb{D}_{yy}$ terms, and write the spin-charge coupled transport equation as

$$\langle g_2 \rangle = \mathbb{D}_2(\langle g_2 \rangle + h_2), \tag{4.7}$$

where $g_2 = (\mathrm{g}_0, \mathrm{g}_y)^T$ and $h_2 = (\mathrm{h}_0, \mathrm{h}_y)^T$ are 2×1 column vectors, and $\mathbb{D}_2$ is a 2×2 matrix given by

$$\mathbb{D}_2 = \begin{bmatrix} f_1 & \frac{i}{\Delta_x}(1 - \Omega f_1) \\ \frac{i}{\Delta_x}(1 - \Omega f_1) & \frac{\Omega}{\Delta_x^2}(1 - \Omega f_1) \end{bmatrix}, \tag{4.8}$$

where

$$f_1 = \frac{\sqrt{\Omega^2 + \Omega_{\mathrm{so}}^2}}{\sqrt{\Omega^2 + \Delta_x^2}\sqrt{\Omega^2 + \Delta_x^2 + \Omega_{\mathrm{so}}^2}}. \tag{4.9}$$

As in chapter 2 and chapter 3, we define the effective non-equilibrium charge density n on the surface of the TI, which is given by $n = \frac{eN}{2}\int \mathrm{d}\varepsilon \frac{1}{2}\mathrm{Tr}[\langle \mathrm{g}(\varepsilon)\rangle] = \frac{eN}{2}\int \mathrm{d}\varepsilon \langle \mathrm{g}_0(\varepsilon)\rangle$, where N is the DOS of the TI surface states at the Fermi energy. We also define the full charge electrochemical potential μ on the surface of the TI by $n = e^2 N \mu$, hence μ is given by $\mu = \frac{1}{2e}\int \mathrm{d}\varepsilon \langle \mathrm{g}_0(\varepsilon)\rangle$. The non-equilibrium spin density on the TI surface is given by $\mathbf{s} = \frac{eN}{4}\int \mathrm{d}\varepsilon \frac{1}{2}\mathrm{Tr}[\langle \boldsymbol{\sigma} \mathrm{g}(\varepsilon)\rangle] = \frac{eN}{4}\int \mathrm{d}\varepsilon \langle \mathbf{g}(\varepsilon)\rangle$. Here $\mathbf{s} = (s_x, s_y, s_z)$, and, s_x, s_y, s_z are the x-, y-, z-components of the spin density on the TI surface, respectively. The 2D charge current density on the surface of the TI is given by $\mathbf{j} = \frac{eN}{2}\int \mathrm{d}\varepsilon \frac{1}{2}\mathrm{Tr}[\langle \mathbf{v} \mathrm{g}(\varepsilon)\rangle]$, where $\mathbf{v} = v_{\mathrm{F}}(\hat{\mathbf{z}} \times \boldsymbol{\sigma})$ is the velocity operator. Here, $\mathbf{j} = (j_x, j_y)$, and j_x and j_y are the x- and y- components of the 2D charge current density, respectively. Because of the spin-momentum locking of the TI surface states, the 2D charge current density $\mathbf{j}$ is related to the non-equilibrium spin

density $\mathbf{s}$ by $\mathbf{j} = 2v_{\rm F}(\hat{\mathbf{z}} \times \mathbf{s})$. Hence, the charge current density j_x on the TI surface along the x-direction is given by $j_x = -2v_{\rm F}s_y$.

As given in Eqs. (3.24) and (3.25) in chapter 3, we define the effective non-equilibrium charge densities for the majority and the minority spin electrons $n_{\uparrow,\downarrow}$ and the corresponding electrochemical potentials $\mu_{\uparrow,\downarrow}$ of the majority and minority spin electrons in the FM, which are related by $n_{\uparrow,\downarrow} = e^2 N_{\uparrow,\downarrow}\mu_{\uparrow,\downarrow}$. So, we have, $\mu_{\uparrow,\downarrow} = \frac{1}{4e}\int \mathrm{d}\varepsilon\ \mathrm{g}_{\uparrow,\downarrow}(\varepsilon)$.

4.4 Transport on the TI surface without any FM

4.4.1 Conservation of charge

First, we show that the spin-charge coupled diffusion equations on the surface of the TI without any tunneling from the FM satisfies the continuity equation for the charge density. In the case of no tunneling, $\gamma = 0$, hence, $h_2 = 0$, $\Omega = 1 - i\omega\tau_{\rm p}$ and $\Delta_x = \mathrm{q}_x v_{\rm F}\tau_{\rm p}$ in Eqs. (4.7), (4.8) and (4.9). Performing the ε integration of Eq. (4.7), we obtain

$$[\mathbb{I}_2 - \mathbb{D}_2]\rho_2 = 0, \tag{4.10}$$

where $\mathbb{I}_2$ is the 2×2 identity matrix and $\rho_2 = (n, 2s_y)^T$. After using $\mathbb{D}_2$ from Eq. (4.8) in Eq. (4.10) with $\Omega = 1 - i\omega\tau_{\rm p}$ and $\Delta_x = \mathrm{q}_x v_{\rm F}\tau_{\rm p}$, we obtain,

$$\begin{bmatrix} 1 - f_1 & -\frac{i}{\Delta_x}(1 - \Omega f_1) \\ -\frac{i}{\Delta_x}(1 - \Omega f_1) & 1 - \frac{\Omega}{\Delta_x^2}(1 - \Omega f_1) \end{bmatrix} \begin{bmatrix} n \\ 2s_y \end{bmatrix} = 0. \tag{4.11}$$

Multiplying Eq. (4.10) by the row vector $v_2 = (\Omega, -i\Delta_x)$ from the left gives $v_2[\mathbb{I}_2 - \mathbb{D}_2]\rho_2 = 0$, which is, after Eq. (4.11),

$$(\Omega - 1)n - 2i\Delta_x s_y = 0. \tag{4.12}$$

Equation (4.12) is the continuity equation for the charge density of the TI surface states in Fourier space. After inverse Fourier transforming Eq. (4.12) to real space, and using $j_x = -2v_{\rm F}s_y$, we obtain the continuity equation for the charge density,

$$\partial_t n + \partial_x j_x = 0. \tag{4.13}$$

The spin-charge coupled transport equations are obtained by invoking the low-frequency, long-wavelength diffusive limit approximations, $\omega\tau_{\rm p} \ll 1, {\rm q}_x l_{\rm p} \ll 1$, and assuming that the Fermi energy lies well above the Dirac point, ${\rm p}_{\rm F} l_{\rm p} \gg 1$, where $l_{\rm p} = v_{\rm F}\tau_{\rm p}$ is the mean free path on the pristine TI surface. These approximations imply $|\Delta_x| \ll |\Omega| \ll 1 \ll \Omega_{\rm so}$. The spin-charge coupled diffusion equations must satisfy the continuity equation, i.e. Eq. (4.13), even after making these approximations. Under these approximations, the Taylor series expansion of the matrix elements of $\mathbb{D}_2$ are,

$$\begin{aligned}
\mathbb{D}_{00} &= \frac{1}{\Omega} - \frac{\Delta_x^2}{2\Omega^3} + \frac{3\Delta_x^4}{8\Omega^5} + \cdots, \\
\mathbb{D}_{0y} &= \mathbb{D}_{y0} = \frac{i\Delta_x}{2\Omega^2} - \frac{3i\Delta_x^3}{8\Omega^4} + \cdots, \\
\mathbb{D}_{yy} &= \frac{1}{2\Omega} - \frac{3\Delta_x^2}{8\Omega^3} + \cdots.
\end{aligned} \tag{4.14}$$

However, in order to satisfy charge conservation given by the continuity equation for the charge density, the expansions of the matrix elements of $\mathbb{D}_2$ have to be such that the equation $v_2[\mathbb{I}_2 - \mathbb{D}_2]\rho_2 = 0$ gives Eq. (4.12), which can be done by expanding each matrix element with different powers of Δ_x (or Ω) given by the following rule at each order of approximation:

To the lowest order approximation, one has to keep the first two terms of $\mathbb{D}_{00}$ and only the first term in each of $\mathbb{D}_{0y}, \mathbb{D}_{y0}, \mathbb{D}_{yy}$ in Eq. (4.14). For the next higher order, one has to keep the first three terms of $\mathbb{D}_{00}$ and the first two terms in each of $\mathbb{D}_{0y}, \mathbb{D}_{y0}, \mathbb{D}_{yy}$ in Eq. (4.14). In general, in the n^{th} order approximation, the rule is to keep the first $(n+1)$ terms of $\mathbb{D}_{00}$ and the first n terms in each of $\mathbb{D}_{0y}, \mathbb{D}_{y0}, \mathbb{D}_{yy}$ in Eq. (4.14).

4.4.2 Comparison to prior theory

The coupled spin-charge transport equations obtained by Burkov *et al.*[77] can be derived after evaluating $\mathbb{D} = \langle \mathbb{K}^{-1}\mathbb{L} \rangle$ using Eqs. (4.3) and (4.6) under diffusive approximation. However, in the following we precisely show that the results of Burkov *et al.*[77] are obtained if one keeps the first two terms in both $\mathbb{D}_{00}$ and $\mathbb{D}_{yy}$ and the first term in both $\mathbb{D}_{0y}$ and $\mathbb{D}_{y0}$ in Eq. (4.14), which do not satisfy the mentioned rules in order to maintain charge conservation. We obtain

$$\begin{aligned}
\mathbb{D}_{00} &= (1 - i\omega\tau_{\rm p})^{-1} - \frac{\Delta_x^2}{2}(1 - i\omega\tau_{\rm p})^{-3} \\
&\approx 1 + i\omega\tau_{\rm p} - \frac{{\rm q}_x^2 v_{\rm F}^2 \tau_{\rm p}^2}{2}, \\
\mathbb{D}_{0y} &= \mathbb{D}_{y0} = \frac{i\Delta_x}{2}(1 - i\omega\tau_{\rm p})^{-2} \approx \frac{i{\rm q}_x v_{\rm F}\tau_{\rm p}}{2}, \\
\mathbb{D}_{yy} &= \frac{1}{2}(1 - i\omega\tau_{\rm p})^{-1} - \frac{3\Delta_x^2}{8}(1 - i\omega\tau_{\rm p})^{-3} \\
&\approx \frac{1}{2}(1 + i\omega\tau_{\rm p}) - \frac{3{\rm q}_x^2 v_{\rm F}^2 \tau_{\rm p}^2}{8}.
\end{aligned} \tag{4.15}$$

In deriving the approximate values of the matrix elements, we have neglected terms of order $\omega^2\tau_{\rm p}^2$, $\omega\tau_{\rm p}{\rm q}_x l_{\rm p}$ and higher. Substituting the values from Eq. (4.15) into Eq. (4.10), we obtain,

$$\begin{bmatrix} -i\omega\tau_{\rm p} + \frac{1}{2}{\rm q}_x^2 v_{\rm F}^2\tau_{\rm p}^2 & -\frac{1}{2}i{\rm q}_x v_{\rm F}\tau_{\rm p} \\ -\frac{1}{2}i{\rm q}_x v_{\rm F}\tau_{\rm p} & \frac{1}{2} - \frac{1}{2}i\omega\tau_{\rm p} + \frac{3}{8}{\rm q}_x^2 v_{\rm F}^2\tau_{\rm p}^2 \end{bmatrix} \begin{bmatrix} n \\ 2s_y \end{bmatrix} = 0. \tag{4.16}$$

After inverse Fourier transforming Eq. (4.16) to real space, the following coupled spin-charge transport equations of Burkov *et al.*[77] are obtained,

$$\partial_t n = D_0 \partial_x^2 n + 2\Gamma \partial_x s_y, \tag{4.17a}$$

$$\partial_t s_y = \frac{3D_0}{2} \partial_x^2 s_y - \frac{s_y}{\tau_{\rm p}} + \Gamma \partial_x n, \tag{4.17b}$$

where $D_0 = v_{\rm F}^2 \tau_{\rm p}/2$ was the diffusion constant, and $\Gamma = v_{\rm F}/2$ was the spin-charge coupling constant. Since, the matrix elements of $\mathbb{D}_2$ given in Eq. (4.15) were not derived according to the above rules for order of approximation, the transport equation Eq. (4.17a) is inconsistent with the continuity equation for the charge density given in Eq. (4.13), if the formal definition of the charge current density $j_x = -2v_{\rm F} s_y$ is used. Alternatively, if the charge current density is defined from the transport equation, Eq. (4.17a), after considering Eq. (4.17a) as the continuity equation for the charge density, as what was done by Burkov *et al.*[77], the resulting new definition of the charge current density, $j_x = -D\partial_x n - 2\Gamma s_y$, becomes inconsistent with the formal definition of the charge current density.

Here, based on a derivation from the quantum kinetic equation, we show that the spin-charge coupled transport equations for the TI surface states obtained by Burkov *et al.*[77] are inconsistent with the continuity equation for the charge density. Burkov *et al.*[77] derived the spin-charge coupled transport equation from the density response function formalism using standard perturbation theory. It can be shown similarly, though it is beyond the scope of this paper, that the expansion in terms of the small parameters $\omega\tau_{\rm p}, {\rm q}_x l_{\rm p}$, in that formalism too has to be such that the resulting transport equations are consistent with the continuity equation for the charge density, for the charge conservation to hold, even after making standard current conserving approximations for the Green's function and the self-energy in perturbation theory.

4.4.3 A different approach to solve the problem

In case of tunneling from the FM to the TI surface, it becomes difficult to expanding the matrix elements of $\mathbb{D}_2$ in non-trivial order so that the resulting transport equations satisfy the continuity equation for the charge density on the TI surface. To overcome the difficulty, we multiply both sides of Eq. (4.7) by $\mathbb{D}_2^{-1}$ to obtain the new matrix equation

$$[\mathbb{D}_2^{-1} - \mathbb{I}_2]\langle g_2 \rangle = h_2, \tag{4.18}$$

where $\mathbb{D}_2^{-1}$ is given by

$$\mathbb{D}_2^{-1} = \begin{bmatrix} \Omega & -i\Delta_x \\ -i\Delta_x & f_2 \end{bmatrix}, \tag{4.19}$$

and,

$$f_2 = \frac{\Delta_x^2}{\Omega}\Big(\frac{1}{f_1\Omega} - 1\Big)^{-1}. \tag{4.20}$$

In the case of zero tunneling, $h_2 = 0$, $\Omega = 1 - i\omega\tau_{\rm p}$ and $\Delta_x = {\rm q}_x v_{\rm F}\tau_{\rm p}$ in Eqs. (4.18), (4.19), (4.20). After performing the ε integration of Eq. (4.18) and using Eq. (4.19), we obtain,

$$\begin{bmatrix} \Omega - 1 & -i\Delta_x \\ -i\Delta_x & f_2 - 1 \end{bmatrix} \begin{bmatrix} n \\ 2s_y \end{bmatrix} = 0. \tag{4.21}$$

The first row of the matrix equation in Eq. (4.21) is the same as Eq. (4.12) that gives Eq. (4.13), which is the continuity equation for the charge density on the TI surface. To obtain the second equation describing the coupled spin-charge transport given by the second row of the matrix equation in Eq. (4.21), the function f_2 in Eq. (4.20) is approximated by series expansions in powers of Δ_x and Ω. However, the continuity equation for the charge

density, i.e., Eq. (4.12) obtained from the first row of the matrix equation in Eq. (4.21), remains satisfied irrespective of the order of approximation for the function f_2. Under the previously noted diffusive approximations, $|\Delta_x| \ll |\Omega| \ll 1 \ll \Omega_{\rm so}$, f_2 can be approximated as $f_2 \approx 2\Omega$, i.e., $f_2 \approx 2 - 2i\omega\tau_{\rm p}$. Then, the second row of the matrix equation in Eq. (4.21) results in

$$-i\Delta_x n + (2\Omega - 1)2s_y = 0. \tag{4.22}$$

Inverse Fourier transforming Eq. (4.22) to real space, we obtain

$$\partial_t s_y + \frac{s_y}{2\tau_{\rm p}} - \frac{v_{\rm F}}{4}\partial_x n = 0. \tag{4.23}$$

Equation (4.23) indicates that the spin relaxation time $\tau_{\rm s}$ satisfies $\tau_{\rm s} = 2\tau_{\rm p}$, which is a property of the spin-momentum locked TI surface states[67, 86], instead of $\tau_{\rm s} = \tau_{\rm p}$ identified from Eq. (4.17b) that was obtained by Burkov *et al.*[77]. In steady state, using $j_x = -2v_{\rm F}s_y$ in Eq. (4.23), we obtain the equation for the charge current density,

$$j_x = -v_{\rm F}^2\tau_{\rm p}\partial_x n. \tag{4.24}$$

It can be recognized from Eq. (4.24) that the diffusion constant $D = v_{\rm F}^2\tau_{\rm p} = v_{\rm F}^2\tau_{\rm tr}^0/2$ instead of $D_0 = v_{\rm F}^2\tau_{\rm p}/2$ in Eq. (4.17a). Here, we obtain the the transport relaxation time (momentum relaxation time) $\tau_{\rm tr}^0$ in the presence of spin overlap considerations, which is $\tau_{\rm tr}^0 = 2\tau_{\rm p}$ because of the spin-momentum locking of the TI surface states[67]. In steady state, Eq. (4.13) and (4.24) give the following transport equations on the TI surface with conductivity $\sigma = e^2ND$ (without any tunneling from the FM),

$$\mathrm{d}_x j_x(x) = 0, \tag{4.25a}$$

$$j_x(x) = -\sigma \mathrm{d}_x \mu(x). \tag{4.25b}$$

4.5 Modified transport on the TI surface coupled to the FM

In the case of nonzero tunneling from the FM to the TI surface, we plug in $\Omega = 1 + \gamma N_+ \tau_\mathrm{p} - i\omega\tau_\mathrm{p}$ and $\Delta_x = \mathrm{q}_x v_\mathrm{F} \tau_\mathrm{p} + i\gamma N_- \tau_\mathrm{p} m_y$ in Eqs. (4.19) and (4.20). After performing the ε integration of Eq. (4.18) and substituting Eq. (4.19), we obtain

$$\begin{bmatrix} \Omega - 1 & -i\Delta_x \\ -i\Delta_x & f_2 - 1 \end{bmatrix} \begin{bmatrix} n \\ 2s_y \end{bmatrix} = \begin{bmatrix} \gamma N \tau_\mathrm{p} n_+ \\ \gamma N \tau_\mathrm{p} m_y n_- \end{bmatrix}, \tag{4.26}$$

where $n_\pm = n_\uparrow \pm n_\downarrow$. We define the dimensionless parameter $\xi = \gamma N_+ \tau_\mathrm{tr} = 2\gamma N_+ \tau_\mathrm{p}$, which is the normalized tunneling rate with respect to the momentum scattering rate on the TI surface, and ξ is proportional to the tunnel conductance. In case of weak tunneling, $\xi \ll 1$, the conditions $|\Delta_x| \ll |\Omega| \ll 1 \ll \Omega_\mathrm{so}$ remains valid, and f_2 given in Eq. (4.20) can be approximated as $f_2 \approx 2\Omega$, i.e., $f_2 \approx 2 + 2\gamma N_+ \tau_\mathrm{p} - 2i\omega\tau_\mathrm{p}$. After inverse Fourier transforming the first row of the matrix equation in Eq. (4.26) to real space, in steady state we obtain

$$\mathrm{d}_x j_x = -\gamma N_+ n + \gamma N n_+ + \frac{\gamma N_- m_y}{v_\mathrm{F}} j_x, \tag{4.27}$$

which is the modified continuity equation for the charge density on the TI surface due to tunneling from the FM to the TI. Similarly, after inverse Fourier transforming the second row of the matrix equation in Eq. (4.26) to real space and using $j_x = -2v_\mathrm{F} s_y$, in steady state we obtain

$$j_x = \frac{1}{(1+\xi)} \Big[- v_\mathrm{F}^2 \tau_\mathrm{p} \partial_x n + \gamma v_\mathrm{F} \tau_\mathrm{p} m_y \big(N_- n - N n_- \big) \Big], \tag{4.28}$$

which is the equation for the current density on the surface of the TI including modifications due to tunneling from the FM to the TI. These two equations, Eqs. (4.27) and 4.28, are

consistent with those we obtained in chapter 3 and what was obtained by Yokoyama *et al.*[51] from a semi-classical drift-diffusion model on the TI surface with tunneling calculated from the Fermi's Golden Rule of scattering between the FM majority/minority electrons and the TI surface states.

In the most general case of spin-selective but spin-non-conserving tunneling, Eqs. (4.26)-(4.28) will be modified. If the strength of tunneling between the TI surface states and the majority/minority bands of the FM are $\gamma_{\uparrow,\downarrow}$ which also depends on the nature of the interface (momentum randomization happens for a rough interface and in-plane momentum conservation holds for a smooth interface). Equation (4.26) will become

$$\begin{bmatrix} \Omega - 1 & -i\Delta_x \\ -i\Delta_x & f_2 - 1 \end{bmatrix} \begin{bmatrix} n \\ 2s_y \end{bmatrix} = \begin{bmatrix} e^2 N \tau_{\mathrm{p}} (\gamma_\uparrow N_\uparrow \mu_\uparrow + \gamma_\downarrow N_\downarrow \mu_\downarrow) \\ e^2 N \tau_{\mathrm{p}} m_y (\gamma_\uparrow N_\uparrow \mu_\uparrow - \gamma_\downarrow N_\downarrow \mu_\downarrow) \end{bmatrix}, \tag{4.29}$$

where, we have $\Omega = 1 + (\gamma_\uparrow N_\uparrow + \gamma_\downarrow N_\downarrow)\tau_{\mathrm{p}} - i\omega\tau_{\mathrm{p}}$ and $\Delta_x = \mathrm{q}_x v_{\mathrm{F}} \tau_{\mathrm{p}} + i(\gamma_\uparrow N_\uparrow - \gamma_\downarrow N_\downarrow)\tau_{\mathrm{p}} m_y$. Then, the modified continuity equation for the charge density on the TI surface, i.e., Eq. (4.27), becomes

$$\mathrm{d}_x j_x = \gamma_\uparrow N_\uparrow (e^2 N \mu_\uparrow - n) + \gamma_\downarrow N_\downarrow (e^2 N \mu_\downarrow - n) + m_y (\gamma_\uparrow N_\uparrow - \gamma_\downarrow N_\downarrow) \frac{j_x}{v_{\mathrm{F}}}. \tag{4.30}$$

The modified diffusion equation for the charge current density on the TI surface, i.e., Eq. (4.28), becomes

$$j_x = \frac{1}{(1+\xi)} \Big[- v_{\mathrm{F}}^2 \tau_{\mathrm{p}} \partial_x n - v_{\mathrm{F}} \tau_{\mathrm{p}} m_y \big\{ \gamma_\uparrow N_\uparrow (e^2 N \mu_\uparrow - n) - \gamma_\downarrow N_\downarrow (e^2 N \mu_\downarrow - n) \big\} \Big], \tag{4.31}$$

where, the new ξ will be redefined by $\xi = (\gamma_\uparrow N_\uparrow + \gamma_\downarrow N_\downarrow)\tau_{\mathrm{tr}}^0$.

Following the literature[51, 67], we define the spin electrochemical potential in the FM

$\mu_s = (\mu_\uparrow - \mu_\downarrow)$, and the charge electrochemical potential in the FM $\mu_c = (\mu_\uparrow + \mu_\downarrow)/2$. In the following, we assume $\mu_s = 0$, and, hence, $\mu_\uparrow = \mu_\downarrow = \mu_c$, consistent with Schwab *et al.*[67] (although the spin up down band edges are different). It can be shown[51] that the spin electrochemical potential $\mu_s(x)$ in the FM will be proportional to the ratio of the conductivity of the TI surface states to the conductivity of the FM, while the charge electrochemical potential $\mu_c(x)$ will be some constant (μ_c^0) plus a variation ($\mu_c^1(x)$) along the length of the contact, i.e., $\mu_c = \mu_c^0 + \mu_c^1(x)$, where $\mu_c^1(x)$ will be proportional to the ratio of the conductivity of the TI surface to the conductivity of the FM. Therefore, $\mu_s(x)$ and $\mu_c^1(x)$ can be neglected with respect to μ_c^0. Equation (4.27) then becomes

$$\mathrm{d}_x j_x = \frac{2\xi\sigma}{l^2}(\mu_c - \mu) + \frac{\xi\eta m_y}{l} j_x, \tag{4.32}$$

and Eq. (4.28) becomes

$$j_x = -\frac{\sigma}{(1+\xi)}\left[\mathrm{d}_x\mu + \frac{\xi\eta m_y}{l}(\mu_c - \mu)\right], \tag{4.33}$$

where, $l = v_F\tau_{tr}^0 = 2v_F\tau_p = 2l_p$ is the transport relaxation length (momentum relaxation length) on the pristine TI surface and $\eta = N_-/N_+$ is the DOS polarization of the FM. The right hand side of Eq. (4.32) can be interpreted as the current injected from the FM to the TI surface through the interface due to tunneling of electrons between the FM and the TI surface. The first term in the right hand side of Eq. (4.32) results from the difference of the electrochemical potential between the FM and the TI surface, and the tunnel conductance of the interface is proportional to $2\xi\sigma/l^2$. The second term in the right hand side of Eq. (4.32) results from the spin-momentum locking of the TI surface states and spin split bands of the FM. The first term in the right hand side of Eq. (4.33) is the diffusion term with the modified conductivity, $\sigma' = \sigma/(1+\xi)$, because tunneling back and forth across the interface serves as a momentum randomizing scattering process for the TI surface states. The second

term in the right hand side of Eq. (4.33) also arises because of the spin-momentum locking of the TI surface states and the spin split bands of the FM. The modification of the charge current density on the TI surface due to tunneling from the FM, given in Eq. (4.33), was not considered by Schwab *et al.*[67]. Now, we will show that considering both Eqs. (4.32) and (4.33), indeed, results in the two-terminal resistance that satisfies Onsager reciprocity. However, ignoring Eq. (4.33), as Schwab *et al.*[67] did, does lead to the violation of the Onsager reciprocity relation. Although we have derived Eqs. (4.32) and (4.33) considering spin-conserving momentum-randomizing tunneling, the forms of (4.32) and (4.33) remain the same with a redefined ξ and η even if we consider spin-non-conserving but spin-selecting momentum randomizing/in-plane momentum conserving tunneling. Then, ξ and η should be redefined as $\xi = (\gamma_\uparrow N_\uparrow + \gamma_\downarrow N_\downarrow)\tau_{\rm tr}^0$ and $\eta = (\gamma_\uparrow N_\uparrow - \gamma_\downarrow N_\downarrow)/(\gamma_\uparrow N_\uparrow + \gamma_\downarrow N_\downarrow)$.

4.6 Considering FM line contact

We begin our consideration of results for specific geometries by considering only line contacts in this section, which allows for more ready comparison to prior work by Schwab *et al*[67]. In a subsequent section we extend our results to consider contacts of nonzero length. In deriving the two terminal resistance between a FM and a point on the TI surface, Schwab *et al.*[67] had considered a FM line contact lying transverse to the transport direction and of infinitesimally small dimension along the transport direction, as shown in Fig. 4.3, with tunneling described by a delta function. We consider 1D transport along the x direction, the FM contact to be of length L along the transport direction located between region $x = 0$ and $x = L$ (we will take limit $L \to 0$) and of width W along the transport-normal direction y. The tunneling from the FM contact to the TI surface is modeled by replacing the tunneling strength γ by $\gamma L f_L(x)$, i.e., replacing ξ by $\xi L f_L(x)$, where $f_L(x)$ is a rectangular function

with value $1/L$ in the region $x = 0$ to $x = L$ and zero otherwise. (Note that $f_L(x) \to \delta(x)$ in the limit $L \to 0$). Following Schwab *et al.*[67], after replacing ξ by $\xi L f_L(x)$ we integrate Eq. (4.32) in a small region $(-\epsilon, L+\epsilon)$ close to the FM contact, and let both $\epsilon \to 0$ and $L \to 0$, to obtain

$$j_x^+ - j_x^- = \frac{2\xi\sigma L}{l^2}\left(\mu_c^0 - \frac{\mu^+ + \mu^-}{2}\right) + \frac{\xi\eta m_y L}{l}\frac{j_x^+ + j_x^-}{2}. \tag{4.34}$$

Here, we denote μ_c^0 to be the electrochemical potential on the FM line contact, $\mu^+ = \mu(0^+)$ to be the electrochemical potential on the TI surface to the right of the FM line contact and $\mu^- = \mu(0^-)$ to be the electrochemical potential on the TI surface to the left of the FM line contact. Similarly, we denote $j_x^+ = j_x(0^+)$ to be the charge current density on the TI surface to the right of the FM line contact and $j_x^- = j_x(0^-)$ to be the charge current density on the TI surface to the left of the FM line contact. To obtain Eq. (4.34), we have used $\int_{-\epsilon}^{L+\epsilon} \mathrm{d}x\ \mathrm{d}_x j_x = j_x(L+\epsilon) - j_x(-\epsilon)$, and, in the limits $\epsilon \to 0$ and $L \to 0$, $j_x(L+\epsilon) = j_x(0^+)$ and $j_x(-\epsilon) = j_x(0^-)$. Also in the limit $\epsilon \to 0$ and $L \to 0$, we have used $\int_{-\epsilon}^{L+\epsilon} \mathrm{d}x f_L(x)\mu \approx \frac{1}{2}[\mu(0^+)+\mu(0^-)]$ and $\int_{-\epsilon}^{L+\epsilon} \mathrm{d}x f_L(x) j_x \approx \frac{1}{2}[j_x(0^+)+j_x(0^-)]$ consistent with the approximations of Schwab *et al.*[67]. It should be noted that the electrochemical potential μ as well as the charge current density j_x on the TI surface will be continuous functions for $L \neq 0$, but the value of the function may be different to the right and left of the contact, i.e., $\mu(L^+) \neq \mu(0^-)$ and $j_x(L^+) \neq j_x(0^-)$ in general. In the limit $L \to 0$ for a line contact, there will be a change in the electrochemical potential on the TI surface across the FM line contact. This change in the electrochemical potential, which will be determined from Eqs. (4.32)- (4.33), was not considered by Schwab *et al.*[67].

Next, we consider Eq. (4.33)), multiply both sides of Eq. (4.33) by $(1+\xi)$, replace ξ by $\xi L f_L(x)$, perform the integration of the resulting equation in a small region $(-\epsilon, L+\epsilon)$ with

the limits $\epsilon \to 0$ and $L \to 0$, and divide the result by ξL, to obtain

$$\frac{j_x^+ + j_x^-}{2} = -\frac{\sigma}{\xi L}\left[(\mu^+ - \mu^-) + \frac{\xi\eta m_y L}{l}\left(\mu_c^0 - \frac{\mu^+ + \mu^-}{2}\right)\right]. \tag{4.35}$$

To obtain Eq. (4.35), we have used $\int_{-\epsilon}^{L+\epsilon} \mathrm{d}x\ \mathrm{d}_x\mu = \mu(L+\epsilon) - \mu(-\epsilon)$, and, in the limits $\epsilon \to 0$ and $L \to 0$, $\mu(L+\epsilon) = \mu(0^+)$ and $\mu(-\epsilon) = \mu(0^-)$. Also, we have used $\int_{-\epsilon}^{L+\epsilon} \mathrm{d}x\ j_x = 0$ in the limits $\epsilon \to 0$ and $L \to 0$. The electrochemical potential μ^+ and μ^- on the TI surface with respect to the electrochemical potential μ_c^0 on the FM will be determined in terms of the current density on the TI surface after solving Eqs. (4.34) and (4.35) with relevant boundary conditions on $j_x^\pm$.

In the measurement set-ups shown in Figs. 4.3(a), 4.3(c) and 4.3(e), a current I is injected from the FM contact to the TI surface to the right of the FM contact, so $j_x^+ = I/W$ and $j_x^- = 0$. Solving Eqs. 4.34 and 4.35, we obtain μ^+ and μ^- to be

$$\mu^+ = \mu_c^0 - \left(1 - \frac{\eta^2 m_y^2}{2}\right)\frac{\xi I L}{4\sigma W} - \frac{l^2}{2\xi\sigma}\frac{I}{WL}, \tag{4.36a}$$

$$\mu^- = \mu_c^0 + \left(1 - \frac{\eta^2 m_y^2}{2}\right)\frac{\xi I L}{4\sigma W} - \frac{l^2}{2\xi\sigma}\frac{I}{WL} + \frac{\eta m_y l}{2\sigma}\frac{I}{W}. \tag{4.36b}$$

The second term on the right side of both Eqs. (4.36a) and (4.36b) is the resistive potential drop due to the charge current flowing on the surface of the TI under the FM contact, where $\sigma W/L$ is the conductance of the TI surface over length L. The third term on the right side of both Eqs. (4.36a) and (4.36b) is the resistive potential drops across the interface due to the charge current flowing from the FM to the TI surface through the interface, where the interface conductance is $(2\xi\sigma/l^2)WL$, and WL is the area of the interface. (Note that $2\xi\sigma/l^2$ is the coefficient of the first term in Eq. (4.32)). From Eq. (4.36a), the potential drop $\Delta\mu(m_y) = (\mu_c^0 - \mu^+)$ is indeed the same for $m_y = \pm 1$, and, hence, the two terminal resistance

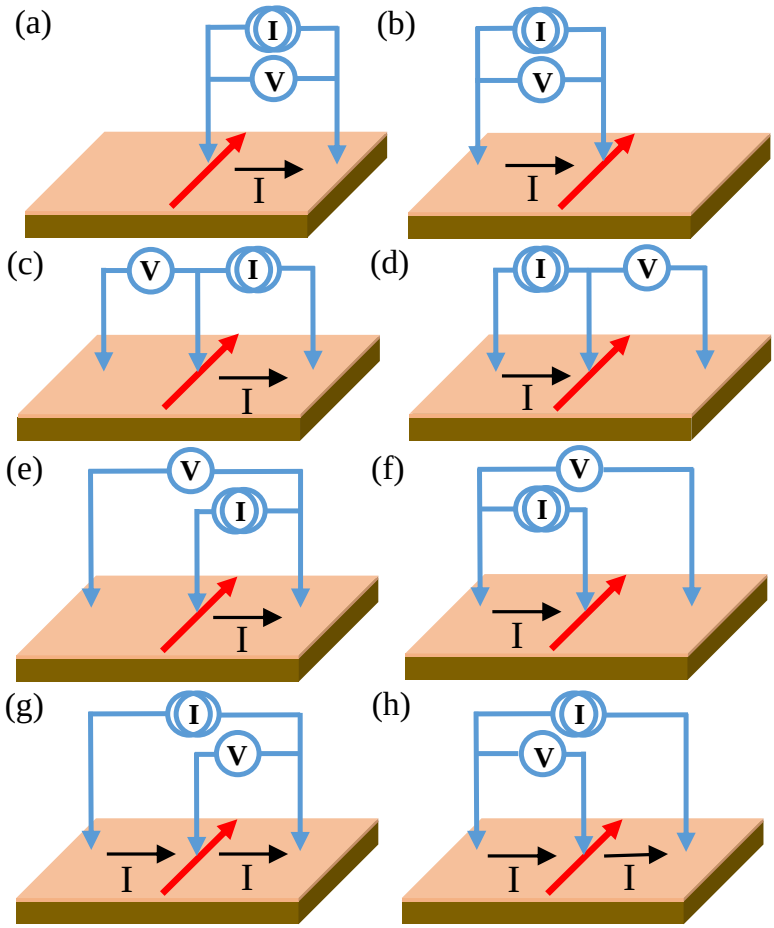

Figure 4.3: Schematics of 1D measurement geometries on the surface of a diffusive TI with a line FM contact indicated by an arrow showing the magnetization direction.

measured between the FM and the TI surface, as shown in Fig. 4.3(a), is independent of the magnetization direction of the FM satisfying the Onsager reciprocity relation. However, the last term in μ^- is non-trivial due to the spin-momentum locking of the TI surface states. From Eq. (4.36b), the potential drop $\Delta\mu(m_y) = (\mu^- - \mu_c^0)$, as shown in Fig. 4.3(c), depends on the sign of m_y. Similarly, from both Eqs. (4.36a) and (4.36b), the potential drop $\Delta\mu(m_y) = (\mu^- - \mu^+)$, as shown in Fig. 4.3(e), also depends on the sign of m_y. So, the measured three terminal resistances, as shown in Figs. 4.3(c) and 4.3(e), will depend on the magnetization direction of the FM. Such measurement set-ups were used to detect the current-induced spin polarization on the TI surface[39, 40]. We define the spin-detection

voltage $\delta\mu$ as the change of the potential drop upon reversing the magnetization direction of the FM, i.e., $\delta\mu = [\Delta\mu(m_y = +1) - \Delta\mu(m_y = -1)]$. In both cases shown in Figs. 4.3(c) and 4.3(d), $\delta\mu = \eta l I/\sigma W$.

In the measurement set-ups shown in Figs. 4.3(b), 4.3(d) and 4.3(f), a current I is extracted out of the FM contact from the TI surface to the left of the FM contact, such that $j_x^+ = 0$ and $j_x^- = I/W$. Then, we obtain μ^+ and μ^- to be

$$\mu^+ = \mu_c^0 - \left(1 - \frac{\eta^2 m_y^2}{2}\right)\frac{\xi I L}{4\sigma W} + \frac{l^2}{2\xi\sigma}\frac{I}{WL} + \frac{\eta m_y l}{2\sigma}\frac{I}{W}, \tag{4.37a}$$

$$\mu^- = \mu_c^0 + \left(1 - \frac{\eta^2 m_y^2}{2}\right)\frac{\xi I L}{4\sigma W} + \frac{l^2}{2\xi\sigma}\frac{I}{WL}. \tag{4.37b}$$

The measurement set-up pair shown in Figs. 4.3(a) and 4.3(b) (and, similarly, the pair Figs. 4.3(c) and 4.3(d) and the pair Figs. 4.3(e) and 4.3(f)) are identical after an 180^0 rotation in the plane. Hence, the solution for the electrochemical potential on the TI surface given in Eqs. (4.37a) and (4.37b) are related to that given in Eqs. (4.36a) and (4.36b), after a change of sign of both I and m_y and the interchange of μ^+ and μ^-. The 180^0 rotation symmetry is also present in Eqs. (4.34) and (4.35), which remain unchanged after letting $j_x^+ \to -j_x^-$, $j_x^- \to -j_x^+$, $m_y \to -m_y$, $\mu^+ \to \mu^-$ and $\mu^- \to \mu^+$. It is seen From Eqs. (4.37b) that the potential drop $\Delta\mu(m_y) = (\mu^- - \mu_c^0)$ is the same for $m_y = \pm 1$, and, hence, the two terminal resistance measured between the FM and the TI surface, as shown in Fig. 4.3(b), remains the same irrespective of the magnetization direction of the FM, satisfying Onsager reciprocity. From Eq. (4.37a), we find that the potential drop $\Delta\mu(m_y) = (\mu_c^0 - \mu^+)$, as shown in Fig. 4.3(d), depends on the sign of m_y. Similarly, from Eqs. 4.37a) and (4.37b), we find that the potential drop $\Delta\mu(m_y) = (\mu^- - \mu^+)$, as shown in Fig. 4.3(f), depends on the sign of m_y. So, the three terminal resistances, as shown in Figs. 4.3(e) and 4.3(f), will depend on the magnetization direction of the FM contact, and $\delta\mu = \eta l I/\sigma W$ for both cases.

In the measurement set-ups shown in Figs. 4.3(g)-(h), a current I is passed on the TI surface from the left of the FM contact to the right of the FM contact, and no current is injected/extracted through the FM contact, hence, $j_x^+ = j_x^- = I/W$. Then, we find the solution for μ^+ and μ^- to be

$$\mu^+ = \mu_c^0 - \left(1 - \frac{\eta^2 m_y^2}{2}\right)\frac{\xi I L}{2\sigma W} + \frac{\eta m_y l}{2\sigma}\frac{I}{W}, \tag{4.38a}$$

$$\mu^- = \mu_c^0 + \left(1 - \frac{\eta^2 m_y^2}{2}\right)\frac{\xi I L}{2\sigma W} + \frac{\eta m_y l}{2\sigma}\frac{I}{W}. \tag{4.38b}$$

The measurement set-up shown in Figs. 4.3(g) and 4.3(h) are identical after an 180^0 rotation in the plane, so, the solution for the electrochemical potential on the TI surface given in Eqs. (4.38a) and (4.38b) (which is same as interchanging μ^+ and μ^-) are related after a change of sign of both I and m_y. The second term in both Eqs. (4.38a) and (4.38b) is the resistive potential drops along the surface of the TI under the FM contact, and the third term in both Eqs. (4.38a) and (4.38b) is non-trivial and because of the spin-momentum locking of the TI surface states. For the geometry of Fig. 4.3(g), we obtain the potential drop $\Delta\mu(m_y) = (\mu_c^0 - \mu^+)$ from Eq. (4.38a), and for the geometry of Fig. 4.3(h), we obtain the potential drop $\Delta\mu(m_y) = (\mu^- - \mu_c^0)$ from Eq. (4.38b), both of which depend on the sign of m_y. Therefore, the three terminal resistances for the geometries of Figs. 4.3(g) and 4.3(h) will depend on the magnetization direction of the FM contact, and could be used for spin-detection with $\delta\mu = \eta l I/\sigma W$ for both cases.

Our results for $\delta\mu$ for three terminal measurement geometries of Figs. 4.3(g) and 4.3(h) match with that of Hong *et al.* calculated in the limit of small tunneling for a FM point contact as a voltage probe on the TI surface[50], as well as that of Yokoyama *et al.* obtained after a perturbative solution of the coupled transport equations of the TI/FM bilayer with tunneling treated as perturbation[51]. From Eqs. (4.38a) and (4.38b), we also find that the

potential drop $\Delta\mu(m_y) = (\mu^- - \mu^+)$ across the TI surface is independent of the sign of m_y, which also is consistent with the result by Yokoyama *et al.*[51]. The circuit pair shown in Figs. 4.3(c) and 4.3(d), the pair shown in Figs. 4.3(e) and 4.3(g), and the pair shown in Figs. 4.3(f) and 4.3(h) are reciprocal pairs. The resistance of each of these circuits can be calculated from Eqs. (4.36)-(4.38). For each reciprocal circuit pair, the Onsager reciprocity relation $R_1(+m_y) = R_2(-m_y)$ is satisfied, where R_1 and R_2 are m_y dependent resistances of reciprocal circuits in each pair.

4.7 Considering nonzero length FM contact

We started with the quantum kinetic equation given in Eq. (4.1) which is derived under the gradient expansion assuming that the $\mathbf{r}$ and t dependence of the Green's function $\mathrm{g}(\mathbf{r}, \mathrm{t}; \mathrm{p_F}\hat{\mathbf{p}}, \varepsilon)$ is smooth in the Fermi scale, i.e., $\mathrm{q}_x \ll \mathrm{p_F}$ and $\omega\tau_\mathrm{p} \ll \mathrm{p_F} l_\mathrm{p}$. Furthermore, Eqs. (4.27) and (4.28) are derived from the matrix equation Eq. (4.26) after approximating $f_2 \approx 2\Omega$ under low-frequency long-wavelength diffusive limit assumption, $\omega\tau_\mathrm{p} \ll 1$ and $\mathrm{q}_x l_\mathrm{p} \ll 1$. The assumptions in the gradient expansion and diffusive limit imply that the charge electrochemical potential μ on the TI surface varies smoothly on the scale of momentum relaxation length on the TI surface. In the solution of Eqs. (4.34) and (4.35), which are derived assuming delta function tunneling, μ has a discontinuity. However, the solution of μ in Eqs. (4.36)-(4.38) must be treated as the solution in the limiting case of the length of the FM contact becoming zero. Also, in experiment, the size of the contact is nonzero and at least an order of magnitude larger than the momentum relaxation length on the TI surface. Hence, the coupled transport equations, Eqs. (4.32) and (4.33), which are derived considering diffusive transport on the TI surface under the FM contact region, need to be resolved for a nonzero contact length. However, and as we will show do, these results for

nonzero contact length continue to follow the Onsager reciprocity relation, and converge back to the corresponding line contact result, $\delta\mu = \eta l I/\sigma W$ in the limit of $L \to 0$. However, it is only beyond the line contact limit that we capture the importance of the tunnel contact in such spin-detection experiments.

The second order differential equation for the electrochemical potential μ on the TI surface under the FM contact is obtained by substituting Eq. (4.33) into Eq. (4.32). Since the FM contact is metallic with a conductivity much higher than the conductivity of the TI surface, the electrochemical potential of the FM $\mu_c(x)$ can be taken to be constant within the FM contact, i.e., $\mathrm{d}_x\mu_c(x) = 0$ and $\mu_c(x) = \mu_c^0$. We define $\mu' = \mu - \mu_c^0$ to be the electrochemical potential on the TI surface with respect to the FM contact. Then, the equations for μ' and the current density j_x on the TI surface become,

$$\mathrm{d}_x^2\mu' - 2bm_y\mathrm{d}_x\mu' + \left(b^2m_y^2 - c^2\right)\mu' = 0, \tag{4.39a}$$

$$j_x = -\sigma'[\mathrm{d}_x\mu' - bm_y\mu'], \tag{4.39b}$$

where $b = \xi\eta/l$ and $c = \sqrt{2\xi(1+\xi)}/l$. From Eq. 4.39, if $\mu'(j)$ is a solution given a current density j on the TI surface, then $\mu'(\alpha j) = \alpha\mu'(j)$ is also a solution. So, the potential difference $(\mu_1 - \mu_2) = (\mu_1' - \mu_2')$ between any two points 1 and 2 on the TI surface, or the potential difference $(\mu - \mu_c^0) = \mu'$ between any point on the TI surface and the FM, will be directly proportional to the current density, implying a linear current-voltage relationship. Also, from Eq. (4.39), after letting $x \to -x$ and $m_y \to -m_y$, either $j_x \to -j_x$ or $\mu' \to -\mu'$ indicting a symmetry of the problem under an 180^0 rotation in the plane. However, to check for Onsager reciprocity, we must solve Eq. (4.39) given specific boundary conditions associated with the reciprocal circuit pairs. The solution of μ' in Eq. (4.39a) is given by $\mu' = A_1e^{r_1x} + A_2e^{r_2x}$, where $r_{1,2} = bm_y \pm c$, and the unknown constants $A_{1,2}$ will be determined from the boundary conditions on j_x, which can be written as $j_x = -\sigma' c(A_1e^{r_1x} - A_2e^{r_2x})$

from Eq. (4.39b). To keep the notation consistent with that of a line contact in the limit $L \to 0$, we denote the electrochemical potentials on the TI surface to the left of the FM contact to be $\mu^- = \mu(x = 0)$ and the electrochemical potentials on the TI surface to the right of the FM contact to be $\mu^+ = \mu(x = L)$. In the following, we find the solutions for μ^+ and μ^- for specific geometries and discuss the linear current-voltage characteristic, the symmetry under an 180^0 rotation in the plane, the spin-detection voltage on the TI surface, the validity of the Onsager reciprocity relation and the importance of the tunnel barrier in such spin-detection experiments.

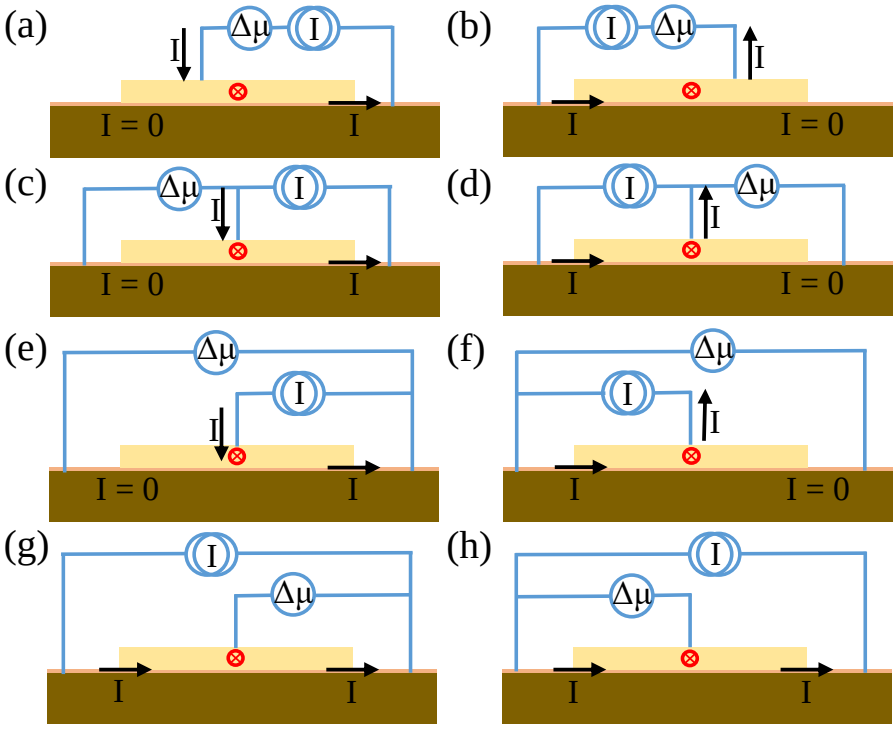

Figure 4.4: Schematics of cross-sectional views of 1D measurement geometries on the surface of a diffusive TI in the vicinity of the FM contact (in the circuits of Fig. 4.2).

We first consider the case in which a current I is injected from the FM to the TI and extracted from one end or the other of the TI surface, as shown in Figs. 4.4(a)-(f). In the case in which the current is extracted from the right end on the TI surface as shown in Figs. 4.4(a), 4.4(c) and 4.4(e), the boundary conditions become $j_x(x = 0) = 0$ and

$j_x(x = L) = I/W$. Hence, μ and j_x are given by

$$\mu = \mu_c^0 - \frac{I\,\mathrm{csch}(cL)}{\sigma' cW} e^{-b\mathrm{m}_y L}\left(\frac{e^{r_1 x} + e^{r_2 x}}{2}\right), \tag{4.40a}$$

$$j_x = \frac{I\,\mathrm{csch}(cL)}{W} e^{-b\mathrm{m}_y L}\left(\frac{e^{r_1 x} - e^{r_2 x}}{2}\right). \tag{4.40b}$$

Then, from Eq. (4.40a) we obtain the solution for μ^+ and μ^- to be

$$\mu^+ = \mu_c^0 - \frac{I\coth(cL)}{\sigma' cW}, \tag{4.41a}$$

$$\mu^- = \mu_c^0 - \frac{I\,\mathrm{csch}(cL)}{\sigma' cW} e^{-b\mathrm{m}_y L}. \tag{4.41b}$$

From Eq. (4.41a), the potential difference $\Delta\mu = (\mu_c^0 - \mu^+)$ does not depend on the magnetization direction of the FM. As a result, the two terminal resistance measured between a FM and a NM contact of Fig. 4.4(a) will remain the same even after reversing the magnetization of the FM, satisfying the Onsager reciprocity relation. However, in the three-terminal measurement of Fig. 4.4(c) in which the potential at the leftmost point on the TI surface is measured with respect to the FM, the potential difference $\Delta\mu(m_y) = (\mu^- - \mu_c^0)$, which is found from Eq. (4.41b), depends on the magnetization direction of the FM. Similarly, in the three terminal measurement of Fig. 4.4(e) in which the potential difference on the TI surface at the two ends is measured, $\Delta\mu(m_y) = (\mu^- - \mu^+)$ from Eqs. (4.41a) and (4.41b), depends on the magnetization direction of the FM.

If a current I is injected on the TI surface from the left end and extracted through the FM contact of Figs. 4.4(b), 4.4(d) and 4.4(f), the boundary conditions will be $j_x(x = 0) = I/W$

and $j_x(x = L) = 0$. Hence, μ and j_x are given by

$$\mu = \mu_c^0 + \frac{I\,\mathrm{csch}(cL)}{\sigma' cW}\left(\frac{e^{r_1 x - cL} + e^{r_2 x + cL}}{2}\right), \tag{4.42a}$$

$$j_x = -\frac{I\,\mathrm{csch}(cL)}{W}\left(\frac{e^{r_1 x - cL} - e^{r_2 x + cL}}{2}\right). \tag{4.42b}$$

Then, from Eq. (4.42a) we obtain μ^+ and μ^- to be

$$\mu^+ = \mu_c^0 + \frac{I\,\mathrm{csch}(cL)}{\sigma' cW} e^{\mathrm{b}m_y L}, \tag{4.43a}$$

$$\mu^- = \mu_c^0 + \frac{I\coth(cL)}{\sigma' cW}. \tag{4.43b}$$

Equation (4.43) can be obtained from Eq. (4.41) after reversing the direction of the injected current I and the magnetization direction m_y of the FM, and interchanging the rightmost and the leftmost potentials μ^+ and μ^-, which reflects the 180^0 rotation symmetry in the plane of the device. In the two-terminal case as shown in Fig. 4.4(b), the potential difference $\Delta\mu = (\mu^- - \mu_c^0)$ from Eq. (4.43b) is independent of the FM magnetization, so the two-terminal resistance will remain the same even after reversal of the magnetization direction of the FM. In the three terminal case as shown in Fig. 4.4(d), the potential difference $\Delta\mu(m_y) = (\mu_c^0 - \mu^+)$ from Eq. (4.43a) depends on the magnetization direction of the FM. Similarly, in the three-terminal case as shown in Fig. 4.4(f), the potential difference $\Delta\mu(m_y) = (\mu^- - \mu^+)$, which is obtained from Eqs. (4.43a) and (4.43b), also depends on the magnetization direction of the FM. Hence, in the three-terminal geometries of Figs. 4.4(c)-(f), there will be a change of resistance under the magnetization reversal of the FM, which can be used for spin detection on the surface of a TI.

In the circuit geometries shown in Figs. 4.4(g)-(h), the same current I is injected in and out of the two ends of the TI surface, and the boundary conditions are $j_x(x = 0) = j_x(x =$

$L) = I/W$. Hence, μ and j_x are given by

$$\mu = \mu_c^0 - \frac{I}{\sigma' cW}\left[\frac{(1-e^{r_2 L})e^{r_1 x} + (1-e^{r_1 L})e^{r_2 x}}{(e^{r_1 L} - e^{r_2 L})}\right], \tag{4.44a}$$

$$j_x = \frac{I}{W}\left[\frac{(1-e^{r_2 L})e^{r_1 x} - (1-e^{r_1 L})e^{r_2 x}}{(e^{r_1 L} - e^{r_2 L})}\right]. \tag{4.44b}$$

Then, from Eq. (4.44a), μ^+ and μ^- are given by

$$\mu^+ = \mu_c^0 - \frac{I\,\mathrm{csch}(cL)}{\sigma' cW}\Big(\cosh(cL) - e^{b\mathrm{m}_y L}\Big), \tag{4.45a}$$

$$\mu^- = \mu_c^0 + \frac{I\,\mathrm{csch}(cL)}{\sigma' cW}\Big(\cosh(cL) - e^{-b\mathrm{m}_y L}\Big). \tag{4.45b}$$

From Eq. (4.45), under the reversal (change of sign) of both the direction of the injected current I and the FM magnetization direction m_y, the potentials on the rightmost and the leftmost points, μ^+ and μ^-, are interchanged, which again is due to the 180^0 rotation symmetry in the plane of the device. In the geometries of Figs. 4.4(g) and 4.4(h), the potential difference $\Delta\mu(m_y) = (\mu_c^0 - \mu^+)$ and $\Delta\mu(m_y) = (\mu^- - \mu_c^0)$, respectively, can be obtained from Eqs. (4.45a) and (4.45b). In both these cases, $\Delta\mu(m_y)$ depends on the magnetization direction of the FM and will change upon reversing the FM magnetization direction. However, the potential difference $\Delta\mu(m_y) = (\mu^- - \mu^+)$ is independent of the magnetization direction of the FM, which is consistent with the Onsager reciprocity relation, and the result by Yokoyama *et al.*[51].

The 2D tunneling current density j_{tun} flowing from the FM to the TI surface through the interface is given by the right hand side of the modified continuity equation for transport on the TI surface, i.e., Eq. (4.32). So, we have,

$$j_{\mathrm{tun}} = \frac{2\xi\sigma}{l^2}(\mu_c^0 - \mu) + \frac{\xi\eta m_y}{l} j_x, \tag{4.46}$$

and, the modified continuity equation for transport on the TI surface now can be written as

$$\mathrm{d}_x j_x = j_{\mathrm{tun}}. \tag{4.47}$$

After integrating the above equation, i.e., Eq. (4.47) from 0 to L, and using the fat that $\int_0^L \mathrm{d}x\ \mathrm{d}_x j_x = j_x(L) - j_x(0)$, we obtain the 1D total tunneling current density $j_{\mathrm{tun}}^{\mathrm{tot}}$ to be

$$j_{\mathrm{tun}}^{\mathrm{tot}} = \int_0^L \mathrm{d}x\ j_{\mathrm{tun}} = j_x(L) - j_x(0). \tag{4.48}$$

The above equation Eq. (4.48) implies current conservation. In all the cases considered above, using Eqs. (4.40)-(4.45) we have checked that current conservation holds.

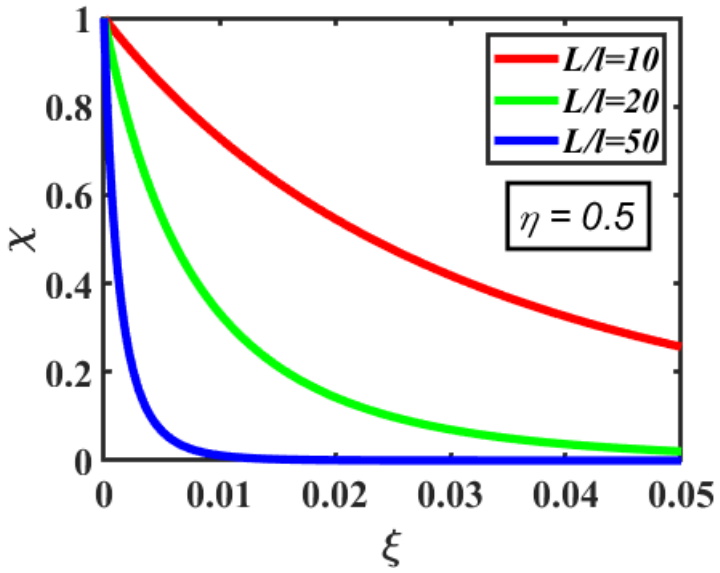

Figure 4.5: Variation of the spin-detection efficiency (χ) with the normalized conductance (ξ) of the FM tunnel contact: The variation is shown for different values of the FM contact length L relative to the transport relaxation length l on the TI surface, $L/l = 10, 20, 50$.

All the potential differences, $\Delta\mu = (\mu_{\mathrm{c}}^0 - \mu^+)$, $\Delta\mu = (\mu^- - \mu_{\mathrm{c}}^0)$, and $\Delta\mu = (\mu^- - \mu^+)$, given by Eqs. (4.41)-(4.45), are proportional to the current I, implying a linear regime of the transport. The circuit geometries shown in Figs. 4.4(c) and 4.4(d), Figs. 4.4(e) and 4.4(g),

and Figs. 4.4(f) and 4.4(h) are reciprocal pairs with the voltage and the current terminals interchanged. In all these reciprocal circuit pairs, the resistance can be calculated using Eqs. (4.41)-(4.45), and in all the cases the Onsager reciprocity relation $R_1(+m_y) = R_2(-m_y)$ is satisfied, where R_1 and R_2 are the m_y dependent resistances of reciprocal circuits in each pair. In all the cases shown in Figs. 4.4(c)-(h) using Eqs. (4.41)-(4.45), we find that the spin-detection voltage, $\delta\mu = [\Delta\mu(m_y = +1) - \Delta\mu(m_y = -1)]$, is given by

$$\delta\mu = \frac{2I}{\sigma' cW} \sinh(bL)\,\mathrm{csch}(cL). \tag{4.49}$$

From Eq. (4.49), in the limit $L \to 0$, we find that $\delta\mu = \eta Il/\sigma W$, which is the same as that obtained assuming tunneling from a delta function for the FM line contact, and that $\delta\mu$ is, indeed, independent of the conductance of the FM tunnel contact. Only for nonzero length FM contact, does $\delta\mu$ depend on the tunneling conductance of the FM contact. For small tunnel conductance, the Taylor series expansion of $\delta\mu$ for small values of ξ gives $\delta\mu = (\eta Il/\sigma W)[1 - \xi(L^2/3l^2)]$. So, in the limit $\xi \to 0$, we also obtain $\delta\mu = \eta Il/\sigma W$, which is independent of the length of the FM contact. We define the efficiency χ of the tunnel barrier as $\chi = \frac{\delta\mu(\xi)}{\delta\mu(\xi\to 0)}$. Therefore, the spin-detection voltage can be written as $\delta\mu(\xi) = \chi\eta Il/\sigma W$. In the limit $L \to 0$ or $\xi \to 0$, we have $\chi \to 1$. Figure 4.5 shows how χ changes with ξ for different values of $L/l = 10, 20, 50$ and $\eta = 0.5$. We have observed that the dependence of χ on η is negligible in the range of interest of the ξ and L/l values, so the variation of χ with ξ for only $\eta = 0.5$ is shown. From Fig. 4.5 we can see that the spin-detection efficiency of the tunnel contact decreases as the conductivity of the FM contact increases. Also, the spin-detection efficiency of the FM contact decreases as the length of the FM contact increases. So, the ideal contact for spin-detection would be a FM line contact. However, in experiments, the FM contact has a nonzero and often substantial length compared to the transport relaxation length l on the TI surface, and a tunnel barrier is

needed to increase the spin-detection efficiency of the contact, which has been demonstrated in the experiments[28, 29, 30, 31, 32, 33, 34, 35, 36, 37, 38, 39, 40].

4.8 Consideration of the NM contacts

The analysis of the circuit geometries shown in Figs. 4.2 and 4.1 with nonzero size contacts of length L can be performed using the circuit diagrams of Fig. 4.4 and with the help of Eqs. (4.41)-(4.45). However, to calculate the resistances for these circuit geometries, the potential drops due to both the FM and the NM contacts and the potential drop on the TI surface between the contacts must be considered. The potential drop on the TI surface between two contacts can be found by solving Eq. (4.25). From Eq. (4.25). If a constant current I flows on the surface of the TI from point 1 to point 2, the potential drop between the two points, 1 and 2, will be $\Delta\mu = (\mu_1 - \mu_2) = IL_{12}/\sigma W$, where L_{12} is the length between points 1 and 2. The potential drop due to the NM contact can be calculated considering the transport on the TI surface under the NM contact. In chapter 2, we have calculated the modified transport equations on the TI surface due to tunneling from the NM contact. In the 1D case, considering the transport on the TI surface along the x-direction, the modified continuity equation of the TI surface states due to tunneling to and from the NM is given by (Eq. (2.73) in chapter 2)

$$\mathrm{d}_x j_x = 2\gamma N_\mathrm{m}(e^2 N\mu_\mathrm{m} - n), \tag{4.50}$$

where, N_m is the per spin DOS of the NM at the Fermi energy, and μ_m is the charge electrochemical potential in the NM. In the previous chapter, we defined the interface transmission time τ_t by $1/\tau_\mathrm{t} = \gamma N_\mathrm{m}$. The modified diffusion equation for the charge current density on

the TI surface due to tunneling from the NM is given by (Eq. (2.74) in chapter 2)

$$j_x = \frac{1}{(1+4\gamma N_{\rm m}\tau_{\rm p})}\Big[- v_{\rm F}^2\tau_{\rm p}{\rm d}_x n - e^2\gamma N_{\rm m} N v_{\rm F}\tau_{\rm p}\mu_{\rm s,y}\Big], \tag{4.51}$$

where, $\mu_{\rm s,y}$ is the y-component of the spin electrochemical potential in the NM. From Eq. (4.50), we obtain the following modified continuity equation for the charge density on the TI surface under the NM (after renaming $\mu_{\rm m} = \mu_{\rm c}$),

$${\rm d}_x j_x = \frac{2\xi\sigma}{l^2}(\mu_{\rm c} - \mu). \tag{4.52}$$

For $\mu_{\rm s,y} = 0$, from Eq. (4.51), we obtain the following modified diffusion equation for the current density on the surface of the TI under the NM,

$$j_x = -\frac{\sigma}{(1+\xi)}{\rm d}_x\mu. \tag{4.53}$$

In case of the NM, we have $N_\uparrow = N_\downarrow = N_{\rm m}$, and, thus, $N_- = 0$, $N_+ = 2N_{\rm m}$; therefore, $\eta = 0$ and $\xi = 4\gamma N_{\rm m}\tau_{\rm p}$. Equations (4.52) and (4.53) also can be obtained from Eqs. (4.32) and (4.33), respectively, after letting $\eta = 0$ for the NM. So, to calculate the potential drops due to the nonzero length NM contact in Figs. 4.2 and 4.1, Eqs. (4.41)-(4.45) can be used after substituting $\eta = 0$.

The resistive potential drop on the TI surface and the resistive drop due to the NM contacts are independent of magnetization direction of the FM contact, and satisfy the Onsager reciprocity relation independently. Therefore, it is sufficient to consider the potential drop due to the FM contacts, as shown in Fig. 4.4, to check the validity of the Onsager reciprocity relation in multi-terminal measurements as shown in Fig. 4.2 and the two-terminal measurements as shown in Fig. 4.1. Considering the transport on the TI surface

under the nonzero length FM contact, we have shown that the Onsager reciprocity relation is satisfied in spin-detection experiments on the surface of a TI, and how the conductivity of the FM tunnel contact affects the efficiency of the spin-detection. Our conclusions remain valid even after considering detailed calculation of the potential drops due to all the other NM contacts and the drops on the TI surface between the contacts.

To illustrate how to include the potential drops considering the NM contacts of Figs. 4.2 and 4.1, we calculate the two-terminal resistances in the circuit geometries shown in Fig. 4.1 using the results obtained for the transport on the TI surface under the FM and the NM contact and the region in between the contacts. For the circuit geometries shown in Figs. 4.1(a) and 4.1(b), if the same current is flowed on the TI surface between the two contacts, the potential difference on the two contacts will be the sum of the potential drop due to the left contact, the potential drop on the TI surface in between the contacts, and the potential drop due to the right contact. The potential drop due to the left FM contact will be obtained from Eq. (4.41a), the potential drop due to the right NM cotact of Fig. 4.1(a) or the right FM contact of Fig. 4.1(b) will be obtained from Eq. (4.43b), and the potential drop on TI surface in between the contacts will be given by $\Delta\mu = IL_{12}/\sigma W$. For both cases shown in Figs. 4.1(a) and 4.1(b), the two-terminal resistances are the same and given by

$$R_{2t} = \frac{\coth(c_1 L_1)}{\sigma_1' c_1 W} + \frac{I L_{12}}{\sigma W} + \frac{\coth(c_2 L_2)}{\sigma_2' c_2 W}. \tag{4.54}$$

Here, $c_i = \sqrt{2\xi_i(1+\xi_i)}/l$ and $\sigma_i' = \sigma/(1+\xi_i)$, where ξ_i is proportional to the conductance of the tunnel barrier for the i^{th} contact, L_i is the length of the i^{th} contact ($i = 1, 2$), and L_{12} is the length between the contacts. The resistance given by Eq. 4.54 is independent of the magnetization direction of the FM contact of Fig. 4.1(a) or the magnetization direction of either of the FM contacts of Fig. 4.1(b). Hence, R_{2t} satisfies the Onsager reciprocity relation. The calculation for all the circuits shown in Fig. 4.2 can be performed similarly.

4.9 Spin-valve-like geometries and comparison to results in the literature

We also consider spin-valve-like four-terminal measurement geometries with two adjacent FM and two non-adjacent NM contacts on the surface of a diffusive TI. Among all the possible circuit geometries with such contact configurations, two of them being the voltage probes and other two being the current probes, we find four possible contact geometries (two sets of reciprocal circuit pairs), as shown in Figs. 4.6(a)-(d), that manifest the effects of magnetic orientations of both the FMs on the four-terminal resistance. We also note that, if the two FM and the two NM contacts are identical in the devices shown in Figs. 4.6(a)-(d), there will be a rotational symmetry axis normal to the plane of the devices. In case of identical contacts in the devices shown in Figs. 4.6(a)-(b), from the calculations based on Eqs. (4.41)-(4.45) we obtain the relationship, $R_{4t}(+\vec{M}_1, +\vec{M}_2) = R_{4t}(-\vec{M}_1, -\vec{M}_2)$, where this relationship satisfies the symmetry under an 180^0 rotation in the plane of the devices. However, we obtain $R_{4t}(+\vec{M}_1, -\vec{M}_2) \neq R_{4t}(-\vec{M}_1, +\vec{M}_2)$ consistent with the equality being not guaranteed by any symmetry or the Onsager reciprocity relation. Similarly, in case of identical contacts in the circuits shown in Figs. 4.6(c)-(d), the four point resistances obtained from our calculations using Eqs. 4.41-4.45 satisfy $R_{4t}(+\vec{M}_1, +\vec{M}_2) = R_{4t}(-\vec{M}_1, -\vec{M}_2)$, but we also obtain $R_{4t}(+\vec{M}_1, -\vec{M}_2) = R_{4t}(-\vec{M}_1, +\vec{M}_2)$ consistent with the Onsager relation since the two symmetric reciprocal device structures are related by an 180^0 rotation in the plane. Other terminal connection possibilities are shown in Figs. 4.6(e)-(f), which are reciprocal circuit pairs. We find from the calculations using the Eqs. (4.41)-(4.45) that the four-terminal resistances will not depend on either of the magnetizations of the FM contacts. This behavior also has been verified experimentally[30, 40] and was attributed to very short spin relaxation time, which is same as the momentum relaxation time on the surface of the

TI due to spin-momentum helical locking. We could, in principle, extend our calculations to derive the multi-terminal resistance for any number of contacts.

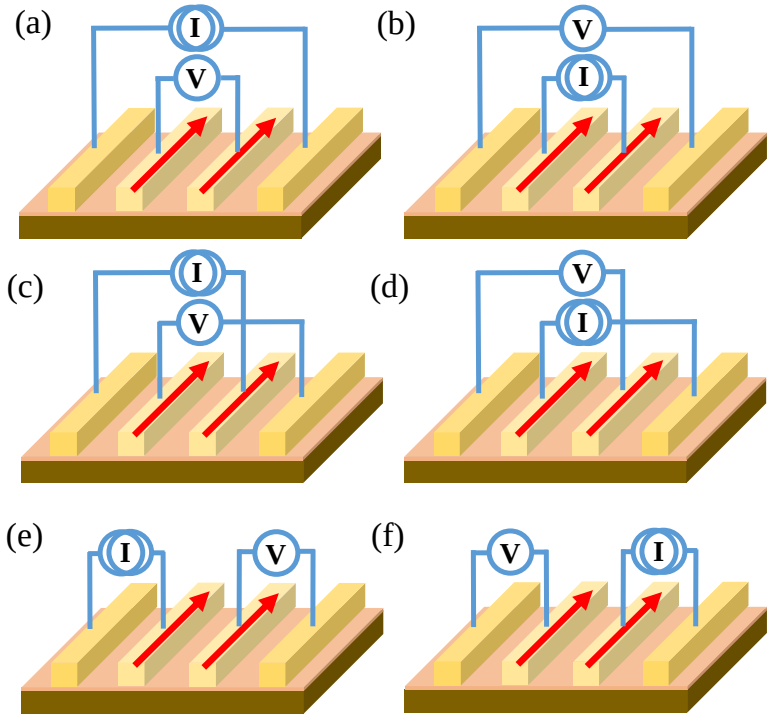

Figure 4.6: Schematics of spin-valve-like measurement geometries with two FM contacts on the TI surface.

Previously, Sayed *et al.*[54] had addressed the issue of Onsager reciprocity in multi-terminal spin-valve-like measurements on the surface of a diffusive TI by deriving the resistance from the solution of a phenomenological one-dimensional diffusion equation in terms of electrochemical potentials of four propagating channels on the surface of the TI, where each channel corresponds to a specific combination of spin orientation (up and down) and direction of propagation (right and left moving), and modeling the FM and NM contacts on the TI surface as line contacts[53, 54]. However, Sayed *et al.*[54] only considered specific cases as those of Figs. 4.2(a)-(b), Fig. 4.1(b) and Figs. 4.6(a)-(b). Our finding matches with the ones obtained by Sayed *et al.*[54] in the case of Figs. 4.2(a)-(b) and Figs. 4.6(a)-(b) with both the FM contacts being considered identical. How-

ever, in the case of two-terminal resistance between the two FM contacts as shown in Fig. 4.1(b), the result of Sayed *et al.*[54] obeyed the Onsager reciprocity relation, i.e., $R_{2t}(+\vec{M}_1, +\vec{M}_2) = R_{2t}(-\vec{M}_1, -\vec{M}_2)$ and $R_{2t}(+\vec{M}_1, -\vec{M}_2) = R_{2t}(-\vec{M}_1, +\vec{M}_2)$, but with the relation $R_{2t}(+\vec{M}_1, +\vec{M}_2) \neq R_{2t}(+\vec{M}_1, -\vec{M}_2)$ instead of R_{2t} being independent of both the magnetization directions of the FM contacts that we have derived in Eq. (4.54). In our model, the TI is purely diffusive and all the spin information is lost after a few momentum scattering events on the TI surface. The loss of information of the spin of electrons (or the information of the magnetizations of the FM contacts) from the two injecting FM contacts is due to the spin-momentum helical locking of the TI surface states, where each momentum scattering also randomizes the spin which is locked to the momentum of the TI surface states. Hence, we find that the two-terminal resistance R_{2t} given in Eq. (4.54) does not depend on either of the FM magnetization directions. It might be the case that the result obtained by Sayed *et al.*[54] is an outcome of their model not being purely diffusive, but only based on a phenomenological diffusion equation of individual spin up and spin down propagation modes, where the spin information is not completely lost even after a significant number of momentum scattering events (although they had to introduce spin-flip scattering artificially to account for that). By contrast, in our theory, the transport equations on the surface of a TI are derived starting from the quantum kinetic equation under diffusive approximations. We believe that the two-terminal resistance between two FM on the surface of a TI in ballistic transport regime will satisfy relations, $R_{2t}(+\vec{M}_1, +\vec{M}_2) = R_{2t}(-\vec{M}_1, -\vec{M}_2)$, $R_{2t}(+\vec{M}_1, -\vec{M}_2) = R_{2t}(-\vec{M}_1, +\vec{M}_2)$, but $R_{2t}(+\vec{M}_1, +\vec{M}_2) \neq R_{2t}(+\vec{M}_1, -\vec{M}_2)$, resembling that of Sayed *et al.*[54].

The two-terminal resistance between a FM and a NM contact on the surface of a ballistic TI was calculated theoretically by Gotte *et al.*[80], but the calculated theoretical result apparently violates the Onsager reciprocity relation. In the ballistic transport regime, the

probability conservation law, i.e., the conservation of charge density, along with the time reversal symmetry, which is achieved by reversing the magnetization direction of the FM, ensures a symmetry of the conductance matrix such that the Onsager reciprocity relation is satisfied in the linear response regime. The calculation for the pure ballistic case to establish the validity of the Onsager reciprocity relation is beyond the scope of this current work. Nevertheless, Semenov *et al.*[81] had understood that the Onsager reciprocity will be satisfied in both the ballistic and the diffusive case, and, hence, they proposed a phenomenological model for the quasi-ballistic mesoscopic regime in which they showed that the reciprocity and even the linear current-voltage relationship around the zero bias are violated. However, a detailed formal derivation based on transmission matrix method similar to that of Buttiker[55], or a calculation based on the quantum kinetic equation, is needed to test such violation of Onsager reciprocity in the mesoscopic regime of transport.

4.10 Summary

In summary, starting from the quantum kinetic equation, we have derived the diffusive transport equations on the surface of a TI coupled to a FM to explain two-terminal and multi-terminal spin detection measurements on the TI surface. In the kinetic equation, the effect of the FM tunnel contact on the transport has been considered by taking into account a self-energy due to tunneling across the TI/FM interface that acts as a source term in the charge transport equations of the carriers on the surface of the TI under the FM tunnel contact. The diffusion equations are solved analytically to calculate the change in chemical potential in the TI and the FM due to the charge current on the TI surface for different measurement geometries. Based on our analytical model, we define a spin-detection voltage as the change in voltage measured on the FM contact on reversing the

FM magnetization direction. We find that the spin-detection voltage depends on the DOS polarization of the FM, the amount of charge current on the TI surface and the conductivity of the tunnel contact. We show that the spin-detection voltage decreases with increasing tunnel conductivity of the tunnel barrier. We also show that the Onsager reciprocity relation is satisfied in both the two-terminal and multi-terminal spin-detection experiments on the surface of a diffusive TI, which resolves conflicting issues in prior literature, as well as explains the results of multi-terminal spin-detection experiments on the surface of a diffusive TI. Our results suggest that the experimental findings of two-terminal resistance that depends on the FM magnetization direction need further interpretation.

Chapter 5

Localization and interaction effects in epitaxial Bi_2Se_3 thin films

Weak anti-localization (WAL), weak localization (WL) and electron-electron interaction (EEI) effects play an important role in the surface and bulk electronic transport of topological insulator (TI) thin films. The two-dimensional (2D) massless Dirac band dispersion of the TI surface states and the distinct massive Dirac-type band structure of the quasi-2D TI bulk states in thin film limit give rise to quantum corrections to the semi-classical Drude conductivity due to quantum mechanical interference and many-body interaction effects. These quantum mechanical corrections to the semi-classical conductivity are quite different for the TI surface states and the TI bulk states, and are also different from that arising in a 2D electron gas (2DEG) due to strong spin-orbit coupling (SOC).

In this chapter, we analyze low-temperature magnetotransport in molecular beam epitaxy (MBE) grown Bi_2Se_3 thin films and interpret the experimental results employing Lu-Shen theory particularly derived for TI system in the 2D limit. The surface and the bulk contributions to the electronic transport are identified based on slopes of logarithmic temperature-dependent conductivities with magnetic fields. The perpendicular field magnetoresistance (MR) is analyzed considering suppression of WAL/WL of the surface/bulk electrons by the applied magnetic field. We propose corresponding theoretical models to explain both the

The results in this chapter have been published as Ref. [87]: R. Dey, A. Roy, T. Pramanik, S. Guchhait, S. Sonde, A. Rai, L. F. Register, and S. K. Banerjee, "Localization and interaction effects of epitaxial Bi_2Se_3 bulk states in two-dimensional limit", *Journal of Applied Physics*, **120**, 164301 (2016), Reproduced with the permission of AIP Publishing. Available: https://doi.org/10.1063/1.4965861. Contribution of the dissertator: The dissertator, Rik Dey, conducted the magnetotransport measurements, analyzed and modeled the magnetotransport data, wrote the manuscript, and is the corresponding author of this publication.

parallel and the tilted field MR as well. The effect of the band structure of TI bulk states is found crucial for an accurate explanation of the magnetotransport in TI thin films.

5.1 Background and Motivation

The surface transport of a diffusive TI has the distinct feature of WAL due to the spin momentum helical locking of the surface states having Dirac band dispersion[4, 5, 24, 25]. The WAL signatures from the surface states of TIs, such as Bi_2Se_3 and Bi_2Te_3, have been widely observed in low temperature transport experiments in a magnetic field[88, 89, 90, 91, 92, 93, 94, 95, 96, 97, 98]. In addition to the surface states, the bulk also contributes to the transport even at low temperatures if the Fermi level lies in the bulk bands[99, 100]. There are significant interests to identify the bulk contribution to the electronic transport properties of TI, since almost all spintronic applications of TI rest on the properties of the surface transport. The bulk transport has been identified by the distinct feature of WL[18, 23], and modeled considering the TI bulk states as 2DEGs with parabolic dispersion and strong SOC[99, 100]. However, because of the massive Dirac-type band dispersion of the TI bulk states, the conductivity correction due to the localization and interactions of the bulk carriers can be quiet different from that for a conventional 2DEG with SOC[18, 23]. Thus, the transport experiments in TI material with significant bulk contribution need re-interpretation in light of the recent theoretical works.

In the following, we interpret the WAL and WL signatures in Bi_2Se_3 thin films with the theory formulated particularly for TI films in the 2D limit[18, 23, 24, 25, 26, 101]. The WAL/WL signatures for the surface/bulk states are best observed in a perpendicularly applied magnetic field that breaks the phase coherence causing a positive/negative MR. Formerly, the observed perpendicular field MR of TI films has been explained[88, 89, 90, 91,

92, 93, 94, 95, 96, 97, 98] by the Hikami-Larkin-Nagaoka (HLN) theory[102] that was originally derived for an electronic system with simple parabolic band dispersion and SOC taken into consideration as impurity scattering. Although, the conventional HLN theory correctly predicts the nature of low field WAL signature resulting from the surface conduction, the theory might not predict the correct WL signature from the bulk states of a TI[18, 23, 102]. We analyze the perpendicular field MR employing the Lu-Shen formula[18, 23] derived for the surface and the bulk states of a TI thin film. The surface and the bulk conductions are singled out from the logarithmic temperature-dependent conductivities that originate from the quantum interference (QI) [WAL/WL from the surface/bulk states] as well as the EEI effects[23]. Here, instead of using the Lee-Ramakrishnan theory for the EEI eefects in a conventional 2DEG[22], we consider the Lu-Shen theory[23] which takes into account the distinct nature of the bulk band dispersion resulting in different value of the slope of logarithmic temperature-dependent conductivity than that obtained in the Lee-Ramakrishnan theory. We further show that the slope varies in a different manner for perpendicular and parallel fields because of different rate (with change of field strength) of phase breaking of electrons in different orientations of fields. We propose corresponding models to explain the parallel and tilted field MR considering that the applied field breaks the phase coherence of electrons for all orientations of field. It is shown that in tilted magnetic fields, the parallel field component introduces an additional contribution in phase breaking of the electrons besides the phase breaking due to the perpendicular component of the magnetic field.

5.2 Material growth

The growth of Bi_2Se_3 thin films has been done in a MBE growth chamber with base pressure 1×10^{-10} mbar and monitored by *in-situ* reflection high energy electron diffrac-

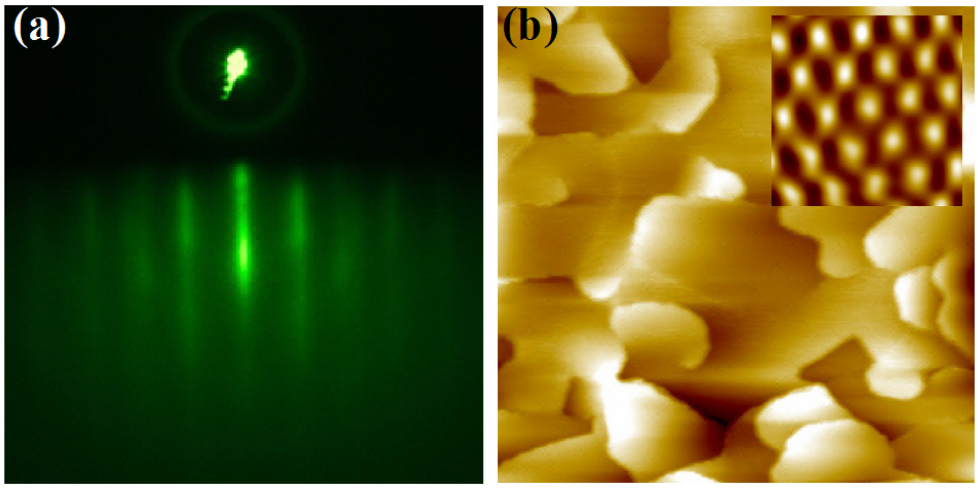

Figure 5.1: Growth and surface characterizations of Bi_2Se_3 thin films: (a) The RHEED pattern of the grown Bi_2Se_3 thin film on Si (111)-(7×7) surface, taken along $[1\bar{1}0]_{Si}$ direction. (b) The 100 × 100 nm^2 STM image of the film shows smooth surface morphology (inset: 20 × 20 nm^2 FFT filtered image showing hexagonal arrangements of the atoms).

tion (RHEED) operated at 13 kV. Bi_2Se_3 films are gown on a P-doped Si(111) (oriented within $\pm 0.5^0$) substrates with resistivity $\sim 1-20$ Ω-cm. The substrates are prepared by the standard heating and flashing technique prior to growth[94]. Bi and Se fluxes, generated by effusion cells, are co-deposited onto the Si substrates at an elevated substrate temperature of 190^0 C[103]. The Se_2/Bi flux ratio is kept at about 20 and the pressure inside the chamber never exceeds 2×10^{-9} mbar during growth. The growth rate is about 0.1 nm/min. After the growth the samples are annealed at the growth temperature for an additional 10 minutes. Figure 5.1(a) shows sharp streaky RHEED pattern of the grown Bi_2Se_3 film on a reconstructed Si(111) − (7 × 7) surface taken along $[1\bar{1}0]_{Si}$ direction, which indicates atomically flat surface morphology.

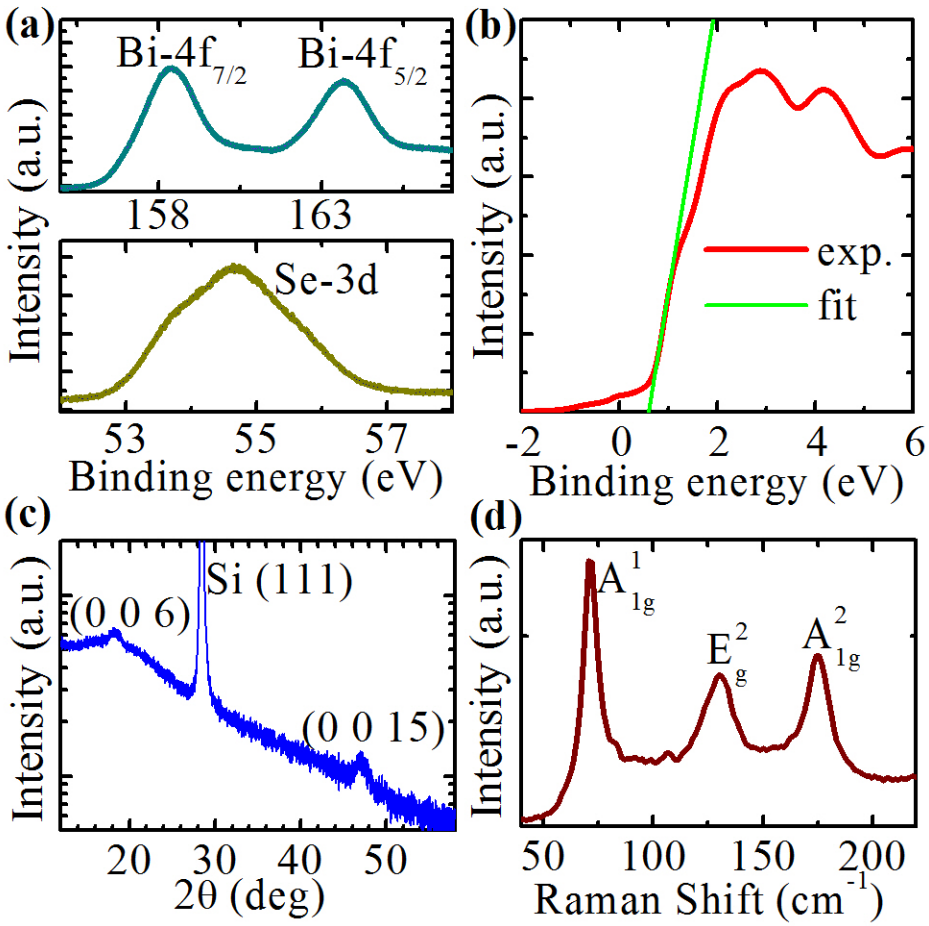

Figure 5.2: Material characterizations of the Bi_2Se_3 thin films: (a) XPS spectra of the grown film showing Bi 4f and Se 3d peaks. (b) UPS spectrum of the film, solid line showing fit to the rising edge. (c) XRD study of the film showing epitaxial growth along the c-axis. (d) Raman spectrum of the film.

5.3 Material characterizations

The post-growth examinations of the surface is done by *in-situ* scanning tunneling microscopy (STM) at room temperature in constant current mode. The 100 × 100 nm^2 STM image, in Fig. 5.1(b), confirms that the surface is smooth and atomically flat. The fast Fourier transform (FFT) filtered STM image of 20 × 20 nm^2 (inset of Fig. 5.1(b)) clearly indicates the hexagonal arrangements of the surface atoms. Further material character-

izations of these thin films are done by *in-situ* x-ray photoelectron spectra (XPS) with monochromatic Al-Kα, ultraviolet photoelectron spectroscopy (UPS) with He-1α gas, and *ex-situ* x-ray diffraction (XRD) with monochromatic Cu-Kα, Raman spectroscopy with 532 nm diode laser. Figure 5.2(a) shows the XPS of the grown film. The two peaks for Bi in Fig. 5.2(a) correspond to Bi $4f_{7/2}$ and Bi $4f_{5/2}$ with binding energies 158.4 eV and 163.7eV, respectively. The Se 3d peak, shown in the same figure, is at energy 54.68 eV. The Bi 4f peaks show blue-shift and the Se 3d peak shows red-shift with respect to the corresponding elemental values[104]. The opposite shifts indicate Bi-Se bond formation and charge transfer from Bi to Se. Figure 5.2(b) shows the valence band spectrum of the film obtained by UPS. The clear hump at binding energy of $\sim$ 2.1 eV corresponding to Bi 6p anti-bonding orbitals[105], while a small hump at zero binding energy corresponds to electron occupation at the Fermi level. From the intersection of the background and the linear fit to the rising edge, the valence band maximum is obtained to be 0.6 eV below the Fermi level. The band gap of Bi_2Se_3 is about $0.3 - 0.35$ eV[4, 5], which implies that the Fermi level E_F lies in the conduction band (CB). Figure 5.2(c) shows (006) and (0015) peaks observed in the XRD spectrum of the epitaxial Bi_2Se_3 film on Si(111). The presence of only (003n) family indicates that the film grows along the c-axis of Bi_2Se_3 following the symmetry of the underlying substrate[106]. The Raman spectrum of the film is shown in Fig. 5.2(d). The Raman spectrum shows peaks centered at about 71 cm^{-1}, 131 cm^{-1} and 175 cm^{-1} corresponding to A^1_{1g}, E^2_g and A^2_{1g}, respectively[107].

5.4 Transport measurements

The transport measurements are performed by standard Van der Pauw method with indium dot contacts at the four corners of the large area rectangular sample in a physical

property measurement system capable of taking magnetic fields up to 9 T and temperatures down to 2 K.

5.4.1 Resistance vs temperature and Hall measurement

The temperature dependence of the resistance (R) of a 5 nm thick sample in absence of any magnetic field is shown in Fig. 5.3(a). The resistance starts to increase at about 150 K and the rapid increase of resistance with decreasing temperature due to freezing of carriers from the Si substrate ceases for temperatures about 40 K. Below 40 K, only the carriers from the Bi_2Se_3 film contribute to the resistance that shows a metallic behavior up to 20 K, and from 20 K down to 2 K, there is an increase in resistance with decreasing temperature showing the presence of insulating ground state. The insulating behavior could be due to localization as well as interaction effects[22, 23], which will be addressed in the following sections. Figure 5.3(b) shows the Hall resistance (R_{Hall}) at 2 K with the magnetic field B perpendicular to the sample surface. The Hall slope is negative indicating the carriers are electrons.

5.4.2 Estimation of carrier concentration and mobility

The total carrier concentration per unit area n_{tot} can be obtained from the Hall resistance $R_{Hall} = -\frac{B}{e}\frac{1}{n_{tot}}$. The calculated Hall coefficient $R_H = |\frac{R_{Hall}}{B}| = (\frac{1}{en_{tot}}) = 2.3$ kΩ/T from Fig. 5.3(b), and estimated $n_{tot} = 3 \times 10^{13}/\text{cm}^2$. The Hall mobility μ is calculated from the resistance R and the carrier concentration n_{tot}. From the resistance R at 2 K, the sheet conductance is calculated to be $\sigma = 1.3 \times 10^{-4}\ \Omega^{-1}$. Using the formula $\sigma = ne\mu$, the obtained mobility $\mu = 27\ \text{cm}^2/\text{V-s}$ at 2 K.

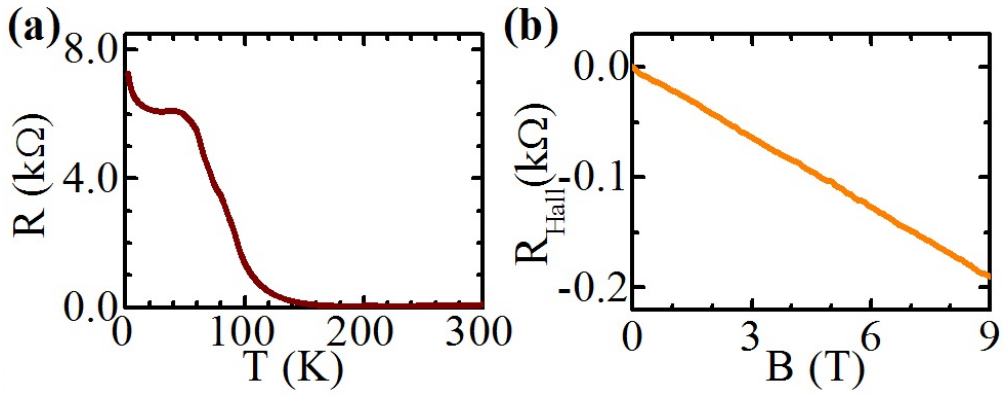

Figure 5.3: Resistance vs temperature and Hall measurement on Bi_2Se_3 thin film: (a) Resistance (R) with temperature (T) in absence of magnetic field. (b) Hall resistance (R_{Hall}) with perpendicular field (B) at $T = 2$ K.

The estimated electron concentration of about $3\times10^{13}/\text{cm}^2$ indicates that both the surface and the bulk states are occupied. However, the Hall resistance is linear with magnetic field, which is possible if the mobilities of the surface electrons and the bulk electrons are similar or mobility of one of the surface/bulk electrons is much lower than the other. The UPS and the Hall measurements both show that the grown films are intrinsically n-type. We obtain later that, in our thin film two surface states and two bulk channels are occupied. So, from the total carrier concentration, the value of k_F is estimated as $k_F = \sqrt{\pi n_{tot}} = 0.97$ nm^{-1}. The sheet conductivity is also given by $\sigma = (\frac{e^2}{h})k_F l_e$, where e is the electronic charge, h is the Planck constant, k_F is the Fermi wave vector and l_e is the mean free path of electrons. From $\sigma = 1.3 \times 10^{-4}\ \Omega^{-1}$, the calculated $k_F l_e = 3.33 > 1$, indicating that the transport in our film can be modeled by quantum diffusive transport theory[23, 24]. From the estimated k_F and using $k_F l_e = 3.33$, the mean free path is calculated to be $l_e = 3.43$ nm.

5.4.3 Magnetoresistance at low temperatures

The MR from the same sample, at different temperatures from $2-20$ K with a magnetic field perpendicular to the sample surface, is shown in Fig. 5.4(a). We have calculated in

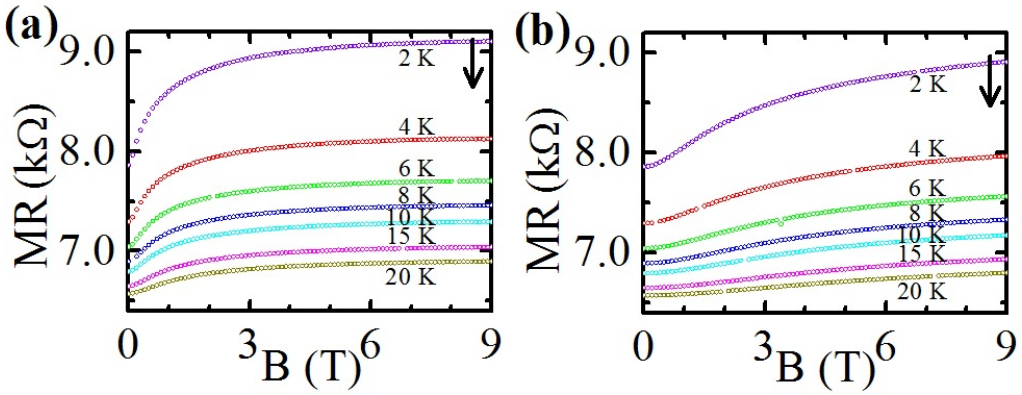

Figure 5.4: Magnetoresistance measurement on Bi_2Se_3 thin film: (a) Magnetoresistance at different temperatures with perpendicular field B. (b) Magnetoresistance at different temperatures with parallel field B.

the last section that all the transport measurements satisfy conditions of quantum diffusive transport regime ($\sigma > e^2/h$). The perpendicular field MR increases with increasing field at all temperatures. The positive MR is an indication of the WAL of the surface states; however, the WL of the bulk electrons cannot be ruled out[18]. In our case, the bulk states fall in quasi-2D limit, because the nominally bulk states will form the bulk sub-bands due to finite thickness along the surface normal direction[19, 20, 21]. Thus, we analyze the WAL/WL phenomenon from the surface/bulk states by fitting our experimental data with the theory of 2D transport in TI thin film in the upcoming sections. Also it is interesting to note that, at all magnetic fields upto 9 T, the resistance decreases with increasing temperature indicating an insulating behavior that can be explained only if the EEI effect is considered[23].

The condition for EEI effect being dominant at low temperatures requires that the thermal diffusion length l_T should be larger than the mean free path l_e [23], where, $l_T = \sqrt{D\hbar/(2\pi k_B T)}$, $\hbar$ is the reduced Planck constant, k_B is the Boltzmann constant and D is the diffusion coefficient. The diffusion coefficient is calculated from the sheet conductivity using the relation $\sigma = e^2 N_F D$, where N_F is the density of state at the Fermi level and given by $N_F = k_F/(2\pi\hbar v_F)$, v_F being the Fermi velocity. Assuming $v_F = 6.2 \times 10^5$ m/s for

Bi_2Se_3[4, 5], we calculate l_T. As we analyze our temperature dependent conductivity in 2−10 K range, and $T \propto l_T^{-2}$, the minimum $l_T = 16.1$ nm at $T = 10$ K. So, in our case $l_T > l_e$ is true for all temperatures below 10 K, which validates the application of Lu-Shen theory[23] to the analysis of the temperature dependence of the conductivity due to both QI and EEI.

Figure 5.4(b) shows positive MR at different temperatures with magnetic field parallel to the sample surface. The parallel field also can destroy the interference of electrons giving rise to an MR similar to what has been addressed by Altshuler and Aronov in a metal[108]. The surface and bulk electrons move in a quasi-2D geometry because of the finite penetration depth of the surface states and the finite thickness of the bulk states. The parallel field acts normally to the quasi-2D trajectories of the electrons giving an Aharonov-Bohm phase to the electrons, and destroys the quantum interference effect. We elaborate on the parallel field MR by fitting our data in later section. Similar to the case of perpendicular magnetic fields, the resistance shows insulating behavior at all applied parallel fields. We explain the insulating behavior and the positive MR considering the interaction and the interference effects of the surface as well as the bulk carriers.

5.5 Analysis of logarithmic temperature-dependent magnetoconductivity at low temperatures

5.5.1 Temperature dependence of conductivity at perpendicular magnetic fields

Figure 5.5(a) shows the linear dependence of conductivity σ with logarithmic temperature $\ln T$ at different perpendicular fields. At low temperature, σ decreases with decreasing temperature showing presence of an insulating ground state. The slope of the curves, $f = (\pi h/e^2)[d\sigma/d(\ln T)]$ obtained by curve fitting in the $2-10$ K range, is plotted with magnetic

field B in Fig. 5.5(b). Both the QI and the EEI effect produce a temperature dependence of the conductivity $\sigma(T) = \kappa(e^2/\pi h)\ln(T/T_0)$, where T_0 is the characteristic temperature associated with interference or interaction effect[23]. The slope κ is determined by the origin of the effect, and κ is a field dependent quantity because magnetic field destroys the interference of electrons. The slope due to QI and EEI effects adds together to give the desired value of the slope,

$$\kappa(B) = \kappa_{qi}(B) + \kappa_{eei}(B), \tag{5.1}$$

where, $\kappa_{qi}(B)$ and $\kappa_{eei}(B)$ are the contributions to the slope due to QI and EEI effects, respectively. Experimentally, we obtain $f(B = 0\ \text{T}) = 1.01$ and $f(B = 9\ \text{T}) = 1.38$, as shown in Fig. 5.5(b). The slope saturates after $B = 6$ T, which indicates that the quantum interference effect is destroyed above that field.

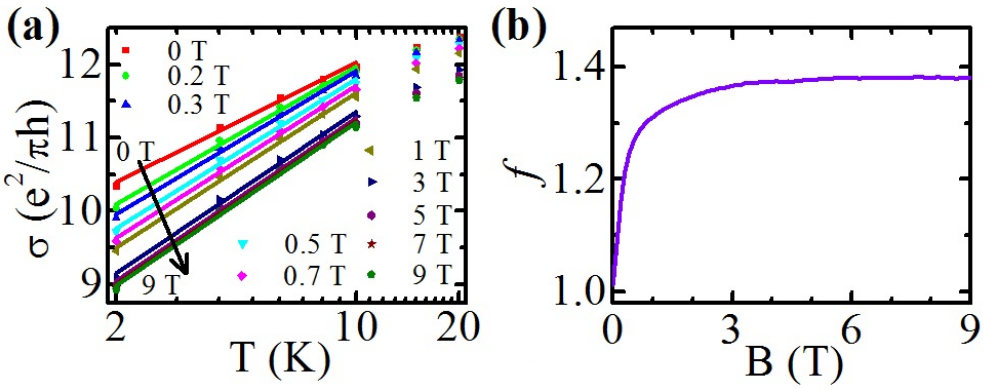

Figure 5.5: Perpendicular field magnetoconductivity with temperature: (a) Logarithmic dependence of magnetoconductivity σ with temperature T at different perpendicular fields, solid line showing $\ln T$ fit. (b) The slope f, calculated from (a), as a function of perpendicular magnetic field B.

In previous magnetotransport experiments of TI[90, 93, 94, 95, 96, 98, 109], the slopes obtained have been analyzed with the Lee-Ramakrishnan theory[22] that was originally derived for 2DEG system with parabolic band dispersion. To obtain a more accurate description of the complex many body effects associated with the TI system, here we employ the theory of Lu-Shen[23] derived particularly for TI thin films in 2D limit. The value of κ_{qi} from the

interference effects (WAL, WL) is given by

$$\begin{aligned} \kappa_{qi}(B=0) &= \alpha p, \\ \kappa_{qi}(B \gg B_\phi) &= 0, \end{aligned} \tag{5.2}$$

where, the parameter p is related to the dependence of phase coherence length l_ϕ to temperature T ($l_\phi \propto T^{-p/2}$), and for a 2D system $p = 1$ if EEI mechanism is responsible for decoherence[23], which is true in our case and the consistency of our assumption is verified later after analyzing the perpendicular field MR data. Here, B_ϕ is the characteristic field for destruction of the interference effect ($B_\phi \propto l_\phi^{-2}$). The value of α, which depends on the nature of WAL or WL, is given by[23]

$$\begin{aligned} \alpha_{WL} &= \frac{r^2(1+r^2)}{(1+3r^2)}, \\ \alpha_{WAL} &= -\frac{(1-r^2)^2}{2(1+3r^2)(1+r^2)}. \end{aligned} \tag{5.3}$$

Here, r is a parameter which depends on the position of the Fermi level in the surface states/bulk bands and the details of the band structure[18, 23, 24], and will be different for the surface and the bulk states. However, the value of $r = 0$ describes the massless limit giving $\alpha_{WL} = 0$ and $\alpha_{WAL} = -1/2$, and $r = 1$ corresponds to the massive limit giving $\alpha_{WL} = 1/2$ and $\alpha_{WAL} = 0$. In a thin film, there might be a small gap opening in the surface states about what would otherwise be the Dirac point[19, 20, 21]. In our case, the Fermi level is located well inside the bulk CB and the gap opening in the surface states will be significantly smaller compared to the Fermi level. So, for the surface states we assume $r = 0$ and take $\alpha_s = -1/2$. The parameter r for the bulk states, that depends on the position of the Fermi level with respect to the CB minimum and the bulk band structure, will be

determined from the experiment. The slope κ_{eei} from the interaction effect will be[23]

$$\begin{aligned}\kappa_{eei}(B=0) &= 1-(\eta_\Lambda+\eta_\Gamma)F,\\ \kappa_{eei}(B\gg B_\phi) &= 1-\eta_\Lambda F.\end{aligned} \tag{5.4}$$

The parameter η_Λ, η_Γ are related to the diffusion and Cooperon channels, respectively, and F is the Coulomb screening strength. The values of η_Λ, η_Γ and F, which are always positive and depend on r of the surface/bulk states, are given by[23]

$$\begin{aligned}\eta_\Lambda &= \frac{(1+r^2)}{2},\\ \eta_\Gamma &= \frac{(1-r^2)^4}{4(1+3r^2)(1+r^2)(1-5r^2)},\\ F &= \frac{2}{\pi}\frac{\arctan\sqrt{\frac{1-x_0^2(1-r^2)}{x_0^2(1-r^2)}}}{\sqrt{1-x_0^2(1-r^2)}},\end{aligned} \tag{5.5}$$

with $x_0 = 4\epsilon_0\epsilon_r h v_F/e^2$, ϵ_0 is the permittivity of the free space, ϵ_r is the relative permittivity of the material and v_F is the Fermi velocity. As we have assumed the massless limit $r = 0$ for the surface states, we take $\eta_\Lambda = 1/2$, $\eta_\Gamma = 1/4$ for the surface states. The values of η_Λ, η_Γ, F for the bulk states are determined from the experiment as discussed next.

5.5.2 Identification of bulk transport

We notice that the slopes of the logarithmic temperature-dependent conductivities at different magnetic fields cannot be explained if we consider only the surface state conduction. If we consider only one surface state is conducting, which was assumed to be the case in previous studies[88, 89, 93], we will get $\kappa_{qi}(B=0) = -1/2$ and $\kappa_{eei}(B=0) = 1-3F/4$ giving a total slope $\kappa(B=0) = 1/2-3F/4$, which is less than $1/2$. At higher fields, we will get that $\kappa_{qi}(B\gg B_\phi) = 0$ and $\kappa_{eei}(B\gg B_\phi) = 1-F/2$ giving a total slope $\kappa(B\gg B_\phi) = 1-F/2$,

which is less than 1. But, the experimental value of the slope, in our case, is always greater than 1, which cannot be explained by assuming one surface state conduction. Even if we consider that both the surfaces are conducting, we still get $\kappa(B=0) = 2(1/2 - 3F/4) = 1 - 3F/2 < 1$ and $\kappa(B \gg B_\phi) = 2(1 - F/2) = 2 - F$, which is inconsistent with the experimental values $f(B = 0\ \mathrm{T}) = 1.01$ and $f(B = 9\ \mathrm{T}) = 1.38$. So, the bulk conduction has to be taken into account to explain our experimental result. However, we rule out the possibility of one single phase coherent channel due to surface-bulk coupling. In case of surface-bulk coupling[90, 91, 92, 94, 109, 110, 111, 112, 113, 114, 115, 116], α in Eq. (5.2) will vary from $-1/2$ to -1 depending on the strength of the coupling giving the value of $\kappa_{qi}(B=0)$ to be in the range $-1/2$ to -1, while $\kappa_{eei}(B=0)$ will be less than 1 for any value of η_Λ, η_Γ or F in Eq. (5.4). So, the total slope given by Eq. (5.1) remains less than $+1/2$ at zero field for any strength of coupling. At higher fields, $\kappa_{qi}(B \gg B_\phi)$ will be zero and $\kappa_{eei}(B \gg B_\phi)$ will be less than 1 for any coupling strength giving the total slope being less than 1, which does not explain the experimental results.

Next, we consider decoupled bulk and surface states contributing to the conduction separately. We take r for the bulk states and x_0 as two unknown parameters which we determine by equating the experimental values of slope to the theoretical values using Eqs. (5.1)−(5.5) at zero field and higher fields. We consider the massless limit for the surface states, which gives the slope κ_s for one surface state,

$$\begin{aligned} &\kappa_s(B=0) = -1/2 + 1 - 3F_s(x_0)/4 = 1/2 - 3F_s(x_0)/4, \\ &\kappa_s(B \gg B_\phi) = 1 - F_s(x_0)/2; \end{aligned} \tag{5.6}$$

where $F_s(x_0)$ is the Coulomb screening strength for the surface electrons is a function of

$x_0 = 4\epsilon_0\epsilon_r h v_F/e^2$, and is given by

$$F_s = \frac{2}{\pi}\frac{\arctan\sqrt{\frac{1-x_0^2}{x_0^2}}}{\sqrt{1-x_0^2}}, \tag{5.7}$$

For the bulk state, we the Fermi level is inside the bulk band, and the exact bulk band structure is also not known in our thin film. So, we take the parameter r, defined in the main text, as a unknown parameter for the bulk state. The value of the slope κ_b for one bulk state will be

$$\begin{aligned}
&\kappa_b(B=0) = \alpha_{WL} + 1 - (\eta_{\Lambda,b}(r) + \eta_{\Gamma,b}(r))F_b(x_0, r), \\
&\kappa_b(B \gg B_\phi) = 1 - \eta_{\Lambda,b}(r)F_b(x_0, r),
\end{aligned} \tag{5.8}$$

where $\eta_{\Lambda,b}(r)$ and $\eta_{\Gamma,b}(r)$ are parameters for the bulk states and are function of r given by Eq. (5.5). Here, $F_b(x_0, r)$ is the Coulomb screening strength for the bulk electrons, and is a function of both r and x_0 given by Eq. (5.5).

The obtained value of the slope can be satisfactorily explained only if we take into account the effect from two surface channels (top and bottom surfaces) and two bulk channels (two degenerate lowest sub-bands of the bulk) together. We consider that minimally two lowest bulk sub-bands (decoupled) are also conducting in the thin film with the two decoupled surface states. Then, we equate the theoretical value of the slope to the experimentally observed value at zero field and higher fields by,

$$\begin{aligned}
&\kappa_s(B=0) + \kappa_b(B=0) = 1.01, \\
&\kappa_s(B \gg B_\phi) + \kappa_b(B \gg B_\phi) = 1.38.
\end{aligned} \tag{5.9}$$

By solving two coupled equations given above with two unknowns r and x_0, we obtain $r = 0.99$ and $x_0 = 0.66$. We obtain $r = 0.99$ for the bulk states denoting the large mass limit

for the bulk sub-bands, which gives $\alpha_b = 0.49$ corresponding to WL of the bulk states[23]. The value of $r \approx 1$ denotes that we can assume the massive limit for the bulk states with $\alpha_b = 1/2$ corresponding to WL of the bulk electrons. From x_0, we obtain $\epsilon_r = 1.79$ for the material, in agreement with previous reports[23]. We identify that quantum corrections from WAL of the two surface channels and WL of the two bulk channels are contributing separately to the transport of the thin film.

5.5.3 Temperature dependence of conductivity at parallel magnetic fields

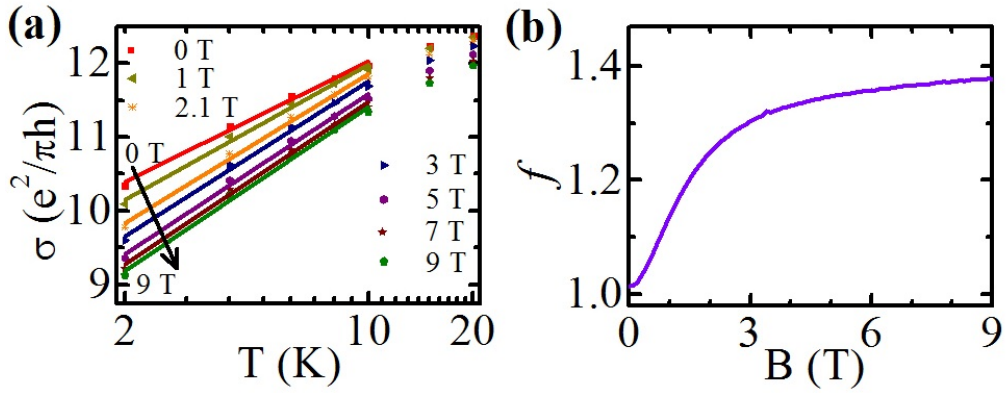

Figure 5.6: Parallel field magnetoconductivity with temperature: (a) Logarithmic dependence of magnetoconductivity σ with temperature T at different parallel fields, solid line showing $\ln T$ fit. (b) The slope f, calculated from (a), as a function of parallel magnetic field B.

Figure 5.6(a) shows the temperature dependence of σ for parallel fields. Similar to Fig. 5.5(a), the conductivity has a linear dependence with $\ln T$ for all applied fields. However, the slope f, calculated from Fig. 5.6(a) and shown in Fig. 5.6(b), has different field dependence for parallel fields compared to that for perpendicular fields. The slope f in Fig. 5.6(b) starts from 1.01 and approaches to the value of 1.38 at higher fields slowly compared to that of Fig. 5.5(b). The high field value of the slope f represents the regime where the magnetic field breaks the electron interference effect (i.e. $B \gg B_\phi$). The parallel magnetic field also breaks

the interference effect of the surface and the bulk electrons due to the finite nonzero spread of electronic wave-functions along the surface normal direction[25, 108]. The electrons are moving in a quasi-2D geometry where their trajectories are not solely in a 2D plane. The magnetic flux enclosed by time-reversed closed trajectory of electrons gives Aharonov-Bohm phase destroying the interference effect of electrons. The finite area of a closed time-reversed trajectory of an electron is much larger in the plane of the surface compared to the area in the plane normal to the surface. For a given field the flux will be larger when the field is normal to the surface compared to the flux when the field lies along the surface, which explains why f changes with field slowly for parallel fields compared to that for perpendicular fields as evident from Fig. 5.5(b) and 5.6(b). The difference of the field dependence of f for perpendicular and parallel fields is also due to different functional dependence of the perpendicular and parallel field MR, which we discuss next.

5.6 Analysis of perpendicular field magnetoresistance

5.6.1 A brief literature review

The perpendicular field breaks the quantum interference of the electrons, and thus, destroys the WAL/WL effect giving rise to an MR. In literature[88, 89, 90, 91, 92, 93, 94, 95, 96, 97, 98, 109, 110, 111], the MR in TI films previously was fitted with the reduced HLN equation[102]

$$\Delta\sigma_{\perp}(B) = \frac{\alpha e^2}{\pi h}\left[\psi\left(\frac{1}{2}+\frac{B_{\phi}}{B}\right) - \ln\left(\frac{B_{\phi}}{B}\right)\right] \tag{5.10}$$

where, $\Delta\sigma_{\perp}(B)$ is the change of magnetoconductivity for perpendicular field, $\psi(x)$ is the digamma function, and the parameter α is $-1/2$ or $+1$ for WAL or WL, respectively, for a single conduction channel. The HLN equation was derived for a 2DEG system with parabolic

band dispersion considering SOC as impurity scattering[102], and the value of α equals $-1/2$ or $+1$ denotes the strength of such SOC scattering classifying the system in simpletic or orthogonal cases[102], respectively. As the surface states of a TI have linear Dirac type band dispersion with spin-momentum locking, it is improper to use directly Eq. (5.10) on the ground of HLN theory. However, the theoretical calculation[18, 23, 24, 25, 115] of quantum correction to conductivity due to interference effects of the electrons from a single surface state of a TI leads to the same equation as Eq. (5.10) with $\alpha = -1/2$ from each surface state. The value of α being $-1/2$ for one surface state comes from a single spin-triplet Cooperon with vanishing Cooperon gap giving rise to WAL[18, 23, 24, 115]. The Cooperon gap of the spin-triplet Cooperon is very small if the Fermi level lies well above the Dirac point in the surface state with small gap opening. In literature[88, 89, 90, 91, 92, 93, 94, 95, 96, 97, 98, 109, 110, 111], Eq. (5.10) was used for fitting the low field MR data in TIs, and the obtained the value of α ranged from $-1/2$ to -1. The value $\alpha = -1$ have been attributed to two surface channels contributing separately to the transport and $\alpha = -1/2$ is for effectively one channel due to coupling of the two surface states presumably via bulk[90, 91, 92, 94, 109, 110, 111, 112, 113, 114, 115, 116]. It also was shown theoretically that if bulk contribution is present along with the surfaces, Eq. (5.10) could give ubiquitous result for the fitting parameters α and B_ϕ depending on the fitting range[18]. Alternatively, to identify the bulk contribution in TI films, the full HLN formula[102] was considered for the bulk channel[99, 100],

$$\begin{aligned}\Delta\sigma_\perp(B) = &-\frac{e^2}{2\pi h}\left[\psi\left(\frac{1}{2}+\frac{B_\phi}{B}\right)-\ln\left(\frac{B_\phi}{B}\right)\right] \\ &+\frac{3e^2}{2\pi h}\left[\psi\left(\frac{1}{2}+\frac{B_\phi+B_{SO}}{B}\right)-\ln\left(\frac{B_\phi+B_{SO}}{B}\right)\right].\end{aligned} \tag{5.11}$$

Here, B_{SO} is the characteristic field strength for SOC scattering, i.e. $B_{SO} \approx 0$ for weak SOC scattering, and $B_{SO} \to \infty$ for strong SOC scattering. Equation (5.10) can be viewed

as a special case of Eq. (5.11), where $\alpha = -1/2$ and $\alpha = +1$ in Eq. (5.10) correspond to $B_{SO} \to \infty$ and $B_{SO} \approx 0$ in Eq. (5.11), respectively. Equation (5.11) was derived for a 2DEG system with simple parabolic band dispersion and considering SOC scattering as perturbation, but in the bulk of a TI the spin-momentum locking term cannot be treated as perturbation as the energy associated with this term is comparable to the parabolic mass term[4, 5]. Although, Eq. (5.11) can be used for bulk transport of a 3D TI film with Fermi level in the bulk lying near the band edge forming a small Fermi surface, since Garate and Glazman [115] have obtained the same form for the perpendicular field magnetoconductance as Eq. (5.11) for 3D bulk transport considering the full bulk band structure in the original calculation without treating the SOC as perturbation. For the bulk of a 3D TI film with small Fermi surface, the first term in Eq. (5.11) is due to one gapless spin-triplet Cooperon and the second term in Eq. (5.11) is due to three spin-singlet soft Cooperons with very small gap[115]. In a TI thin film, the 3D bulk bands will form 2D sub-bands due to finite thickness along the surface normal direction[19, 20, 21], and Eq. (5.11) could no longer be valid for describing the bulk transport of a TI thin film in the 2D limit; because neither can we use Eq. (5.11) on the ground of HLN theory as HLN theory consider SOC as perturbation, nor can we take the model on the ground of the theory of 3D bulk transport in TIs as the quantization of 3D bulk band into 2D sub-bands in TI thin films was not considered by Garate and Glazman[115].

5.6.2 Explanation of perpendicular field magnetoresistance with the theory derived for TI

The change in conductivity, $\Delta\sigma = \sigma(B) - \sigma(0)$, with magnetic field B applied perpendicular to the sample surface is shown in Fig. 5.7(a) at different temperatures (2 - 20 K). The theory of bulk transport of a 2D TI in a perpendicular magnetic field is formulated

by Lu-Shen[18, 24]. It is shown that the magnetoconductivity from a the bulk states will be given by Eq. (5.10) with α ranging from $-1/2$ to $+1/2$ depending on the position of the Fermi level and the details of the band dispersion. So the conductivity correction from the bulk states could vary from WAL to WL resulting from the one gapless triplet or one gapless singlet Cooperon mode, respectively[18, 24]. Following Lu-Shen and considering two surfaces (s1,s2) and two degenerate bulk sub-bands (b1,b2) conductions in our thin film, the change in magnetoconductivity will be given by

$$\Delta\sigma_{\perp}(B) = \frac{e^2}{\pi h} \sum_{\substack{i=s1,s2,\\ b1,b2}} \alpha_i \left[\psi\left(\frac{1}{2} + \frac{B_{\phi,i}}{B}\right) - \ln\left(\frac{B_{\phi,i}}{B}\right)\right]. \tag{5.12}$$

Here, we only consider the change of magnetoconductivity due to the destruction of interference effect in an applied field and neglect the many body interaction effects, as the change of conductivity due to EEI effect will be almost an order of magnitude lower than that due to QI effects as estimated[23]. The form of Eq. (5.12) remains the same even if the Zeeman effect or the Hexagonal warping effect of the bands are considered, and there will be inconsequential change in the values of α_is[18, 23, 25, 117]. However, in our case $\alpha_{s1} = \alpha_{s2} \approx -1/2$ for the surface states, as the Fermi level lies in the CB well above the Dirac point even if there is a gap opening in the surface states at the Dirac point[19, 20, 21]. From the fitting of the slope of logarithmic temperature-dependent conductivities at different magnetic fields, we has obtained that $\alpha_{b1} = \alpha_{b2} \approx +1/2$ for the massive bulk states. Further, we do not consider any coupling between different surface channels or bulk channels or surface-bulk.

Now, grouping together the contributions from only the two surface or only the two bulk channels, the change of magnetoconductivity in perpendicular field is obtained by adding

quantum corrections from these (grouped together) two channels as[24]

$$\begin{aligned}\Delta\sigma_{\perp}(B) = \alpha_{\pm\frac{1}{2}}\frac{e^2}{\pi h}\left[\psi\left(\frac{1}{2}+\frac{B_{\phi,1}}{B}\right)-\ln\left(\frac{B_{\phi,1}}{B}\right)\right] \\ + \alpha_{\pm\frac{1}{2}}\frac{e^2}{\pi h}\left[\psi\left(\frac{1}{2}+\frac{B_{\phi,2}}{B}\right)-\ln\left(\frac{B_{\phi,2}}{B}\right)\right].\end{aligned} \tag{5.13}$$

The value of $\alpha_{\pm\frac{1}{2}} = \pm\frac{1}{2}$ is fixed for surface or the bulk channels. Now grouping the logarithm term together and the digamma term together, we obtain

$$\begin{aligned}\Delta\sigma_{\perp}(B) &= \alpha_{\pm\frac{1}{2}}\frac{e^2}{\pi h}\left[\psi\left(\frac{1}{2}+\frac{B_{\phi,1}}{B}\right)+\psi\left(\frac{1}{2}+\frac{B_{\phi,2}}{B}\right)-\ln\left(\frac{B_{\phi,1}}{B}\right)-\ln\left(\frac{B_{\phi,2}}{B}\right)\right] \\ &= \alpha_{\pm\frac{1}{2}}\frac{e^2}{\pi h}\left[\psi\left(\frac{1}{2}+\frac{B_{\phi,1}}{B}\right)+\psi\left(\frac{1}{2}+\frac{B_{\phi,2}}{B}\right)-2\ln\left(\frac{\sqrt{B_{\phi,1}B_{\phi,2}}}{B}\right)\right] \\ &\approx 2\alpha_{\pm\frac{1}{2}}\frac{e^2}{\pi h}\left[\psi\left(\frac{1}{2}+\frac{\sqrt{B_{\phi,1}B_{\phi,2}}}{B}\right)-\ln\left(\frac{\sqrt{B_{\phi,1}B_{\phi,2}}}{B}\right)\right].\end{aligned} \tag{5.14}$$

In the last step, we use the approximation[111, 114] that, $\psi(1/2+x_1)+\psi(1/2+x_2) \approx 2\psi(1/2+\sqrt{x_1x_2})$ for $x_1, x_2 < 1$, while the logarithmic part is kept exact. The digamma functions only differs from the above approximation in low fields $B < B_{\phi,1}, B_{\phi,2}$, and the logarithmic functions (they are exact, no approximation) are dominating in the low field limits. In the high field limits, i.e., $B > B_{\phi,1}, B_{\phi,2}$, the digamma functions are $\psi(1/2 + B_{\phi,1}/B) \approx \psi(1/2+B_{\phi,2}/B) \approx \psi(1/2)$ are dominating. So, the approximation Eq. (5.14) gives reasonably good results for all fields. Using the approximation in Eq. (5.14), and taking $\alpha = 2\times(-1/2) = -1$ for the two surfaces and $\alpha = 2\times(+1/2) = +1$ for the two bulk states, Eq. (5.12) reduces to

$$\begin{aligned}\Delta\sigma_{\perp}(B) = -\frac{e^2}{\pi h}\left[\psi\left(\frac{1}{2}+\frac{B_{\phi,s}}{B}\right)-\ln\left(\frac{B_{\phi,s}}{B}\right)\right] \\ + \frac{e^2}{\pi h}\left[\psi\left(\frac{1}{2}+\frac{B_{\phi,b}}{B}\right)-\ln\left(\frac{B_{\phi,b}}{B}\right)\right].\end{aligned} \tag{5.15}$$

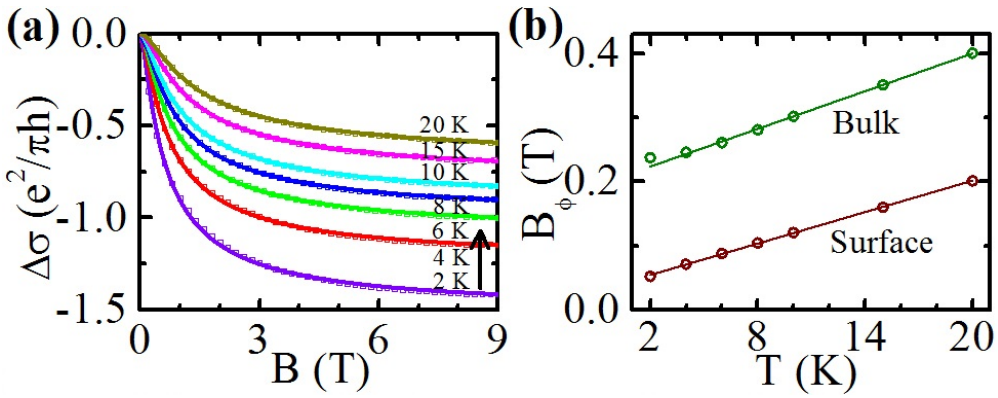

Figure 5.7: Change of conductivity with perpendicular magnetic field at different temperatures: (a) Change of conductivity $\Delta\sigma$ with perpendicular field B at different temperature T from 2 K - 20 K, solid line showing fit using Eq. (5.15). (b) B_ϕ with T for surface and bulk extracted from curve fitting in (a), solid lines are linear fit.

Equation (5.15) is valid to describe the perpendicular field MR data upto 9 T field range provided $k_F l_e > 1$ (indicating diffusive transport regime) and $l_B > l_e$, where $l_B = \sqrt{\hbar/(4eB)}$ is the magnetic length of Cooperon at a given applied magnetic field B [23, 24]. As $B \propto l_B^{-2}$, the minimum $l_B = 4.28$ nm at $B = 9$ T. So, in our case, $l_B > l_e$ is true for all fields upto 9 T, which validates the application of Eq. (5.15) to the analysis of the perpendicular field MR data. We analyze our data in Fig. 5.7(a) with Eq. (5.15), and considered the effective phase coherence field strengths $B_{\phi,s}$ and $B_{\phi,b}$ for the surface and the bulk states as the fitting parameters. The fitted curves are shown as solid lines in Fig. 5.7(a). Equation (5.15) explains the perpendicular field transport data for the wide range of field and temperatures very well with minimal fitting parameters. The extracted values of the fitting parameters $B_{\phi,s}$ and $B_{\phi,b}$ are shown in Fig. 5.7(b). Figure 5.7(b) shows that B_ϕ's for the surface and the bulk states vary linearly with temperature T. From Fig. 5.7(b), we obtain the following T (in Kelvin) dependency of $B_{\phi,s}$ (in Tesla) and $B_{\phi,b}$ (in Tesla),

$$\begin{aligned} B_{\phi,s} &= 0.0082 + 0.0379 \times T, \\ B_{\phi,b} &= 0.0098 + 0.2038 \times T. \end{aligned} \tag{5.16}$$

5.6.3 Estimation of the phase coherence lengths

The phase coherence field strengths $B_{\phi,i}$'s are related to the phase coherence lengths $l_{\phi,i}$'s, where $i = s, b$ corresponds to the surface and the bulk channel, respectively, by[23, 24],

$$B_{\phi,i} = \frac{\hbar}{4e}\left[\frac{1}{l_i^2} + \frac{1}{l_{\phi,i}^2}\right], \tag{5.17}$$

where, the parameter l_i is related to the impurity scattering and spin orbit scattering times, and also depends on the mass of the Dirac bands. In both the massless (surface states) and large mass (bulk states) limits, the value of $1/l_i^2$ becomes very small. The linear T dependence of the parameter $B_{\phi,i}$ comes from the dependence of $l_{\phi,i}$ with T, since $l_{\phi,i} \propto T^{-0.5}$ and l_i is independent of temperature T. The phase coherence lengths for the surface and bulk states are obtained after comparing Eq. (5.16) and Eq. (5.17), and we obtain

$$\begin{aligned} \frac{\hbar}{4el_{\phi,s}^2} &= 0.0379 \times T, \\ \frac{\hbar}{4el_{\phi,b}^2} &= 0.2038 \times T. \end{aligned} \tag{5.18}$$

Figure 5.8 shows variation of l_ϕ with T for the surface and the bulk states. At 2 K, the obtained value of the phase coherence lengths for the surface and the bulk states are 47 nm and 20 nm, respectively. As $l_\phi \propto T^{-p/2}$, so $p = 1$ implying EEI to be the responsible decoherence mechanism for both the surface and the bulk carriers. The temperature dependence of the phase coherence length is consistent with our pre-assumption of $p = 1$ in Eq. (5.2).

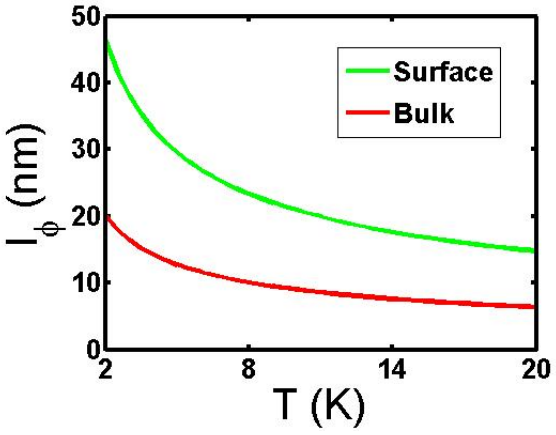

Figure 5.8: Variation of the phase coherence length with temperature for the surface states and the bulk states: The phase coherence lengths, l_ϕ's, are extracted from B_ϕ's of Fig. 5.7(b).

5.7 Analysis of parallel field magnetoresistance

5.7.1 A brief literature review

In the literature, the parallel field MR in TI films has been analyzed with a formula similar to Altshuler-Aronov conductivity correction in metal[25, 108, 118, 119] using

$$\Delta\sigma_{\parallel}(B) = \frac{\alpha e^2}{\pi h} \ln\left(1 + \frac{B^2}{B_0 B_\phi}\right), \tag{5.19}$$

where, $\Delta\sigma_{\parallel}(B)$ is the change of magnetoconductivity for parallel field, and B_0 is associated with effective thickness l_{eff} ($B_0 \propto l_{eff}^{-2}$) in which the electronic wave-function is confined in the direction perpendicular to the surface, and α is the same parameter used in Eq. (5.10). Previously[118], the parallel field MR were analyzed with Eq. (5.19), and the parameters α and B_0 were used to determine the contributions from the two surfaces. It was shown that the value of α changes from $-1/2$ to -1 and B_0 increases (alternatively l_{eff} decreases) as the coupling between the two surfaces decreases[118]. But, in weak coupling limit with significant

bulk transport, the bulk states would have an additive contribution to the conductivity along with the surface states. Recently, the bulk contribution in TI to the parallel field magnetoresistance was explained employing a formula derived analogously as Eq. (5.11) considering the bulk as a 2DEG system with strong SOC[120]. However, such formula will not provide a correct understanding of the transport behavior of the 2D bulk states in TI thin films. In the next section, we derive a formula analogous to Eq. (5.19) that will be applicable to both the surface states and the bulk states in a TI thin film.

5.7.2 Theory for parallel field magnetoresistance

Equation (5.19) is derived considering the finite penetration depth of the surface states or the thickness of the film[25], the form remains the same even if the parallel field MR is because of the surface roughness[121] or the Zeeman effect due to hexagonal warping of the band structure[122]. Although it is difficult to distinguish these different effects by analyzing the parallel field MR, as contributions from all of them can be absorbed into the parameter B_0 that we show below, and the WAL and WL effect can be easily identified by the parameter α.

The quantum correction to the conductivity due to the interference effect is given by[23, 24, 25]:

$$\delta\sigma = -\frac{2e^2 D_i}{\pi\hbar}\sum_{\mathbf{q}} C_i(\mathbf{q}), \tag{5.20}$$

where the Cooperon $C_i(\mathbf{q})$ in the momentum representation is[23, 24, 25]

$$C_i(q) = \alpha_i \frac{1}{D_i q^2 + \tau_i^{-1}}. \tag{5.21}$$

Here, $\mathbf{q}$ is the momentum transfer in the Cooperon channel, D_i is the diffusion constant of

the i^{th} channel, and τ_i is related by $D_i\tau_i = l_i^2$. The value of α_i is $-1/2$ for one massless surface state, and $+1/2$ for one massive bulk state[23, 24].

Now, with an external magnetic field B applied parallel to the surface, the Cooperon takes the form[25]

$$C_i(q) = \alpha_i \frac{1}{D_i q^2 + \tau_i^{-1} + \tau_{B,i}^{-1}}, \tag{5.22}$$

where,

$$\tau_{B,i}^{-1} = \frac{4eD_i}{\hbar}\frac{B^2}{B_{0,i}}. \tag{5.23}$$

The form of Eq. (5.23) remains the same even if the parallel field MR is because of the surface roughness[121] ($\tau_{B,i,r}$, $B_{0,i,r}$), or the Zeeman effect due to hexagonal warping of the band structure[122] ($\tau_{B,i,w}$, $B_{0,i,w}$), or some finite thickness ($\tau_{B,i,t}$, $B_{0,i,t}$) or penetration depth[25] ($\tau_{B,i,d}$, $B_{0,i,d}$) effect of the electronic wave-function. All of them has an additive contribution to $\tau_{B,i}^{-1}$, or an inverse additive contributions to the parameter $B_{0,i}$, given by

$$\tau_{B,i}^{-1} = \tau_{B,i,r}^{-1} + \tau_{B,i,w}^{-1} + \tau_{B,i,t}^{-1} + \tau_{B,i,d}^{-1}. \tag{5.24}$$

Also, the parameter $B_{0,i,j}$ (for $j = r, w, t, d$) is given by

$$B_{0,i,j} = \beta_j^{-1}\frac{\hbar}{4e}\frac{1}{l_{0,i,j}^2}, \tag{5.25}$$

where β_j^{-1} is a pre-factor and $l_{0,i,j}$ is associated length corresponding to roughness (j=r), warping (j=w), thickness (j=t) or penetration depth (j=d). However, we consider an effective length $l_{eff,i}$ associated with $\tau_{B,i}$ or $B_{0,i}$ by

$$B_{0,i} = \frac{\hbar}{4el_{eff,i}^2}, \tag{5.26}$$

The length scale $l_{eff,i}$ is a root mean square of all the $l_{0,i,j}$ with an weight of β_j^{-1}.

The quantum correction to the conductivity in an applied parallel field can be calculated[25], by inserting Eq. (5.22) into Eq. (5.20), and converting the summation to integration with the upper limit of $q_{max} = l_{e,i}^{-1}$ ($l_{e,i}$ is the momentum relaxation length for i^{th} channel) and lower limit $q_{min} = l_{\phi,i}^{-1}$, as

$$\begin{aligned}
\delta\sigma(B) &= -\frac{2e^2 D_i}{\pi\hbar}\int_{l_{\phi,i}^{-2}}^{l_{e,i}^{-2}} \frac{d^2\mathbf{q}}{(2\pi)^2}\alpha_i \frac{1}{D_i q^2 + \tau_i^{-1} + \tau_{B,i}^{-1}} \\
&= -\frac{e^2}{\pi h}\int_{\tau_{\phi,i}^{-1}}^{\tau_{e,i}^{-1}} d(D_i q^2)\alpha_i \frac{1}{D_i q^2 + \tau_i^{-1} + \tau_{B,i}^{-1}} \\
&= -\alpha_i \frac{e^2}{\pi h}\ln\left(\frac{\tau_{e,i}^{-1} + \tau_i^{-1} + \tau_{B,i}^{-1}}{\tau_{\phi,i}^{-1} + \tau_i^{-1} + \tau_{B,i}^{-1}}\right).
\end{aligned} \tag{5.27}$$

The scattering times are given by $D_i\tau_{e,i} = l_{e,i}^2$ and $D_i\tau_{\phi,i} = l_{\phi,i}^2$. The change of magnetoconductivity $\Delta\sigma_\parallel(B)$ will be given by

$$\begin{aligned}
\Delta\sigma_\parallel(B) &= \delta\sigma(B) - \delta\sigma(0) \\
&= -\alpha_i \frac{e^2}{\pi h}\ln\left(\frac{\tau_{e,i}^{-1} + \tau_i^{-1} + \tau_{B,i}^{-1}}{\tau_{e,i}^{-1} + \tau_i^{-1}}\right) + \alpha_i \frac{e^2}{\pi h}\ln\left(\frac{\tau_{\phi,i}^{-1} + \tau_i^{-1} + \tau_{B,i}^{-1}}{\tau_{\phi,i}^{-1} + \tau_i^{-1}}\right) \\
&= -\alpha_i \frac{e^2}{\pi h}\ln\left(1 + \frac{\tau_{B,i}^{-1}}{\tau_{e,i}^{-1} + \tau_i^{-1}}\right) + \alpha_i \frac{e^2}{\pi h}\ln\left(1 + \frac{\tau_{B,i}^{-1}}{\tau_{\phi,i}^{-1} + \tau_i^{-1}}\right).
\end{aligned} \tag{5.28}$$

Now, for quantum diffusion limit, $l_{e,i} \ll l_B = \sqrt{\hbar/(4eB)}$ and $B_{0,i} > B$ (generally $B_{0,i} \propto l_{eff,i}^{-2}$ is large as $l_{eff,i}$ is small) implies $\tau_{e,i}^{-1} \gg \tau_{B,i}^{-1}$. So, the first term in Eq. (5.28) can be neglected, and $\Delta\sigma_\parallel(B)$ will be given by

$$\begin{aligned}
\Delta\sigma_\parallel(B) &= \alpha_i \frac{e^2}{\pi h}\ln\left(1 + \frac{\tau_{B,i}^{-1}}{\tau_{\phi,i}^{-1} + \tau_i^{-1}}\right) \\
&= \alpha_i \frac{e^2}{\pi h}\ln\left(1 + \frac{B^2}{B_{0,i}B_{\phi,i}}\right).
\end{aligned} \tag{5.29}$$

Here, we have used the definitions of $B_{\phi,i}$ in Eq. (5.17) and $B_{0,i}$ in Eq. (5.23). The above equation has the same form as Eq. (5.19) and we consider it to explain the magnetoresistance arising both from the surface and the bulk states in our thin film.

5.7.3 Explanation of parallel field magnetoresistance with the theory derived for TI

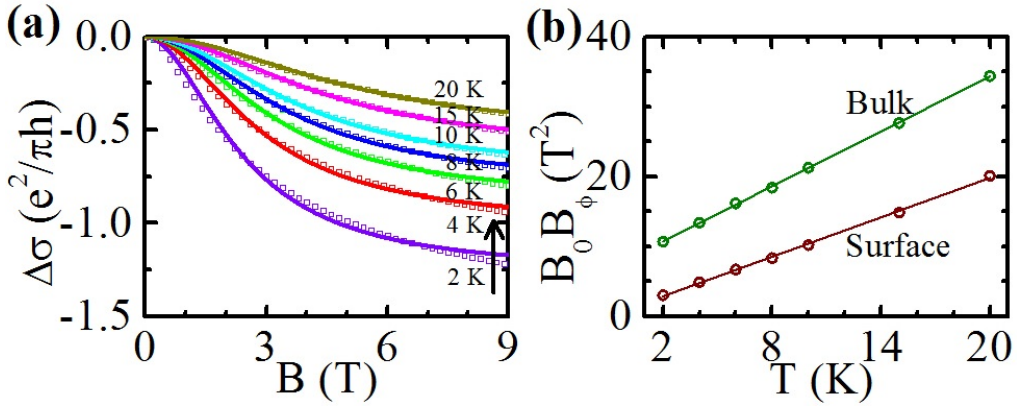

Figure 5.9: Change of conductivity with parallel magnetic field at different temperatures: (a) Change of conductivity $\Delta\sigma$ with parallel field B at different temperatures T from 2 K - 20 K, solid line showing fit using Eq. (5.31). (b) $B_0 B_\phi$ with T for surface and bulk extracted from curve fitting in (a), solid lines are fit.

In Fig. 5.9(a), we show the change in conductivity $\Delta\sigma$ with magnetic field B applied parallel to the sample surface. We find that the bulk state of TI thin film in the 2D limit will produce parallel field MR that can be described by Eq. (5.29) with α varying from $-1/2$ to $+1/2$ depending upon the details of Fermi level and the bulk band structure[18, 24], similar to what is obtained for perpendicular field MR. The value of α remains same, because the underlying phenomenon for perpendicular and parallel field MR is phase breaking of the electrons which can be captured by the same Cooperon mode. Similarly, the contribution to the transport from each surface state will be described by Eq. (5.29) with $\alpha = -1/2$[25]. In our case, as the two surfaces (s1,s2) and two degenerate bulk subbands (b1,b2) are conducting,

so the change in magnetoconductivity in parallel field can be expressed as

$$\Delta\sigma_{\parallel}(B) = \frac{e^2}{\pi h} \sum_{\substack{i=s1,s2,\\ b1,b2}} \alpha_i \ln\left(1 + \frac{B^2}{B_{0,i}B_{\phi,i}}\right). \tag{5.30}$$

We further consider $\alpha_{s1} = \alpha_{s2} = -1/2$ for the surface states and $\alpha_{b1} = \alpha_{b2} = +1/2$ for the bulk states, and assume $B_{0,s1}B_{\phi,s1} \approx B_{0,s2}B_{\phi,s2} \approx B_{0,s}B_{\phi,s}$ and $B_{0,b1}B_{\phi,b1} \approx B_{0,b2}B_{\phi,b2} \approx B_{0,b}B_{\phi,b}$. Based on the assumptions, Eq. (5.30) is rewritten as

$$\Delta\sigma_{\parallel}(B) = -\frac{e^2}{\pi h} \ln\left(1 + \frac{B^2}{B_{0,s}B_{\phi,s}}\right) + \frac{e^2}{\pi h} \ln\left(1 + \frac{B^2}{B_{0,b}B_{\phi,b}}\right). \tag{5.31}$$

The value of $\alpha = 2 \times (-1/2) = -1$ for the two surface states and $\alpha = 2 \times (+1/2) = +1$ for the two bulk sub-bands are used in the above equation, while the products $B_{0,s}B_{\phi,s}$ and $B_{0,b}B_{\phi,b}$ have been treated as free fitting parameters. Fig. 5.9(a) shows that Eq. (5.31) could satisfactorily describe the change of magnetoconductivity in parallel magnetic fields considering both the surface and the bulk conductions. The fitting parameter B_0B_ϕ for the surface and the bulk states are shown in Fig. 5.9(b). As B_0 is independent of temperature while B_ϕ increases linearly with increasing temperature (Fig. 5.7(b)), the extracted parameter B_0B_ϕ changing linearly with T as shown in Fig. 5.9(b) is consistent. The linear dependence of $B_{0,i}B_{\phi,i}$ with temperature T are obtained to be

$$\begin{aligned} B_{0,s}B_{\phi,s} &= 0.9406 + 1.0196 \times T, \\ B_{0,b}B_{\phi,b} &= 1.3099 + 8.1438 \times T, \end{aligned} \tag{5.32}$$

where $B_{0,s}B_{\phi,s}$ and $B_{0,b}B_{\phi,b}$ are given in Tesla^2, and T is given in Kelvin.

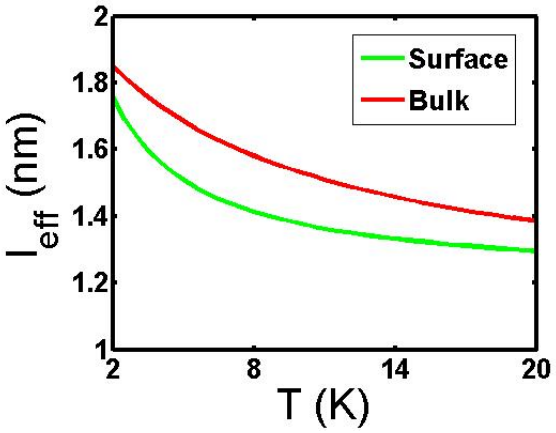

Figure 5.10: Variation of the spread of the wave functions with temperature for the surface states and the bulk states: The spread of the wave functions, l_{eff}'s, are extracted from B_0's obtained from $B_0 B_\phi$'s given in Fig. 5.9(b) and B_ϕ's given in Fig. 5.7(b).

5.7.4 Estimation of the spread of the wave functions

From Eq. (5.16) and Eq. (5.32), the value of $B_{0,s}$ and $B_{0,b}$ are calculated. The corresponding values of l_{eff}'s are evaluated using Eq. (5.26) for the surface and the bulk states, and plotted with T in Fig. 5.10. The values of the effective thicknesses l_{eff}, in which the wave functions are confined, are order of a nanometer which is consistent with literature[4, 5].

5.8 Analysis of tilted field magnetoresistance

5.8.1 Preliminary understanding of the experimental data

We have observed that the perpendicular as well as the parallel field breaks the phase coherence of the surface and the bulk electrons. Now, we measure MR for different field orientations at 2 K. Fig. 5.11(a) shows change in conductivity $\Delta\sigma$ with magnetic field B at different θ ranging from 30^0 to 85^0, where θ is the angle between the magnetic field and the

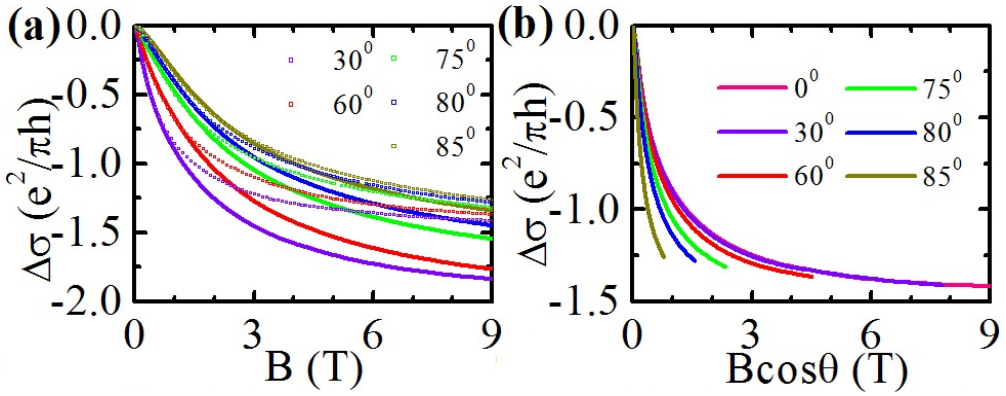

Figure 5.11: Change of conductivity with magnetic field for different field orientations: (a) Change of conductivity $\Delta\sigma$ with magnetic field B at different θ at 2 K, solid lines are fit with Eq. (5.33). (b) $\Delta\sigma$ with the perpendicular component $B\cos\theta$ from (a).

surface normal direction. We first consider fitting the data with contributions of conductivity from the perpendicular as well as the parallel components of the field, using Eqs. (5.15) and (5.31), by the following formula:

$$\Delta\sigma(B,\theta) = \Delta\sigma_{\perp}(B\cos\theta) + \Delta\sigma_{\parallel}(B\sin\theta). \tag{5.33}$$

The fitting of the tilted field data using Eq. (5.33) is shown in Fig. 5.11(a) by the solid lines. Equation (5.33) can describe the tilted field data for low range of fields and overestimates it for higher fields, which were also observed in a previous study[119]. The $\Delta\sigma$ at different angles are shown with perpendicular component of the field $B\cos\theta$ in Fig. 5.11(b). The MR for $\theta = 30^0$ overlaps with the perpendicular field MR ($\theta = 0^0$), but MR for higher θ deviates from that at $\theta = 0^0$. The deviation indicates that the change of magnetoconductivity is larger from that expected if only perpendicular component of the field were breaking the phase coherence. The deviation is because the parallel field component breaks the phase coherence of electrons too, which could not be pictured by Eq. (5.33). So, we derive an expression of magnetoconductivity based on Ref. [121].

5.8.2 Theory for tilted field magnetoresistance

In a tilted magnetic field, the quantum correction to the conductivity due to the interference effect (WAL, WL) will be given by

$$\delta\sigma(B) = -\frac{2e^2 D_i}{\pi\hbar}\sum_{\mathbf{q}} \alpha_i \frac{1}{D_i q^2 + \tau_i^{-1} + \tau_{B_\parallel,i}^{-1}}, \tag{5.34}$$

where

$$\tau_{B_\parallel,i}^{-1} = \frac{4eD_i}{\hbar}\frac{B_\parallel^2}{B_{0,i}} = \frac{D_i}{l_{B_\parallel}^2}, \tag{5.35}$$

where, $i = s, b$ corresponds to the surface and the bulk channels. Here, $B_\parallel (= B\sin\theta)$ is the parallel component of the magnetic field B, and the perpendicular component of the field $B_\perp (= B\cos\theta)$ will quantize the energy levels into Landau levels. So, the Cooperon momentum $\mathbf{q}$ is quantized as[23, 24]

$$q_n^2 = (n+\frac{1}{2})\frac{4eB_\perp}{\hbar} = (n+\frac{1}{2})\frac{1}{l_{B_\perp}^2}, \tag{5.36}$$

with n denoting the n^{th} Landau level. Following Equation (5.27), the sum in Equation 5.34) can be performed as[23, 24],

$$\begin{aligned}\delta\sigma(B) &= -\alpha_i\frac{e^2}{\pi h}\sum_{q_n^2=(n+\frac{1}{2})\frac{4eB_\perp}{\hbar}} d(q_n^2)\frac{1}{q_n^2 + (D_i\tau_i)^{-1} + (D_i\tau_{B_\parallel,i})^{-1}} \\ &= -\alpha_i\frac{e^2}{\pi h}\sum_{q_n^2=(n+\frac{1}{2})l_{B_\perp}^{-2}} d(q_n^2)\frac{1}{q_n^2 + l_i^{-2} + l_{B_\parallel}^{-2}}.\end{aligned} \tag{A.9d}$$

The summation is performed keeping the upper limit $q_{n,max} = l_{e,i}^{-1}$ and the lower limit $q_{n,min} = l_{\phi,i}^{-1}$, and we obtain

$$\delta\sigma(B) = -\alpha_i \frac{e^2}{\pi h}\left[\psi\left(\frac{1}{2}+\frac{l_{e,i}^{-2}+l_i^{-2}+l_{B_\parallel}^{-2}}{l_{B_\perp}^{-2}}\right)-\psi\left(\frac{1}{2}+\frac{l_{\phi,i}^{-2}+l_i^{-2}+l_{B_\parallel}^{-2}}{l_{B_\perp}^{-2}}\right)\right]. \tag{5.37}$$

The change of magnetoconductivity $\Delta\sigma_{tilt}(B) = \delta\sigma(B) - \delta\sigma(0)$ will be given by

$$\begin{aligned}\Delta\sigma_{tilt}(B) = &-\alpha_i \frac{e^2}{\pi h}\left[\psi\left(\frac{1}{2}+\frac{l_{e,i}^{-2}+l_i^{-2}+l_{B_\parallel}^{-2}}{l_{B_\perp}^{-2}}\right)-\ln\left(\frac{l_{e,i}^{-2}+l_i^{-2}}{l_{B_\perp}^{-2}}\right)\right]\\ &+\alpha_i \frac{e^2}{\pi h}\left[\psi\left(\frac{1}{2}+\frac{l_{\phi,i}^{-2}+l_i^{-2}+l_{B_\parallel}^{-2}}{l_{B_\perp}^{-2}}\right)-\ln\left(\frac{l_{\phi,i}^{-2}+l_i^{-2}}{l_{B_\perp}^{-2}}\right)\right].\end{aligned} \tag{5.38}$$

In quantum diffusion limit, $l_{e,i} \ll l_{B_\perp}$, i.e. $l_{B_\perp}^{-2} \ll l_{e,i}^{-2}$, so the first bracket in Equation (5.38) can be ignored, and $\Delta\sigma_{tilt}(B)$ becomes

$$\begin{aligned}\Delta\sigma_{tilt}(B) &= \alpha_i \frac{e^2}{\pi h}\left[\psi\left(\frac{1}{2}+\frac{l_{\phi,i}^{-2}+l_i^{-2}+l_{B_\parallel}^{-2}}{l_{B_\perp}^{-2}}\right)-\ln\left(\frac{l_{\phi,i}^{-2}+l_i^{-2}+l_{B_\parallel}^{-2}}{l_{B_\perp}^{-2}}\right)\right]\\ &= \alpha_i \frac{e^2}{\pi h}\left[\psi\left(\frac{1}{2}+\frac{B_{\phi,i}+\frac{B_\parallel^2}{B_{0,i}}}{B_\perp}\right)-\ln\left(\frac{B_{\phi,i}}{B_\perp}\right)\right].\end{aligned} \tag{A.9f}$$

5.8.3 Explanation of tilted field magnetoresistance

In case of our thin film, the contributions from the two surfaces and two bulk subbands will add up in the conductivity. So, the change in magnetoconductivity in tilted field will be given by

$$\Delta\sigma_{tilt}(B) = \frac{e^2}{\pi h}\sum_{\substack{i=s1,s2,\\ b1,b2}} \alpha_i\left[\psi\left(\frac{1}{2}+\frac{B_{\phi,i}+\frac{B_\parallel^2}{B_{0,i}}}{B_\perp}\right)-\ln\left(\frac{B_{\phi,i}}{B_\perp}\right)\right]. \tag{5.39}$$

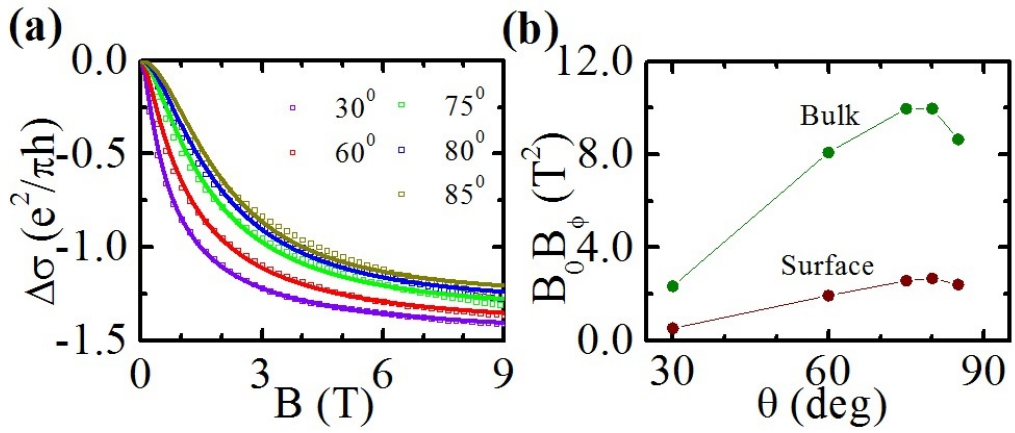

Figure 5.12: Explanation of change of conductivity with magnetic field for different field orientations: (a) Change of conductivity $\Delta\sigma$ with magnetic field B at different θ at 2 K, solid lines are fit with Eq. (5.40). (b) $B_0 B_\phi$ with θ for the surface and the bulk states, extracted from curve fitting in (a), solid lines are guide to eye.

where, $\alpha = -1/2$ for each surface state and $\alpha = +1/2$ for each bulk states. Since, we have two surface states and two bulk states contributing to the transport in our thin film, we use $\alpha = -1$ for the two surface states in total and $\alpha = +1$ for the two bulk states in total, and assume B_0 and B_ϕ are same for the two surface states and separately for the two bulk states. Then from Equation (5.39), we get the following equation to explain the tilted field data

$$\begin{aligned}\Delta\sigma_{tilt}(B) = \\ -\frac{e^2}{\pi h}\left[\psi\left(\frac{1}{2}+\frac{B_{\phi,s}(1+\frac{B_\parallel^2}{B_{0,s}B_{\phi,s}})}{B_\perp}\right)-\ln\left(\frac{B_{\phi,s}}{B_\perp}\right)\right] \\ +\frac{e^2}{\pi h}\left[\psi\left(\frac{1}{2}+\frac{B_{\phi,b}(1+\frac{B_\parallel^2}{B_{0,b}B_{\phi,b}})}{B_\perp}\right)-\ln\left(\frac{B_{\phi,b}}{B_\perp}\right)\right].\end{aligned} \tag{5.40}$$

The values of $B_{\phi,s}$ and $B_{\phi,b}$ at 2 K are taken from Fig. 5.7(b), and $B_{0,s}$ and $B_{0,b}$ are chosen as free parameters. Fig. 5.12(a) shows that Eq. (5.40) can satisfactorily explain the tilted field MR. In Fig. 5.12(b), the extracted fitting parameter B_0 is shown by multiplying it with B_ϕ for comparison with the value of $B_0 B_\phi$ in Fig. 5.9(b). For the angle $\theta = 30^0$, $B_0 B_\phi$

is small indicating that the MR can be explained by only considering the perpendicular component of the field, which agrees with the fact that the data for $\theta = 30^0$ coincides with the perpendicular field data in Fig. 5.11(b). For higher angles, the obtained value of $B_0 B_\phi$ is almost the same of that obtained in Fig. 5.9(b) at 2 K. The consistency of the value of $B_0 B_\phi$ shows that the tilted field MR could be described by Eq. (5.40) considering dephasing of the electrons by the perpendicular as well as the parallel components of the field.

5.9 Comparison of our analysis to prior analyses in the literature

To explain the logarithmic temperature-dependent conductivities as well as the perpendicular field magnetoconductivity, we assume that the surface-bulk coupling is weak in our thin film, and consider both the surface and the bulk contributions separately. For the Fermi level lying inside the bulk band, such weak surface-bulk coupling is possible due to low surface-bulk scattering rate if the relative orbital pseudo-spin orientation of the surface and bulk states at the Fermi level are anti-parallel[123]. In literature[90, 91, 92, 94, 109, 110, 111, 112, 113, 114, 115, 116], the surface-bulk coupling was identified based on fitting only the perpendicular field magnetoconductivity with reduced HLN equation to extract the prefactor α, where $\alpha = -1/2$ denotes strong coupling. However, it was pointed out[18] that fitting the reduced HLN equation can be ambiguous when the bulk contribution is also present. Here we take a different route to first identify the separate bulk contribution from analysis of the logarithmic temperature-dependent conductivities at different magnetic fields using the Lu-Shen theory, and then incorporate the appropriate theory of bulk conduction along with the surface to explain the perpendicular field magnetoconductivity. Previously, an approach to explain the experiment using Lu-Shen theory was considered to analyze the logarithmic temperature dependent conductivities in antidot nanostructured Bi_2Te_3 thin

films[124]. The reason for the validity of our prescription underlies in the fact that quantum correction to the conductivity due to localization and interaction effects of the carriers at finite temperature and magnetic fields can be pictured by the same Cooperon modes of the carriers[23]. The electrons from single surface state form one spin triplet Cooperon with vanishing Cooperon gap, while the bulk state electrons can form either a gapless triplet or a gapless singlet Cooperon mode depending on the value of the band structure parameter r in Eq. 5.3. The value of $\alpha = -1/2$ or $+1/2$ in the reduced HLN equation represents one triplet or one singlet Cooperon, respectively. In case of strong surface-bulk coupling[115], the surface and the bulk Cooperons will be coupled giving rise to a different gapless Cooperon mode that will govern the quantum conductivity correction with value of $\alpha = -1/2$. We can explain the slopes of logarithmic temperature-dependent conductivities only if we consider two surface states forming two triplet Cooperon modes ($\alpha = -1/2$ for each Cooperon) and two bulk state forming two singlet Cooperon modes ($\alpha = +1/2$ for each Cooperon). Next, to analyze the perpendicular field magnetoconductivity we associate the two triplet surface Cooperons and two singlet bulk Cooperons being responsible for WAL and WL, respectively. Since, we already have ruled out the surface-bulk coupling, we do not further attempt fitting the perpendicular field magnetoconductivity with reduced HLN equation to extract the prefactor α. As we have determined that the perpendicular field destroys the WAL due to two triplet surface Cooperons and WL due to two singlet bulk Cooperons, we invoke the same concept to examine the parallel and tilted field data satisfactorily.

5.10 Summary

In summary, we have performed a detailed low temperature magnetotransport analysis in epitaxial Bi_2Se_3 thin film. The surface and the bulk contributions to the conduction are

identified considering weak antilocalization and weak localization of the surface and the bulk states, respectively. The Lu-Shen theory is used for analyzing the logarithmic temperature-dependent conductivities, and the perpendicular field magnetoconductivity is explained with the HLN-like formula considering the modifications made by Lu-Shen. Based on Lu-Shen's modifications, we have presented a theory of parallel and tilted field magnetoresistance incorporating the effects of the weak localization contributions from the bulk states in the 2D limit. We provide an experimental verification of the Lu-Shen theory for the localization and interaction effects of the surface states and the 2D bulk states in thin film of TI. The experimental results are interpreted on basis of the theory derived specifically for a 2D TI system taking into account of the effects of the distinct Dirac-type band structure. The magnetoresistance observed for any orientation of the magnetic field could be satisfactorily explained considering the phase breaking of the surface and the bulk electrons by the applied magnetic field. We show that for a more accurate understanding of the localization and interaction effects of the bulk states in TI thin films in the 2D limit, the effect of the Dirac-type band structure on the magnetotransport should be considered. However, low temperature and higher magnetic field data with varying thickness and carrier concentration, in the future, would provide more insight into the underlying physics of the combined surface and the bulk transport in topological insulator thin films.

Chapter 6

Two-terminal devices with topological insulator and ferromagnet

A distinct feature of the two dimensional (2D) surface states of a three dimensional (3D) topological insulators (TIs) is the Dirac-band dispersion with spin-momentum locking, which provides that any charge current carried by these states will induce a spin accumulation on the surface of the TI. In recent experiments, the charge current-induced spin accumulation on the surface of 3D TIs, such as Bi_2Se_3, Bi_2Te_3, $(Bi_xSb_{1-x})_2Te_3$, $Bi_{1.5}Sb_{0.5}Te_{1.7}Se_{1.3}$, $BiSbTeSe_2$, Bi_2Te_2Se and Sb_2Te_3, were electrically measured by the voltage probed with ferromagnetic (FM) tunnel contact in three-terminal or four-terminal potentiometric measurement geometries[28, 29, 30, 31, 32, 33, 34, 35, 36, 37, 38, 39, 40]. In such experiments, the voltage on the FM contact depends on the magnitude of the charge current and the projection of the spin polarization onto the FM magnetization direction. In the literature, two-terminal magnetoresistance between two FM contacts on the surface of TIs have been reported[56, 57] and the observed two-terminal resistance changed with reversal of the FM magnetization directions or the reversal of the current direction on the TI surface. However, measurement of two-terminal resistance on TI surface with only one FM contact is lacking.

The results in this chapter have been published as (1) Ref. [82]: R. Dey, A. Roy, T. Pramanik, A. Rai, S. H. Shin, S. Majumder, L. F. Register, and S. K. Banerjee, "Detection of current induced spin polarization in epitaxial Bi_2Te_3 thin film", *Applied Physics Letters*, **110**, 122403 (2017), Reproduced with the permission of AIP Publishing. Available: https://doi.org/10.1063/1.4978691. Contribution of the dissertator: The dissertator, Rik Dey, fabricated the devices, conducted the measurements, analyzed the data, wrote the manuscript, and is the corresponding author of this publication. (2) Ref. [83]: S. Majumder, S. Guchhait, R. Dey, L. F. Register, and S. K. Banerjee, "Large magnetoresistance at room temperature in ferromagnet/topological insulator contacts", *IEEE Transactions on Nanotechnology*, **15**, 671 (2016), Copyright 2016 IEEE, Reprinted with permission. Available: https://doi.org/10.1109/TNANO.2016.2572003. Contribution of the dissertator: The dissertator, Rik Dey, contributed towards device fabrication, transport measurements, data analysis and manuscript writing.

In this chapter, we measure the two-terminal resistance between a FM and a nonmagnetic (NM) contact deposited on the surface of Bi_2Te_3 films. The two-terminal resistance changes with the magnetization direction of the FM, and, with an applied magnetic field sweep the two-terminal resistance shows a hysteresis tracking the magnetization of the Fe. The change of the two-terminal resistance with reversal of the magnetization direction of the FM apparently violates Onsager reciprocity relation. We suggest a possible explanation of such apparent violation of Onsager reciprocity related to the hyperfine interaction of the nuclear spins in the heavy atoms of Bi_2Te_3 and the conduction electrons, with a longer lifetime of the nuclear spins that do not changes orientation with the applied magnetic field.

6.1 Experimental measurement set-up

In the experiment, we fabricate all of our devices either on epitaxially grown Bi_2Te_3 thin film or on exfoliated Bi_2Te_3 flakes. The epitaxial growth of a 4 nm Bi_2Te_3 thin film was done on a Si substrate at a substrate temperature of 350^0C. The details of the growth and characterizations of the Bi_2Te_3 thin film was reported before[94, 95, 125]. We also mechanically exfoliate Bi_2Te_3 flake of thickness $\approx$ 100 nm from a bulk crystal on a SiO_2(300 nm)/Si substrate using the standard Scotch tape method, and the flake are characterized by Raman spectroscopy and the thicknesses is measured by atomic force microscopy. The devices are patterned either in a Hall bar geometry or in a two-terminal geometry, as shown in Fig. 6.1, with standard etching, lithography, e-beam evaporation and liftoff processes. The transport measurements are performed in a Physical Property Measurement System capable of cooling down to 2 K with magnetic field up to 9 T.

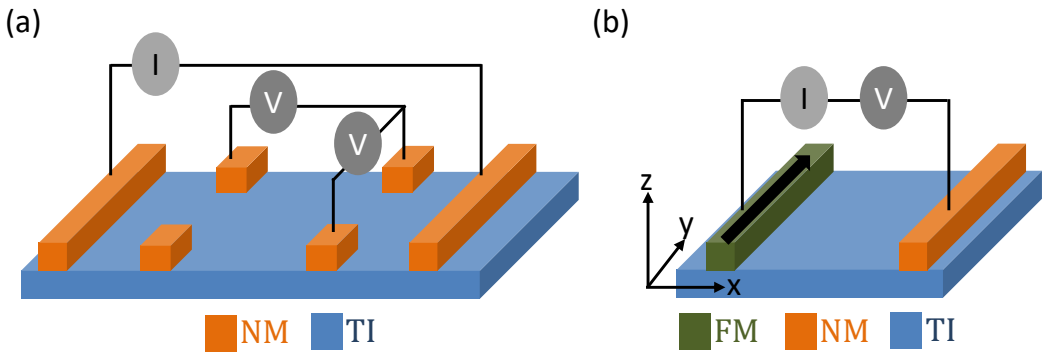

Figure 6.1: Schematic of contact configurations for transport measurement on TI surface and two-terminal resistance measurement with FM contact: (a) Schematic of Hall bar geometry for Hall and MR measurement on TI surface, (b) Schematic of two terminal measurement setup with a FM and a NM contact.

6.2 Transport measurement on epitaxial Bi_2Te_3 film

To measure the transport properties of the 4 nm thick Bi_2Te_3 film, we fabricate six-terminal Hall bar with NM Ti/Au contacts deposited on the surface of the thin film as shown in Fig. 6.1(a). The transverse Hall resistance and the longitudinal resistance are measured with magnetic field applied perpendicular to the sample surface. Figure 6.2(a) shows the Hall resistance R_H of the thin film at 2 K. The Hall resistance is linear with a negative slope, indicating the carriers are electrons. The 2D carrier concentration obtained from the slope of the linear fit is $n_{2D} = 1.4 \times 10^{14}$ cm^{-2}. Such a high electron concentration indicates that both the surface and the bulk states are occupied[94, 95, 125]. Assuming two 2D surface states and at least two degenerate quasi-2D (because of our thin film) bulk states being populated, i.e. at least 4 states being filled, an upper limit of k_F is estimated from the carrier concentration n_c using $k_F = \sqrt{\pi n_c}$, and we obtain $k_F = 2$ nm^{-1}.

The longitudinal conductivity $\sigma(B)$ are obtained from the longitudinal resistance and shows the signature of weak antilocalization (WAL). We plot in Fig. 6.2(b) the change of

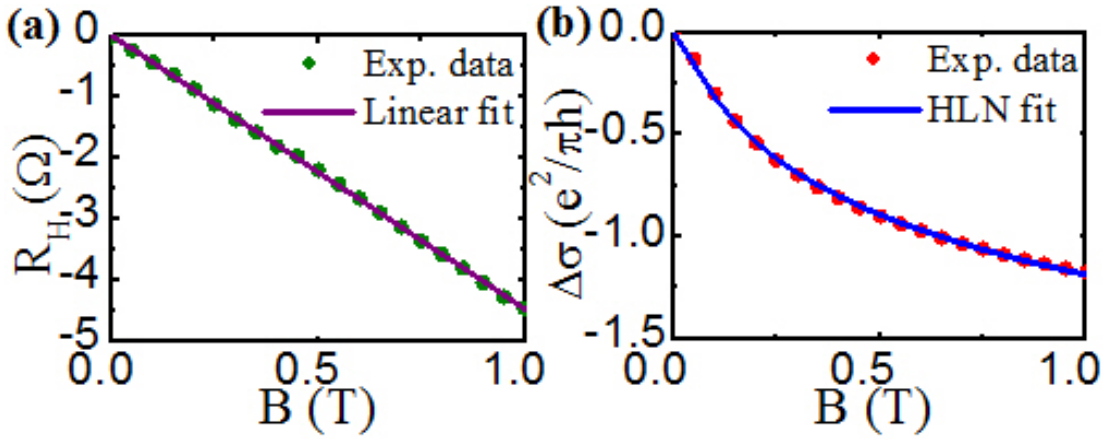

Figure 6.2: Magnetotransport measurement on epitaxial Bi_2Te_3 thin film: (a) Hall resistance R_H with magnetic field B perpendicular to the sample surface at 2 K, solid line is the linear fit. (b) Change of conductivity $\Delta\sigma$ with magnetic field B perpendicular to the sample surface at 2 K, solid line is the HLN fit.

conductivity $\Delta\sigma(B) = \sigma(B) - \sigma(B = 0)$ with magnetic field B applied perpendicular to the surface at 2 K. The sharp cusp near zero field is due to destruction of phase coherence of the electrons in an applied perpendicular field. The magnetoconductivity is explained with the Hikami-Larkin-Nagaoka (HLN) formula[87, 94, 95, 102, 125]:

$$\Delta\sigma(B) = \alpha\frac{e^2}{\pi h}\left[\psi\left(\frac{1}{2} + \frac{\hbar}{4el_\phi^2 B}\right) - \ln\left(\frac{\hbar}{4el_\phi^2 B}\right)\right], \tag{6.1}$$

where l_ϕ is the phase coherence length, h is the Planck's constant and α is a fitting parameter. From the HLN fitting shown in Fig. 2(b), we obtain $l_\phi = 121$ nm and $\alpha = -0.46$. The value of $\alpha \approx -1/2$ implies that both the surface and the bulk states are coupled and behave like a single phase coherent channel[94, 95, 125]. In our thin film, the 3D electron concentration $n_{3D} = 3.5 \times 10^{20}$ cm^{-3} is close to the saturated electron concentration $n_{sat} = 4 \times 10^{20}$ cm^{-3} in Bi_2Te_3 that corresponds to the stabilized Fermi level[126]. As the bulk Fermi level is very close to the Fermi level stabilized on the surface, the band-bending near the surface will be small causing negligible Rashba spin splitting of the quantum confined bulk states.

6.3 Two-terminal measurement on epitaxial Bi_2Te_3 film with Fe contact

For the two-terminal measurement as shown in Fig. 6.1(b), FM and NM contacts are deposited on the surface of the TI along the y direction and a charge current is passed between the contacts in the x direction. We want the FM to be magnetized along the $\pm y$ direction while the voltage drop will be measured between the two electrodes with a given charge current. We fabricate a device, as shown in Fig. 6.1(b), of dimensions $L = 30$ μm in the x- direction and $W = 35$ μm in the y- direction with Fe as the FM and Ti/Au as the NM contact. We evaporate a patterned MgO(1 nm)/Fe(20 nm) stack on the top surface of the Bi_2Te_3 thin film. The thin layer of MgO helps in resolving the issue of resistance mismatch between the metallic Fe and the TI thin film, as well as protects the surface states of the TI from the ferromagnetic exchange interaction that can break the time reversal symmetry. The Fe contact is rectangular in shape with the easy axis lying in the y-direction, and is capped with 21 nm of Au. The magnetic field is applied parallel to the surface along the length of the Fe bar (along the easy axis), perpendicular to the direction of the current (x- direction) as shown in Fig. 6.1(b). Two terminal voltage(V)-current(I) measurements are recorded at each applied magnetic field as we sweep the field. The resistance R at each magnetic field is obtained from the linear V-I characteristic, two of such data are shown in the insets of Fig. 6.3 and 6.4. Two sets of measurements are performed at 2 K to obtain the resistance at different magnetic fields, one with the applied current ramped from zero to a positive value, and another with the current ramped from negative to a positive value.

Figure 6.3 shows the resistance R with the magnetic field sweep from a positive field of 1000 Oe to a negative field of -1000 Oe and back to a positive field of 1000 Oe. In the first set of measurements shown in Fig. 6.3, the resistance is obtained from the V-I characteristic

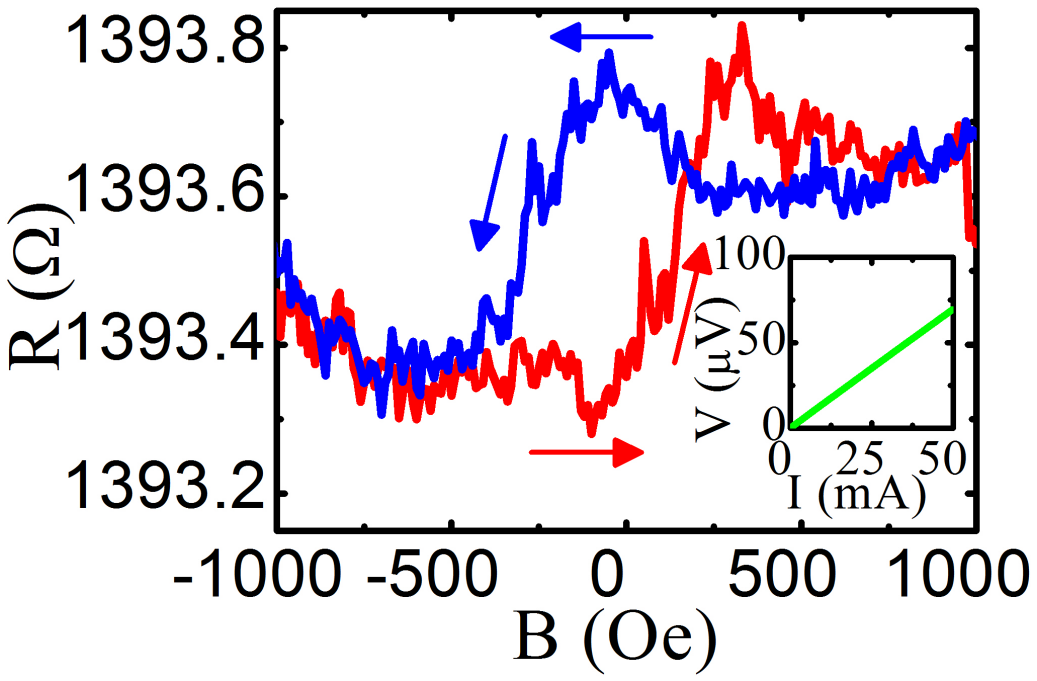

Figure 6.3: Magnetoresistance between FM and NM contacts on the surface of the epitaxial Bi_2Te_3 thin film measured with unidirectional current: Resistance (R) obtained from linear $V - I$ characteristic at each field B at 2 K, one such measurement at zero field is shown in the inset for applied current from 0 μA to 50 μA. The resistance shows hysteresis that follows that of magnetization of the FM contact.

with current values of 0 μA to 50 μA. The inset of Fig. 6.3 shows one such V-I plot at zero field. From the hysteresis of resistance with applied field shown in Fig. 6.3, it is seen that a high resistive state is obtained at positive magnetic field, while a low resistive state is obtained at negative field. Similar hysteresis is observed in the second set of measurements as shown in Fig. 6.4, where we have obtained the resistance from V-I characteristic with current values of -50 μA to 50 μA. The inset of Fig. 6.4 shows one such V-I plot at zero magnetic field. As seen in Fig. 6.4, the resistance is higher for positive magnetic fields and lower for negative fields, consistent with that of Fig. 6.3. Also, the hysteresis in Fig. 6.4 resembles the one in Fig. 6.3 showing a similar coercive field value. The hysteresis loop observed in the resistance versus applied magnetic field is almost square shape with a coercive field value of about 250 Oe. The hysteresis loop is shifted towards a negative field value, which can be

due to the exchange bias between ferromagnetic Fe and the anti-ferromagnetic oxide of Fe. Also, the local peaks seen in the resistance near the coercive field values can be attributed to the magnetic domain reversal in the multi-domain Fe contact[28]. However, the hysteresis overall shows a single step-like behavior when the FM magnetization direction changes from $+y$ to $-y$ and vice-versa. We obtain the value of the change of resistance ΔR, which is defined as the difference between the measured two-terminal resistance when the FM is up and down, to be 0.3 Ω from the experiment.

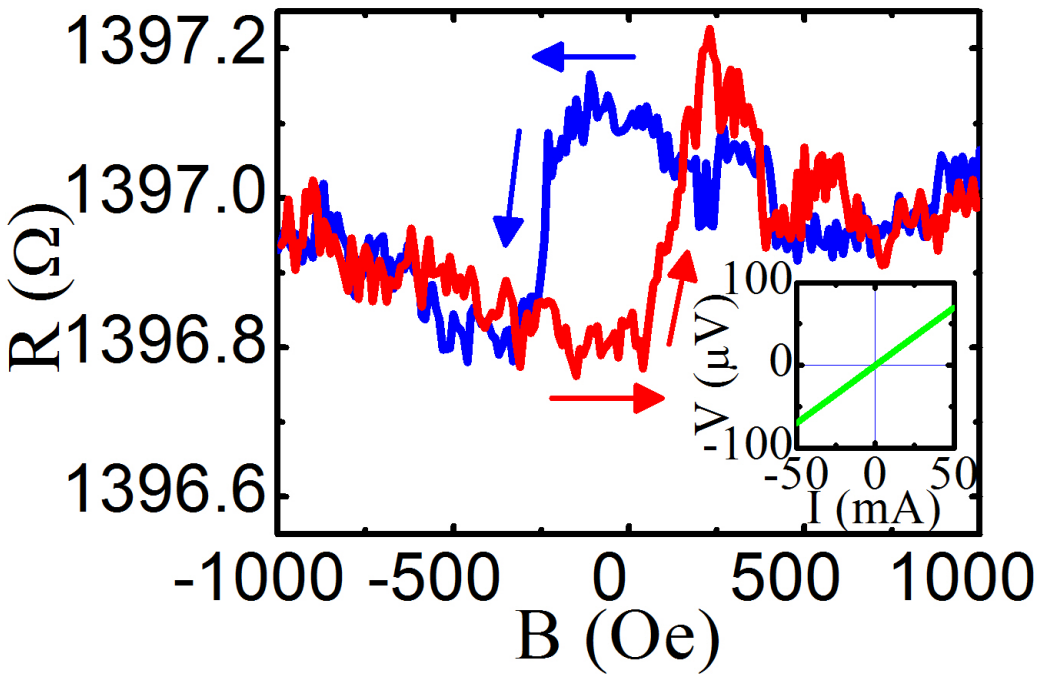

Figure 6.4: Magnetoresistance between FM and NM contacts on the surface of the epitaxial Bi_2Te_3 thin film measured with bidirectional current: Resistance (R) obtained from linear $V - I$ characteristic at each field B at 2 K, one such measurement at zero field is shown in the inset for applied current from -50 μA to 50 μA. The resistance shows hysteresis that follows that of magnetization of the FM contact.

The observed hysteresis in the resistance measured both for positive and negative currents show that the magnetoresistive voltage drop is directly proportional to the magnitude and the sign of the applied current giving a linear V-I characteristics. This consideration rules out the possibility that the observed hysteresis is due to the anisotropic magnetoresistance or

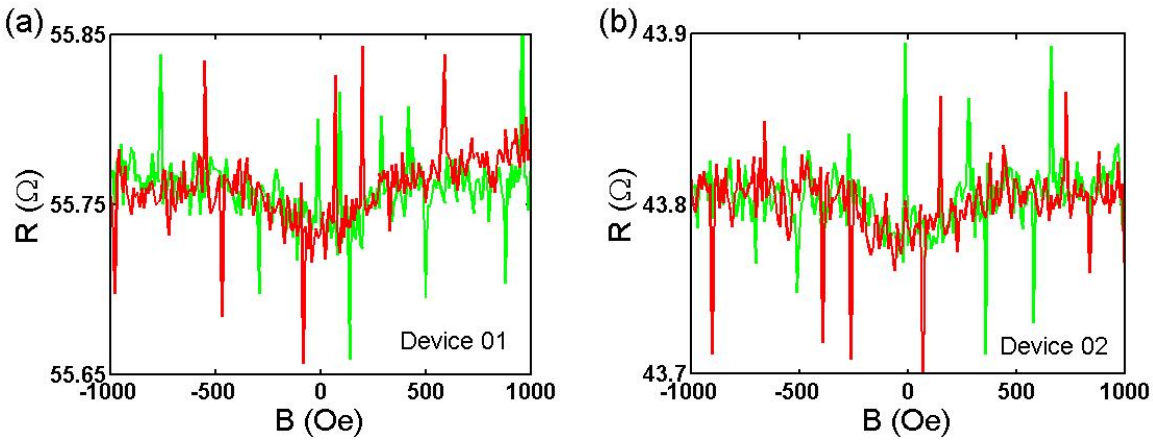

Figure 6.5: Magnetoresistance between FM and NM contacts on Au thin films: Two terminal magnetoresistance between a ferromagnetic MgO/Fe and a nonmagnetic Ti/Au contact deposited on the surface of a 10 nm thick Au film shows no hysteresis. Data for two separate devices are given in (a) and (b).

the anisotropic tunnel magnetoresistance of the Fe contacts, as the voltage drop due to these effects are only proportional to the magnitude of current and not the direction[28, 29, 30]. Also, the Hall effect from the film due to the perpendicular component of fringe fields of the Fe, or the spin Hall effect of the bulk can be excluded as these effects will give rise to a signal much smaller than that we have observed[28, 29, 30]. Further, the anomalous Hall effect or the anomalous Nernst effect of the Fe contact is excluded after doing a controlled experiment.

6.4 Controlled experiments on Au films

As a supporting evidence to show that the observed spin signal is indeed arising from the Bi_2Te_3 thin film, and not due to other spurious effects such as anisotropic magnetoresistance or anisotropic tunnel magnetoresistance or the anomalous Hall effect or the anomalous Nernst effect in the ferromagnetic Fe contact, we repeat the experiments on Au film of 10 nm thickness. We fabricated identical two-terminal device with ferromagnetic MgO/Fe and

nonmagnetic Ti/Au contacts of the same dimensions and thicknesses of the ones we have used for measurement on Bi_2Te_3. As shown in Figure 6.5, the measured resistance in an applied magnetic field is parabolic, which is a characteristic of metallic film, and no hysteresis with field sweep is observed. This results confirms none of the spurious effects in Fe is responsible for the observed hysteresis in the resistance with magnetic field sweep in our Bi_2Te_3 sample. So, we conclude that the hysteresis observed in the measurement on the TI thin film is because of the Bi_2Te_3 thin film.

6.5 Two-terminal measurement on exfoliated Bi_2Te_3 film with Fe contact

The devices used for magneto-transport measurements on exfoliated Bi_2Te_3 flakes consists of Fe as the FM contact and Ti/Au as the NM contact. The FM were deposited by e-beam evaporation and patterned by e-beam lithography. For the FM contact, a vertical stack of SiO_2(2 nm)/Fe(50 nm) was deposited on the Bi_2Te_3 flakes, and the Fe was capped by Au. Two-terminal V-I measurements were performed, as schematically illustrated in Fig. 6.6 with the magnetization easy-axis of the Fe bar along the y-direction, which is normal to the direction of current flow (in the x-direction). The definition of positive and negative current flow, and up and down magnetization (along the y axis) of the Fe are shown in Fig. 6.6. The magnetic orientation of the Fe was set using an external in-plane magnetic field prior to each V-I trace. Two sets of V-I data were collected at room temperature, $V_{H,\uparrow}$ for magnetization up in the Fe contact and $V_{H,\downarrow}$ for magnetization down in the Fe contact, as shown in Fig. 6.6. The voltage difference $\Delta V = V_{H,\uparrow} - V_{H,\downarrow}$ is obtained by subtracting these two sets of V-I data, as illustrated in Fig. 6.6.

Figure 6.7 displays ΔV with the applied current I for the device, with multiple runs

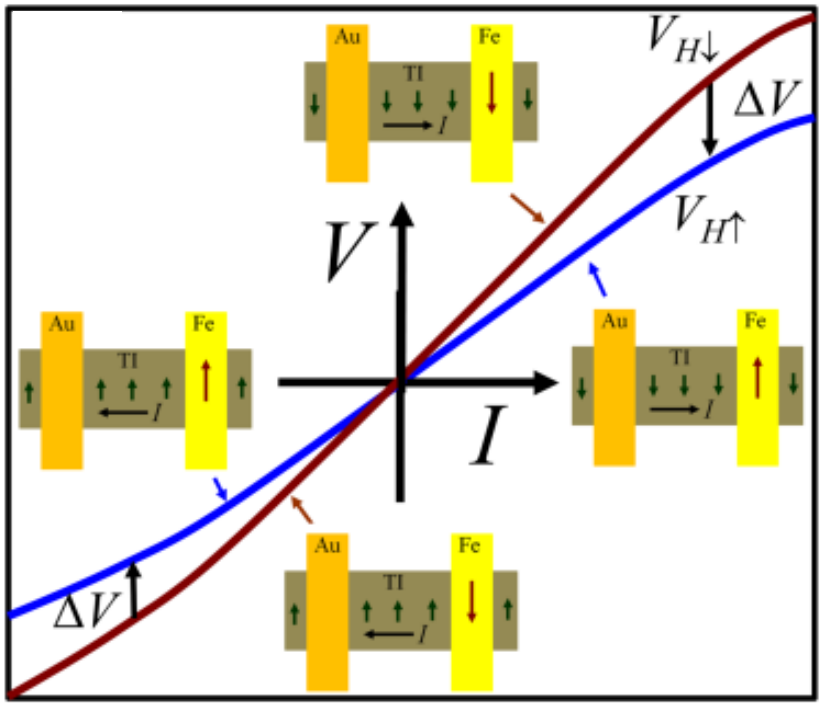

Figure 6.6: Voltage-current characteristics with FM and NM contacts on the surface of TI for different magnetization orientations of the FM: Illustration of extraction of ΔV from voltage-current (V-I) characteristics for up and down Fe magnetization orientations. The orientation of the net magnetic moment of electrons on the TI surface for the positive and negative current sweep is also shown with smaller arrows on the TI.

including both positive-to-negative and negative-to-positive current sweeps, and pre-aligning the magnet and then resetting it to zero and pre-aligning again. The observed effect is highly reproducible and independent of the measurement order. The sign of ΔV and the change thereof with the current direction is consistent with the experiment performed on the epitaxial Bi_2Te_3 sample, since the FM and the NM contacts are interchanged and so the convention for the direction of the current flow. The V-I characteristic (shown in Fig. 6.6), and so the ΔV-I characteristic (shown in Fig. 6.7), exhibit tunneling behavior (nonlinear V-I for higher current) due to the presence of the SiO_2 layer between the Bi_2Te_3 surface and Fe contact. From the linear region of the curve, we obtain that ΔV is in the scale of 4 mV for current in the order of 40 μA, at room temperature.

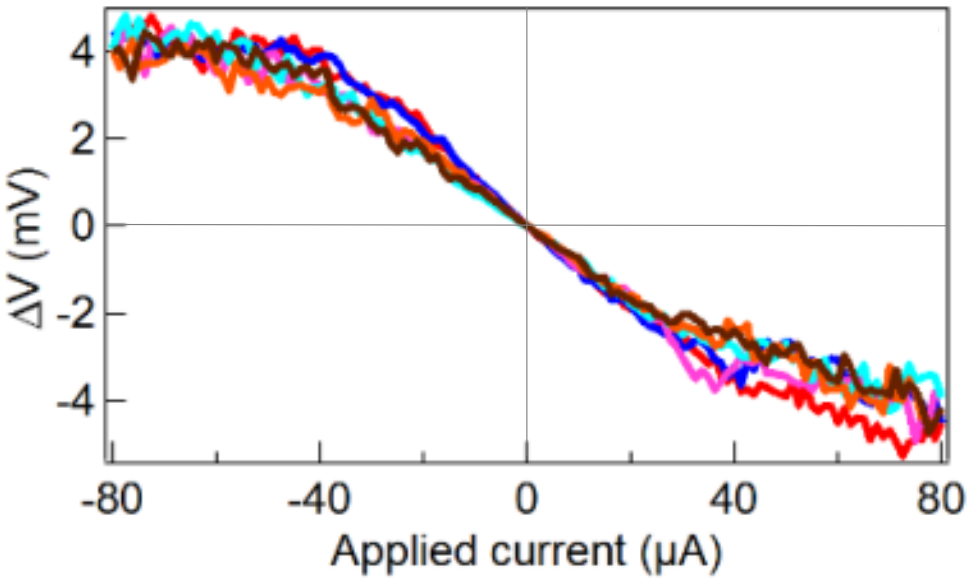

Figure 6.7: Change of voltage-current characteristic upon reversal of the magnetization direction of the FM: ΔV as a function of applied current I at room temperature for multiple runs, including positive to negative current sweep, two consecutive runs with pre-aligning the Fe bar initially and then resetting the magnet to zero and again pre-aligning it, and then repeated for applied negative to positive current sweeps. All runs show similar behavior, exhibiting the reproducibility of these measurements

6.6 Comparison to two-terminal experiments with two FM contacts on TI reported in the literature

In the literature, two-terminal measurements on the surface of TIs were performed using two FM contacts, as in [56] with 40 nm thick Ni contacts on exfoliated Bi_2Se_3 flakes of 10 - 20 nm thickness and in [57] with 50 nm thick $Ni_{21}Fe_{79}$ contacts on exfoliated $BiSbTeSe_2$ flakes of 7 nm thickness. In both of those measurements, two different resistive states were observed with both the FM being aligned in one direction or both the FM being aligned in the reverse direction. Such a change of resistance with reversal of the magnetization directions of both

the FM violates the Onsager reciprocity relation. Also, in both of those experiments, change of resistances with change of the applied current direction were observed, i.e., the resistances showed spin-diode-like behavior in the I-V characteristics. In the literature, Semenov *et al.*[81] proposed a phenomenological model for the violation of the Onsager reciprocity and the violation of the linear I-V relationship around the zero bias, but only in the quasi-ballistic mesoscopic regime of the transport on the TI surface. In our case, we have performed two-terminal measurements with only one FM and other NM contact, and we have obtained linear I-V characteristic around the zero bias, although the Onsager reciprocity relation is violated.

6.7 Explanation of the two-terminal magnetoresistance with FM contact on the TI surface

Very recently, Tian *et al.*[127] observed spin memory effect in three-terminal spin detection experiments on the surface of a TI and postulated that one possible reason for the spin memory effect might be the hyperfine interaction between the nuclear spin in the atom and the conduction electron spin, in which atomic nuclear spin has a much larger lifetime giving rise to a memory effect. In case of two-terminal magneto-resistance experiments involving FM contacts on the surface of TIs, such hyperfine interaction could similarly give rise to change of resistance upon magnetic field reversal. Since the nuclear spins in the atoms do not relax to become reversed with the reversal of the FM magnetization, the Onsager reciprocity relation could not be applied, since application of the Onsager reciprocity relation requires time reversal invariance, which is achieved by reversing all the internal magnetic moments and the external magnetic fields in the system. In chapter 4, we have shown that in the purely diffusive regime of transport, the Onsager reciprocity relation is maintained

in detection of charge current-induced spin polarization of the TI surface states. In the experiments, the transports on the TI surfaces are mostly diffusive. Therefore, the change of resistance with reversal of FM magnetizations in these two-terminal measurements with FM contacts must have a different source than the reason provided for three and four-terminal spin detection experiments, in which the voltage on the FM contact changes with the FM magnetization direction because of the charge current-induced spin polarization of the TI surface states.

6.8 Summary

In summary, we experimentally measured the resistance between a FM and a NM contact on the surface of a epitaxially grown Bi_2Te_3 thin film as well as on the surface of exfoliated Bi_2Te_3 films. The two-terminal resistance between the FM and the NM contacts shows hysteresis with the applied field tracking that of the magnetization of the FM contact. We provide an explanation for the detected spin signal indicating the role of hyperfine interaction between the conduction electron spin and the long-lived nuclear spin states in such measurements.

Chapter 7

Sputter depositions of Bi_2Te_3 and Bi_2Te_3-Fe heterostructures

In this chapter, we discuss the method to obtain thin films of Bi_2Te_3 by sputter deposition from a single Bi_2Te_3 sputtering target and how to tune the sputtering parameter to obtain different compositions such as Bi_4Te_3 and Bi_2Te_3. Next, we discuss the deposition of Bi_2Te_3-Fe heterostructure by sputtering, and report magnetic hysteresis measurement showing the effect of the underlying Bi_2Te_3 thin film on the magnetic properties of these heterostructures.

7.1 Conditions for composition tuning of sputtered Bi_xTe_y

The sputtering target that we use is a 99.999% pure Bi_2Te_3 composite material and we have deposited all our thin films in a direct current (DC)-magnetron sputtering system with base pressure in the order of 10^{-7} Torr and in an Ar sputtering environment. By tuning the sputtering pressure of Ar and the DC power of the target, we have obtained both the compositions Bi_4Te_3 and Bi_2Te_3 by sputtering from a single Bi_2Te_3 target under different conditions. The different compositions that we obtain are identified from x-ray diffraction (XRD) and Raman spectroscopy. We also have varied the substrate temperature to improve the crystallinity and the composition of the sputtered films. In the following, we describe qualitatively the mechanism behind obtaining different compositions of the film from the same sputtering target.

In the literature[128], it is known that the sputter yield of Bi atom is higher than that of

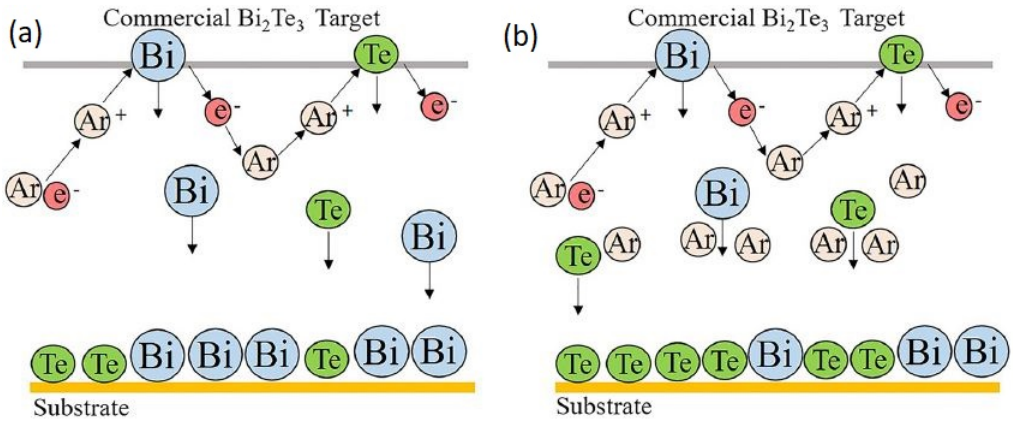

Figure 7.1: Schematic representation of the effect of sputtering pressure on Te content in the composition of the sputtered film: (a) Sputtering yield of Te being lower than Bi, lower sputter pressure results in lower Te content, (b) Increasing the sputtering pressure of sputter gas (Ar) increases the Te content in the deposited film. Reprinted by permission from The Minerals, Metals & Materials Society: Springer, *Journal of Electronic Materials*, Vol. **46**, No. 11, "[Bi]:[Te] Control, Structural and Thermoelectric Properties of Flexible Bi_xTe_y Thin Films Prepared by RF Magnetron Sputtering at Different Sputtering Pressures", P. Nuthongkum, R. Sakdanuphab, M. Horprathum, and A. Sakulkalavek, Copyright 2017. Available: https://doi.org/10.1007/s11664-017-5671-x. (Ref. [128] in this dissertation)

Te atom. If the sputtering pressure is low, more Bi atoms will reach the substrate than Te atoms, then the composition of the film will be Bi-rich, as shown in Fig 7.1(a). However, Bi atom has larger atomic mass than Te atom, hence, Bi atoms are bigger in size than the Te atoms. So, if the pressure of the sputter gas Ar is increased, Bi atoms being bigger in size than the Te atoms will be more likely to collide with the Ar atoms than the collision rate of Te with Ar. So, with increase in the Ar pressure, the relative composition of Bi in the sputter deposited film Bi_xTe_y can be made lower, as shown in Fig 7.1(b). However, due to increase in the pressure of the Ar gas, Te atoms will collide with Ar atoms too, and the rate of deposition will decrease significantly. Also, with the increase of the power of sputtering, more Ar ion will hit the target and the rate of emission of both Bi and Te atoms will increase. However, since the sputter yield changes with the power of the sputtering source, by tuning the power of the sputtering source the composition of the deposited film also can be tuned. It has been

shown previously[129] that with increase of sputtering power the relative composition of Te content in Bi_xTe_y increases. Hence, it is desirable to increase the DC power of the target appropriately along with an increase of the pressure of the sputter gas to optimize the control of the composition of the Bi_xTe_y films and to maintain a reasonable rate of sputtering.

7.2 Sputter deposition of Bi_4Te_3 thin films on Si substrates

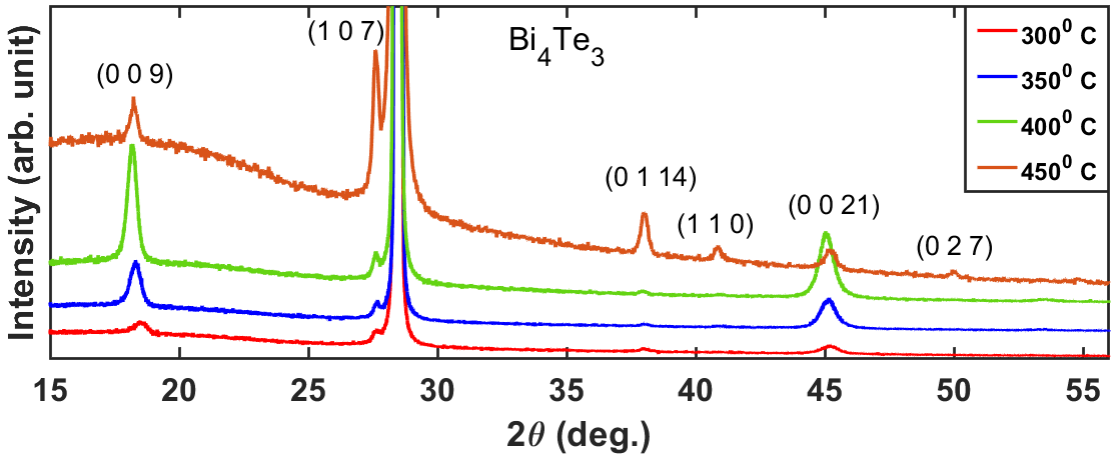

Figure 7.2: XRD measurements on sputtered Bi_4Te_3 thin films sputtered at different substrate temperatures from 300^0C to 450^0C.

The Bi_4Te_3 thin films are deposited on Si(111) and Si(100) substrates with Ar pressure of 5 mTorr and DC power of 10 W for 30 minutes, in each deposition, at substrate temperatures ranging from 300^0C to 450^0C . The deposited films are not annealed after deposition, however the pressure in the chamber is maintained at 30 mTorr after the deposition until the substrate temperature cools down to room temperature to avoid any Te evaporation at high temperatures (after deposition and before cooling when no Te atom can reach and compensate the Te deficiency due to evaporation). The XRD patterns of the deposited thin films on Si(111) are shown in Fig. 7.2 with all the peak positions identified with the corresponding crystal planes of Bi_4Te_3. The XRD patterns show that the intensity of the peaks

increases with increasing substrate temperature upto 400^0C, implying better crystallinity of the deposited films due to increased mobility of the constituent atoms at higher temperature during deposition. However, once we increases the substrate temperature further to 450^0C, there are additional peaks appearing in the XRD spectrum indicating that the quality of the thin film diminishes, which might be due to extra Te evaporation that cannot be compensated. From the (1 0 7) and (0 0 21) peaks of the XRD pattern, we calculate the lattice parameters of the deposited Bi_4Te_3 thin films, and obtain $a = 4.41$ Å, and $c = 42.1$ Å in close agreement with those reported in the literature[130].

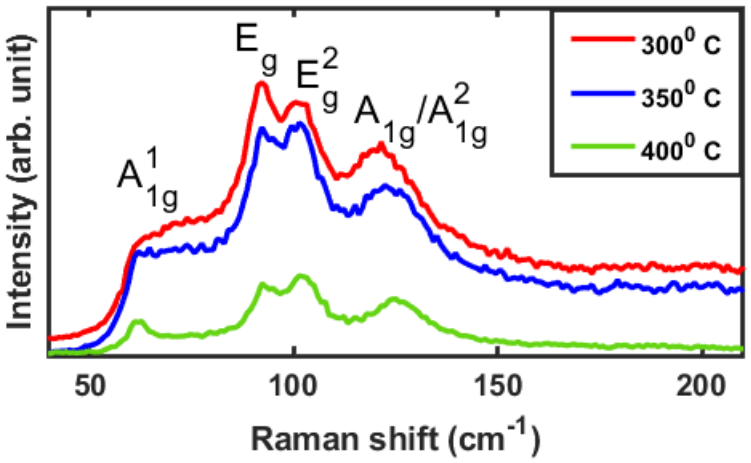

Figure 7.3: Raman spectra of sputtered Bi_4Te_3 thin films sputtered at different substrate temperatures from 300^0C to 400^0C.

We further study the Raman vibrational spectroscopy of the sputtered Bi_4Te_3 films. Figure 7.3 shows the Raman spectra of the sputtered Bi_4Te_3 films deposited at substrate temperature of 300^0C, 350^0C and 400^0C (we do not show the data for the film deposited at 450^0C, since we already find out from the XRD result that the quality of the film deposited at 450^0C is not good). The peaks at 62 cm^{-1}, 92.3 cm^{-1} and 101.4 cm^{-1} match exactly with that of Bi_4Te_3 with A^1_{1g}, E_g and E^2_g modes of vibrations, respectively[131]. However, the Raman peak at 120.6 cm^{-1} for 300^0C, 122.4 cm^{-1} for 350^0C, and 124.2 cm^{-1} for 400^0C, are in-between the reported A_{1g} (at 114.9 cm^{-1}) and A^2_{1g} (at 132.2 cm^{-1}) modes[130, 131].

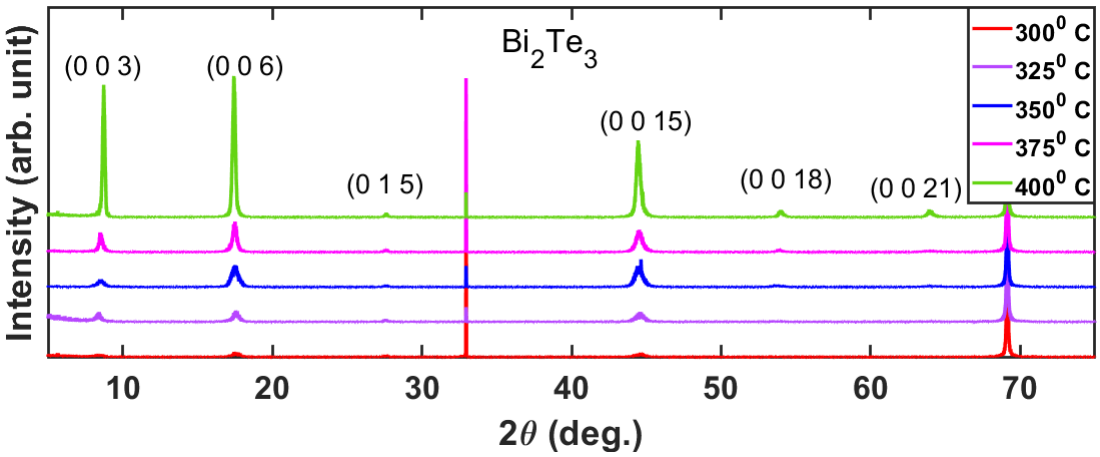

Figure 7.4: XRD measurements on sputtered Bi_2Te_3 thin films sputtered at different substrate temperatures from 300^0C to 400^0C.

7.3 Sputter deposition of Bi_2Te_3 thin films on Si substrates

To obtain Bi_2Te_3 composition, which has less Bi content than in Bi_4Te_3, we have increased the pressure of the Ar gas and also have increased the DC power, as described before. The Bi_2Te_3 thin films are deposited on Si(100) substrates with Ar pressure of 30 mTorr and DC power of 20 W for 30 minutes, in each deposition, at substrate temperatures ranging from 300^0C to 400^0C. The deposited films are not annealed after deposition, and the pressure in the chamber is maintained at 30 mTorr after the deposition until the substrate temperature cools down to room temperature to avoid any Te evaporation at high substrate temperatures. The XRD patterns of the deposited Bi_2Te_3 thin films are shown in Fig. 7.4 with all the peak positions identified with the corresponding crystal planes of Bi_2Te_3. All the predominant peaks in the XRD spectrum of Bi_2Te_3 correspond to the (0 0 3n) family of plane which are perpendicular to the c-axis of the Bi_2Te_3 crystal lattice, except for the peak at (0 1 5), which is natural if the underlying substrate is rough. The XRD patterns show that with increasing substrate temperature the intensities of the peaks increase implying better crystallinity of

the deposited films. From the (0 1 5) and (0 0 15) peaks of the XRD pattern, we calculate the lattice parameters of the deposited Bi_4Te_3 thin films, and we obtain $a = 4.40$ Å, and $c = 30.51$ Å in agreement with those in the literature[130].

We observe that once we take the samples out of the chamber to the ambient atmosphere, there are clear color change in the films, which are deposited at 375^0C and 400^0C, that did not occur for films deposited at 350^0C. We have observed such color change in all the Bi_4Te_3 films, and we associate the color change with oxidation of excess Bi in atmosphere. It has been shown in the literature[132] that above a critical substrate temperature the Te content in sputtered Bi_xTe_y films decreases. In chapter 6, we have mentioned that the epitaxial Bi_2Te_3 films were grown at 350^0C[94, 95, 125]. We postulate that above the substrate temperature of 350^0C, the Te atoms evaporate from the deposited films due to low vapor pressure of Te, and the films become Te deficient and Bi rich, and the excess Bi gets oxidized in the atmosphere. Hence, we consider 350^0C as the optimum substrate temperature to obtain Bi_2Te_3 sputtered films with best composition and good crystallinity supported by the x-ray reflectivity (XRR) analysis of these Bi_2Te_3 films sputtered at different substrate temperatures.

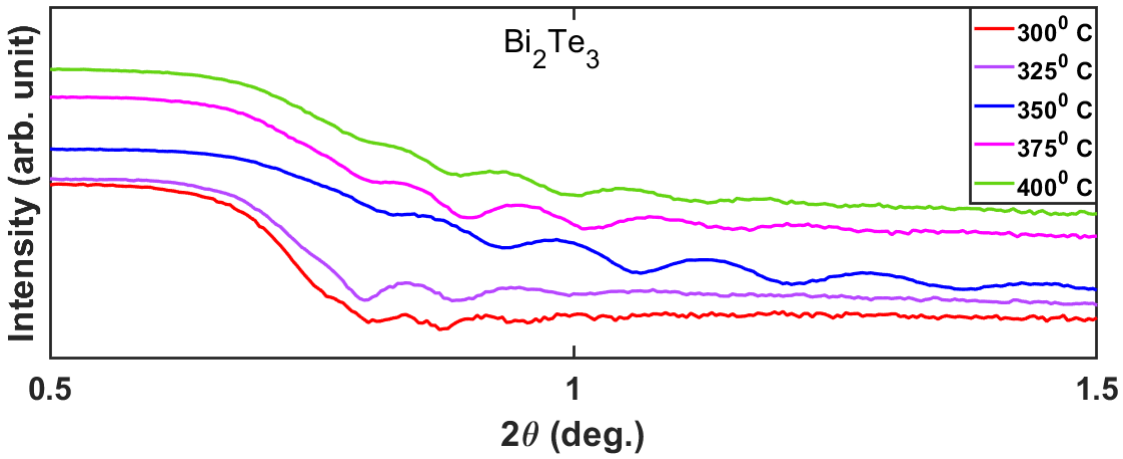

Figure 7.5: XRR measurements on sputtered Bi_2Te_3 thin films sputtered at different substrate temperatures from 300^0C to 400^0C.

Figure 7.5 shows the XRR pattern of the sputtered Bi_2Te_3 films deposited at substrate temperature ranging from 300^0C to 400^0C. The oscillations in the XRR patterns of the Bi_2Te_3 films deposited at 300^0C and 325^0C die out rapidly at very small 2θ values indicating roughness and poor crystallinity of the films. The oscillations in the XRR patterns of the Bi_2Te_3 films deposited at 375^0C and 400^0C stay longer than that of 300^0C and 325^0C, but die out before that of 350^0C. The oscillation in the XRR pattern of the Bi_2Te_3 film deposited at 350^0C are very clear and stay even upto 2θ of 1.5^0, which indicates that the substrate temperature of 350^0C is optimum for the deposition of the sputtered Bi_2Te_3 film. The thickness of the Bi_2Te_3 film sputtered at substrate temperature of 350^0C is 33 nm.

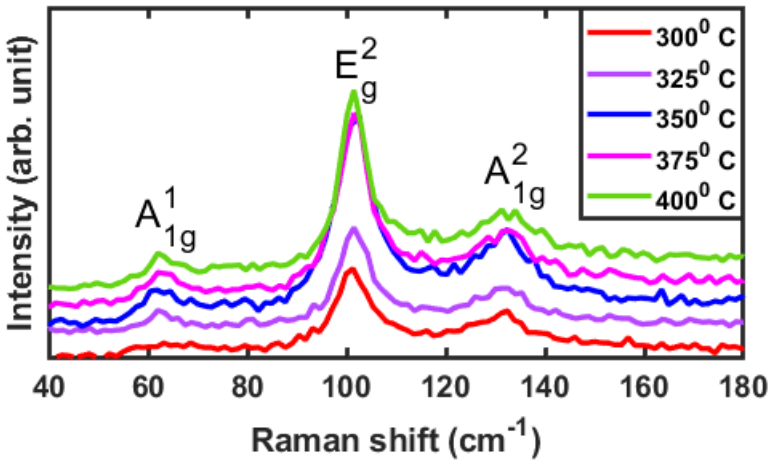

Figure 7.6: Raman spectra of sputtered Bi_2Te_3 thin films sputtered at different substrate temperatures from 300^0C to 400^0C.

Figure 7.6 shows the Raman spectra of the sputtered Bi_2Te_3 films deposited at substrate temperature ranging from 300^0C to 400^0C. All the Bi_2Te_3 films sputtered at different substrate temperature of 300^0C to 400^0C show Raman spectra at 62 cm^{-1}, 101.5 cm^{-1} and 132.5 cm^{-1}, which are associated with the A^1_{1g}, E^2_g and A^2_{1g} modes, respectively, and match exactly with those reported in the literature[130, 131].

7.4 Sputter deposition of Bi_2Te_3 thin films on different substrates

From Fig. 7.4, we can see that all the XRD peaks of the sputtered Bi_2Te_3 films corresponds to (0 0 3n) family of planes except (0 1 5) peak. The presence of (0 1 5) peak indicates that the sputtered films are not perfectly single crystalline. However, the Si substrates that we have used for deposition of the sputtered Bi_2Te_3 films had native oxides on top of it, which had made the surface atomically rough. To remove the unwanted (0 1 5) peak in the deposited Bi_2Te_3 thin films, we use HF-dip to remove the native oxide from the Si substrate. We also use different substrates with atomically smooth surfaces for deposition. The Si substrate after HF-dip was transfered inside the chamber within few minutes. As a different substrate than Si, we use sapphire (Al_2O_3) and thermally grown SiO_2 on Si. Because of controlled oxidation, the surface of a thermally grown SiO_2 is smooth. The sputtering conditions for the deposition are kept the same as before, with a substrate temperature of 350^0C but with a reduced sputtering time of 5 minutes. As the surface of the sputtered Bi_2Te_3 thin film also is prone to oxidation in the atmosphere, we perform one sputter deposition on Si with the same sputtering conditions (the one used to sputter Bi_2Te_3 on different substrates and shown in Fig. 7.7) but with a capping layer of indium tin oxide (ITO).

The 2θ-ω XRD scans of the sputtered Bi_2Te_3 films deposited on different substrates are shown in Fig. 7.7. The data shown in Fig. 7.7 are the logarithmic value of the actual measured intensities and then shifted in the y-axis for clear visibility (data shown in Figs. 7.2 and 7.4 are just the measured intensities shifted in the y-axis). From the XRD spectra in Fig. 7.7, we can see that the (0 1 5) peak is absent indicating single crystallinity of the sputtered Bi_2Te_3 films. The thicknesses of the films are about 6 nm each calculated both from the XRR (not shown here) and full width half maximum (FWHM) of the XRD peaks. We also observe that the intensities of both (0 0 18) and (0 0 21) peaks are prominent in

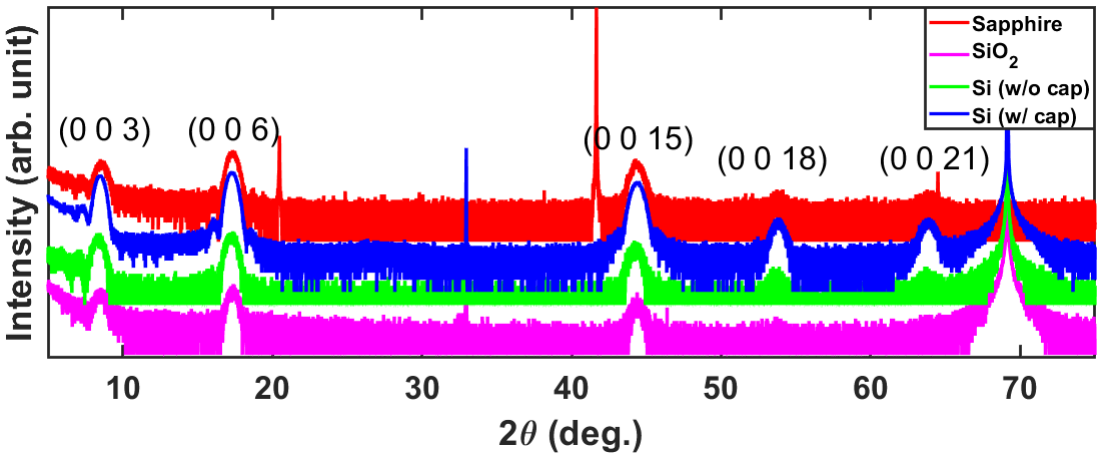

Figure 7.7: XRD measurements on sputtered Bi_2Te_3 thin films on different substrates with and without capping layer: without (w/o) any capping layer on sapphire, SiO_2 and Si, and on Si with (w/) capping layer of ITO.

the sputtered film with ITO capping. In Fig. 7.7, the FWHM of any peak for different films is almost the same as the other, because the broadness of the peaks are due to the finite thickness of the films in the surface normal direction.

To obtain further information about the crystalline size and tilts of the grains in the sputtered Bi_2Te_3 thin films, we perform ω scans (rocking curve) around (0 0 6) and (0 0 15) peaks. Figure 7.8 shows rocking curves of (0 0 6) and (0 0 15) peaks for the Bi_2Te_3 thin films sputtered on Si and capped by ITO. The rocking curve of (0 0 6) peak has a very sharp peak convoluted with a broader peak, as shown in Fig. 7.8(a). However, the sharp peak is absent in the rocking curve of (0 0 15), as shown in Fig. 7.8(b). The FWHM of the peak in the rocking curve of (0 0 15) is about 2^0.

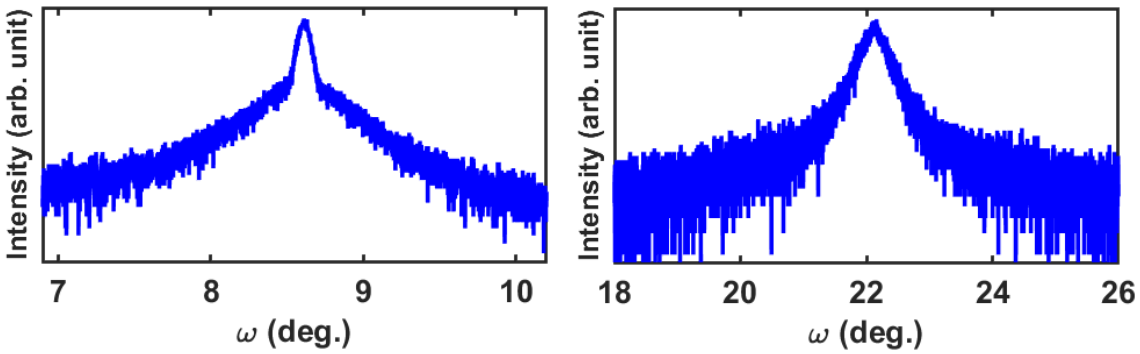

(a) (b)

Figure 7.8: Rocking curve of (0 0 6) and (0 0 15) peaks: The data are shown in (a) and (b) for (0 0 6) and (0 0 15) peaks, respectively.

7.5 Magnetic properties of sputtered Bi_2Te_3-Fe heterostructures

Towards fabricating and characterizing topological insulator (TI)- ferromagnetic material (FM) based spintronic devices, the next step is to grow TI-FM heterostructure. We sputter Bi_2Te_3-Fe heterostructures on high resistive Si substrates and cap the surface of Fe either with VO_x or with ITO to prevent any oxidation of the Fe films. It is desirable to have an insulating capping layer to reduce any current shunting in such devices, however, ITO capping may be useful for studying magneto optic Kerr imaging (MOKE) of the heterostructure. We also vary the thickness of the Fe layer keeping the thickness of the Bi_2Te_3 the same. Controlled samples with same thickness of Fe on Si are grown and capped with either VO_x or ITO. We measure room temperature magnetic hysteresis of these controlled samples as well as of those samples with Bi_2Te_3-Fe heterostructure using vibrating sample magnetometer (VSM).

The magnetic hysteresis measurement on these devices are shown in Fig. 7.9. The easy axis of the deposited Fe films lie in the plane of the surface of these heterostructures. Figure 7.9(a) shows the normalized magnetization curves with the applied magnetic field sweep along the easy axis of the Fe film in a Si/Fe/VO_x sample as well as in a Si/Bi_2Te_3/Fe/VO_x

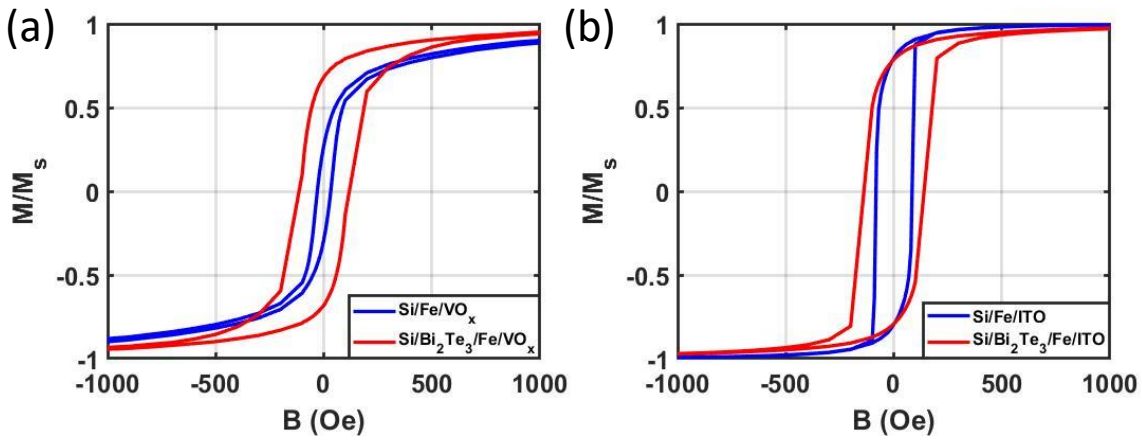

Figure 7.9: Magnetization hysteresis of Fe and Bi_2Te_3-Fe heterostructures: (a) 5.5 nm Fe thickness with VO_x cap, (b) 19.8 nm Fe thickness with ITO cap.

sample with Fe thickness of 5.5 nm in both the samples and the thickness of Bi_2Te_3 being 15 nm. Figure 7.9(b) shows the normalized magnetization curves with the applied magnetic field sweep along the easy axis of the Fe film in a Si/Fe/ITO sample as well as in a $Si/Bi_2Te_3/Fe/ITO$ sample with Fe thickness of 19.8 nm in both the samples, and the thickness of Bi_2Te_3 is kept the same as 15 nm. From both Figs. 7.9(a) and 7.9(b), it is clear that the coercive field value of the Bi_2Te_3-Fe heterostructure is larger than that of the Fe thin film in both the cases. The enhancement of the coercive field could be due to strong spin-orbit coupling proximity effect arising from the Bi_2Te_3 film.

7.6 Summary

In summary, we have sputtered both Bi_4Te_3 and Bi_2Te_3 thin films from a single Bi_2Te_3 sputtering target by optimizing the sputtering conditions. Thin films of Bi_4Te_3 and Bi_2Te_3 are deposited on Si and structural characterizations are performed on those thin films to obtain information about the crystalline quality and material composition. We also obtain high quality crystalline thin films of Bi_2Te_3 deposited on HF-cleaned Si, sapphire and ther-

mally grown SiO_2 substrates. Next, we deposit Bi_2Te_3-Fe heterostructure by sputtering and measure the magnetic hysteresis of the heterostructures to compare with that of Fe without the Bi_2Te_3 film. These films are capped with either VO_x or ITO to prevent oxidation of the exposed surface in the environment. From the magnetic hysteresis measurement, we obtain that the proximity coupling of Bi_2Te_3 to Fe enhances the coercive field of Fe, which could be due to strong SOC from the underlying Bi_2Te_3.

Chapter 8

Conclusion

8.1 Summary of the dissertation

This dissertation focuses on the theoretical study of the spin-to-charge and charge-to-spin conversion that can take place on the surface of a three-dimensional (3D) topological insulator (TI) due to the remarkable property of spin-momentum locking of the two-dimensional (2D) surface states of the TI, as well as, on the experimental realization of such TIs and analysis of the transport properties of these TIs in various conditions such as in an applied magnetic field or in proximity to a ferromagnet. The main aim of this research is to provide a sound foundation on the theory and analysis of various electronic transport properties of the TI and offer a better understanding of the spin-charge manipulation on the TI surface for potential spintronics applications. In chapter 2, chapter 3 and chapter 4, we derive a theory of the electronic transport of TI surface states in proximity to a non-magnetic material (NM) or a ferromagnetic material (FM) based on quantum kinetic equations of non-equilibrium Green's functions. We then calculate the efficiency of spin current-to-charge current conversion as well as efficiency of detection of charge current-induced spin polarization on the TI surface, and support our results with actual experimental facts to provide a thorough understanding of the physics behind the experiments. Chapter 5, chapter 6 and chapter 7 discuss experiments on epitaxially grown, exfoliated and sputtered TI thin films. In chapter 5, we characterize the bulk contribution to the electronic transport in a TI thin film along with the conduction from the surface states. In chapter 6, we measure the two-terminal re-

sistance between a FM and a NM contacts on the surface of Bi_2Te_3 films. Chapter 7 focuses on the growth and characterization of sputtered Bi_2Te3 thin films and magnetic properties of sputtered Bi_2Te3-Fe stacks. The main conclusions of each chapter are summarized below.

In chapter 2, the theory of spin current-to-charge current conversion, known as the inverse Edelstein effect (IEE), on the surface of a TI is discussed specifically in the set-up of spin-pumping experiment with TI/NM/FM heterostructure. We calculate the open-circuit voltage that will be developed at two ends on a TI surface to oppose the induced charge current flow on the TI surface due to spin current injection. We find that the open-circuit voltage depends on the transport relaxation length on the TI surface, the transmission rate of electrons through the TI/NM interface as well as the dimensions of the device used in such experiments. We find that the magnitude of the open-circuit voltage decreases with decreasing resistance of the TI/NM interface.

In chapter 3, the theory of IEE on the surface of a TI is discussed in the set-up of spin-polarized tunneling experiment in which a spin-polarized charge current is injected from the FM to the TI surface through a tunnel barrier and an open circuit voltage is measured between two ends on the TI surface. We calculate the open-circuit voltage and discuss the effect of the size of the devices on the magnitude of the open-circuit voltage. We also find that the magnitude of the open-circuit voltage decreases as the tunnel resistance of the TI/FM interface decreases.

In chapter 4, we develop the theory described in chapter 3 to analyze the voltage measured in a multi-terminal measurement geometry to detect the charge current-induced spin polarization of the TI surface states. We consider line FM contacts as well as non-zero length FM contacts in our calculations and show how the spin detection efficiency of the FM tunnel contact decreases with the length of the contact. We also find that the spin detection

efficiency decreases with decreasing contact resistance of the tunnel contact.

One of the main conclusion of chapter 2, chapter 3 and chapter 4 is the crucial importance of tunnel contact (or interface) on the spin-charge conversion efficiency on the TI surface, which requires careful design of the tunnel barrier or the interface in obtaining a better spin-to-charge conversion efficiency.

In chapter 4, we also theoretically establish the validity of Onsager reciprocity relation in resistance measurement in multi-terminal and two-terminal experiments consisting of FM and NM contacts on the surface of a diffusive TI. We specifically show that the two-terminal resistance consisting of one or both FM contacts does not depend on the magnetization direction of the FM contact(s). However, in chapter 6, we experimentally observe that the two-terminal resistance between a FM Fe and an NM Au contacts on the surface of Bi_2Te_3 changes with the reversal of the FM magnetization direction. We give a possible resolution of the apparent violation of the Onsager reciprocity relation indicating role of long-lived nuclear spin states that do not relax back or change direction even after the reversal of the FM magnetization direction, thus Onsager relation cannot be applied.

In chapter 5, we provide the low temperature magnetotransport measurements in an epitaxially grown Bi_2Se_3 thin film and give a thorough analysis of the transport results discussing the effect of localizations and interactions both from the surface states and the bulk states of the TI thin film. In chapter 7, detailed growth and structural characterization method are provided to obtain sputtered Bi_2Te_3 thin films with good crystallinity. We also measure magnetic hysteresis in sputtered Bi_2Te_3-Fe heterostructure and show how Bi_2Te_3 can affect the magnetic properties of Fe.

8.2 Scope of future work

In the following we describe some possible future research directions that are be based on the outcomes of this dissertation.

In deriving the transport of the TI surface states coupled to a NM or a FM, we have considered gapless linear Dirac-cone dispersion relation for these surface states. However, in a TI thin film or in proximity to a FM magnetized in the surface normal direction, there will be a gap opening around what would otherwise be the Dirac point. If the Fermi energy lies well above the Dirac point, which is generally the case for a doped TI sample (such unintentional doping occurs during the growth of the sample), the linear dispersion relation for the surface states is still a very good approximation. However, there could be hexagonal warping effect in the band structure of the surface states away from the Dirac point, as in Bi_2Te_3, and such effect must be taken into account. In intrinsic TIs, the Fermi surface will lie near the Dirac point, hence, the effect of the gap opening has to be considered. It would be a straight-forward extension of our work presented in chapter 2, chapter 3 and chapter 4 to consider the case of TI surface states with a gap around the Dirac point or with hexagonal warping effect present away from the Dirac point.

In chapter 5, we have shown that the bulk states also contribute to the electronic transport of TI films even at low temperatures because of the Fermi energy lying in the bulk band due to unintentional doping during growth. However, we have shown that the transport properties of the bulk states can be quite different from the surface states, for example weak localization from the bulk states and weak antilocalization from the surface states. The band dispersion of the TI bulk states in thin films are also quite different from the one with traditional material having Rashba spin-orbit coupling. Identification of bulk contribution and further analysis of the effects from the bulk states are necessary from a spintronics

point of view, since most of the spintronic applications are based on the properties of the TI surface states. Hence, the properties of these bulk states in spin current-to-charge current conversion and charge current-induced spin polarization need to be understood in the light of what we have shown in chapter 2, chapter 3 and chapter 4 for the surface states.

Apart from taking into consideration of the gap opening in the surface states and quasi-2D bulk bands in TI thin films, there could be tunneling of electrons between the two opposite surfaces in a 3D TI. It is another possible research direction in which the effect of such tunneling on spin-charge conversion in a TI thin film could be analyzed. Also, there could be significant bulk surface scattering present, as we have found in epitaxial Bi_2Te_3 thin films presented in chapter 6. The bulk-surface scattering will also effect the spin-charge conversion efficiency and consideration of the bulk-surface coupling in the transport is a potential area of research.

We have derived the transport of the TI surface states considering only impurity scattering on the surface of the TI. In chapter 5, by analyzing the low temperature magnetotransport in a Bi_2Se_3 thin film, we have identified that electron-electron interaction has a crucial rule on the transport properties of both the surface states and the bulk states and cannot be ignored. Similarly, in the finite temperature, electron-phonon interaction will be present in the TI. In a TI/FM heterostructure, magnon scattering of the TI surface states will play a role too due to proximity to a FM. The effects of all other scattering mechanism besides only impurity scattering need to be taken into account to obtain more reliable predication of charge-spin conversion efficiencies in room temperature spintronics devices.

One of the main conclusion of chapter 2, chapter 3 and chapter 4 is that the efficiency of spin current-to-charge current conversion as well as the detection efficiency of charge current-induced spin polarization on the TI surface depend on the tunnel conductance of

the TI/NM or the TI/FM interface. In our theoretical model, the tunneling strength is a phenomenological parameter described by the tunneling Hamiltonian. To obtain a realistic value for the tunneling strength, first principle density functional theory (DFT) calculations are needed. Hence, it is of practical interest to do such DFT calculations in TI/NM and TI/FM heterostructure and incorporate such calculations in the non-equilibrium transport equations to get more realistic estimate for these efficiencies.

In chapter 4, we have theoretically shown that the Onsager reciprocity relation is satisfied for multi-terminal and two-terminal resistance measurements on the surface of a diffusive TI with FM tunnel contacts. However, in chapter 6 we report experimental results on two-terminal resistance between a FM and a NM contact on Bi_2Te_3 and show apparent violation of the reciprocity relation. We propose an explanation of the experimental results based the hyperfine interactions of conduction electron with the long-lived spin magnetic moments of the heavy atoms in Bi_2Te_3. It was shown in the literature that such violation of reciprocity relation in two-terminal resistance between two FM contacts on the TI surface could take place in the quasi-ballistic limit. To narrow down the possible reasons for the apparent violation of the Onsager reciprocity, more experiments should be done specifically designed in the quasi-ballistic regime of transport. Also, a theory with detailed formal derivation starting from quantum kinetic equation and applied in the quasi-ballistic transport regime is needed to test the validity of such violations.

In chapter 7, we have presented results on sputtered Bi_2Te_3-Fe heterostructures and have shown that the presence of the Bi_2Te_3 film increases the coercive field of the Fe film that could be due to strong spin obit coupling proximity effect from Bi_2Te_3. The proximity effect can be utilized for switching of the FM due to spin-transfer torque and field-like torque from the Bi_2Te_3, and preparing such devices by sputtering has great technological advantages as such devices could be integrated easily to other magnetic devices.

Bibliography

[1] M. Z. Hasan and C. L. Kane, "*Colloquium* : Topological insulators," *Rev. Mod. Phys.*, vol. 82, pp. 3045–3067, Nov 2010.

[2] X.-L. Qi and S.-C. Zhang, "Topological insulators and superconductors," *Rev. Mod. Phys.*, vol. 83, pp. 1057–1110, October 2011.

[3] Y. Ando, "Topological insulator materials," *Journal of the Physical Society of Japan*, vol. 82, no. 10, p. 102001, 2013.

[4] Y. Xia, D. Qian, D. Hsieh, L. Wray, A. Pal, H. Lin, A. Bansil, D. Grauer, Y. S. Hor, R. J. Cava, and M. Z. Hasan, "Observation of a large-gap topological-insulator class with a single Dirac cone on the surface," *Nature Physics*, vol. 5, pp. 398–402, May 2009.

[5] H. Zhang, C.-X. Liu, X.-L. Qi, X. Dai, Z. Fang, and S.-C. Zhang, "Topological insulators in Bi_2Se_3, Bi_2Te_3 and Sb_2Te_3 with a single Dirac cone on the surface," *Nature Physics*, vol. 5, pp. 438–442, May 2009.

[6] D. Hsieh, Y. Xia, D. Qian, L. Wray, J. Dil, F. Meier, J. Osterwalder, L. Patthey, J. Checkelsky, N. P. Ong, A. V. Fedorov, H. Lin, A. Bansil, D. Grauer, Y. S. Hor, R. J. Cava, and M. Z. Hasan, "A tunable topological insulator in the spin helical Dirac transport regime," *Nature*, vol. 460, no. 7259, p. 1101, 2009.

[7] Y. Ando and M. Shiraishi, "Spin to charge interconversion phenomena in the interface and surface states," *Journal of the Physical Society of Japan*, vol. 86, no. 1, p. 011001, 2017.

[8] Y. Fan and K. L. Wang, "Spintronics based on topological insulators," *SPIN*, vol. 06, no. 02, p. 1640001, 2016.

[9] V. Edelstein, "Spin polarization of conduction electrons induced by electric current in two-dimensional asymmetric electron systems," *Solid State Communications*, vol. 73, no. 3, pp. 233 – 235, 1990.

[10] K. Shen, G. Vignale, and R. Raimondi, "Microscopic theory of the inverse Edelstein effect," *Phys. Rev. Lett.*, vol. 112, p. 096601, Mar 2014.

[11] U. Roy, R. Dey, T. Pramanik, B. Ghosh, L. F. Register, and S. K. Banerjee, "Magnetization switching of a metallic nanomagnet via current-induced surface spin-polarization of an underlying topological insulator," *Journal of Applied Physics*, vol. 117, no. 16, p. 163906, 2015.

[12] B. Ghosh, R. Dey, L. F. Register, and S. K. Banerjee, "A simulation study of voltage-assisted low-energy switching of a perpendicular anisotropy ferromagnet on a topological insulator," *Journal of Computational Electronics*, vol. 16, pp. 120–126, Mar 2017.

[13] M. H. Fischer, A. Vaezi, A. Manchon, and E.-A. Kim, "Spin-torque generation in topological insulator based heterostructures," *Phys. Rev. B*, vol. 93, p. 125303, Mar 2016.

[14] B. Ghosh, R. Dey, L. F. Register, and S. K. Banerjee, "Voltage-controlled low-energy switching of nanomagnets through Ruderman-Kittel-Kasuya-Yosida interactions for magnetoelectric device applications," *Journal of Applied Physics*, vol. 120, no. 3, p. 034303, 2016.

[15] S. Sayed, S. Hong, E. E. Marinero, and S. Datta, "Proposal of a single nano-magnet memory device," *IEEE Electron Device Letters*, vol. 38, no. 12, pp. 1665–1668, 2017.

[16] A. W. Stephan, J. Hu, and S. J. Koester, "Performance estimate of inverse RashbaEdelstein magnetoelectric devices for neuromorphic computing," *IEEE Journal on Exploratory Solid-State Computational Devices and Circuits*, vol. 5, pp. 25–33, June 2019.

[17] W. Tian, W. Yu, J. Shi, and Y. Wang, "The property, preparation and application of topological insulators: A review," *Materials*, vol. 10, no. 7, p. 814, 2017.

[18] H.-Z. Lu and S.-Q. Shen, "Weak localization of bulk channels in topological insulator thin films," *Phys. Rev. B*, vol. 84, p. 125138, Sep 2011.

[19] C.-X. Liu, H. Zhang, B. Yan, X.-L. Qi, T. Frauenheim, X. Dai, Z. Fang, and S.-C. Zhang, "Oscillatory crossover from two-dimensional to three-dimensional topological insulators," *Phys. Rev. B*, vol. 81, p. 041307, January 2010.

[20] K. He, Y. Zhang, C.-Z. Chang, C.-L. Song, L.-L. Wang, X. Chen, J.-F. Jia, Z. Fang, X. Dai, W.-Y. Shan, S.-Q. Shen, Q. Niu, X.-L. Qi, S.-C. Zhang, X.-C. Ma, and Q.-K. Xue, "Crossover of the three-dimensional topological insulator Bi_2Se_3 to the two-dimensional limit," *Nature Physics*, vol. 6, pp. 584–588, June 2010.

[21] J. Linder, T. Yokoyama, and A. Sudbø, "Anomalous finite size effects on surface states in the topological insulator Bi_2Se_3," *Phys. Rev. B*, vol. 80, p. 205401, Nov 2009.

[22] P. A. Lee and T. V. Ramakrishnan, "Disordered electronic systems," *Rev. Mod. Phys.*, vol. 57, pp. 287–337, April 1985.

[23] H.-Z. Lu and S.-Q. Shen, "Finite-temperature conductivity and magnetoconductivity of topological insulators," *Phys. Rev. Lett.*, vol. 112, p. 146601, Apr 2014.

[24] W.-Y. Shan, H.-Z. Lu, and S.-Q. Shen, "Spin-orbit scattering in quantum diffusion of massive Dirac fermions," *Phys. Rev. B*, vol. 86, p. 125303, Sep 2012.

[25] G. Tkachov and E. M. Hankiewicz, "Weak antilocalization in HgTe quantum wells and topological surface states: Massive versus massless Dirac fermions," *Phys. Rev. B*, vol. 84, p. 035444, Jul 2011.

[26] H.-Z. Lu, J. Shi, and S.-Q. Shen, "Competition between weak localization and antilocalization in topological surface states," *Phys. Rev. Lett.*, vol. 107, p. 076801, Aug 2011.

[27] S. Zhang and A. Fert, "Conversion between spin and charge currents with topological insulators," *Phys. Rev. B*, vol. 94, p. 184423, Nov 2016.

[28] Li, CH and vant Erve, OMJ and Robinson, JT and Liu, Y and Li, L and Jonker, BT, "Electrical detection of charge-current-induced spin polarization due to spin-momentum locking in Bi_2Se_3," *Nature nanotechnology*, vol. 9, no. 3, pp. 218–224, 2014.

[29] J. Tang, L.-T. Chang, X. Kou, K. Murata, E. S. Choi, M. Lang, Y. Fan, Y. Jiang, M. Montazeri, W. Jiang, Y. Wang, L. He, and K. L. Wang, "Electrical detection of spin-polarized surface states conduction in $(Bi_{0.53}Sb_{0.47})_2Te_3$ topological insulator," *Nano Letters*, vol. 14, no. 9, pp. 5423–5429, 2014.

[30] A. Dankert, J. Geurs, M. V. Kamalakar, S. Charpentier, and S. P. Dash, "Room temperature electrical detection of spin polarized currents in topological insulators," *Nano Letters*, vol. 15, no. 12, pp. 7976–7981, 2015.

[31] L. Liu, A. Richardella, I. Garate, Y. Zhu, N. Samarth, and C.-T. Chen, "Spin-polarized tunneling study of spin-momentum locking in topological insulators," *Phys. Rev. B*, vol. 91, p. 235437, Jun 2015.

[32] J. S. Lee, A. Richardella, D. R. Hickey, K. A. Mkhoyan, and N. Samarth, "Mapping the chemical potential dependence of current-induced spin polarization in a topological insulator," *Phys. Rev. B*, vol. 92, p. 155312, Oct 2015.

[33] E. K. de Vries, A. M. Kamerbeek, N. Koirala, M. Brahlek, M. Salehi, S. Oh, B. J. van Wees, and T. Banerjee, "Towards the understanding of the origin of charge-current-induced spin voltage signals in the topological insulator Bi_2Se_3," *Phys. Rev. B*, vol. 92, p. 201102, Nov 2015.

[34] F. Yang, S. Ghatak, A. A. Taskin, K. Segawa, Y. Ando, M. Shiraishi, Y. Kanai, K. Matsumoto, A. Rosch, and Y. Ando, "Switching of charge-current-induced spin polarization in the topological insulator $BiSbTeSe_2$," *Phys. Rev. B*, vol. 94, p. 075304, Aug 2016.

[35] A. Dankert, P. Bhaskar, D. Khokhriakov, I. H. Rodrigues, B. Karpiak, M. V. Kamalakar, S. Charpentier, I. Garate, and S. P. Dash, "Origin and evolution of surface spin current in topological insulators," *Phys. Rev. B*, vol. 97, p. 125414, Mar 2018.

[36] C. H. Li, O. M. vant Erve, S. Rajput, L. Li, and B. T. Jonker, "Direct comparison of current-induced spin polarization in topological insulator Bi_2Se_3 and InAs Rashba states," *Nature Communications*, vol. 7, p. 13518, 2016.

[37] C. H. Li, O. M. J. van t Erve, Y. Y. Li, L. Li, and B. T. Jonker, "Electrical detection of the helical spin texture in a p-type topological insulator Sb_2Te_3," *Scientific reports*, vol. 6, p. 29533, 2016.

[38] C. H. Li, O. M. J. van t Erve, C. Yan, L. Li, and B. T. Jonker, "Electrical detection of charge-to-spin and spin-to-charge conversion in a topological insulator Bi_2Te_3 using BN/Al_2O_3 hybrid tunnel barrier," *Scientific reports*, vol. 8, p. 10265, 2018.

[39] J. Tian, I. Miotkowski, S. Hong, and Y. P. Chen, "Electrical injection and detection of spin-polarized currents in topological insulator Bi_2Te_2Se," *Scientific reports*, vol. 5, p. 14293, 2015.

[40] Y. Ando, T. Hamasaki, T. Kurokawa, K. Ichiba, F. Yang, M. Novak, S. Sasaki, K. Segawa, Y. Ando, and M. Shiraishi, "Electrical detection of the spin polarization due to charge flow in the surface state of the topological insulator $Bi_{1.5}Sb_{0.5}Te_{1.7}Se_{1.3}$," *Nano Letters*, vol. 14, no. 11, pp. 6226–6230, 2014.

[41] J. R. Sánchez, L. Vila, G. Desfonds, S. Gambarelli, J. Attané, J. De Teresa, C. Magén, and A. Fert, "Spin-to-charge conversion using Rashba coupling at the interface between non-magnetic materials," *Nature communications*, vol. 4, p. 2944, 2013.

[42] J.-C. Rojas-Sánchez, S. Oyarzún, Y. Fu, A. Marty, C. Vergnaud, S. Gambarelli, L. Vila, M. Jamet, Y. Ohtsubo, A. Taleb-Ibrahimi, P. Le Fèvre, F. Bertran, N. Reyren, J.-M. George, and A. Fert, "Spin to charge conversion at room temperature by spin pumping into a new type of topological insulator: α-Sn films," *Phys. Rev. Lett.*, vol. 116, p. 096602, Mar 2016.

[43] Y. Shiomi, K. Nomura, Y. Kajiwara, K. Eto, M. Novak, K. Segawa, Y. Ando, and E. Saitoh, "Spin-electricity conversion induced by spin injection into topological insulators," *Phys. Rev. Lett.*, vol. 113, p. 196601, Nov 2014.

[44] M. Jamali, J. S. Lee, J. S. Jeong, F. Mahfouzi, Y. Lv, Z. Zhao, B. K. Nikoli, K. A. Mkhoyan, N. Samarth, and J.-P. Wang, "Giant spin pumping and inverse spin hall effect in the presence of surface and bulk spinorbit coupling of topological insulator Bi_2Se_3," *Nano Letters*, vol. 15, no. 10, pp. 7126–7132, 2015.

[45] C. N. Wu, Y. H. Lin, Y. T. Fanchiang, H. Y. Hung, H. Y. Lin, P. H. Lin, J. G. Lin, S. F. Lee, M. Hong, and J. Kwo, "Strongly enhanced spin current in topological insulator/ferromagnetic metal heterostructures by spin pumping," *Journal of Applied Physics*, vol. 117, no. 17, p. 17D148, 2015.

[46] P. Deorani, J. Son, K. Banerjee, N. Koirala, M. Brahlek, S. Oh, and H. Yang, "Observation of inverse spin Hall effect in bismuth selenide," *Phys. Rev. B*, vol. 90, p. 094403, Sep 2014.

[47] F. B. Abdulahad, J.-H. Lin, Y. Liou, W.-K. Chiu, L.-J. Chang, M.-Y. Kao, J.-Z. Liang, D.-S. Hung, and S.-F. Lee, "Spin chemical potential bias induced surface current

evidenced by spin pumping into the topological insulator Bi_2Te_3," *Phys. Rev. B*, vol. 92, p. 241304, Dec 2015.

[48] K. T. Yamamoto, Y. Shiomi, K. Segawa, Y. Ando, and E. Saitoh, "Universal scaling for the spin-electricity conversion on surface states of topological insulators," *Phys. Rev. B*, vol. 94, p. 024404, Jul 2016.

[49] K. Kondou, R. Yoshimi, A. Tsukazaki, Y. Fukuma, J. Matsuno, K. Takahashi, M. Kawasaki, Y. Tokura, and Y. Otani, "Fermi-level-dependent charge-to-spin current conversion by Dirac surface states of topological insulators," *Nature Physics*, vol. 12, no. 11, pp. 1027–1031, 2016.

[50] S. Hong, V. Diep, S. Datta, and Y. P. Chen, "Modeling potentiometric measurements in topological insulators including parallel channels," *Phys. Rev. B*, vol. 86, p. 085131, Aug 2012.

[51] T. Yokoyama and Y. Tserkovnyak, "Spin diffusion and magnetoresistance in ferromagnet/topological-insulator junctions," *Phys. Rev. B*, vol. 89, p. 035408, Jan 2014.

[52] P. Li and I. Appelbaum, "Interpreting current-induced spin polarization in topological insulator surface states," *Phys. Rev. B*, vol. 93, p. 220404, Jun 2016.

[53] S. Hong, S. Sayed, and S. Datta, "Spin circuit model for 2D channels with spin-orbit coupling," *Scientific reports*, vol. 6, p. 20325, 2016.

[54] S. Sayed, S. Hong, and S. Datta, "Multi-terminal spin valve on channels with spin-momentum locking," *Scientific reports*, vol. 6, p. 35658, 2016.

[55] M. Buttiker, "Symmetry of electrical conduction," *IBM Journal of Research and Development*, vol. 32, pp. 317–334, May 1988.

[56] J. Tian, I. Childres, H. Cao, T. Shen, I. Miotkowski, and Y. P. Chen, "Topological insulator based spin valve devices: Evidence for spin polarized transport of spin-momentum-locked topological surface states," *Solid State Communications*, vol. 191, pp. 1 – 5, 2014.

[57] M. Zhang, X. Wang, S. Zhang, Y. Gao, Z. Yu, X. Zhang, M. Gao, F. Song, J. Du, X. Wang, L. He, Y. Xu, and R. Zhang, "Unique current-direction-dependent ON-OFF switching in $BiSbTeSe_2$ topological insulator-based spin valve transistors," *IEEE Electron Device Letters*, vol. 37, pp. 1231–1233, Sept 2016.

[58] R. Dey, N. Prasad, L. F. Register, and S. K. Banerjee, "Conversion of spin current into charge current in a topological insulator: Role of the interface," *Phys. Rev. B*, vol. 97, p. 174406, May 2018.

[59] W. Luo, W. Y. Deng, H. Geng, M. N. Chen, R. Shen, L. Sheng, and D. Y. Xing, "Perfect inverse spin Hall effect and inverse Edelstein effect due to helical spin-momentum locking in topological surface states," *Phys. Rev. B*, vol. 93, p. 115118, Mar 2016.

[60] H. Geng, W. Luo, W. Deng, L. Sheng, R. Shen, and D. Xing, "Theory of inverse Edelstein effect of the surface states of a topological insulator," *Scientific Reports*, vol. 7, no. 1, p. 3755, 2017.

[61] J. Bardeen, "Tunnelling from a many-particle point of view," *Phys. Rev. Lett.*, vol. 6, pp. 57–59, Jan 1961.

[62] N. B. Kopnin and A. S. Melnikov, "Proximity-induced superconductivity in two-dimensional electronic systems," *Phys. Rev. B*, vol. 84, p. 064524, Aug 2011.

[63] N. B. Kopnin, I. M. Khaymovich, and A. S. Mel'nikov, "Predicted multiple cores of a magnetic vortex threading a two-dimensional metal proximity coupled to a superconductor," *Phys. Rev. Lett.*, vol. 110, p. 027003, Jan 2013.

[64] H. G. Hugdal, J. Linder, and S. H. Jacobsen, "Quasiclassical theory for the superconducting proximity effect in Dirac materials," *Phys. Rev. B*, vol. 95, p. 235403, Jun 2017.

[65] A. Zyuzin, M. Alidoust, and D. Loss, "Josephson junction through a disordered topological insulator with helical magnetization," *Phys. Rev. B*, vol. 93, p. 214502, Jun 2016.

[66] I. V. Bobkova, A. M. Bobkov, A. A. Zyuzin, and M. Alidoust, "Magnetoelectrics in disordered topological insulator Josephson junctions," *Phys. Rev. B*, vol. 94, p. 134506, Oct 2016.

[67] P. Schwab, R. Raimondi, and C. Gorini, "Spin-charge locking and tunneling into a helical metal," *EPL (Europhysics Letters)*, vol. 93, no. 6, p. 67004, 2011.

[68] M. B. Walker, "Surface relaxation and quasiparticle interactions in conduction-electron spin resonance," *Phys. Rev. B*, vol. 3, pp. 30–41, Jan 1971.

[69] J. Rammer and H. Smith, "Quantum field-theoretical methods in transport theory of metals," *Rev. Mod. Phys.*, vol. 58, pp. 323–359, Apr 1986.

[70] D. C. Langreth and J. W. Wilkins, "Theory of spin resonance in dilute magnetic alloys," *Phys. Rev. B*, vol. 6, pp. 3189–3227, Nov 1972.

[71] D. Wortmann, H. Ishida, and S. Blügel, "Embedded Green-function formulation of tunneling conductance: Bardeen versus Landauer approaches," *Phys. Rev. B*, vol. 72, p. 235113, Dec 2005.

[72] J. Kim, Y.-T. Chen, S. Karube, S. Takahashi, K. Kondou, G. Tatara, and Y. Otani, "Evaluation of bulk-interface contributions to Edelstein magnetoresistance at metal/oxide interfaces," *Phys. Rev. B*, vol. 96, p. 140409, Oct 2017.

[73] Q. Song, H. Zhang, T. Su, W. Yuan, Y. Chen, W. Xing, J. Shi, J. Sun, and W. Han, "Observation of inverse Edelstein effect in Rashba-split 2DEG between $SrTiO_3$ and $LaAlO_3$ at room temperature," *Science Advances*, vol. 3, no. 3, 2017.

[74] E. Lesne, Y. Fu, S. Oyarzun, J. Rojas-Sánchez, D. Vaz, H. Naganuma, G. Sicoli, J.-P. Attané, M. Jamet, E. Jacquet, J.-M. George, A. Barthlmy, H. Jaffrs, A. Fert, M. Bibes, and L. Vila, "Highly efficient and tunable spin-to-charge conversion through Rashba coupling at oxide interfaces," *Nature materials*, 2016.

[75] R. Dey, L. F. Register, and S. K. Banerjee, "Modeling all-electrical detection of the inverse Edelstein effect by spin-polarized tunneling in a topological-insulator/ferromagnetic-metal heterostructure," *Phys. Rev. B*, vol. 97, p. 144417, Apr 2018.

[76] R. Dey, L. F. Register, and S. K. Banerjee, "Erratum: Modeling all-electrical detection of the inverse Edelstein effect by spin-polarized tunneling in a topological-insulator/ferromagnetic-metal heterostructure [Phys. Rev. B 97, 144417 (2018)]," *Phys. Rev. B*, vol. 98, p. 219908, Dec 2018.

[77] A. A. Burkov and D. G. Hawthorn, "Spin and charge transport on the surface of a topological insulator," *Phys. Rev. Lett.*, vol. 105, p. 066802, Aug 2010.

[78] K. Taguchi, T. Yokoyama, and Y. Tanaka, "Giant magnetoresistance in the junction of two ferromagnets on the surface of diffusive topological insulators," *Phys. Rev. B*, vol. 89, p. 085407, Feb 2014.

[79] S. Modak, K. Sengupta, and D. Sen, "Spin injection into a metal from a topological insulator," *Phys. Rev. B*, vol. 86, p. 205114, Nov 2012.

[80] M. Götte, T. Paananen, G. Reiss, and T. Dahm, "Tunneling magnetoresistance devices based on topological insulators: Ferromagnet-insulator-topological-insulator junctions employing Bi_2Se_3," *Phys. Rev. Applied*, vol. 2, p. 054010, Nov 2014.

[81] Y. G. Semenov, X. Duan, X.-L. Li, and K. W. Kim, "Conductance nonreciprocity on the surface of a topological insulator with magnetic electrodes," *Journal of Physics and Chemistry of Solids*, 2017.

[82] R. Dey, A. Roy, T. Pramanik, A. Rai, S. Heon Shin, S. Majumder, L. F. Register, and S. K. Banerjee, "Detection of current induced spin polarization in epitaxial Bi_2Te_3 thin film," *Applied Physics Letters*, vol. 110, no. 12, p. 122403, 2017.

[83] S. Majumder, S. Guchhait, R. Dey, L. Register, and S. K. Banerjee, "Large magnetoresistance at room temperature in ferromagnet/topological insulator contacts," *IEEE Transactions on Nanotechnology*, vol. 15, no. 4, p. 671, 2016.

[84] E. G. Mishchenko, A. V. Shytov, and B. I. Halperin, "Spin current and polarization in impure two-dimensional electron systems with spin-orbit coupling," *Phys. Rev. Lett.*, vol. 93, p. 226602, Nov 2004.

[85] E. I. Rashba, "Spin currents in thermodynamic equilibrium: The challenge of discerning transport currents," *Phys. Rev. B*, vol. 68, p. 241315, Dec 2003.

[86] X. Liu and J. Sinova, "Reading charge transport from the spin dynamics on the surface of a topological insulator," *Phys. Rev. Lett.*, vol. 111, p. 166801, Oct 2013.

[87] R. Dey, A. Roy, T. Pramanik, S. Guchhait, S. Sonde, A. Rai, L. F. Register, and S. K. Banerjee, "Localization and interaction effects of epitaxial Bi_2Se_3 bulk states in two-dimensional limit," *Journal of Applied Physics*, vol. 120, no. 16, p. 164301, 2016.

[88] J. Chen, H. J. Qin, F. Yang, J. Liu, T. Guan, F. M. Qu, G. H. Zhang, J. R. Shi, X. C. Xie, C. L. Yang, K. H. Wu, Y. Q. Li, and L. Lu, "Gate-voltage control of chemical potential and weak antilocalization in Bi_2Se_3," *Phys. Rev. Lett.*, vol. 105, p. 176602, October 2010.

[89] J. G. Checkelsky, Y. S. Hor, R. J. Cava, and N. P. Ong, "Bulk band gap and surface state conduction observed in voltage-tuned crystals of the topological insulator Bi_2Se_3," *Phys. Rev. Lett.*, vol. 106, p. 196801, May 2011.

[90] J. Chen, X. Y. He, K. H. Wu, Z. Q. Ji, L. Lu, J. R. Shi, J. H. Smet, and Y. Q. Li, "Tunable surface conductivity in Bi_2Se_3 revealed in diffusive electron transport," *Phys. Rev. B*, vol. 83, p. 241304, June 2011.

[91] Y. S. Kim, M. Brahlek, N. Bansal, E. Edrey, G. A. Kapilevich, K. Iida, M. Tanimura, Y. Horibe, S.-W. Cheong, and S. Oh, "Thickness-dependent bulk properties and weak antilocalization effect in topological insulator Bi_2Se_3," *Phys. Rev. B*, vol. 84, p. 073109, August 2011.

[92] N. Bansal, Y. S. Kim, M. Brahlek, E. Edrey, and S. Oh, "Thickness-independent transport channels in topological insulator Bi_2Se_3 thin films," *Phys. Rev. Lett.*, vol. 109, p. 116804, Sep 2012.

[93] S.-P. Chiu and J.-J. Lin, "Weak antilocalization in topological insulator Bi_2Te_3 microflakes," *Phys. Rev. B*, vol. 87, p. 035122, January 2013.

[94] A. Roy, S. Guchhait, S. Sonde, R. Dey, T. Pramanik, A. Rai, H. C. P. Movva, L. Colombo, and S. K. Banerjee, "Two-dimensional weak anti-localization in Bi_2Te_3 thin film grown on Si(111)-(7×7) surface by molecular beam epitaxy," *Applied Physics Letters*, vol. 102, no. 16, p. 163118, 2013.

[95] R. Dey, T. Pramanik, A. Roy, A. Rai, S. Guchhait, S. Sonde, H. C. P. Movva, L. Colombo, L. F. Register, and S. K. Banerjee, "Strong spin-orbit coupling and Zeeman spin splitting in angle dependent magnetoresistance of Bi_2Te_3," *Applied Physics Letters*, vol. 104, no. 22, p. 223111, 2014.

[96] Y. Takagaki, B. Jenichen, U. Jahn, M. Ramsteiner, and K.-J. Friedland, "Weak antilocalization and electron-electron interaction effects in Cu-doped Bi_2Se_3 films," *Phys. Rev. B*, vol. 85, p. 115314, March 2012.

[97] M. Liu, C.-Z. Chang, Z. Zhang, Y. Zhang, W. Ruan, K. He, L.-L. Wang, X. Chen, J.-F. Jia, S.-C. Zhang, Q.-K. Xue, X. Ma, and Y. Wang, "Electron interaction-driven insulating ground state in Bi_2Se_3 topological insulators in the two-dimensional limit," *Phys. Rev. B*, vol. 83, p. 165440, April 2011.

[98] J. Wang, A. M. DaSilva, C.-Z. Chang, K. He, J. K. Jain, N. Samarth, X.-C. Ma, Q.-K. Xue, and M. H. W. Chan, "Evidence for electron-electron interaction in topological insulator thin films," *Phys. Rev. B*, vol. 83, p. 245438, June 2011.

[99] H. B. Zhang, H. L. Yu, D. H. Bao, S. W. Li, C. X. Wang, and G. W. Yang, "Weak localization bulk state in a topological insulator Bi_2Te_3 film," *Phys. Rev. B*, vol. 86, p. 075102, Aug 2012.

[100] L. Zhang, M. Dolev, Q. I. Yang, R. H. Hammond, B. Zhou, A. Palevski, Y. Chen, and A. Kapitulnik, "Weak localization effects as evidence for bulk quantization in Bi_2Se_3 thin films," *Phys. Rev. B*, vol. 88, p. 121103, Sep 2013.

[101] H.-Z. Lu and S.-Q. Shen, "Weak localization and weak anti-localization in topological insulators," *Proc. SPIE, Spintronics VII*, p. 9167, Aug 2014.

[102] S. Hikami, A. Larkin, and Y. Nagaoka, "Spin-orbit interaction and magnetoresistance in the two dimensional random system," *Progress of Theoretical Physics*, vol. 63, no. 2, pp. 707–710, 1980.

[103] L. He, F. Xiu, Y. Wang, A. V. Fedorov, G. Huang, X. Kou, M. Lang, W. P. Beyermann, J. Zou, and K. L. Wang, "Epitaxial growth of Bi_2Se_3 topological insulator thin films on Si (111)," *Journal of Applied Physics*, vol. 109, no. 10, p. 103702, 2011.

[104] G. Zhang, H. Qin, J. Teng, J. Guo, Q. Guo, X. Dai, Z. Fang, and K. Wu, "Quintuple-layer epitaxy of thin films of topological insulator Bi_2Se_3," *Applied Physics Letters*, vol. 95, no. 5, p. 053114, 2009.

[105] H. Li, L. Gao, H. Li, G. Wang, J. Wu, Z. Zhou, and Z. Wang, "Growth and band alignment of Bi_2Se_3 topological insulator on H-terminated Si(111) van der Waals surface," *Applied Physics Letters*, vol. 102, no. 7, p. 074106, 2013.

[106] J. E. Brom, Y. Ke, R. Du, D. Won, X. Weng, K. Andre, J. C. Gagnon, S. E. Mohney, Q. Li, K. Chen, X. X. Xi, and J. M. Redwing, "Structural and electrical properties

of epitaxial Bi_2Se_3 thin films grown by hybrid physical-chemical vapor deposition," *Applied Physics Letters*, vol. 100, no. 16, p. 162110, 2012.

[107] X. Liu, D. J. Smith, J. Fan, Y.-H. Zhang, H. Cao, Y. P. Chen, J. Leiner, B. J. Kirby, M. Dobrowolska, and J. K. Furdyna, "Structural properties of Bi_2Te_3 and Bi_2Se_3 topological insulators grown by molecular beam epitaxy on GaAs(001) substrates," *Applied Physics Letters*, vol. 99, no. 17, p. 171903, 2011.

[108] B. Al'tshuler and A. Aronov, "Magnetoresistance of thin films and of wires in a longitudinal magnetic field," *JETP Lett.,*, vol. 33, no. 10, p. 499, 1981.

[109] Y. Takagaki, A. Giussani, K. Perumal, R. Calarco, and K.-J. Friedland, "Robust topological surface states in Sb_2Te_3 layers as seen from the weak antilocalization effect," *Phys. Rev. B*, vol. 86, p. 125137, Sep 2012.

[110] A. A. Taskin, S. Sasaki, K. Segawa, and Y. Ando, "Manifestation of topological protection in transport properties of epitaxial Bi_2Se_3 thin films," *Phys. Rev. Lett.*, vol. 109, p. 066803, Aug 2012.

[111] J. Lee, J. Park, J.-H. Lee, J. S. Kim, and H.-J. Lee, "Gate-tuned differentiation of surface-conducting states in $Bi_{1.5}Sb_{0.5}Te_{1.7}Se_{1.3}$ topological-insulator thin crystals," *Phys. Rev. B*, vol. 86, p. 245321, Dec 2012.

[112] Z. Li, I. Garate, J. Pan, X. Wan, T. Chen, W. Ning, X. Zhang, F. Song, Y. Meng, X. Hong, X. Wang, L. Pi, X. Wang, B. Wang, S. Li, M. A. Reed, L. Glazman, and G. Wang, "Experimental evidence and control of the bulk-mediated intersurface coupling in topological insulator Bi_2Te_2Se nanoribbons," *Phys. Rev. B*, vol. 91, p. 041401, Jan 2015.

[113] M. Brahlek, N. Koirala, M. Salehi, N. Bansal, and S. Oh, "Emergence of decoupled surface transport channels in bulk insulating Bi_2Se_3 thin films," *Phys. Rev. Lett.*, vol. 113, p. 026801, Jul 2014.

[114] H. Steinberg, J.-B. Laloë, V. Fatemi, J. S. Moodera, and P. Jarillo-Herrero, "Electrically tunable surface-to-bulk coherent coupling in topological insulator thin films," *Phys. Rev. B*, vol. 84, p. 233101, Dec 2011.

[115] I. Garate and L. Glazman, "Weak localization and antilocalization in topological insulator thin films with coherent bulk-surface coupling," *Phys. Rev. B*, vol. 86, p. 035422, Jul 2012.

[116] D. Kim, P. Syers, N. P. Butch, J. Paglione, and M. S. Fuhrer, "Coherent topological transport on the surface of Bi_2Se_3," *Nature Communications*, vol. 4, p. 2040, Jun 2013.

[117] C. M. Wang and F. J. Yu, "Effects of hexagonal warping on surface transport in topological insulators," *Phys. Rev. B*, vol. 84, p. 155440, Oct 2011.

[118] C. J. Lin, X. Y. He, J. Liao, X. X. Wang, V. S. IV, W. M. Yang, T. Guan, Q. M. Zhang, L. Gu, G. Y. Zhang, C. G. Zeng, X. Dai, K. H. Wu, and Y. Q. Li, "Parallel field magnetoresistance in topological insulator thin films," *Phys. Rev. B*, vol. 88, p. 041307, Jul 2013.

[119] X. Wang, X. He, T. Guan, J. Liao, C. Lin, K. Wu, Y. Li, and C. Zeng, "Transport properties of topological insulator Bi_2Se_3 thin films in tilted magnetic fields," *Physica E: Low-dim. Syst. and Nanostruct.*, vol. 46, pp. 236 – 240, 2012.

[120] H. Wang, H. Liu, C.-Z. Chang, H. Zuo, Y. Zhao, Y. Sun, Z. Xia, K. He, X. Ma, X. Xie, Q.-K. Xue, and J. Wang, "Crossover between weak antilocalization and weak localization of bulk states in ultrathin Bi_2Se_3 films," *Scientific reports*, vol. 4, p. 5817, 2014.

[121] G. M. Minkov, A. V. Germanenko, O. E. Rut, A. A. Sherstobitov, L. E. Golub, B. N. Zvonkov, and M. Willander, "Weak antilocalization in quantum wells in tilted magnetic fields," *Phys. Rev. B*, vol. 70, p. 155323, Oct 2004.

[122] P. Adroguer, D. Carpentier, J. Cayssol, and E. Orignac, "Diffusion at the surface of topological insulators," *New Journal of Physics*, vol. 14, no. 10, p. 103027, 2012.

[123] K. Saha and I. Garate, "Theory of bulk-surface coupling in topological insulator films," *Phys. Rev. B*, vol. 90, p. 245418, Dec 2014.

[124] H.-C. Liu, H.-Z. Lu, H.-T. He, B. Li, S.-G. Liu, Q. L. He, G. Wang, I. K. Sou, S.-Q. Shen, and J. Wang, "Tunable interaction-induced localization of surface electrons in antidot nanostructured Bi_2Te_3 thin films," *ACS Nano*, vol. 8, no. 9, pp. 9616–9621, 2014. PMID: 25184364.

[125] R. Dey, *Perpendicular and parallel field magnetoresistance in molecular beam epitaxy grown Bi_2Te_3*. PhD thesis, 2014.

[126] J. Suh, D. Fu, X. Liu, J. K. Furdyna, K. M. Yu, W. Walukiewicz, and J. Wu, "Fermi-level stabilization in the topological insulators Bi_2Se_3 and Bi_2Te_3: Origin of the surface electron gas," *Phys. Rev. B*, vol. 89, p. 115307, Mar 2014.

[127] J. Tian, S. Hong, I. Miotkowski, S. Datta, and Y. P. Chen, "Observation of current-induced, long-lived persistent spin polarization in a topological insulator: A rechargeable spin battery," *Science Advances*, vol. 3, no. 4, 2017.

[128] P. Nuthongkum, R. Sakdanuphab, M. Horprathum, and A. Sakulkalavek, "[Bi]:[Te] control, structural and thermoelectric properties of flexible Bi_xTe_y thin films prepared by RF magnetron sputtering at different sputtering pressures," *Journal of Electronic Materials*, vol. 46, pp. 6444–6450, Nov 2017.

[129] Y. Saito, P. Fons, K. Makino, K. V. Mitrofanov, F. Uesugi, M. Takeguchi, A. V. Kolobov, and J. Tominaga, "Compositional tuning in sputter-grown highly-oriented Bi–Te films and their optical and electronic structures," *Nanoscale*, vol. 9, no. 39, pp. 15115–15121, 2017.

[130] V. Russo, A. Bailini, M. Zamboni, M. Passoni, C. Conti, C. S. Casari, A. Li Bassi, and C. E. Bottani, "Raman spectroscopy of Bi-Te thin films," *Journal of Raman Spectroscopy*, vol. 39, no. 2, pp. 205–210, 2008.

[131] H. Xu, Y. Song, W. Pan, Q. Chen, X. Wu, P. Lu, Q. Gong, and S. Wang, "Vibrational properties of epitaxial Bi_4Te_3 films as studied by Raman spectroscopy," *AIP Advances*, vol. 5, no. 8, p. 087103, 2015.

[132] P. Nuthongkum, A. Sakulkalavek, and R. Sakdanuphab, "RSM base study of the effect of argon gas flow rate and annealing temperature on the [Bi]:[Te] ratio and thermoelectric properties of flexible Bi-Te thin film," *Journal of Electronic Materials*, vol. 46, pp. 2900–2907, May 2017.